Model-Based Process Identification for Pharmaceutical Synthesis

Zur Erlangung des akademischen Grades eines
Doktors der Ingenieurwissenschaften (Dr.-Ing.)
von der KIT-Fakultät für Elektrotechnik und Informationstechnik des
Karlsruher Instituts für Technologie (KIT)

angenommene
Dissertation
von

M.Sc. Moritz Schulze
geboren am 14.11.1987 in Stuttgart

Tag der mündlichen Prüfung: 13. Oktober 2023
Referentin: Prof. Dr.-Ing. Ulrike Krewer
Koreferent: Prof. Dr.-Ing. Andreas Seidel-Morgenstern

Preface

The work of this thesis was conducted during my employment as a research associate at the Institute of Energy and Process Systems Engineering of the TU Braunschweig between November 2016 and May 2021. My supervisors were the institute head Prof. Dr.-Ing. Ulrike Krewer and Prof. Dr.-Ing. René Schenkendorf, leader of the Pharmaceutical Process Systems Engineering group.

The first part of this thesis originates from a collaboration with the Physical and Chemical Foundations of Process Engineering research group, headed by Prof. Dr.-Ing. Seidel-Morgenstern, of the Max Planck Institute for Dynamics of Complex Technical Systems Magdeburg. My direct collaborator was Dr.-Ing. Susann Triemer, who designed, characterized and run the experimental setups for the partial synthesis of artemisinin. The corresponding mathematical equations describing the reactor and the chemical reaction networks were developed in joint work. I implemented the different models, and performed the modeling activities for the identification and the analysis of the synthesis process. This work was supported by the International Max Planck Research School for Advanced Methods in Process Systems Engineering at Magdeburg, of which I became a member at the turn of the year 2018/2019.

I also was affiliated with the Center for Pharmaceutical Engineering at the TU Braunschweig, where in cooperation with Dr.-Ing. Lasse Frey I supervised and guided the development of a computer vision program for the automatic detection of mixing properties in micro reactors. In 2019, I was abroad for a three months research stay at the Argonne National Laboratory, USA, where I worked together with Sven Leyffer, Ph.D., and Mohan Krishnamoorthy, Ph.D., on robust parameter estimation for high energy physics experiments.

The research findings in this thesis have been published in scientific journals and presented at conferences. A list of publications with contributions from my side is given on the following pages.

Research publications

Journal articles

1. Tappe, A. A., Schulze, M., and Schenkendorf, R. "Neural ODEs and Differential Flatness for Total Least Squares Parameter Estimation". In: *IFAC-PapersOnLine* 55.20 (2022), pp. 421–426.

2. Triemer, S.*, Schulze, M.*, Wriedt, B., Schenkendorf, R., Ziegenbalg, D., Krewer, U., and Seidel-Morgenstern, A. "Kinetic Analysis of the Partial Synthesis of Artemisinin: Photooxygenation to the Intermediate Hydroperoxide". In: *Journal of Flow Chemistry* 11.3 (2021), pp. 641–659.

3. Schulze, M. and Schenkendorf, R. "Robust Model Selection: Flatness-Based Optimal Experimental Design for a Biocatalytic Reaction". In: *Processes* 8.2 (2020), pp. 233–238.

4. Frey, L. J., Vorländer, D., Rasch, D., Ostsieker, H., Müller, B., Schulze, M., Schenkendorf, R., Mayr, T., Grosch, J.-H., and Krull, R. "Novel Electrodynamic Oscillation Technique Enables Enhanced Mass Transfer and Mixing for Cultivation in Micro-Bioreactor". In: *Biotechnology Progress* 35.5 (2019).

5. Schulze, M. and Schenkendorf, R. "Flatness-Based Design of Experiments for Model Selection". In: *IFAC-PapersOnLine* 51.15 (2018), pp. 233–238.

6. Emenike, V. N., Schulze, M., Schenkendorf, R., and Krewer, U. "Model-Based Optimization of the Recombinant Protein Production in Pichia Pastoris Based on Dynamic Flux Balance Analysis and Elementary Process Functions". In: *27th European Symposium on Computer Aided Process Engineering*. Vol. 40. Computer Aided Chemical Engineering. Elsevier, 2017, pp. 2815–2820.

Conference contributions

1. Schulze, M. and Schenkendorf, R. "Flatness-Based Model Selection of Benzaldehyde Lyase Catalysed Biochemical Reaction Network". Oral presentation. International Conference on Mathematics in (Bio)Chemical Kinetics and Engineering (MaCKiE) 2017 (Budapest, Hungary). May 25–27, 2017.

---

*: contributed equally

2. Schulze, M. and Schenkendorf, R. "Flatness-Based Design of Experiments for Model Selection". Oral presentation. 18th IFAC Symposium on System Identification (SYSID) (Stockholm, Sweden). July 9–11, 2018.

3. Schulze, M. and Schenkendorf, R. "Robust Design of Experiments for Model Selection Using Inverse Modeling". Oral presentation. 5th European Congress of Applied Biotechnology (ECAB) (Florence, Italy). Sept. 15–19, 2019.

4. Schulze, M. and Schenkendorf, R. "Novel Aspects of Differential Flatness in Computer Aided Process Engineering: A Biopharmaceutical Manufacturing Perspective". Oral presentation. Computer Aided Process Engineering Forum (CAPE Forum) (Liège, Belgium). Nov. 24–26, 2019.

5. Schulze, M. "Parameter Identifiability of Artemisinin Synthesis Using Design of Experiments". Poster presentation. 3rd Braunschweig International Symposium on Pharmaceutical Engineering Research (SPHeRE) (Braunschweig, Germany). Sept. 25–27, 2019.

6. Schulze, M. "Semi-Synthesis of Anti-Malaria Drug Artemisin: Modeling and Parameter Identifiability". Poster presentation. 4th Indo-German Workshop on Advances in Materials, Reactions & Separation Processes (Berlin, Germany). Feb. 24–26, 2020.

7. Triemer, S., Schulze, M., Schenkendorf, R., Krewer, U., and Seidel-Morgenstern, A. "Kinetic Investigation of a Photo- and Acid-Catalyzed Natural Product Synthesis in a Two-Phase Continuously Operated Tubular Reactor". Poster presentation. 10. ProcessNet-Jahrestagung Und 34. DECHEMA-Jahrestagung Der Biotechnologen (Online conference). Sept. 21–24, 2020.

8. Triemer, S., Schulze, M., Schenkendorf, R., Krewer, U., and Seidel-Morgenstern, A. "Kinetic Model for the Photocatalyzed Oxidation Step in the Partial Synthesis of an Antimalarial". Oral presentation. Annual Meeting on Reaction Engineering 2021 (Online conference). May 10–12, 2021.

9. Schulze, M., Schenkendorf, R., and Emenike, V. N. "An Algebraic Design of Experiments Method for a Bioenzymatic Reaction Network". Poster presentation. 12th European Symposium on Biochemical Engineering Sciences (ESBES) (Lisbon, Portugal). Sept. 9–12, 2018.

Biberach an der Riß, July 2023　　　　　　　　　　　　　　　　　　*Moritz Schulze*

Abstract

Mathematical modeling is a powerful tool to understand and design pharmaceutical syntheses, and is explicitly promoted by regulatory agencies within the progressive Quality by Design initiative. Since pharmaceutical syntheses frequently exhibit substantial mechanistic complexity with significant uncertainties about the involved reactions and other physical phenomena, systematic approaches following process systems engineering (PSE) principles facilitate the process identification procedure and enable reliable process analysis.

In this thesis, multiple concepts have been developed for the model-based process identification of pharmaceutical syntheses using PSE tools. The major part deals with the development of a mechanistic model for the two steps of the semi-synthesis of the antimalarial artemisinin (ART). In a milliscale flow reactor, the photo-induced conversion of dihydroartemisinic acid (DHAA) to a hydroperoxide is followed by an acid-catalyzed sequence in a second reactor yielding ART. The main challenges for the identification of this semi-synthesis process were limited available measurement information and incomplete knowledge about the occurring reaction mechanisms. Here, model-based design of experiments (MBDoE) ensured that the experimental measurements were sensitive to the model parameters. This enabled the description of the three-dimensional radiative transfer by the Beer-Lambert law. Relative deviations between simulated predictions from the applied two-fluid model and the observed formation of the hydroperoxide in the first step were 7.3 % on average. A global sensitivity analysis (GSA) revealed that the experimentally determined distribution factor of the two-fluid model had the largest impact on the species concentrations among the model parameters.

For the acid-catalyzed sequence, more than 60 different model candidates were proposed. High estimated reaction orders and another GSA identified the acid concentration to be the key factor, that significantly impact the reaction rates and the overall selectivity of ART. The selected model candidate for the acid-catalyzed reaction network was connected to the photo reactor and resulted in deviations of 14 % on average for the prediction of ART concentrations. The overall process was then optimized for ART yields under the consideration of parametric uncertainty, against which the developed process model showed to be very robust. The ART yield increased from 55 % to 61 % when the acid was fed before the photo reactor instead of dosed downstream at the synthesis reactor inlet. The optimized space-time yield reached 7.7 g/(ml d).

As for the semi-synthesis of ART, model selection problems frequently suffer from high non-linearities, significant uncertainties and missing mechanistic knowledge. Traditional approaches based on the integration of the underlying differential equations might lead to sub-optimal or misleading results. In the last part of this thesis differential flatness is therefore proposed as an alternative and exploited for model selection problems under parametric uncertainty for the first time. In this concept, an inverse model is identified, where the optimal controls from a robustified MBDoE ensure improved model selection trajectories, that are expressed analytically with low computational costs. The developed method was successfully applied to a biocatalytic reaction step simulating the carboligation of aldehydes. This showed that differential flatness can be a viable alternative for challenging model selection problems beyond its traditional use in control theory.

Kurzfassung

Mathematische Modellierung kann entscheidend zum Verständnis und bei der Auslegung von pharmazeutischen Syntheseprozessen beitragen und wird von Regulierungsbehörden im Rahmen der Quality by Design-Initiative ausdrücklich gefördert. Da pharmazeutische Synthesen häufig eine erhebliche mechanistische Komplexität aufweisen und Unsicherheiten über die beteiligten Reaktionen und andere physikalische Phänomene bestehen, bedarf es systematischer Ansätze, die den Prinzipien der Systemverfahrenstechnik (engl. Process Systems Engineering, PSE) folgen und somit eine verlässliche Prozessidentifikation und -analyse ermöglichen.

In dieser Arbeit wurden mehrere Konzepte für die modellbasierte Prozessidentifikation von pharmazeutischen Synthesen unter Verwendung von PSE-Methoden entwickelt. Der Hauptteil befasst sich mit der Entwicklung eines mechanistischen Modells für die zwei Schritte der Partialsynthese des Antimalaria-Wirkstoffes Artemisinin (ART). In einem kleinskaligen Durchflussreaktor folgt der photoinduzierten Umwandlung von Dihydroartemisininsäure (DHAA) in ein Hydroperoxid eine säurekatalysierte Reaktionskaskade hin zu ART. Die größten Herausforderungen für die Identifizierung dieses Synthese-Prozesses waren begrenzt verfügbare Messinformationen und unvollständiges Wissen über die auftretenden Reaktionsmechanismen. Der Einsatz von modellbasierter Versuchsplanung (engl. Model-Based Design of Experiments, MBDoE) stellte hierbei sicher, dass die experimentellen Messungen sensitiv gegenüber den Modellparametern waren. Dies ermöglichte die Beschreibung der dreidimensionalen Wärmestrahlung durch das Lambert-Beersche Gesetz. Die relativen Abweichungen zwischen Vorhersagen aus dem angewendeten Zwei-Fluid-Modell und der Konzentrations-Messdaten des Hydroperoxids im ersten Schritt betrugen durchschnittlich 7.3 %. Eine globale Sensitivitätsanalyse (GSA) ergab, dass der experimentell bestimmte Verteilungsfaktor des Zwei-Fluid-Modells den größten Einfluss auf die Spezieskonzentrationen unter den Modellparametern hatte.

Für die säurekatalysierte Reaktionskaskade wurden mehr als 60 verschiedene Modellkandidaten aufgestellt und analysiert. Hohe geschätzte Reaktionsordnungen und eine weitere GSA identifizierten die Säurekonzentration als den Schlüsselfaktor, der die Reaktionsraten und die Gesamtselektivität von ART erheblich beeinflusst. Der ausgewählte Modellkandidat für das säurekatalysierte Reaktionsnetzwerk wurde mit dem Photoreaktor-Modell verbunden und führte zu Abweichungen von durchschnittlich 14 % bei der Vorhersage der ART-Konzentrationen. Die Partialsynthese wurde dann unter Berücksichtigung der identifizierten Unsicherheiten in den

Modellparametern für eine hohe ART-Ausbeute optimiert, wobei sich das entwickelte Prozessmodell als sehr robust erwies. Die ART-Ausbeute stieg von 55 auf 61 %, wenn die Säure vor dem Photoreaktor zugeführt wurde anstatt am Einlass des nachgeschalteten Synthesereaktors. Die optimierte Raum-Zeit-Ausbeute erreichte 7.7 g/(ml d).

Wie bei der Partialsynthese von ART trifft man bei der Modellselektion regelmäßig auf signifikante Nichtlinearitäten, nicht vernachlässigbare Unsicherheiten und fehlendes mechanistisches Wissen. Traditionelle Ansätze, die auf der Integration der zugrunde liegenden Differentialgleichungen basieren, können dabei in suboptimalen oder irreführenden Ergebnissen resultieren. Im letzten Teil dieser Arbeit wird infolgedessen die differentielle Flachheit als Alternative vorgeschlagen und erstmals auf die Modellselektion bei gleichzeitiger Berücksichtigung von Unsicherheiten in Modellparametern übertragen. Bei diesem Ansatz wird ein inverses Modell identifiziert, welches im Gegensatz zur numerischen Integration analytische Lösungen liefert, die in einem robustifizierten MBDoE eingesetzt schließlich zu optimalen Steuerungsgrößen für die Modellselektion führen. Die entwickelte Methode wurde erfolgreich an einem biokatalytischen Reaktionsschritt angewendet, der die Carboligation von Aldehyden simuliert. Die Ergebnisse zeigten, dass die differentielle Flachheit jenseits ihrer traditionellen Verwendung in der Regelungstechnik eine nützliche Alternative bei anspruchsvoller Modellselektion darstellen kann.

Danksagung

Eine längere Reise findet ihr Ende. Sie wäre ohne die Begleitung, Unterstützung und Förderung von einigen besonderen Menschen so nicht möglich gewesen.

Vielen Dank Ulrike für die Möglichkeit meinem Wunsch der Forschung in Prozessmodellierung nachgehen zu können. Dein entgegen gebrachtes Vertrauen dies in einer Kooperation mit dem Max Planck Institut Magdeburg zu verfolgen, weiß ich zu schätzen. Gleichfalls trifft das auf Deinen Rat und Dein ehrliches Feedback in Gesprächen und Reviews zu. Ein weiteres Dankesehr geht an Prof. Andreas Seidel-Morgenstern für die Gelegenheit, dass ich Teil des Artemisinin-Projektes sein konnte. In den zahlreichen konstruktiven Diskussionen konnte ich meinen Betrachtungshorizont, insbesondere über eine reine Daten-Betrachung hinaus, deutlich erweitern. Danke auch für die Zusage als Zweitgutachter!

Lieber René, vielen Dank für Vieles! Ohne Deine fachliche Expertise wäre die Qualität und die Tiefe dieser Dissertation statistisch signifikant niedriger gewesen. Du hattest zu jeder Zeit ein offenes Ohr und zu jede meiner Fragen eine fundierte Antwort. Danke auch für Deinen steten Einsatz, den Du für alle in Deiner Gruppe regelmäßig erbracht hast.

Susann, ein großes Dankeschön! Für etliche spannende und häufig auch sehr lange Diskussionen, bei denen Du auch zu Unzeiten stets konzentriert und energetisch beigetragen hast. Sie hatten durchaus ein gewisses Suchtpotential. Dein Wissen über Reaktionsmechanismen, das weit über die Partialsynthese von Artemisinin reicht, und dein unermüdlicher Einsatz im Labor haben maßgeblich zur erfolgreichen Entwicklung des Modells beigetragen.

Vielen Dank an Prof. Dr. rer. nat. Dirk Ziegenbalg und Dr. Benjamin Wriedt für deren Unterstützung bei der Beschreibung und Quantifizierung der Lichtstrahlung im Photoreaktor. Bedanken möchte ich mich auch bei Dr. Sven Leyffer, der es mir ermöglichte für einen Forschungsaufenthalt ans Argonne National Laboratory in die Vereinigten Staaten zu kommen. In konstruktiver Zusammenarbeit mit ihm und Dr. Mohan Krishnamoorthy, konnte ich bereits angeeignetes Wissen anwenden, und Neues wieder mit nach Deutschland zurück nehmen.

Danke Victor und Xie für eine unbeschwerliche Zeit, die wir gemeinsam mit René als Forschungsgruppe hatten. Das gilt ebenso für weitere Kolleg*innen des Instituts und anderer Institute. Danke

Wilfried für Dein Engagement meinen regelmäßigen Anfragen zu Hard- und Software nachzugehen! Danke Lasse und unseren Studierenden Hari und Mateo für eine kurzweilige und erfolgreiche Zusammenarbeit zur Charakterisierung von Mikroreaktoren. Ein Dank geht ebenso an Henning für seine Arbeiten zu Sensitivitätsanalysen.

Liebe Inga, ein riesiges Dankeschön an Dich! Dein Rat in der nicht immer bunten Doktoratszeit war Gold wert. Tausend Dank für Dein nahezu unerschöpfliches Verständnis! Danke auch an alle meine Freundinnen und Freunde, die mich während meiner Zeit als Doktorand begleitet haben, und ohne die das Leben nur maximal halb so lustig wäre. Zuletzt möchte ich mich bei meiner Familie bedanken. Ihr hattet ohne Zweifel einen bedeutenden Anteil daran, dass ich diese Dissertation schreiben und mein Doktorat erfolgreich abschließen konnte.

Biberach an der Riß, Juli 2023 *Moritz Schulze*

Glossary

Abbreviations and Acronyms

AA	Artemisinic acid
ACT	Artemisinin-based combination therapy
AD	Amorphadiene
AIC	Akaike information criterion
ANOVA	Analysis of variance
API	Active pharmaceutical ingredient
ART	Artemisinin
CI	Confidence interval
COD	Coefficient of dispersion
DCA	9,10-dicyanoanthracene
DHAA	Dihydroartemisinic acid
DoE	Design of experiments
eOLS	Extended ordinary least squares
FIM	Fisher information matrix
GSA	Global sensitivity analysis
iPDA	Iteratively refined PDA
LED	Light-emitting diode
MBDoE	Model-based design of experiments
MC	Monte-Carlo
MIMO	Multiple input multiple output
MLE	Maximum likelihood estimate
MPI	Max Planck Institute
MSE	Mean squared error
MVUE	Minimum variance unbiased estimator
NMR	Nuclear magnetic resonance
ODE	Ordinary differential equation
OLS	Ordinary least squares
PAT	Process analytical technology

PDF	Probability density function
PEM	Point estimate method
PINN	Physics-informed neural network
PLL	Profile log likelihood
PO	Hydroperoxide
PS	Photosensitizer
PSE	Process systems engineering
QbD	Quality by design
SA	Sensitivity analysis
SI	Supporting information
SVD	Singular value decomposition
TFA	Trifluoroacetic acid
UA	Uncertainty analysis
WHO	World Health Organization

Latin Symbols

Symbol	Description	Default unit
A	Cross-sectional area of tube channel	cm^2
$\boldsymbol{A}$	Adjacency matrix	
AIC	Akaike information criterion	
AIC_c	Corrected Akaike information criterion	
B	B-spline	
c	Concentration	mol/l
C_0	Distribution factor in drift flux model	
CI	Confidence interval	
COD	Coefficient of dispersion	1
$\boldsymbol{C}_\theta$	Parameter covariance matrix	
d	Channel diameter	cm^2
D	Diffusion coefficient	m^2/s
f	(Model) Function	
$\boldsymbol{FIM}$	Fisher information matrix	
f_x	State equation	
f_y	Output equation	
g	Constraint function	
Ha	Hatta number	

$\boldsymbol{h}^{\text{flat}}$	Mapping function of flat outputs	
$\boldsymbol{IM}$	Information matrix	
j	Mass transfer flux	mol/(l min)
K	Number of estimated parameters	
k	Kinetic rate coefficient	1/min
$\tilde{k}$	Normalized kinetic rate coefficient	
$k_1 a$	Volumetric mass transfer coefficient	1/min
$\widetilde{k_1 a}$	Proportionality factor of mass transfer coefficient	$\sqrt{1/\text{cm}/\text{min}}$
l	Length	cm
l_{opt}	Optical path length	cm
L_{p}	Volumetric incident photon flux	mol/(l s)
$\tilde{L}_{\text{p}}$	Proportionality factor of photon flux	mol/(l s)
L_{UC}	Unit cell length	cm
L_{p}^{a}	Local volumetric rate of photon absorption	mol/(l s)
M	Molar mass	kg/mol
m	Reaction order	
N	Number of data points	
n	Number or dimension, e.g., size of a vector	
n	Number of moles	mol
OVL	Overlap metric	
p	Pressure	bar
pdf	Probability density function	
P_{LED}	LED power (percentage)	LED$-\%$
PLL	Profile log likelihood	
$\Pr\{\cdot\}$	Probability	
q_0	Absolute incident photon flux	mol/s
R	Universal gas constant (8.314 J/(K mol))	J/(K mol)
r	Rate of reaction	mol/(l min)
$\bar{r}$	Net rate of reaction	mol/(l min)
R	Recovery	1
RSS	Residual sum of squares	mol^2/l^2
S	Local sensitivity	
S	Sobol' index	1
s^2	Sample variance	
S	source, sink	kg/(l min)
S^{m}	source, sink (molar-based)	mol/(l min)
$\boldsymbol{SM}$	Sensitivity matrix	
STY	Space-time yield	mol/(l min)

T	Temperature	K
t	Time	min
u	(Model / System / Function) Input or control	
u	Velocity	cm/min
v	Right singular vector	
V	Volume	ml
$\dot{V}$	Volumetric flow	ml/min
w	Weight factors in point estimate method	
$\boldsymbol{w}$	Mass fraction	1
X	Conversion	1
x	State variable	
$\boldsymbol{x}$	Molar fraction	1
y	(Model / System / Function) Output	
$y^{\star}$	Physical system output	
$\tilde{y}$	(Experimental) data point	
Y	Yield	1
z	Spatial reactor coordinate	cm
Z	Standard normal distribution	

Greek Symbols

Symbol	Description	Default unit
α	Void fraction in two-fluid model	1
β	Gas holdup in two-fluid model	1
χ^2	Quantile of chi-square distribution	
δ	Indicator function	
ϵ	Random error term	
η	Stochastic measurement error	
γ	Flat output	
κ	Napierian absorption coefficient	1/(mol cm)
λ	Penalty weight factor	
μ	Mean	
ν	Rate of reaction	mol/(l min)
ν	Stoichiometric number	
Ω	Input space of $\boldsymbol{u}$	
Φ	Quantum yield	1

ϕ	Confidence level	
Ψ	Mapping function of inverse model	
ρ	Density	kg/mol
σ	Standard deviation	
σ	Singular value	
Σ	Measurement covariance matrix	
σ^2	Variance	
τ	Residence time	min
τ_Δ	Lifetime of singlet oxygen	µs
θ	Model parameter	
θ^*	Nominal parameter	
$\theta^\star$	True parameter	
$\tilde{\theta}$	Meta parameter	
ϑ	Spreading parameter in PEM	
$\hat{\theta}$	Estimated (model) parameter	
ξ	Design / Optimization variable	

Special Symbols

Symbol	Description
$\mathbb{E}[\cdot]$	Expectation operator
$\mathcal{J}$	Objective function
$\mathcal{L}$	Likelihood function
$\mathcal{M}$	Mathematical model (candidate)
$\mathbf{M}$	Set of model candidates
$\mathcal{N}$	Normal distribution
$\mathbb{N}$	Set of natural numbers
O	Input vector sets in point estimate method
$\mathbb{R}$	Set of real numbers
$\mathcal{U}$	Uniform distribution
$\mathbb{V}[\cdot]$	Variance operator
$[\cdot]$	Concentration

Subscripts and Superscripts

Symbol	Description
0	Initial or reference
b	Batch
c	Continuous
Dopt	D-optimal
ED	Euclidean distance
eq	Equality
f	Final
flat	Related to differential flatness
g	Gaseous
ineq	Inequality
l	Lumped
l	Liquid
N	Normed
opt	Optical
photo	Photooxygenation
r	Reactor
rED	Robust euclidean distance
rSTY	Robust space-time yield
s	Superficial
syn	Synthesis (related to acid-catalyzed sequence)
T	Total
T	Transpose
*	Nominal
⋆	True

Contents

1 Motivation and Scope

Modeling and simulation of physical systems has become ubiquitous in many sciences. The importance of process modeling stems from the fact that it is a prerequisite for system understanding, process control, process optimization and process design [1]. For solving the corresponding problems in chemical and biochemical processes, the scientific discipline of process systems engineering (PSE) provides the necessary systematic framework [2]. PSE has been drawing increasingly attention in pharmaceutical manufacturing as its tools and methods comply with the regulatory framework of Process Analytical Technology (PAT) [3] and the Quality by Design (QbD) approach [4, 5] that were introduced in the pharmaceutical industry around 20 years ago. This trend is equally mirrored in the published scientific literature, Figure 1.1. Conventionally, laboratory testing of samples collected from batch runs ensures the pharmaceutical quality standards. In contrast, the QbD approach advocates a systematic and risk-based methodology for the design, development and manufacturing of medicines as "quality cannot be tested into products; it should be built-in or should be by design" [3]. QbD and the QbD-consistent PAT framework both emphasize process understanding and control based on scientific principles [7] and the utilization of innovative process and strategic technologies and tools [3, 8]. Consequentially, the application of mathematical models for supporting process design, analytical procedures, and process monitoring and control is explicitly promoted from a regulatory perspective [8–10]; and PSE is foreseen to play an essential role in the development of future pharmaceutical processes [2, 11–16].
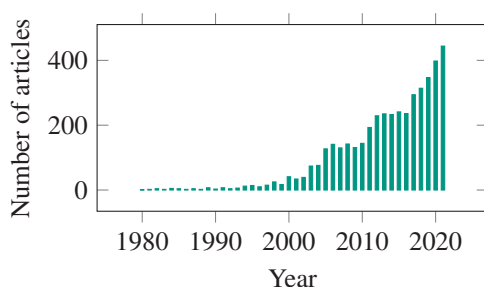

Figure 1.1: Increasing importance of process modelling, a key discipline of process systems engineering, in the pharmaceutical industry. Data was extracted from Scopus database with the following keywords employed in a *logical and* search within article title, abstract, and keywords: process, modelling, pharmaceutical [6].

1.1 Process Systems Engineering for Pharmaceutical Synthesis

To develop and optimize the synthetic production of active pharmaceutical ingredients (APIs) by (bio)chemical reactions, knowledge of the underlying mechanism and kinetics, that decisively determine the macroscopic process behavior and therefore reactor design, is key [17–19]. However, the identification of such a kinetic model is by no means a trivial task, even for well-studied reaction networks [20]. A major difficulty is the vast number of possible reactions, reaction intermediates and products [21], that is, a lack of information about the reaction network – a recurring problem in (bio)chemical syntheses and a major bottleneck for model-based process development [22, 23]. Additional challenges for identifying a process model with an underlying (bio)chemical reaction network arise from complex flow phenomena, limited availability of measurement data and substantial non-linearities in the process dynamics [24–27]. In such challenging settings, systematic approaches following PSE principles facilitate the model identification procedure [27, 28].

In model identification, notably model selection and parameter estimation, model-based design of experiments plays a pivotal role in the sense that it systematically reduces uncertainties in model structure and model parameters while keeping the experimental effort small [29–33]. Consideration of uncertainties is of significant importance as inference drawn from the usage of the model heavily relies on the accuracy of the model itself, its parameters and its input conditions [34]. This particularly holds for pharmaceutical processes where patient safety is paramount. To cope with parametric uncertainties, e.g., due to imperfect measurements, and variability in process inputs, sensitivity analysis offers a versatile toolbox to study the behavior of a (bio)chemical process and its influencing factors [35–37]. Methods for sensitivity analysis can be likewise applied in model-based process design to robustify against the uncertainties and variability, thereby increasing the design's reliability [38–40].

For pharmaceutical syntheses frequently exhibit substantial complexity and encounter model and parameter uncertainties, model identification and integration of uncertainties in model-based activities is an active research field [41–43]. In parameter estimation, the standard procedure with a great success history for many academic and industrial problems is the consideration of output residuals to estimate model parameter values, known as least squares [27]. It involves a comparison of the commonly integrated model dynamics with the available measurement data. However, in cases with high uncertainties and strong non-linearities, alternative approaches have been proposed in literature that ease the parameter estimation procedure and can lead to more reliable parameter estimates. Several approaches have in common that they release themselves from integrating the model dynamics, but propose functional relations for the model predictions and constrain these relations by the model dynamics [44–47]. In contrast, the application of an

inverse model inherently considers the model dynamics, that makes it able to precisely back-calculate the inputs of the model for a given system trajectory. Here, inverting models based on differential flatness, a system property introduced in 1992 [48], has been proven beneficial in postulating a well-posed parameter estimation problem [49]. Differential flatness strategies avoid the numerical problems linked to the integration of the process-underlying differential equations, reduce the need for experimentally determining corresponding initial conditions, enable straight-forward feed-forward control, and ease optimization problems by smoothing objective functions and providing analytic gradient and hessian functions [49, 50].

1.2 Partial Synthesis of the Antimalarial Artemisinin

The partial synthesis of the antimalarial API artemisinin (ART) and its continuous production is a prominent example of the challenges in pharmaceutical development and manufacturing of (bio)chemical syntheses. Malaria causes around 230 million infections and demands more than
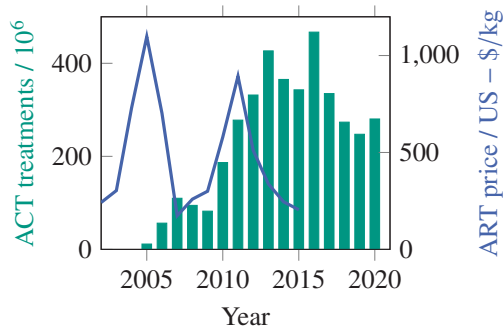
Figure 1.2: High price of artemisinin-based combination therapies (ACTs), and high volatility in both ACT treatments [51, 52] and artemisinin (ART) price [53] hinder a fast and successful fight against malaria on the globe.

400,000 fatalities each year with very high shares of children under five years of more than 75 % in the past [51]; although it is both preventable and curable if diagnosed and treated promptly in a correct manner. Medicines based on ART, referred to as artemisinin-based combination therapies (ACTs), show the best efficacy against malaria and are therefore recommended as first-line treatment by the World Health Organization since 2001 [54]. Unfortunately, next to other drivers, the relatively high and volatile price of ACTs hinders a fast and successful fight against the disease, Figure 1.2, in particular as malaria primarily appears in countries with low economic strength [55]. Despite a decrease since 2010, ACT prices are still much more expensive than other antimalarials [56]. New technologies for the production of ART have barely entered the ART market for high investment risks: Industrial attempts by companies Amyris and

Figure 1.3: Integration of the artemisinin partial synthesis starting from the extract byproduct dihydroartemisinic acid (DHAA) increases the artemisinin (ART) yield of the plant-based production [61]. Traditionally, ART production relies on solvent extraction of the existing ART in the plant and subsequent se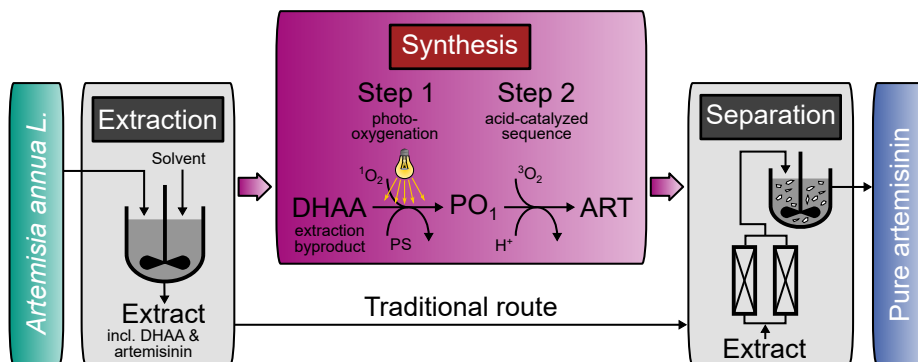paration by multi-stage crystallization and normal-phase liquid chromatography to obtain purified ART [62]. The partial synthesis consists out of two major steps. In the photooxygenation, the DHAA is converted to the hydroperoxide PO_1 by consuming singlet oxygen, that is photochemically produced with the help of a photosensitizer (PS). In the second step, ART is formed in an acid-catalyzed sequence. The Figure is reproduced and adapted from [61].

Sanofi have ceased operation [57]. One major cause of the price volatility are oscillations in the artemisinin supply, that are rooted in an unpredictable ART demand and a varying production of the natural source [53, 56]. The sole industrial supply technology of ART is the extraction of ART from leaves of the plant *Artemisia annua*. The bottlenecks of this established process are long production cycles, varying crop yields, competition for agricultural land, and a distinct inflexibility of the supply chain [56]. Next to the classical extraction of ART, processes based on syntheses from advanced precursors termed partial or semi-syntheses, like the Amyris and Sanofi examples, promise economic potential. Additional research stimuli result from findings that ART and its derivatives are not only antimalarial, but exhibit further active properties like anti-cancer, anti-inflammatory or anti-viral [58], and therefore motivate drug repurposing [59].

In contrast to batch and semi-batch operations of the Amyris and Sanofi partial syntheses, Lévesque and Seeberger [60] introduced a promising continuous-flow photochemical conversion of dihydroartemisinic acid (DHAA) to ART. DHAA is converted to artemisinin in a two-step process of a photooxygenation and a subsequent acid-catalyzed reaction cascade, Figure 1.3. The authors reported ART yields of up to 69 % based on initial DHAA concentration [60, 63]. The successful conversion of DHAA to ART by the presence of light has been previously observed during drying of *A. annua* [64] as DHAA is also found in the plant itself. Triemer and co-workers [65] combined the previous findings and produced ART from DHAA in the usually discarded extract of *A. annua* plants in a continuous photo-flow reactor. They made use of the in the plant existent chlorophylls as photosensitizers, resulting in a synthetic process that naturally supplies

the required photosensitizer and performs at least equally well as in the case of using pure reagents, Figure 1.3.

The proposed continuous photo-flow process for the production of ART is a promising route to decrease the medication costs with the prospective of a sustainable manufacturing process that helps to attain the vision of a world free of malaria. However, the physical phenomena in the two-phase flow reactor and the occurring (photo)chemical reactions exhibit a substantial degree of complexity, that are not sufficiently well understood to be used for process design and to be finally translated into a large-scale industrial manufacturing process. To this end, strategies within PSE exploit the potential of having a mathematical description of the real process at hand following a systematic model identification procedure. Characteristically for pharmaceutical synthesis, the process model identification for the partial synthesis of ART is in particular challenged by the identification of the reaction mechanisms, that are partly unknown. Further difficulties are the low number of measurable components and restricted possibilities to draw samples due to the process' complexity. Another challenge lies in the technology of flow photochemistry [66], that is, in the quantification of the two-phase fluid dynamics and the radiative heat transfer.

1.3   Scope and Structure of Thesis

The core research challenge in this work is the reliable identification of process models for pharmaceutical synthesis by following PSE strategies. In a first part of this thesis, the partial synthesis of artemisinin from dihydroartemisinic acid in a continuous-flow experimental setup is considered. A process model is to be developed for obtaining mechanistic and process-related insights. It should have manageable complexity to facilitate process understanding of the most influential parameters and to enable straightforward model-based process optimization. The difficulty originates in the limited available measurement data on the one and the complexity and incomplete knowledge of the occurring physical phenomena on the other hand – a common setting in pharmaceutical synthesis.

In a second part, inverse modeling is exploited for the problem of identifying a mathematical model for (bio)chemical syntheses in the pharmaceutical industry under the consideration of parametric uncertainties. Notably, the following research question is addressed: Is the utilization of inverse modeling techniques based on differential flatness a beneficial alternative to established methods for model identification? For answering, a first transfer of the differential flatness concept from control theory to model selection problems in (bio)chemical syntheses has to be performed. As a case study, a biocatalytic process from a carboligation reaction system that forms an essential precursor in pharmaceutical synthesis is investigated.

The specific goals of this work can be summarized as follows:

1. To identify a process model in the photooxygenation step that takes the interplay between light, mass transfer and chemical reactions into account.

2. To exploit the identified process model describing the photooxygenation for an analysis of the process behavior that is supported by a global sensitivity analysis.

3. To develop different reaction networks that potentially describe the acid-catalyzed sequence step of the partial synthesis. Subsequently, to perform a systematic identification analysis of the proposed networks with the help of the available sparse measurement data.

4. To utilize the overall process model, i.e., combining the identified photooxygenation model with the best reaction network candidate of the acid-catalyzed sequence, for a yield-based process optimization.

5. To develop a robust model selection strategy for pharmaceutically related (bio)chemical processes based on differential flatness.

6. To show that differential flatness is a beneficial alternative in model identification of pharmaceutical syntheses by applying the developed strategy to an enzymatic reaction network.

Following this introductory Chapter 1, Chapter 2 and 3 contain the fundamentals for the Chapters 4, 5 and 6, where the main research contributions are presented. A corresponding graphic outline is given in Figure 1.4. The thesis is closed with a concluding Chapter 7. Summaries of the Chapters are given in the following.

Chapter 2 – Introduction to the Artemisinin Partial Synthesis and the Applied Experimental Setups.   After a short background on the partial synthesis of artemisinin, industrial and academic approaches to a continuous production are discussed. Closing, the experimental setups for the partial synthesis are explained.

Chapter 3 – Mathematical Methodologies.   The mathematical fundamentals of the systematic strategy, that is used for the identification of the process models describing the experimental setups, are presented.

Chapter 4 – Step 1: Photooxygenation.   With the information from the preceding two Chapters, the model describing the photooxygenation is first identified and then exploited for a model-based analysis using global sensitivities. The identified structure of the process model is further used in Chapter 5.

Chapter 5 – Step 2: Acid-Catalyzed Sequence.   The challenge of identifying a model for the acid-catalyzed sequence is discussed in detail, and the systematic solution strategy is presented. Different model candidates are proposed that are afterwards used to identify the most probable candidate predicting both continuous flow and batch measurement data. Finally, the developed overall process model is applied in a process optimization study for improving artemisinin yields.

Chapter 6 – Differential Flatness for Model Identification.   The general question of a reliable identification of a process model is discussed. Differential flatness is then proposed for the task of model selection of (bio)chemical syntheses in the pharmaceutical industry under the consideration of parametric uncertainties. The approach is applied to an enzymatic reaction network.

Chapter 7 – Conclusions and Future Directions.   In this final Chapter, a summary with the main findings is provided. A discussion about open questions and research ideas, that might be addressed in the future, concludes this Thesis.
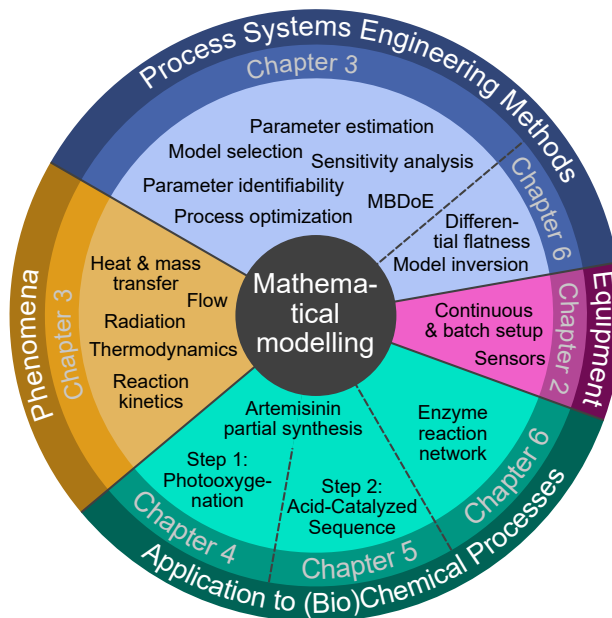

Figure 1.4: Graphic outline of this Thesis indicating the Chapters where phenomena of (bio)chemical reaction engineering, process systems engineering methods and experimental setups are introduced and the Chapters where they are applied (MBDoE: model-based design of experiments).

2 Introduction to the Artemisinin Partial Synthesis and the Applied Experimental Setups

In this Chapter, the partial synthesis of artemisinin, that is fundamental to the Chapters 4 and 5, is introduced and a current state of research on continuous artemisinin production is given. Subsequently, the experimental setups, that provided the data for the process model identification of the partial synthesis, i.e., the targeted continuous flow setup and an additional setup for batch experiments, are explained. For the interested reader, additional information about malaria, artemisinin and its production is given in the Appendix A.

2.1 Partial Synthesis

Today, the *Artemisia annua* plant is the sole global source of artemisinin (ART) [67], that is obtained by extraction, with main cultivation areas in China, Vietnam and East Africa [68]. The weight content of ART in wild and cultivated types is low and, depending on climatic conditions and chemotype, widely ranges from 0.01 to 1.5 wt−% based on dry matter [69–72], with unpublished reports of 2 wt−% [68]. Most often the leaves of the plant are considered, although ART content in the flowers might be higher [73]. The low ART weight content in the *A. annua* plant and the stimuli described in Section 1.2 are responsible for extensive research in artemisinin and its derivatives [74]. Next to extraction from its natural source, the production of ART can be categorized into two further approaches: Total syntheses from readily available and cheap chemical stocks, and semi- or partial syntheses, that either start with extraction byproducts or with species from heterologous production, see also Section A.3 and Figure A.4 in the Appendix. Potential starting points for a partial synthesis are artemisinic acid (AA) and dihydroartemisinic acid (DHAA), that are both oxidation products of amorphadiene (AD) in the metabolism of *A. annua* [75]. In opposite to AA, where its precise metabolic role is still under discussion [64, 75, 76], DHAA is a known direct precursor of ART spontaneously converting to ART on exposure to air and sunlight [75], which implicates a correlation between DHAA and ART contents in the plant [72, 77]. Thus, the DHAA content of studies in the published literature
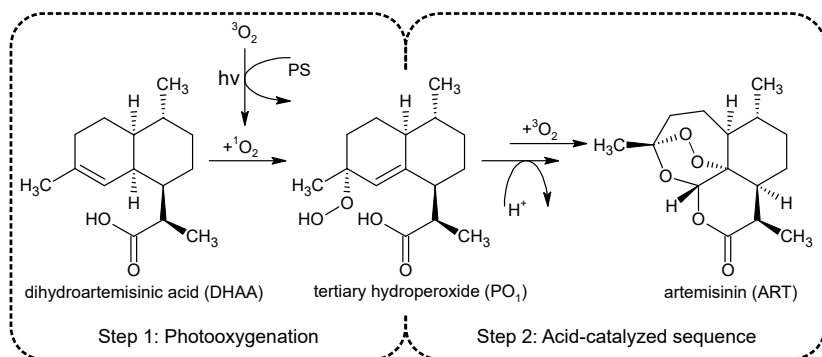
Figure 2.1: Simplified semi-synthetic path from dihydroartemisinic acid (DHAA) to artemisinin (ART) based on the fundamental works by Acton and Roth [83–85] with the singlet oxygen formed by a photo-induced process (PS: photosensitizer).

as well differs widely. It ranges from below $0.1 \, wt-\%$ based on dry matter [76, 78] ($<15 \%$ relative to ARTcontent) to $1.8 \, wt-\%$ (190% relative) [72]. AA's content is up to 10-fold higher than the ART content [77], but is observed to be negatively correlated to both ART and DHAA content [72].

The total synthesis of ART is a very complicated and expensive endeavor due to its molecular structure with several asymmetric carbon atoms and a relatively unstable endoperoxide intermediate [79]. A first total synthesis approach was published by Schmid and Hofheinz from LaRoche in 1983 [80]. On the other hand, partial syntheses from artemisinin precursors are potential and cost-effective alternatives [81, 82]. Fundamental studies about the semi-synthetic pathway from AA to ART were published by Acton and Roth beginning in 1989 [83–85].In a first step, AA is hydrogenated to DHAA [86]. Following, the partial synthesis of ART from DHAA can be summarized into two further steps, that are similar in different synthetic pathways via DHAA [81], including the metabolism in the *A. annua* plant [87], Figure 2.1. DHAA is first oxygenated to the DHAA hydroperoxide PO_1 in a stereoselective ene-type reaction initiated by *in situ* generated singlet oxygen. The singlet oxygen is not necessarily formed by a photo-induced process, but might also be chemically generated [81, 86]. In an acid-catalyzed sequence with several steps including a chemical oxidation, the final molecule ART is gained.

Based on the preparatory work by Acton and Roth and studies about AD production in bacteria [88, 89] and AA production in yeast [75, 90], the semi-synthesis of ART has been attempted to be industrialized by the companies Amyris and Sanofi [81, 86, 91]. In the Amyris approach, the chemical conversion from AA to ART was not suitable for scale-up, a prerequisite for a successful industrialization [92]. ART yields of the partial synthesis reached 40 to 45 % and pure ART was obtained with a yield of 19 % [91]. Albeit, Amyris is still working on ART [92], and in 2017, they reported a semi-synthesis starting with AD instead of AA as it is produced in a 2-fold higher molar yield, obtaining pure ART with a yield of 60 % [93]. The cheaper and less advanced intermediate

AD has also been investigated in very recent publications [94, 95]. Despite process improvements by Sanofi to the Amyris process, the built plant for the production of ART ceased operation in 2015 mainly due to low ART market prices [53, 57]. After its shutdown, Sanofi sold the factory to Huvepharma in Hungary, that, according to its CEO, produced 20 t of semi-synthetic ART in 2017 [92]. Similar to the Amyris process, Sanofi used a DHAA derivative, i.e., an anhydride of DHAA, to prevent loss reactions. Contrary to the Amyris counterpart, Sanofi employed a photochemically induced process for the generation of singlet oxygen, thereby mimicking the biosynthetic pathway. They applied tetraphenylporphyrin (TPP) as photosensitizer and added trifluoroacetic acid (TFA) in dichloromethane before entering the photo reactor in order to have both steps happening in one reactor. The overall Sanofi process yield for pure ART from AA is 55 % [91], a significant improvement to the Amyris process. In 2016, Burgard et al. [96] from Sanofi published an improvement to their process. The energy-intensive mercury lamps were replaced by LED modules and the omission of the derivatization step to the DHAA anhydride was investigated. The replacement with LED lamps resulted in a yield of 50 % and a total reaction time of 8 h. Additionally, using DHAA instead of its derivative gave yields between 47 to 59 % for different measurement campaigns and batches, and a maximum yield of 62 % for diastomeric pure DHAA.

2.2 Continuous Manufacturing of Artemisinin

Both the Amyris and the Sanofi process are run in batch and semibatch reactors, as it is standard in the pharmaceutical industry until today. Batch processes are not very well understood on a micro-scale, have low yields, are difficult to scale-up, and therefore inherently hinder a good product quality [97]. Continuous processes in turn, as established in the chemical industry, offer considerable potential in improving efficiency, safety, material consumption, scale-up, process understanding, monitoring and control, and in finding new synthetic routes, leading ultimately to increased product quality and economic benefits, for both development and manufacturing [98]. Relating to the process in this work, the photooxygenation of DHAA to PO_1 requires efficient irradiation of the reactant solution and sufficient supply of oxygen to achieve good yields within an acceptable time frame. Likewise, sufficient supply of oxygen is needed in the acid-catalyzed section. Milliscale flow reactors in Taylor flow mode offer high surface area between gas and liquid phase and efficient irradiation of the substrate due to the small channel depths. Flow microreactors are therefore suitable for the production of ART using the here considered partial synthesis route, not least as multiple phases and photoreactions are involved. Besides the manufacturing perspective, the same advantages of continuous flow microreactors are beneficial for the study of kinetic reactions alike [99–102]. Additionally, the regulatory Quality-by-design and Process Analytical Technology initiatives by the U.S. Food and Drug Administration stimulate
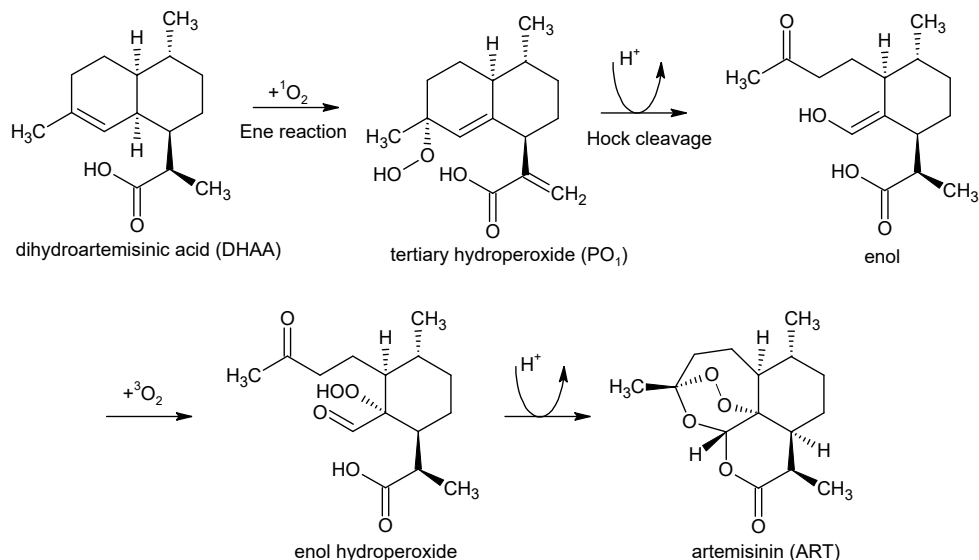
Figure 2.2: Semi-synthetic path from dihydroartemisinic acid (DHAA) to artemisinin (ART) [60].

innovations such as continuous manufacturing processes [98]; see the work by Mascia et al. [103] for an end-to-end continuous pharmaceutical process example.

The research groups of Seeberger and Seidel-Morgenstern have been developing a continuous process for the production of artemisinin and derivatives, starting from extraction, across synthesis up to purification [60, 63, 65, 104–109]. For the synthesis part, the pathway starting from DHAA is extensively explored, and led to a significant reduction in residence times to several minutes for the production of ART because of the use of milliscale flow reactors. Next to the provision of DHAA from heterologous production, the authors suggest to utilize the DHAA content of the plant itself.

Converting DHAA to ART was conducted in a single flow reactor with three different sections [63]. The first section comprised the photoreactor, the trailing two sections temperature-controlled regions for the acid-catalyzed synthesis. The conversion from DHAA to ART proceeds along the pathway that is shown in Figure 2.2. DHAA reacts with singlet oxygen, that is formed photochemically using either TPP [60] or dicyanoanthracene (DCA) [63] as photosensitizer, in an ene-type reaction to the desired hydroperoxide PO_1, besides other hydroperoxides [63]. Next, by terminal protonation with TFA, a Hock cleavage is induced that converts PO_1 to the enol. With the addition of triplet oxygen, the enol reacts to the enol hydroperoxide, that further reacts to the final product ART under acidic conditions.

In a first attempt with TPP and TFA in dichloromethane and a mercury lamp, a by chromatography purified ART yield of 39 % was achieved with a total residence time in the reaction lines of

only 4.5 min [60]. Later, the more chemically-stable DCA replaced TPP, toluene replaced dichloromethane, and an LED module replaced the mercury lamp [63]. The selectivity of the photooxygenation was increased by setting the reaction temperature to $-20\,°C$, and an ART yield of 65 % was achieved resulting in a space-time yield of 3.5 g/(ml d). Following a temperature screening of both the photo reactor and the reaction line temperature, a maximum ART yield of 69 % was achieved [63]. In contrast to the utilization of synthetically produced photosensitizers, Triemer et al. [65] showed that in a similar setup the DHAA-containing crude plant extract can be directly used to produce artemisinin in similar yields, i.e., 67 %, where the present chlorophylls act as natural photosensitizers.

The experimental setups, whose measurement data is used in this study, build upon the introduced continuous processes in [60], [63] and [65], and are explained in more detail in the following Sections.

2.3   Experimental Setups for Artemisinin Synthesis

For the identification of the process model describing the continuous partial synthesis of ART, Chapters 4 and 5, measurement data is required. The corresponding continuous setup was designed and constructed by Susann Triemer and co-workers at the Max Planck Institute Magdeburg, Figure 2.3. She also run the experiments, collected and analyzed the measurement samples. To support the kinetic analysis of the continuous reaction system under study, experiments in a batch reactor have been likewise performed by Susann Triemer in parallel. Detailed descriptions of the setups, the used equipment, and the operational and measurement procedures are found in her dissertation [61], and are summarized in the following.

The main components are two reactors that are connected in series: The photoreactor and a reaction unit for the subsequent acid-catalyzed sequence, also referred to as synthesis reactor. The inner diameters of the fluorinated ethylene propylene tubing are 0.8 mm in the photoreactor and 1.6 mm in the acid-catalyzed part beginning with the three-way valve, Figure 2.3a. Through this tubing, liquids are pumped by syringe pumps to ensure constant and low-fluctuating flows. Gas is provided by the in-house gas supply and regulated to 7 bar by two pressure regulators at the end of the liquid and gas line. Inside the photoreactor, the tubing is coiled around two polystyrene pillars, and shielded from light at the beginning and at the end to allow for equilibration. The lengths of the tubing can be varied in five steps from 1 to 10 m. The stainless-steel casing has two polystyrene windows on its opposite sides, through which LED modules with $25 \cdot 25$ mm emission windows emit light in a 120° angle and in wavelengths of either 417 nm or 660 nm.By design, the coiled tubing is completely irradiated by each of the LED modules and light cannot

(a) Flow scheme.

(b) Scheme of photo reactor cross section from the top.
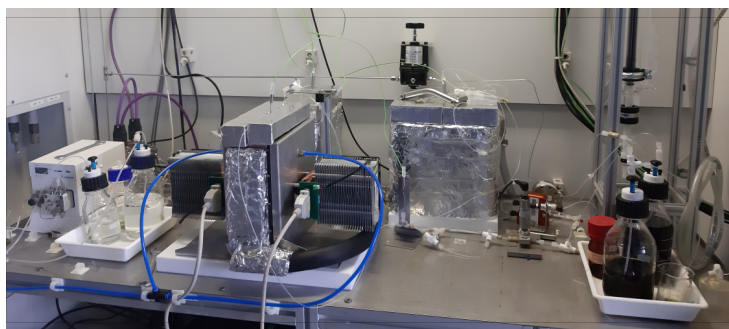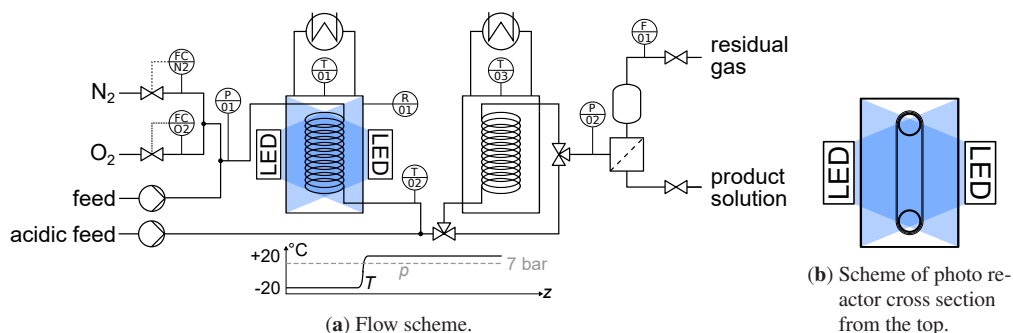
(c) Reactor system.
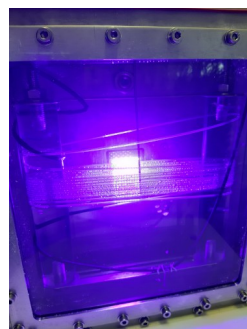
(d) Photoreactor.

Figure 2.3: Continuous photo-flow reactor setup at the Max Planck Institute Magdeburg for the semi-synthesis of artemisinin. The schemes are reproduced and adapted, and the pictures are reprinted from [108] and [61].

leave the reactor. The temperature in the photoreactor is controlled by a cooling liquid that fills the casing.

In the acid-catalyzed section, the inner diameter of the FEP tubing is doubled to retard the pressure drop while providing sufficient reaction volume to allow the slower conversion to ART to finish. The tubing is coiled around a stainless-steel frame, that is located in a stainless-steel casing with the possibility of temperature control.

Phase separation occurs first in a membrane unit before the gas stream enters a stainless steel cylinder for a second phase separation to prevent liquid affecting the downstream devices. The gas flow is measured by a mass flow meter, and its liquid counterpart is sampled for subsequent measuring by proton nuclear magnetic resonance (^{1}H-NMR).

The setup can be operated in two different modes. First, in photooxygenation mode the two-phase flow does not enter the acid-catalyzed reaction line and no acidic feed is supplied (Chapter 4), see three-way-valve in Figure 2.3. Second, in full synthesis mode the two-phase flow first passes through the photoreactor to produce the hydroperoxide reactant PO_1, and, dosed with acid, enters

(**a**) Scheme of Taylor flow conditions in a circular channel.

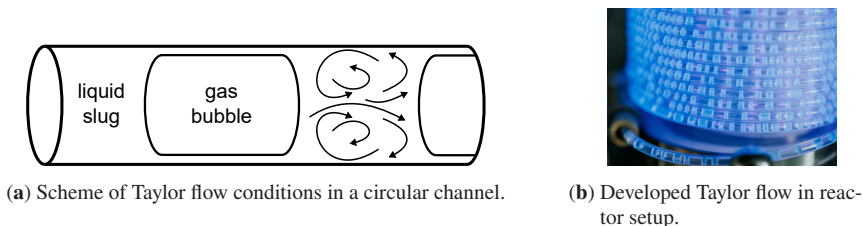(**b**) Developed Taylor flow in reactor setup.

Figure 2.4: Total flow rates between 0.5 and 2 ml/min ensure Taylor flow conditions in the continuous reactor setup. Taylor flow is characterized by alternating gas bubbles and liquid slugs, thin film formation between bubbles and wall, and Taylor recirculation within the slugs. The picture is reprinted from [61].

the synthesis reactor (Chapter 5). The specific procedures for operating in one of the two modes are described in the following Section.

2.3.1 Continuous Steady-State Experiments

The photoreactor and the synthesis reactor are kept at -20 and $20\,^{\circ}$C, respectively. DHAA and DCA are dissolved in toluene. Before operation, the whole system is rinsed with the solvent and N_2. The total flow rate is varied between 0.5 and 2 ml/min to ensure Taylor flow conditions, Figure 2.4. Correspondingly, the gas flow rates are set by the mass flow controllers to a gas-liquid ratio of 4:1 (v:v). If acid is required, TFA is dissolved and dosed prior to the synthesis reactor in a ratio of 9:1 (v:v, based on the liquid volume). After a system pressure of 7 bar stabilizes, the LED modules with set light intensity are switched on, and the experiment starts. As soon as the system reaches steady-state, samples of the reactor effluent in duplicate or triplicate are collected. After sampling, a new experiment can be started by altering the experimental conditions and repeating the described procedure. Thus, each of the samples drawn at the end of the line corresponds to one steady-state operating point. The samples are analyzed offline and not necessarily on the same day by ^{1}H-NMR.

2.3.2 Batch Experiments

With the goal of a more complete insight into the investigated dynamic kinetics in the acid-catalyzed sequence, time-resolved experiments in a batch reactor are performed next to the continuous ones. Since radiative and mass transfer in batch reactors is in general limiting [100], the batch experiments aim at the acid-catalyzed reaction steps that do not involve oxygen.

The reactant PO_1 is prepared using the continuous setup described above on the day before the batch experiments. The reactor effluent is stored in a brown flask overnight in a fridge at $4\,^{\circ}$C, and is directly used as feed in the upcoming batch experiments. A double-walled glass reactor with

temperature control ensuring 20 °C is rinsed with nitrogen before dissolved TFA in 1 mL toluene is added to the 30 ml solution in the reactor. A syringe attached to a rubber stopper is used for sampling. The samples are directly quenched with triethylamine dissolved in 0.4 ml toluene, and analyzed by ^{1}H−NMR as in the continuous experiments.

3   Mathematical Methodologies

In this Chapter, the key steps of the systematic approach to model identification are outlined. They are used for the development of a mathematical process model simulating the continuous experimental setup from the previous Chapter and for the model-based analysis of its process behavior. A brief introduction into the discipline of process systems engineering, on which the systematic approach is based, is followed by the theoretical foundations to build the process model and the mathematical fundamentals for the model identification and the model-based analysis. Contents of this Chapter have been published in [110] and [108].

3.1   Process Systems Engineering

The term *process systems engineering* (PSE) was coined at the 1st Process Systems Engineering conference in Kyoto in 1982 [111, 112]. Originally applied in chemical engineering and in various different fields nowadays [2], PSE is about the systematic and model-based solution of systems problems [113]. For an effective implementation of Quality by Design and Process Analytical Technology strategies, PSE offers useful modeling and simulation tools, which is especially true for the fast growing biopharmaceutical market [114–116]. At a systems problem's core in PSE lies a mathematical representation of a physical process, i.e., a mathematical process model $\mathcal{M}$, Equation (3.1), shown in Figure 3.1. It represents a system with model parameters $\theta \in \mathbb{R}^{n_\theta}$ and defined boundaries, across which inputs $u \in \mathbb{R}^{n_u}$ and outputs of the system $y \in \mathbb{R}^{n_y}$ might exist, see also Figure 3.2a. The vector function $f : \mathbb{R}^{n_u} \to \mathbb{R}^{n_y}$ relates the inputs of the system to its outputs; thus, describing the system's behavior.

The two systematic and iterative PSE work cycles in Figure 3.1 are referred to as identification and application cycle. The former ensures the reliable identification of a process model, whereas the latter here illustrates process design, but might be replaced by other tasks like prediction, scale-up, process control, fault detection, or gaining process understanding. Importantly, the link between the two cycles is the process model $\mathcal{M}$, Section 3.3. That is, the systematic identification of a reliable process model is crucial for the informative value of subsequent application tasks [28, 33, 117].
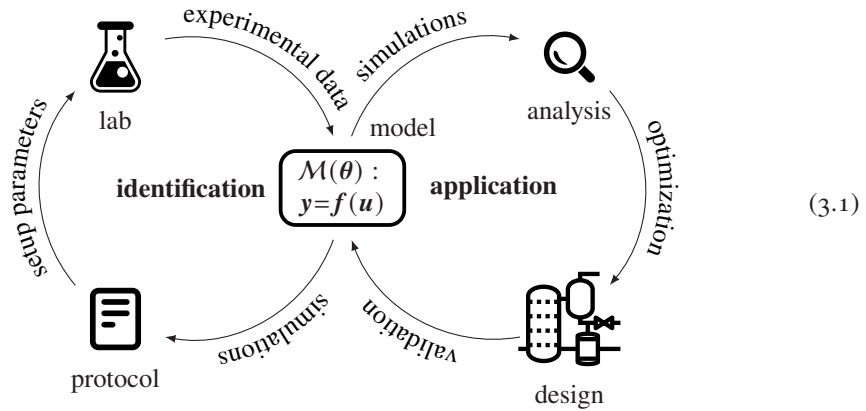
Figure 3.1: Process systems engineering work cycles, namely the identification and the application cycle. The important connection between them is the process model $\mathcal{M}$, that must be reliably identified before it can be applied and valid inference drawn.

3.2 Identifying a Process Model

Identifying a process model $\mathcal{M}$ from data $\tilde{y}$ requires to mathematically model the inherently random data. The most common approach is to assume that a data point $\tilde{y}_i, i \in \{1, 2, \dots, N\}$, follows the additive noise model

$$\tilde{y}_i = y_i + \epsilon_i, \tag{3.2}$$

with y_i the output of the process model $\mathcal{M}$, and ϵ_i a random error term, also referred to as residual [27]. A corresponding diagram is given in Figure 3.2a, where the same additive noise model applies to the real system output $y_i^\star$ with η_i the stochastic measurement error. For quantification
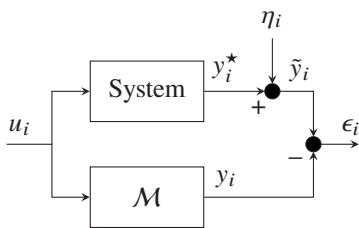
(**a**) Additive noise model, Equation (3.2).
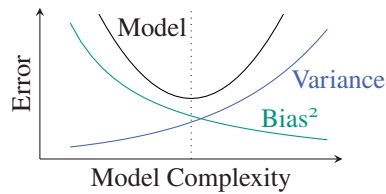
(**b**) Bias variance tradeoff, Equation (3.3).

Figure 3.2: Identifying a process model from data involves assuming a data model, e.g., the additive noise model. Its model error shows contradicting trends for bias and variance with increasing structural complexity.

of the predictive capabilities of $\mathcal{M}$, the mean squared error between the data and the model output is a natural choice and reads in a probabilistic setting as [118]

$$\text{MSE}(\mathcal{M}) = \mathbb{E}\left[(\tilde{Y} - Y)^2\right] = \underbrace{(Y^\star - \mathbb{E}[Y])^2}_{(\text{bias error})^2} + \underbrace{\mathbb{E}\left[(Y - \mathbb{E}[Y])^2\right]}_{\text{variance error}} + \mathbb{V}[H^2], \tag{3.3}$$

where capital letters are used to indicate that the variables are in general of random nature, and $\mathbb{E}[\cdot]$ and $\mathbb{V}[\cdot]$ are the expected value and the variance operator, respectively. Next to the non-reducible measurement variance $\mathbb{V}[H^2]$, Equation (3.3) tells us that the model error is composed of a bias and a variance error term, that both need to be reduced at the same time for a minimum prediction error. However, the two terms have opposite trends, i.e., increasing structural complexity by, for example, adding model parameters, decreases the bias but increases the variance term and leads to overfitting [119], Figure 3.2b. Identifying a process model from data will therefore always consider a tradeoff between bias and variance, that is usually driven by the principle of parsimony, i.e., to have a model structure complexity as simple as possible, but no simpler [120]. While identifying a process model from data, one frequently faces two challenges: (i) selecting a model structure $\mathcal{M}$ following the principle of parsimony, and (ii) estimating its model parameters θ. Model selection is required when the mathematical description of the system's behavior is not or not fully known, but potential descriptions can be postulated. It then comprises the structural identification of a model from the set of proposed model candidates, that is, the detection of the interplay between inputs u, outputs y and parameters θ. Contrarily, parameter estimation means to determine numerical values for a subset of the model parameters θ that cannot be identified by other means, e.g., by values found in literature or based on previous experience. To draw inference about a model structure and its parameters from data, the inherent randomness of the data is commonly mathematically described by a probability density function $\text{pdf}(\tilde{y}|\theta, \mathcal{M})$ (PDF), that evaluates the probability of the data $\tilde{y}$ given the parameters θ and a model $\mathcal{M}$. A standard representative of PDFs is based on the Normal or Gauss distribution $\mathcal{N}$:

$$\text{pdf}(\tilde{y}|\mu, \sigma, \mathcal{N}) = \frac{1}{\sqrt{2\pi\sigma^2}} \exp\left[-\frac{(\tilde{y} - \mu)^2}{2\sigma^2}\right], \tag{3.4}$$

with realization or data $\tilde{y}$ of the random variable $\tilde{Y}$, and the two parameters of the Normal distribution μ and σ, the mean and the standard deviation, respectively [119].

In both challenges, i.e., precise parameter estimation and reliable model selection, approaches following model-based design of experiments (MBDoE) have proven beneficial over the last few decades [29, 121–123], Section 3.7, as they ensure high informative content in the experimental data, and have therefore become an important part within PSE. A detailed scheme of the identification cycle including MBDoE, that is used in this work and loosely guides through this Chapter, is given and explained in Figure 3.3.
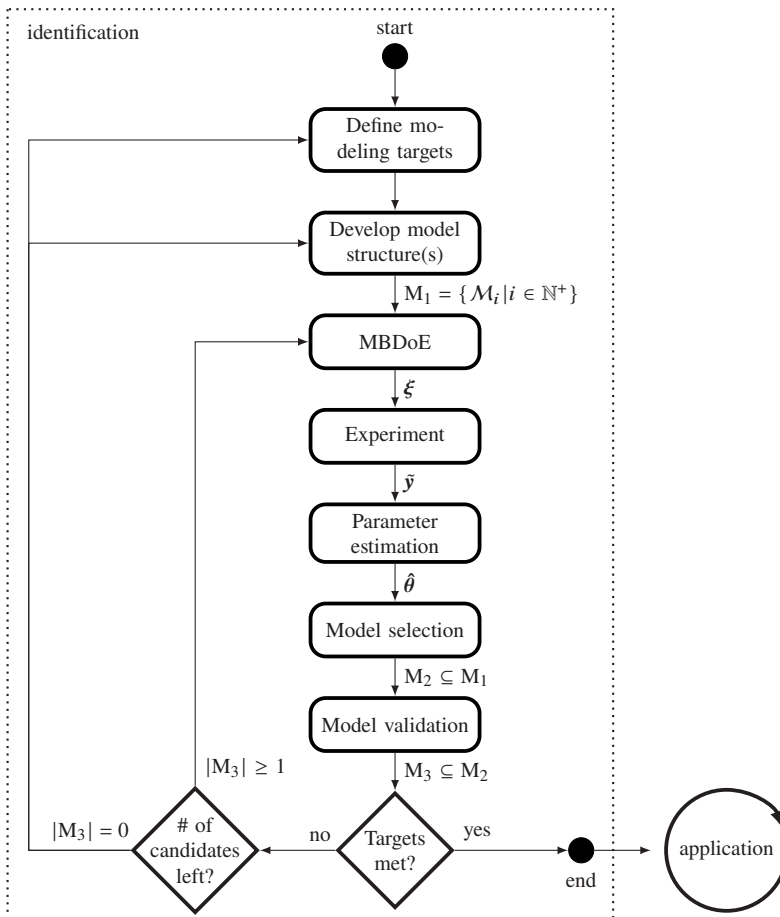
Figure 3.3: Systematic strategy for model identification [118, 124]: A closer look into the iterative identification cycle in Figure 3.1. Defining the targets of the modeling scenario determines the type and the complexity of the model. Constraints on the amount of data and its quality, on computational and human resources, on experiences and expert knowledge, and on available time should be considered at this stage. Subsequently, different model structures are postulated resulting in a set of model candidates $M_1 = \{\mathcal{M}_i | i \in \mathbb{N}^+\}$. Identifying a model requires experimental data with the experiments designed by, at best model-based, design of experiments (MBDoE). The design vector $\boldsymbol{\xi}$ determines the experimental settings, that deliver highly informative data $\tilde{\boldsymbol{y}}$. Estimating the model parameters, yielding $\hat{\boldsymbol{\theta}}$, and model selection ideally leaves one model candidate, that is validated and can be deployed for application scenarios afterwards. If the targets are not met, different scenarios are possible depending on the number of candidates left: reconsider the targets, construct new model candidates, or design a new experiment.

3.3 Mathematical Models for (Bio)Chemical Processes

Dynamic process models in PSE, that describe (bio)chemical processes, are commonly mathematically described by ordinary differential equations (ODEs). Their state-space formulation comprises a state and an output equation, where the former describes the dynamic behavior and the latter the measured quantities of the system. The state equation reads

$$\frac{\mathrm{d}x}{\mathrm{d}t} = f_x(x(t), u(t), \theta), \tag{3.5a}$$

with t the independent variable, here time, $x \in \mathbb{R}^{n_x}$ the time-dependent system states, $u \in \mathbb{R}^{n_u}$ the time-dependent system inputs or controls, $\theta \in \mathbb{R}^{n_\theta}$ the parameter vector, and $f_x : \mathbb{R}^{n_x} \times \mathbb{R}^{n_u} \times \mathbb{R}^{n_\theta} \to \mathbb{R}^{n_y}$ a vector field defining the dynamics of the system. For the forward solution of the ODEs initial conditions

$$x(t = 0) = x_0 \tag{3.5b}$$

must be provided. The output function is defined as

$$y(t) = f_y(x(t), u(t), \theta), \tag{3.5c}$$

with $f_y : \mathbb{R}^{n_x} \times \mathbb{R}^{n_u} \times \mathbb{R}^{n_\theta} \to \mathbb{R}^{n_y}$ the (non-)linear output function. In many cases, the system outputs are a (linear) function of the system states only; that is, $y(t) = f_y(x(t))$.

In first principles modeling, the state equation, Equation (3.5a), is based on physics and (bio)chemistry principles and yields a process model $\mathcal{M}$, Equation (3.1), whose dynamic behavior is fully determined by the set of the three Equations (3.5). Essential in the case of (bio)chemical processes are (bio)chemical kinetics, that might be driven by photon transfer as in the artemisinin partial synthesis. If the reaction kinetics are combined with a reactor model, a process model is obtained. The reactor model comprises the description of the physical phenomena occurring within the reactor, namely the setup-specific flow conditions and mass transfer. Balance equations for the conserved quantities mass, momentum and energy, where the chemical kinetics are integrated, are postulated and form the differential equations (3.5a). In the adjacent Sections, both parts of the process model are introduced, before the focus is shifted towards the model identification aspects.

3.3.1 Modeling of Chemical Reactions

In a chemical reaction

$$aA + bB \longrightarrow cC + dD \tag{3.6}$$

with reactants A and B, products C and D, and their stoichiometric coefficients a, b, c and d, the rate of reaction is

$$r = \frac{1}{\nu_i}r_i = \frac{1}{\nu_i V}\frac{\mathrm{d}n_i}{\mathrm{d}t}, \quad \forall i \in \{A, B, C, D\}, \tag{3.7}$$

with n the number of moles, V the volume of the reaction mixture, and ν the stoichiometric number [26]. The stoichiometric numbers are the negatives and positives of the stoichiometric coefficients in the reaction (3.6) for the reactants and the products, respectively, e.g., $\nu_B = -b$. For constant volume V, the rate of reaction r from Equation (3.7) can be written in terms of the concentrations as

$$r = \frac{1}{\nu_i}\frac{\mathrm{d}c_i}{\mathrm{d}t}. \tag{3.8}$$

If species i is involved in several reactions k, its rate of concentration change is thus

$$\bar{r}_i = \frac{\mathrm{d}c_i}{\mathrm{d}t} = \sum_k \nu_{i,k} r_k. \tag{3.9}$$

To describe the rate of reactions r_k, kinetic laws can be utilized, that are discussed after key measures for chemical reactions are introduced in the following.

Key Measures for Chemical Reactions

The residence time is crucial for reaction engineering, as precise understanding of the reactor behavior necessitates the knowledge of the velocity distribution within the reactor [26]. Alternatively, when no velocity distribution is available or ideal reactor behavior is assumed, a superficial residence time can be calculated for a two-phase flow reactor from

$$\tau^s = \frac{V}{\dot{V}_{l,0} + \dot{V}_{g,0}}, \tag{3.10}$$

with V the considered reactor volume and $\dot{V}_{l,0}$ and $\dot{V}_{g,0}$ the initial liquid and gas volumetric flow, respectively. Note that the superficial residence time in the continuous setup introduced in Chapter 2 will underestimate the actual residence time as the gas flow rate will decrease with the formation of hydroperoxides and artemisinin in the photooxygenation and acid-catalyzed sequence, respectively.

The yield of the formed species C relative to the consumed species B in the reaction (3.6) in a constant volume reactor is [125]

$$Y_C = \frac{[C] - [C]_0}{[B]_0} \frac{-\nu_B}{\nu_C}, \tag{3.11}$$

where square brackets indicate concentration and the subscript 0 marks the reference state, e.g., the initial conditions. The corresponding conversion of species B is [125]

$$X_B = \frac{[B]_0 - [B]}{[B]_0}. \tag{3.12}$$

For reactor evaluation, the space-time yield is another important measure, that gives insight about production efficiency of the formed species C relative to the reactor volume and time [125]:

$$STY_C = \frac{\dot{n}_C}{V}, \tag{3.13}$$

with $\dot{n}_C$ the molar production rate of species C. Lastly, the recovery of the species B indicates the amount of species C_i descendant of B that could be found in measurements:

$$R_B = \frac{\sum_i [C_i]}{[B]_0}. \tag{3.14}$$

Kinetic Laws

The stoichiometric description of the chemical reaction in Equation (3.6) yields species balances, but does not necessarily give insight about the reaction mechanism and velocity described by the rate of reaction r, Equation (3.8). Commonly, kinetic laws are postulated following the idea of mass action kinetics. Considering the chemical reaction in Equation (3.6), its rate of reaction might then be defined as [26]

$$r = k[A]^{m_A}[B]^{m_B}, \tag{3.15}$$

with kinetic rate coefficient k, and the occurring powers m_i referred to as reaction orders. Reactions whose rates follow their stoichiometric equations, i.e., the reaction orders equal the absolute values of their stoichiometric numbers ν_i, are referred to as *elementary reactions*. The number of reactants involved in an elementary reaction, also termed *molecularity*, is usually one, two, or occasionally three [26]. In non-elementary reactions, the reaction orders in Equation (3.15) might not align with stoichiometry, or the kinetic law for the reaction rate r itself might assume a different structure. However, non-elementary reactions are often a summary of elementary reactions, that take place in the considered mechanism and that is often a consequence of made assumptions considering the mechanism [26].

For deriving a process model, the kinetic laws describing the (bio)chemical reaction network must be connected to a reactor model that describes the experimental setup. In the adjacent Section, the two-fluid model is introduced, that was used to simulate the continuous experimental reactor setup, Section 2.3.

3.3.2 Modeling of Multiphase Flow Reactors

Motivation for the Two-Fluid Model

Generally speaking, reactor models consider mass, momentum and energy balances; and the radiative transport equation if photo-induced processes are involved. Because of the complex and diverse nature of multiphase flows, there is a vast number of different mathematical models that commonly average the local formulations of the aforementioned field equations in some form [126]. A well-established approach is the multi-fluid model with its special case the two-fluid model, in particular in nuclear reactor technology and in the petroleum industry, where it is successfully applied for diverse flow regimes and in different operating situations [126–128]. In the microreactor community, on the contrary, multifluid models are less frequently considered [129, 130]. The reasons are twofold; first, the phase interface is not explicitly captured despite its importance. And second, the required interfacial transfer descriptions are based on isolated particles that do not reflect reality in small channels [130]. However, opposite to the goal of a precise resolution of the fluid interfaces, successful multifluid approaches for microchannel systems do exist in literature yielding good model-data fits [131–135]. Furthermore, data and correlations for microchannel (flow) properties that might be used for closure relations in multifluid models are widespread in the literature, see [136] and references therein. Additionally, in the experimental setup at hand, only small relative pressure drops over the reactor (0.1 to 0.5 bar at 7 bar absolute pressure) and a low slip between gas and liquid phase were observed, Equation 4.19, supporting the omission of a differential momentum balance [131]. Moreover, the reactor was operated isothermally, resulting in the assumption of absence of an internal thermal gradient and therefore allowed to neglect an energy balance.

Material Balances of the Two-Fluid Model

In the two-fluid model, each of the two phases is balanced separately. In a phase $k \in \{l, g\}$ (l: liquid, g: gaseous) that is in steady-state and does not exhibit diffusion, the mass species balance of a species i along the spatial reactor coordinate z of a flow reactor is [126]

$$\frac{\mathrm{d}(\alpha_k A \rho_k w_{k,i} u_k)}{\mathrm{d}z} = \sum_j \alpha_k A S_{k,i,j}. \tag{3.16}$$

ρ_k is the density of the phase, u_k is the velocity of the phase, $w_{k,i}$ is the weight fraction of species i in the phase, and the terms $S_{k,i,j}$ on the right-hand-side denote sources and sinks of species i in phase k, namely chemical reactions and mass transfer from one to the other phase. The cross-sectional area of the channel A is the sum of the unspecified cross-sectional areas A_g and A_l that are covered by the gas volumetric flow $\dot{V}_g$ and the liquid volumetric flow $\dot{V}_l$, respectively,

$$A = A_g + A_l. \tag{3.17}$$

They are linked via the gas fraction α_g, or short α:

$$\alpha_g = \alpha = \frac{A_g}{A}, \quad \alpha_l = 1 - \alpha = \frac{A_l}{A}. \tag{3.18}$$

The phase velocities are then given as

$$u_g = \frac{\dot{V}_g}{A_g} = \frac{\dot{V}_g}{\alpha A}, \quad u_l = \frac{\dot{V}_l}{A_l} = \frac{\dot{V}_l}{(1 - \alpha)A}. \tag{3.19}$$

Thus, alternatively, Equation (3.16) can be reformulated:

$$\frac{\mathrm{d}(\rho_k w_{k,i} \dot{V}_k)}{\mathrm{d}z} = \sum_j \alpha_k A S_{k,i,j}. \tag{3.20}$$

In the following, we derive the balances for the gas and the liquid phase, and might drop the phase index k for clarity if free of confusion.

Liquid Phase. In the liquid phase, we derive the species mass balance on a concentration basis. With mass fraction $w_{l,i} = \frac{c_i M_i}{\rho_l}$ (M_i: molar mass of species i), we obtain from Equation (3.20)

$$\frac{\mathrm{d}(c_i \dot{V}_l)}{\mathrm{d}z} = \sum_j (1 - \alpha) A S_{l,i,j}^{\mathrm{m}}, \tag{3.21}$$

where the sources and sinks are now molar-based, denoted by the superscript m. Despite mass transfer from the gas phase into the liquid phase, and composition changes of the liquid phase due to reactions, the liquid density is assumed to be constant over the reaction line. Hence, to ensure mass continuity, the volumetric liquid flow is constant resulting in

$$\frac{dc_i}{dz} = \frac{1}{u_l}(r_i + j_i), \tag{3.22}$$

where $\bar{r}_i$ is the net rate of reaction, Equation (3.9), and $\bar{j}_i$ is the net material transfer from the gas to the liquid phase.

Gas Phase. For the gas phase, a derivation based on molar fractions is preferred. The mass fraction can be converted to molar fraction via

$$x_i = w_{g,i}\frac{M}{M_i}, \tag{3.23}$$

where the total molar mass of the gas phase is $M = \sum_i x_i M_i$. Assuming an ideal gas mixture, the density can be calculated from [137]

$$\rho_g = \frac{pM}{RT} \tag{3.24}$$

with the total pressure p, the universal gas constant R, and the temperature T. The molar fraction of a species i in an ideal gas mixture is [137]

$$x_i = \frac{V_i}{V_g}. \tag{3.25}$$

Plugging the provided relations into the species balance, Equation (3.20), results in

$$\frac{d\left(\frac{p}{RT}x_i \dot{V}_g\right)}{dz} = \sum_j \alpha A S^m_{g,i,j}. \tag{3.26}$$

Assuming constant pressure and temperature, see Section 3.3.2, we obtain for the molar fraction of species i

$$\frac{dx_i}{dz} = \frac{1}{\dot{V}_g}\left(\frac{RT}{p}\sum_j \alpha A S^m_{g,i,j} - x_i\frac{d\dot{V}_g}{dz}\right) \tag{3.27}$$

The derivative of the volumetric gas flow follows from Equation (3.26), if we set the species i to the gas phase (i.e., $x_g = 1$):

$$\frac{d\dot{V}_g}{dz} = \frac{RT}{p}(1 - \alpha)A\sum_i \bar{j}_i, \tag{3.28}$$

with mass transfer terms j_i as the only sinks and sources. Please note that $(1 - \alpha)$ on the right hand side of Equation (3.28) is the correction of the mass transfer, since the mass transfer terms $\bar{j}_i$ are based on the liquid volume.

The foundations for the modeling of chemical reactions, Section 3.3.1, and multiphase flows, Section 3.3.2, have been laid out. The process model can therefore be built and subsequently be identified as outlined in the coming Sections.

3.4 Parameter Estimation

Estimating parameters of process models is pivotal in PSE. Methods for parameter estimation are therefore vast in literature [138, 139]. In a frequentist setting, parameter inference is often quantified with a $100(1 - \phi)\%$ confidence interval for the true parameter $\theta^\star$, where

$$\Pr\{\theta^\star \in [lb(\tilde{Y}), ub(\tilde{Y})]\} = 1 - \phi, \tag{3.29}$$

with $\tilde{Y}$ a vector of random variables representing the data and lb and ub the lower and upper bound of the confidence interval, respectively [140]. That is, when resampling the data 100 times, $(1 - \phi)100$ of the corresponding intervals will cover the true parameter $\theta^\star$. Ideally, parameter estimation will result in a confidence interval as short as possible [140]. To find such an optimal estimator $\hat{\theta}(\tilde{Y})$, a look at the mean squared error gives again insight (compare with Equation (3.3)) showing a similar bias and variance error term:

$$\begin{aligned} \mathrm{MSE}(\hat{\theta}) &= \mathbb{E}[(\hat{\theta} - \theta^\star)^2] \\ &= \underbrace{(\mathbb{E}[\hat{\theta}] - \theta^\star)^2}_{\text{(bias error)}^2} + \underbrace{\mathbb{E}\left[(\hat{\theta} - \mathbb{E}[\hat{\theta}])^2\right]}_{\text{variance error}}. \end{aligned} \tag{3.30}$$

In practice, estimators are searched that have zero bias and minimum variance, referred to as minimum variance unbiased estimators (MVUEs). A popular representative is the maximum likelihood estimator (MLE), that is asymptotically optimal, as it is unbiased with an approximate Normal distribution and has minimum variance for large enough data sets, i.e., it is asymptotically an MVUE [141]. The maximum likelihood estimate follows from maximizing the likelihood function given data $\tilde{y}$ and a statistical model $\mathcal{M}$:

$$\hat{\boldsymbol{\theta}}_{\mathrm{MLE}} = \arg\max_{\boldsymbol{\theta}} \mathcal{L}(\boldsymbol{\theta}|\tilde{\boldsymbol{y}}, \mathcal{M}). \tag{3.31}$$

Based on Equation (3.4), the logarithmic likelihood function with independent additive Normal errors, that have zero means, is:

$$\log \mathcal{L}(\boldsymbol{\theta}, \boldsymbol{\sigma}|\tilde{\boldsymbol{y}}, \mathcal{M}) = -\frac{1}{2} \sum_{j=1}^{n_y(t_k)} \sum_{k=1}^{n_t} \left[\log(2\pi\sigma_j^2(t_k)) + \left(\frac{\tilde{y}_j(t_k) - y_j(t_k, \boldsymbol{\theta})}{\sigma_j(t_k)} \right)^2 \right]. \tag{3.32}$$

Here, it is considered, that different samples at time points t_k might have different numbers of data points $n_y(t_k)$. The total number of data points is then $N = \sum_{j=1}^{n_y(t_k)} \sum_{k=1}^{n_t} 1$.

A $(1 - \phi)100\%$ asymptotic confidence interval for a parameter θ_i is evaluated as follows:

$$\hat{\theta}_i \pm z_{1-\phi/2}\sqrt{C_{\theta,ii}}, \tag{3.33}$$

with z the $1-\phi/2$ quantile of $Z \sim \mathcal{N}(0, 1)$, and $C_{\theta,ii}$ the diagonal entries of the parameter covariance matrix $\boldsymbol{C}_\theta$. The latter can be approximated via the inverse of the Fisher information matrix (FIM)

$$\boldsymbol{C}_\theta \approx \textbf{FIM}^{-1}, \tag{3.34}$$

with the FIM named in honor of Ronald A. Fisher [142, 143], that can be calculated from

$$\textbf{FIM} = -\mathbb{E}\left[\left. \frac{\partial^2 \,\text{pdf}(\tilde{\boldsymbol{y}}|\boldsymbol{\theta})}{\partial\boldsymbol{\theta}\partial\boldsymbol{\theta}^\mathsf{T}} \right|_{\theta^\star} \right]. \tag{3.35}$$

In the case of independent Gaussian errors, Equation (3.32), the FIM can be calculated as [141]:

$$\textbf{FIM} \stackrel{N}{=} \left[\underbrace{\left.\frac{\partial \boldsymbol{y}(\boldsymbol{\theta})}{\partial\boldsymbol{\theta}}\right|_{\theta^\star}}_{\textit{SM}} \right]^\mathsf{T} \boldsymbol{\Sigma}^{-1} \left.\frac{\partial \boldsymbol{y}(\boldsymbol{\theta})}{\partial\boldsymbol{\theta}}\right|_{\theta^\star}, \tag{3.36}$$

with $\boldsymbol{\Sigma}$ the measurement covariance matrix, and $\boldsymbol{SM} = \partial\boldsymbol{y}/\partial\boldsymbol{\theta}$ the sensitivity matrix of the model parameters. The FIM in Equation (3.36) generally cannot be evaluated due to lack of knowledge about the true parameter value $\boldsymbol{\theta}^\star$. In practice, the FIM is therefore approximated using either Equation (3.35) or Equation (3.36) by utilizing the MLE. In the former case, the FIM follows from the log likelihood function, Equation (3.32) [141]:

$$\textbf{FIM} \approx -\left.\frac{\partial^2 \log \mathcal{L}(\boldsymbol{\theta})}{\partial\boldsymbol{\theta}\partial\boldsymbol{\theta}^\mathsf{T}}\right|_{\hat{\theta}_{\text{MLE}}}. \tag{3.37}$$

Alternatively, the FIM can be determined from the parameter sensitivities:

$$\textbf{FIM} \approx [\boldsymbol{SM}|_{\hat{\theta}_{\text{MLE}}}]^\mathsf{T}\boldsymbol{\Sigma}^{-1}\boldsymbol{SM}|_{\hat{\theta}_{\text{MLE}}}. \tag{3.38}$$

Hence, the second alternative is especially helpful if data is not or not yet present. Accordingly, the FIM in Equation (3.37) is usually termed the observed FIM, and the FIM in Equation (3.38) is referred to as expected FIM [144].

A special case in parameter estimation forms, if the errors in the log likelihood function in Equation (3.32) are additionally identically distributed. The log likelihood function can then be reduced to the widely applied ordinary least squares (OLS) objective function for parameter estimation [27]:

$$\mathcal{J}_{\text{OLS}}(\boldsymbol{\theta}) = RSS(\boldsymbol{\theta}) = \sum_{j=1}^{n_y(t_k)} \sum_{k=1}^{n_t} \left(\tilde{y}_j(t_k) - y_j(t_k, \boldsymbol{\theta}) \right)^2. \tag{3.39}$$

Thus, in OLS parameter estimation, the goal is to minimize the residual sum of squared errors (RSS) over the parameter space. Frequently, the measurement variance σ^2 cannot be deduced from the experimental data, but instead, it is considered another parameter to estimate. In OLS parameter estimation, the measurement variance can be obtained *a posteriori* from its maximum likelihood estimate

$$\hat{\sigma}^2 = \frac{RSS(\hat{\boldsymbol{\theta}}_{\text{MLE}})}{N}. \tag{3.40}$$

Note that in the maximum likelihood approach, it is inherently assumed that the model structure is known and indeed simulates the physical system, Figure 3.2a. However, frequently, the correct model structure is not given or only partially known. Thus, methods beyond Fisher's likelihood theory have to be applied, with the goal of selecting a model structure from a set of model candidates, referred to as model selection as explained in the following Section.

3.5   Model Selection

The here used iterative approach to model selection, where from a set of model candidates $\mathcal{M}_i$ the best candidate according to a chosen criterion is searched, Figure 3.3, is very common in (bio)chemical process models [145, 146]. Criteria for model assessment and selection are subject to different dimensions: falsifiability, explanatory adequacy, interpretability, faithfulness, goodness-of-fit, complexity/simplicity and generalizability [27]. In general, there is no master strategy for model selection and therefore no universal criterion [147]. If data abundance is not an issue, splitting the data set into a training, validation and an external test data set is a straightforward approach. However, several methods have been developed that make better use of the available data, where an additional test data set might not absolutely be necessary [118]. Next to the computationally expensive cross validation, and statistical tests, information criteria are widely applied [118]. In general, information criteria can be expressed as functions of model-data mismatch and model complexity, thereby considering the bias variance dilemma, Figure 3.2b. A

well-known information criterion is the Akaike information criterion (AIC) or its small-sample analog, the corrected Akaike information criterion AIC_c [120]. It evaluates the model response residuals as well as the model complexity in terms of the dimension of the model parameter vector:

$$AIC = -2\mathcal{L}(\hat{\theta}_{MLE}) + 2K, \qquad (3.41)$$

with K the number of estimated parameters, that is in general not equal to the number of estimated process model parameters. The corrected AIC is

$$AIC_c = AIC + \frac{2K(K+1)}{N-K-1}, \qquad (3.42)$$

where its use is recommended for N/K ratios below 40 [120]. From Equation (3.41), it is obvious that the AIC inherently considers the bias variance tradeoff, Equation (3.3), by penalizing the goodness-of-fit measure, i.e., the log likelihood value at the MLE, through the number of estimated parameters K. Hence, selecting a best model candidate using the AIC basically means to perform a maximum likelihood estimation of the model parameters, as outlined in Section 3.4. Note that the AIC is a relative measure and therefore must be interpreted as such, where AIC values ranging from large negative values to values as high as $304,000$ have been observed [120]. In this work, the AIC serves as a heuristic and supports the model selection procedure.

In situations when parametric uncertainties in the model are considered, alternative criteria are better suited than the AIC, as it solely considers a point estimate within the parameter space, the MLE, and the corresponding model responses [147]. For instance, the so-called overlap approach emphasizes the fact that in reality, model parameters are uncertain, which is in turn not regarded in many common discrimination criteria as the AIC or the Bayesian information criterion [148]. Assuming additive measurement noise and according to the Doob-Dynkin lemma [149], the identified model parameters $\hat{\theta}$ can be considered to be random variables. The overlap approach accounts for parameter uncertainties by considering the trajectory confidence intervals. The overlap of two models considering parametric uncertainties is

$$OVL = \sum_{k=0}^{T} \frac{2\sqrt{\sigma_{1,k}^2 \sigma_{2,k}^2}}{\sigma_{1,k}^2 + \sigma_{2,k}^2} \exp \frac{-0.5(\mu_{1,k} - \mu_{2,k})^2}{\sigma_{1,k}^2 + \sigma_{2,k}^2}, \qquad (3.43)$$

where $\mu_{i,k}$ and $\sigma_{i,k}$ are the expected value and the variance of the output function of model i at time point k resulting from the stochastic nature of the parameters, respectively. Thus, a larger overlap value between one pair of model candidates over another emphasizes the fact that the model candidates of the first pair is less distinguishable in their uncertain predictions.

Concluding, criteria and objectives for parameter estimation and model selection have been outlined. That is in the former case in particular the goodness-of-fit measure RSS, Equation

(3.39), the estimated measurement variance, Equation (3.40), and the confidence intervals for parameters, Equation (3.29). In model selection, the AIC evaluates the bias-variance trade-off for estimated model candidates, Equation (3.40), and the the OVL represents an alternative when parametric uncertainties are considered. In the following, the related issue of parameter identifiability is addressed.

3.5.1 Assessment of model structure and estimated parameters

Estimating parameters of nonlinear models is often a difficult task with several causing factors [150]. One major reason is the question of parameter identifiability, i.e., if the model parameters can be uniquely determined with respect to the model structure and the available data. This issue is closely related to parameter sensitivities, as only residuals, Equation 3.39, that are sensitive to parameters can be identified. Even in simple (bio)chemical models, parameter identifiability might not be given [151, 152]. Besides easing parameter estimation, parameter identifiability studies enable reliable physical interpretation of the determined magnitudes of the model parameters. In parameter identifiability, the literature distinguishes between structural and practical identifiability. The former, in literature also referred to as theoretical identifiability or simply identifiability, deals with the situation if the structure of our model permits a unique determination of the model parameters before seeing the data. The latter, also named estimability, answers the question if the model parameters are identifiable from a given data set. A practically identifiable parameter is therefore also theoretically identifiable, but the reverse conclusion does not hold. This stresses out that both dimensions of parameter identifiability should be investigated [151]. To optimally assist the parameter estimation problem, structural identifiability should be checked best before the estimation is addressed [153]. Furthermore, between locally and globally identifiable parameters is differentiated. Locally identifiable parameters can only be recovered in sub spaces of the parameter space, whereas globally identifiable parameters are identifiable everywhere.

Structural Identifiability

In the case of linear models, structural identifiability is well understood and effective methods are available. On the contrary, methods for structural identifiability of non-linear models are limited in applicability and usability, and are an on-going research topic. Among others, existing methods are the Taylor series method, the generating series method, the similarity approach method, approaches relying on the implicit function theorem, and methods based on differential algebra [27, 154]. Established toolboxes are the DAISY toolbox [155], that is based on the

differential algebra approach and has global scope, and the GenSSI toolbox [156]. However, these methods suffer from computational burden, lacking ready-to-use implementations, or limited applicability [153, 157]. A remedy can be found in sensitivity-based local approaches that can be seen as a bridge between methods testing structural identifiability and methods testing practical identifiability, as they do not need measurement data, but might require the number and location of the measurements, and a usually local parameter estimate for evaluation [153]. Furthermore, they do not use the model structure information in a direct sense, but by way of parameter sensitivities [153]. On the other hand, their biggest advantage compared to methods testing structural identifiability is the straightforward usability and applicability to all models that allow the calculation of sensitivities coefficients with respect to the model parameters.

Sensitivity coefficients of the sensitivity matrix introduced in Section 3.4, see for example Equation (3.36), are calculated at a time point t_k and for a nominal parameter vector $\boldsymbol{\theta}^*$ as

$$S_{ij}(t_k) = \left. \frac{\partial y_i(t_k, \boldsymbol{\theta})}{\partial \theta_j} \right|_{\boldsymbol{\theta}^*}. \tag{3.44}$$

A sensitivity matrix can then be constructed from the sensitivity coefficients:

$$\boldsymbol{SM} = \begin{pmatrix} S_{11}(t_1) & \cdots & S_{1n_\theta}(t_1) \\ \cdots & \ddots & \cdots \\ S_{n_y 1}(t_1) & \cdots & S_{n_y n_\theta}(t_1) \\ \vdots & \vdots & \vdots \\ S_{11}(t_{n_t}) & \cdots & S_{1n_\theta}(t_{n_t}) \\ \cdots & \ddots & \cdots \\ S_{n_y 1}(t_{n_t}) & \cdots & S_{n_y n_\theta}(t_{n_t}) \end{pmatrix}. \tag{3.45}$$

By inspecting the sensitivity matrix, two issues can be investigated. First, if a parameter is non-identifiable, that is, $\boldsymbol{SM}$ is rank-deficient [158]. Second, parameter dependencies can be inferred [153]. Several methods are available that exploit the sensitivity matrix [153]. An easy-to-use algorithm, that also works for large size models, is based on a singular value decomposition (SVD) of $\boldsymbol{SM}$. It hunts down parameter non-identifiabilities and dependencies simultaneously, where the number of involved parameters is not limited [159]. The SVD of $\boldsymbol{SM}$ is

$$\boldsymbol{SM} = \boldsymbol{u}_1 \sigma_1 \boldsymbol{v}_1^\mathsf{T} + \cdots + \boldsymbol{u}_{n_\theta} \sigma_{n_\theta} \boldsymbol{v}_{n_\theta}^\mathsf{T} \tag{3.46}$$

with left singular vectors $\boldsymbol{u}_i$, singular values σ_i, and right singular vectors $\boldsymbol{v}_i$. By inspection of the right singular vectors $\boldsymbol{v}_i$ with singular values $\sigma_i = 0$, i.e., the non-zero elements of $\boldsymbol{v}_i$,

the combinations of parameters are obtained that cause the model to be non-identifiable. The difficulty lies in the definition of a singular value being zero. Plotting the singular values in decreasing order and on a logarithmic scale, rank-deficient matrices typically show a gap that is clearly visible [159]. Further disadvantages of the SVD method are that only linear parameter dependencies are detected, and that the *SM* is evaluated at a single point in the parameter space, that, though unlikely, might be non-regular [159]. A straightforward workaround is the evaluation of multiple points in the parameter space [159].

Practical Identifiability

Practical identifiability might be tested following three different approaches:

1. Monte-Carlo simulations,

2. methods based on the FIM, or

3. optimization-based approaches.

Monte-Carlo simulations rely on a large amount of repeated simulations that can become computationally intensive [160–162]. On the other hand, approaches based on the FIM, see Section 3.4, are in general easy to compute. Here, a (nearly) singular FIM indicates non-identifiable parameters.

Optimization-based approaches are the third option to practical identifiability. Their resulting workload might be low when local multi-start optimization approaches are used during parameter estimation [28], as the parameter estimation results can be investigated for practical identifiability. Basically, the optimization runs are initialized with different samples within the parameter space, and are compared after they have been completed. Visualization supports the identification if parameters are practically locally or globally identifiable, where in the ideal case all runs yield the same estimated parameter vector, that is, globally identifiable parameters. A further optimization-based and established approach is the exploitation of the profile likelihood [163, 164]. It is able to specify if a parameter is structurally, practically or non-identifiable, and gives improved confidence intervals over asymptotic ones, Equation (3.33) [165]. Moreover, it might be used to uncover (non-)linear functional relations between the parameters and does not suffer from the downside that methods based on local parameter sensitivities, thus including methods based on the FIM, can only detect linear dependencies between parameters that are rooted in structural non-identifiability [163]. The profile likelihood of a model parameter θ_k is

$$PLL_k(\theta_k) = \max_{\theta_i, \forall i \in \{1,\ldots,n_\theta\} \neq k} \log \mathcal{L}(\boldsymbol{\theta}), \qquad (3.47)$$

with the measurement variance σ^2 being estimated from Equation (3.40). Approximate $100(1 - \phi)\%$ confidence intervals for each parameter are given by [165]

$$2 \log \mathcal{L}(\hat{\boldsymbol{\theta}}_{\text{MLE}}) - 2PLL_k(\theta_k) < \chi^2_{1-\phi;1}, \qquad (3.48)$$

where $\chi^2_{1-\phi;1}$ is the $1 - \phi$ quantile of the chi-square distribution with one degree of freedom. If the profile likelihood has a unique minimum and exceeds the ϕ confidence thresholds in both directions forming a likelihood shape, i.e., if it is possible to determine bounded confidence intervals from Equation (3.48), the parameter is considered practically and structurally identifiable [163]. If the profile likelihood is perfectly flat, a structurally non-identifiable parameter is present. A profile likelihood, that does not exceed the threshold in one or both directions, is a structurally, but not practically identifiable parameter.

3.6   Global Sensitivities

Proposed sensitivity-based methods for parameter identifiability in Section 3.5.1 are based on local parameter sensitivities, Equation (3.45), that may lead to suboptimal or misleading results in model-based design of experiments [166], sensitivity analyses [37], and process design and optimization under uncertainty [114, 167]. The two main reasons for unsatisfying performance of local sensitivity methods are that they approximate the sensitivities in a linear fashion, thereby failing to describe the underlying nonlinearities, and that they are evaluated around a local parameter estimate, that is potentially biased as the true values are usually not known [166]. Hence, a consideration of global parameter sensitivities might be crucial for reliable problem-solving strategies. Generally speaking, taking parametric uncertainty into account splits up into two disciplines: sensitivity analysis (SA) and uncertainty analysis (UA), that are closely related but aim at different findings. The goal of a SA is to determine the relative influences of uncertain inputs $\boldsymbol{u}$ on the model outputs $\boldsymbol{y}$, Equation 3.1. In pharmaceutical manufacturing and development, it can therefore be used to understand system behavior, and to specify critical process parameters and critical material attributes on critical quality attributes. Moreover, SA can assist in issues of parameter identifiability, as it is an extensive framework that complements the sensitivity-based methods for parameter identifiability described in Section 3.5.1. UA, on the other hand, assigns uncertainties to inputs, referred to as uncertainty quantification, and propagates them through the model, coined uncertainty propagation, yielding quantitative evidence about the output uncertainties. Parametric uncertainties should be considered in all kinds of PSE problems [35] like MBDoE [29, 168–170] or process design and optimization [171], especially in the pharmaceutical industry with its high quality standards. Ideally, SA and UA are run in parallel with an UA usually performed first [37].

3.6.1 Uncertainty Propagation

Propagating input uncertainties is frequently performed by the calculation of mathematical moments of the model outputs $\boldsymbol{y}$ in Equation (3.1), that are basically evaluations of integrals. The two most used moments, the first raw and the second central moment, are the expected value, or mean, and the variance (compare with the mean and the variance for the Normal distribution in Equation (3.4)). Interpreting the input variables in our model as a vector of continuous random variables $\boldsymbol{U}$, the mean and the variance of a random model output Y are calculated via

$$\mu = \mathbb{E}[Y] = \mathbb{E}[f(\boldsymbol{U})] = \int_{\Omega} f(\boldsymbol{u}) \, \mathrm{pdf}(\boldsymbol{u}) \mathrm{d}\boldsymbol{u}, \tag{3.49a}$$

$$\sigma^2 = \mathbb{V}[Y] = \mathbb{V}[f(\boldsymbol{U})] = \int_{\Omega} (f(\boldsymbol{u}) - \mu)^2 \, \mathrm{pdf}(\boldsymbol{u}) \mathrm{d}\boldsymbol{u}, \tag{3.49b}$$

with $\mathrm{pdf}(\boldsymbol{u})$ the probability density function of $\boldsymbol{U}$, and Ω the input space in $\mathbb{R}^{n_u}$. $f(\boldsymbol{u})$ represents a generic (non)linear function. Usually, no closed solutions of the integrals on the right side of Equations (3.49a) and (3.49b) are available for nonlinear problems, and therefore must be evaluated numerically. The brute-force method in UP to determine the moments in Equations (3.49) is the propagation of input uncertainties by repetitive model evaluations for samples that have been generated from the input space. Methods, that use random values to approximate a quantity and often serve as benchmarks for more efficient methods, are referred to as Monte Carlo (MC) methods. The mean and the variance in MC methods is approximated using the sample mean $\bar{Y}$ and the sample variance s^2:

$$\mu \approx \bar{Y} = \frac{1}{n_{\mathrm{MC}}} \sum_{i=1}^{n_{\mathrm{MC}}} f(\boldsymbol{U}_i), \tag{3.50a}$$

$$\sigma^2 \approx s^2 = \frac{1}{n_{\mathrm{MC}} - 1} \sum_{i=1}^{n_{\mathrm{MC}}} \left(f(\boldsymbol{U}_i) - \bar{Y} \right)^2, \tag{3.50b}$$

with n_{MC} the number of drawn input samples. One major drawback of the MC method is the usually large number of samples that is needed to obtain a good approximation. This is a general problem of the integrals in Equations (3.49), whose evaluations are computationally expensive, in particular, if the recommended bias-free numerical evaluation path is chosen [148, 172]. In the case of complex functions $f(\boldsymbol{u})$ and a high number of input variables n_u, the determination of the integrals even might be prohibitive due to the so-called *curse of dimensionality*. Alternatively, the point estimate method (PEM), initially developed for generic multi-dimensional integration problems over symmetrical regions, is a credible and practical method for uncertainty propagation with low computational cost; see [173] and references within. In PSE, the PEM has been successfully applied to robustify various optimization problems, including non-symmetrical probability

density functions, correlated model parameters, and imprecise parameter uncertainties [114, 174, 175].

The Point Estimate Method

The PEM approximates the integrals in Equation (3.49) by summing over n_{PEM} weighted sampling points

$$\int_\Omega f(\boldsymbol{u})\,\text{pdf}(\boldsymbol{u})\,\text{d}\boldsymbol{u} \approx \sum_{l=1}^{n_{\text{PEM}}} w_l f(\boldsymbol{u}_l), \tag{3.51}$$

with weight factors w_l and input vector realizations $\boldsymbol{u}_l$. In detail, assuming a nominal input vector $\boldsymbol{u}^*$, dedicated model input vector realizations, $\boldsymbol{u}_l$, form an input vector set, $\boldsymbol{u}_l \in O := \{\boldsymbol{u}^*, O_1, -O_1, O_2, -O_2, O_3, -O_3\}$, where

$$O_1 := \{\boldsymbol{u}^*[i] + \vartheta, \ \forall i \in \{1, \ldots, n_u\}\},$$

$$O_2 := \{\boldsymbol{u}^*[(i,j)] + [+\vartheta, +\vartheta], \ \forall i, \underset{j>i}{j} \in \{1, \ldots, n_u\}\},$$

$$O_3 := \{\boldsymbol{u}^*[(i,j)] + [-\vartheta, +\vartheta], \ \forall i, \underset{j>i}{j} \in \{1, \ldots, n_u\}\}.$$

Here, $\boldsymbol{u}^*[i]$ means that the ith element of the nominal parameter vector, $\boldsymbol{u}^*$, is permuted via the spreading parameter, ϑ, and $\boldsymbol{u}^*[(i,j)]$ that the ith and the jth elements are modified, respectively. Note that the weight factors, w_l, as well as the spreading parameter, ϑ, are determined via a corresponding algebraic equation system; the interested reader is referred to [173] and references therein. Based on the input samples, $\boldsymbol{u}^*$, the statistics of a given nonlinear function can be approximated. For instance, the approximations of the expected value and the variance as stated in Equations (3.49a) and (3.49b) read as

$$\mu \approx w_0 f(\boldsymbol{u}_0) + w_1 \sum_l^{|O_{w_1}|} f(\boldsymbol{u}_l) + w_2 \sum_l^{|O_{w_2}|} f(\boldsymbol{u}_l), \tag{3.53a}$$

$$\sigma^2 \approx w_0(f(\boldsymbol{u}_0) - \mu)^2 + w_1 \sum_l^{|O_{w_1}|} (f(\boldsymbol{u}_l) - \mu)^2 + w_2 \sum_l^{|O_{w_2}|} (f(\boldsymbol{u}_l) - \mu)^2, \tag{3.53b}$$

with $O_{w_1} := \{O_1, -O_1\}$ and $O_{w_2} := \{O_2, -O_2, O_3, -O_3\}$. Please note that the overall parameter sample number, n_{PEM}, used in Equations (3.53a) and (3.53b) scales quadratically to the dimension of uncertain model inputs:

$$n_{\text{PEM}} = 2n_u^2 + 1. \tag{3.54}$$

Table 3.1: Weights and spread parameter of the PEM for a standard Gaussian distribution [173].

Approximation Scheme	w_0	w_1	w_2	ϑ
PEM5 (Equations (3.53a) and (3.53b))	$1 + \frac{n_u^2 - n_u}{18}$	$\frac{4 - n_u}{18}$	$\frac{1}{36}$	$\sqrt{3}$
PEM3 (Equations (3.55a) and (3.55b))	$1 - \frac{n_u}{\vartheta^2}$	$\frac{1}{2\vartheta^2}$	-	ϑ

At the cost of accuracy (i.e., approximation error introduced via Equation (3.52)), the required sample numbers in Equations (3.53a) and (3.53b) can be reduced according to:

$$\mu \approx w_0 f(\boldsymbol{u}_0) + w_1 \sum_l^{|O_{w_1}|} f(\boldsymbol{u}_l), \tag{3.55a}$$

$$\sigma^2 \approx w_0 (f(\boldsymbol{u}_0) - \mu)^2 + w_1 \sum_l^{|O_{w_1}|} (f(\boldsymbol{u}_l) - \mu)^2, \tag{3.55b}$$

where the overall parameter sample number, n_{PEM}, scales linearly to the dimension of uncertain model parameters:

$$n_{\text{PEM}} = 2n_u + 1. \tag{3.56}$$

Equations (3.53) and (3.55) are exact for monomials of up to degrees five and three [173]. Thus, the terms PEM5 and PEM3 are used to distinguish between the two PEM approximation schemes. In Table 3.1, we summarize the values for the weights, w_l, and the spread parameter, ϑ, assuming a standard Gaussian distribution. In the case of PEM3, the spread parameter, ϑ, can be considered to be a design parameter, which is frequently set to the corresponding PEM5 value; that is, $\vartheta = \sqrt{3}$. Please note that any parametric or non-parametric probability distribution of relevant model inputs can be considered via a (non)linear transformation step, including input correlations [174].

3.6.2 Global Sensitivity Analysis

A global sensitivity analysis (GSA) apportions the uncertainty in a model output y to the uncertainty in each model input u. Benefits of a sensitivity study are that it may lead to an identifiable model, a reduced model [176], improved system control [177], or process understanding. For example, the determination of critical process parameters on critical quality attributes in pharmaceutical products can be investigated by a GSA. However, sensitivity analyses of process models are rarely performed, and if, they often lack reliability with a major reason that the input space is not properly explored, e.g., in local sensitivity analyses [178]. An overview of current GSA

methods is given in [179] and [180], where inference is often drawn from different visualizations as outlined in [181]. The variance-based Sobol' method has been successfully applied in various engineering situations, not least because the variance is a very important and widely used measure of uncertainty [37]. The Sobol' method comes with model independence, meaning that there are no assumptions on the model's behavior like linearity or monotonicity. Additionally, it has the ability to capture the influence of each of the inputs over their whole ranges and the interaction effects among all combinations of inputs [37]. One of its biggest drawbacks is the computational effort that is required to calculate the first-order and interaction effects that are based on Monte Carlo simulations. To reduce the computational burden, next to efficient sampling strategies, meta-modeling is usually employed with *polynomial chaos expansion* the most prominent representative of surrogate models for GSA [36, 182]. Alternatively, also Bayesian settings are a possibility to decrease the computational effort [183]. They are also referred to as density-based or moment-independent methods, and are therefore suitable if more extensive sensitivity measures than variances are required [179, 184].

Sobol' Method

Variance-based sensitivity indices are also referred to as Sobol' indices, because of Sobol's work on the decomposition of integrable functions in summands, also known as ANOVA (analysis of variance) representation, and the proposition of a quasi MC algorithm for the calculation of the corresponding sensitivity indices [185]. The derivation of the Sobol' indices and their mathematical computation are outlined in the Appendix, Sections B.3 and B.4. The first Sobol' index is

$$S_i = \frac{\mathbb{V}_{U_i}[\mathbb{E}_{U_{\sim i}}[Y|U_i]]}{\mathbb{V}[Y]}, \tag{3.57}$$

that is also known as the first-order sensitivity index of U_i on Y, where $\sim i$ includes all indices apart from i [37]. Thus, the first-order Sobol' index measures the relative first-order effect of U_i on Y and must be ≤ 1 [186]. Higher-order indices with order n, that are able to capture interaction effects between inputs, can be computed as well according to

$$S_{i_1 i_2 \ldots i_n} = \frac{\mathbb{V}[\mathbb{E}[Y|U_{i_1}, U_{i_2}, \ldots, U_{i_n}]]}{\mathbb{V}[Y]}, \tag{3.58}$$

where we now have dropped the indices of the expectation and variance operators in the numerator with the convention that the argument conditioning the expectation operator, i.e., $U_{i_1}, U_{i_2}, \ldots, U_{i_n}$,

is likewise the set over which we apply the variance operator. Considering independent inputs, or more precisely orthogonal inputs, the following relation holds [37]:

$$\sum_i^{n_u} S_i + \sum_i^{n_u} \sum_{j>i}^{n_u} S_{ij} + \sum_i^{n_u} \sum_{j>i}^{n_u} \sum_{k>j}^{n_u} S_{ijk} + \cdots + S_{123\ldots n_u} = 1. \tag{3.59}$$

Hence, a complete picture of the sensitivities would encompass the determination of $2^{n_u}-1$ terms, too cumbersome to calculate and to analyze. Therefore, a total effect index, that comes at the same computational cost as the first order indices [37], is usually used:

$$S_{\mathrm{T}i} = 1 - \frac{\mathbb{V}[\mathbb{E}[Y|U_{\sim i}]]}{\mathbb{V}[Y]}, \tag{3.60}$$

that measures all order effects that involve the input U_i. Please note that the sum of the total indices in general exceeds 1 as contributions from higher-order indices appear in each of the participating inputs.

The Sobol' method is tailored for independent model inputs, but dependent model parameters might occur in reality [36, 187]. A direct way to deal with dependent inputs is to use isoprobabilistic transformation concepts, such as the Rosenblatt and the Nataf transformation [188]. Sampling from correlated inputs considering copulas has been combined with density-based methods likewise [189]. Alternatively, covariance-based sensitivity indices have been introduced in [190] that are derived from the same function decomposition as for the Sobol' indices.

3.7 Model-based Design of Experiments

Identifying a reliable process model is a challenging problem, particularly in (bio-)chemical engineering where often reaction kinetics are not known *a priori*, see Section 1.1. Even if the stoichiometries have been established, the mathematical rate laws, Equation (3.15), might not be readily revealed [26]. Furthermore, model parameters like kinetic constants are usually unknown and have to be estimated, Section 3.4, or suffer from great uncertainty and parameter dependencies. One major tool in the systematic identification strategy in Figure 3.3 is therefore the model-based design of experiments (MBDoE). MBDoE facilitates model identification by planning experiments with high informative output under the consideration of the formulated process model or the postulated model candidates, thereby reducing development time and cost [29, 191, 192]. MBDoE approaches have proven beneficial over the last few decades [29, 121–123], among which a sequential approach of designing experiments as shown in Figure 3.3, is known to robustify the overall design of experiment [193].

In general, Design of experiments (DoE) is applied in both academic and industrial problems, and accordingly covers a broad range of different approaches, methods, and targeted goals [33, 194]. They all have in common that designing an experiment means to predict the design vector ξ of setup parameters, that can be altered when performing an experiment, to meet a previously defined target. The prediction of the design vector ξ often involves solving an optimization problem. The literature distinguishes between statistical design of experiment and MBDoE approaches. Methods of the former, e.g., factorial designs or response surface methods, are popular and commonly used because of their simplicity, but are not able to sufficiently handle complex dynamic systems for the same reason [33]. DoE concepts, that can be considered as a combination of statistical and model-based DoE, also exist in literature [195]. Moreover, in contrast to the usually offline performed DoE, one might distinguish adaptive online MBDoE, that instantly exploits measurement information from a running experiment as soon as it is available [196]. While all experimental designs aim at decreasing experimental effort for high information content in the designed experiments, specific goals of MBDoE are versatile. In the following, we focus on the challenge of precise parameter identification and reliable model selection. Likewise, practical identifiability, Section 3.5.1, might be considered in MBDoE [192].

3.7.1 Design of Experiments for Model Selection

Common goal of different DoE strategies for model selection is to maximize some measure on the distance between the different model candidates with the prospect that the measurement data from the designed experiment ideally fits to only one of the candidates.Different specific objective functions for the model selection problem can be found in literature [197–199]. In Bayesian settings, where probability distributions are available, the Kullback-Leibler divergence, Equation (B.9), is a natural choice [200–202]. In contrast, in point estimate frameworks and if measurement deviations are assumed to be constant, a common criterion for model selection, that can be interpreted as Euclidean distances between predicted outputs of M different model candidates, is [203]

$$\mathcal{J}_{\text{ED}}(\xi) = \sum_{i=1}^{M-1} \sum_{j=i+1}^{M} \sum_{k=1}^{n_t} \Big[y_i(\xi, t_k) - y_j(\xi, t_k) \Big]^2, \tag{3.61}$$

with $\xi \in \mathbb{R}^{n_\xi}$ the experimental design vector, that summarizes the variables or parameters that are available and planned to be altered during the course of the designed experiment. For a robust

formulation of the objective function against parametric uncertainty, a straightforward implementation is the addition of another term, that penalizes the propagated uncertainty quantified by the variances of the models' outputs, Equation (3.49b):

$$\mathcal{J}_{\text{rED}}(\boldsymbol{\xi}) = \lambda \sum_{i=1}^{M-1} \sum_{j=i+1}^{M} \sum_{k=1}^{n_t} \Big(\mathbb{E}[\boldsymbol{y}_i(\boldsymbol{\xi}, t_k)] - \mathbb{E}[\boldsymbol{y}_j(\boldsymbol{\xi}, t_k)] \Big)^2 + (1 - \lambda) \sum_{i=1}^{M} \sum_{k=1}^{n_t} \mathbb{V}[\boldsymbol{y}_i(\boldsymbol{\xi}, t_k)], \quad (3.62)$$

with $\lambda \in [0, 1]$ the penalty weight factor leading to Pareto optimal points for different values of λ. The expectations $\mathbb{E}$ and variances $\mathbb{V}$ are with respect to the model parameters $\boldsymbol{\theta}$.

3.7.2 Design of Experiments for Parameter Precision

To decrease the uncertainties in the model parameters of the selected model candidate and thereby strengthening the reliability of the analyzed model, DoE for parameter precision is an effective tool [33]. Here, MBDoE aims at minimizing the covariance matrix of the model parameters, $\boldsymbol{C}_\theta$ in Equation (3.34), by maximizing the parameter sensitivities on the measured outputs [27]. The predictive reduction in the uncertainty of a model parameter will ultimately result in a smaller confidence interval for the estimated model parameter, Section 3.4. As shown in Section 3.5.1, $\boldsymbol{C}_\theta$ might be derived from the FIM and the limiting case of the Cramér-Rao inequality, Equation Equation (3.34). For the MBDoE the FIM has to be predicted, as the data to build the likelihood in Equation (3.37) is not yet available, i.e., the expected FIM has to be used, Equation (3.38). If the measurement covariance matrix is diagonal with equal magnitude for all its entries, it can be dropped in Equation (3.38). An effective information matrix can then be postulated:

$$\boldsymbol{IM}(\boldsymbol{\xi}|\hat{\boldsymbol{\theta}}) = \sum_{i=1}^{N_{\text{T}}} \boldsymbol{SM}_i(\boldsymbol{\xi}|\hat{\boldsymbol{\theta}})^\top \boldsymbol{SM}_i(\boldsymbol{\xi}; \hat{\boldsymbol{\theta}}), \quad (3.63)$$

with N_{T} the number of experimental runs or samples, that is a sum over the already collected samples N_0 plus the samples from the DoE N_{DoE} that have not yet been collected, i.e., $N_{\text{T}} = N_0 + N_{\text{DoE}}$. Several criteria for DoE that are based on the FIM are available in literature [27]. The D-optimal criterion minimizes the volume of the parameter covariance matrix; i.e., the determinant of the FIM. It is a widely used criterion as it considers parameter correlations and is invariant against re-parameterizations of the model [204]:

$$\mathcal{J}_{\text{Dopt}}(\boldsymbol{\xi}) = \det \boldsymbol{IM}(\boldsymbol{\xi}|\hat{\boldsymbol{\theta}}). \quad (3.64)$$

Note that a minimization of the determinant of the parameter covariance matrix is equal to a maximization of the determinant of the FIM.

3.8 Mathematical Optimization

The objective functions for the parameter estimation problem, Equation (3.39), the DoE for model selection, Equations (3.61) and (3.62), and the DoE for parameter precision, Equation (3.64), are embedded into a mathematical optimization problem. As a generalized problem to parameter estimation with respect to the type of optimization, DoE frequently leads to an optimal control problem of the form

$$
\min_{\boldsymbol{x}(t), \boldsymbol{u}(t), \boldsymbol{\theta}} \quad \mathcal{J}(\boldsymbol{x}(t_{\mathrm{f}}))
$$

$$
\begin{aligned}
\text{s.t.} \quad & \text{process model: Equations (3.5a) \& (3.5b),} \\
& \boldsymbol{g}_{\mathrm{eq}}(\boldsymbol{x}(t), \boldsymbol{u}(t), \boldsymbol{\theta}) = 0, \\
& \boldsymbol{g}_{\mathrm{ineq}}(\boldsymbol{x}(t), \boldsymbol{u}(t), \boldsymbol{\theta}) \leq 0,
\end{aligned}
\tag{3.65}
$$

with $\mathcal{J}$ the scalar objective function, $t \in [t_0, t_{\mathrm{f}}]$ the "time" parameter, $\boldsymbol{g}_{\mathrm{eq}} : \mathbb{R}^{n_x \times n_u \times n_\theta} \rightarrow \mathbb{R}^{n_{\mathrm{eq}}}$ and $\boldsymbol{g}_{\mathrm{ineq}} : \mathbb{R}^{n_x \times n_u \times n_\theta} \rightarrow \mathbb{R}^{n_{\mathrm{ineq}}}$ the equality constraints and the inequality constraints, respectively [205].

For solving the optimization problem in Equation (3.65), different methods are available [206]. A short summary is given in the Appendix B.5. The optimization problems in the following Chapters are solved with local gradient-based methods [207] using either the free and open source solver Ipopt [208] or a quasi-Newton solver [209]. Moreover, in particular for the parameter estimation runs, a multi-start approach is followed to escape local minima and obtain better insight of the design space [28]. For the implementations, Julia is used [210].

Having laid out in this Chapter the fundamentals about first how to build a process model for (bio)chemical processes and second how to mathematically and reliably identify such a process model, the following three Chapters make use of the presented methods. That is, in Chapters 4 and 5, the building and identification of a process model for the artemisinin semi-synthesis; and in Chapter 6, the combination of the outlined methods with the differential flatness concept for a (bio)chemical reaction network.

4 Step 1: Photooxygenation

In this Chapter, the first step of the semi-synthesis to artemisinin, the photooxygenation of dihydroartemisinic acid to the intermediate hydroperoxide, is investigated. First, the reaction network and the process model are derived. Second, the results are presented, that include a qualitative analysis of the experimental results followed by a model-based analysis of the system characteristics.

Contents of this chapter including Tables and Figures have been published in [108] as a shared co-first authorship between Susann Triemer and Moritz Schulze. Individually contributed parts by Susann Triemer, that are necessary for understanding, are summarized or reproduced with appropriate annotations.

4.1 Reaction Network of the Photooxygenation of Dihydroartemisinic Acid

In this Section, a summary is given about the reactions occurring during the photooxygenation of dihydroartemisinic acid (DHAA), that has been written by Susann Triemer in [108]. The photooxygenation of DHAA to hydroperoxides proceeds via two main reaction steps (Figure 4.1):

1. photosensitized formation of singlet oxygen and
2. ene-type reaction to an hydroperoxide.

The corresponding simplified reaction network is given in Figure 4.1. The photosensitizer, here 9,10-dicyanoanthracene (DCA), is excited to a singlet state by absorbing light in the blue wavelength region (400 to 500 nm) and is subsequently quenched following one of many possible quenching routes [211, 212]. In the major pathway, triplet oxygen quenches singlet state DCA to one singlet oxygen molecule leaving DCA in its triplet state. This triplet state DCA can form another singlet oxygen molecule thereby reducing DCA to its ground state. Thus the overall quantum yield can be as high as 2, while its actual value strongly depends on the solvent, the dissolved oxygen concentration and further present quenchers [212]. In benzene, a maximum quantum yield of singlet oxygen extrapolated to indefinite oxygen concentration is reported to lie
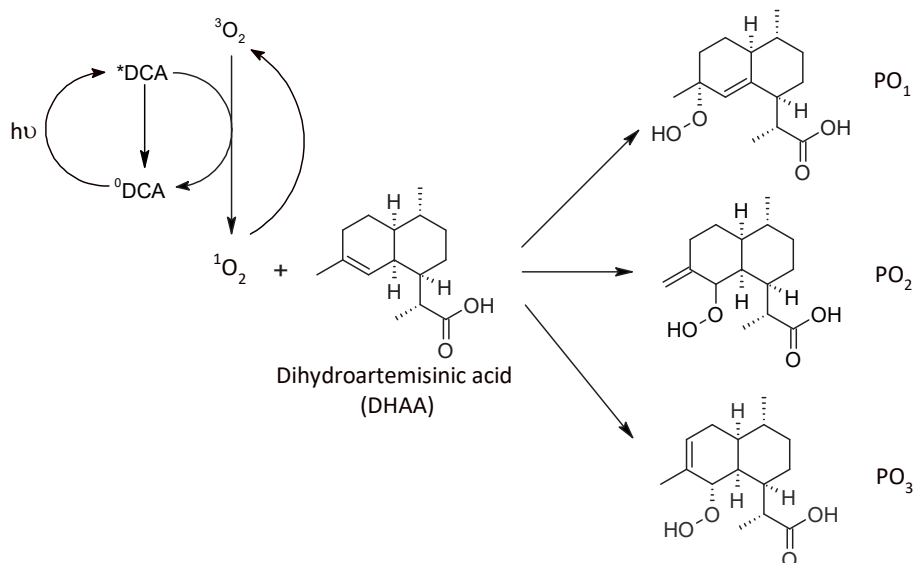
Figure 4.1: Simplified reaction network of the photooxygenation of dihydroartemisinic acid (DHAA) to the targeted hydroperoxide PO$_1$ – a precursor in the artemisinin semi-synthesis. The photosensitizer 9,10-Dicyanoanthracene (DCA) enables the *in situ* formation of singlet oxygen. Figure is reprinted from [108].

in the range of 1.56 to 1.71 [212–214]. A thorough derivation of the reaction network that leads to singlet oxygen, and that is used in this work, is given in Susann Triemer's dissertation [61].

The formed singlet oxygen can either react with DHAA or be quenched to its triplet state. The reaction with DHAA follows a 1,5-sigmatropic H-shift matching an ene-type reaction referred to as Schenk-reaction [215]. Three different hydroperoxides can be formed from this mechanism, with the tertiary hydroperoxide PO$_1$ being the major product. At the same time, PO$_1$ is the intermediate to artemisinin (ART) and therefore the targeted product of the photooxygenation. All of the hydroperoxides are only semi-stable decomposing within several weeks following diverse rearrangement and degradation reactions [216]. Main byproduct of the photooxygenation is arteannuin H, that originates from the secondary allylic hydroperoxide [217, 218] and is lumped into the byproduct PO$_X$ in the kinetic model at a later stage, Section 4.2.1.

4.2 Process Model for the Photooxygenation of Dihydroartemisinic Acid

The difficulty in obtaining reliable reaction kinetics for the photooxygenation of DHAA lies in the interaction of the chemical reaction network with photon and mass transfer processes.
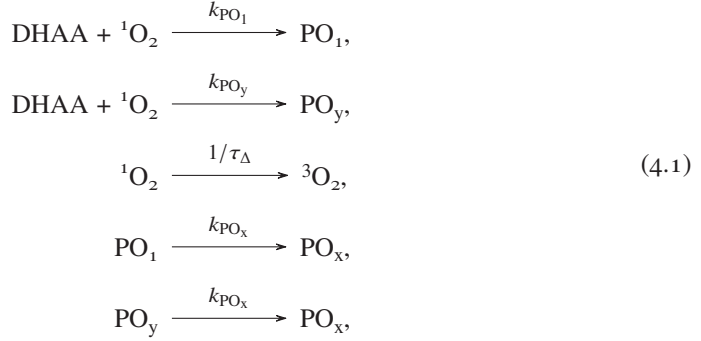
Both phenomena are complex to describe and depend strongly on the reactor system applied. Accordingly, the identified process model is assembled from two main parts, a kinetic and a reactor model. The kinetic model describes the (photo-induced) chemical reactions and is independent of the process setup. The reactor model, instead, reproduces the fluid dynamics of the two-phase flow, including the interfacial transfer equations, and is dependent on the photo-flow reactor system used. Both components of the process model, that integrates the kinetics into the reactor model, are introduced in the following subsections. In the end, a short background on how model-based design of experiments (MBDoE) is used to identify the process model and how the model parameters are estimated and assessed is outlined.

The kinetic and the reactor model have been developed in close collaboration with Susann Triemer [108], with her master thesis [219] serving as a starting point.

4.2.1 Kinetic Rate Equations for the Photooxygenation

The reaction scheme of the kinetic model is shown in Figure 4.1. The tertiary hydroperoxide PO_1 is the species of interest, that is, it is further converted to artemisinin. The two secondary hydroperoxides PO_2 and PO_3 are lumped together to the byproduct species PO_y. In the conducted photooxygenation experiments, the recovery of the measured products PO_1 and PO_y make up around 95 % of the total amount of reacted DHAA. The missing 5 % are attributed to re-arrangement and degradation products formed between sampling and measurement. To cover these additional and presently chemically unidentified products and the respective reactions, an additional species PO_x is introduced, which is produced from PO_1 and PO_y. Identical reaction rate constants are assumed. This approach is motivated by the lack of data on species and re-actions, as it allows to lump the unknown and unquantifiable reactions and side products. This approach may be replaced by a more detailed mechanism once that more is known on the side reactions. Alternatively, separate loss reactions might lead to additional complications during

the identification of their reaction constants and would therefore make a physical interpretation difficult. Hence, the chemical reaction network is

$$\text{DHAA} + {}^1\text{O}_2 \xrightarrow{\quad k_{\text{PO}_1} \quad} \text{PO}_1,$$

$$\text{DHAA} + {}^1\text{O}_2 \xrightarrow{\quad k_{\text{PO}_y} \quad} \text{PO}_y,$$

$$\hspace{4em}{}^1\text{O}_2 \xrightarrow{\quad 1/\tau_\Delta \quad} {}^3\text{O}_2, \hspace{6em} (4.1)$$

$$\hspace{4em}\text{PO}_1 \xrightarrow{\quad k_{\text{PO}_x} \quad} \text{PO}_x,$$

$$\hspace{4em}\text{PO}_y \xrightarrow{\quad k_{\text{PO}_x} \quad} \text{PO}_x,$$

with kinetic rate constants k_i, $i \in \{\text{PO}_1, \text{PO}_y, \text{PO}_x\}$, and the lifetime of singlet oxygen τ_Δ. The corresponding reaction rates are expressed as elementary reactions, Section 3.3.1, resulting in the following rates of formation derived from Equation (3.15):

$$r_{\text{PO}_1} = k_{\text{PO}_1}[\text{DHAA}][{}^1\text{O}_2], \hspace{4em} (4.2a)$$

$$r_{\text{PO}_y} = k_{\text{PO}_y}[\text{DHAA}][{}^1\text{O}_2], \hspace{4em} (4.2b)$$

$$r_{\text{PO}_x} = k_{\text{PO}_x}([\text{PO}_1] + [\text{PO}_y]). \hspace{4em} (4.2c)$$

Since singlet oxygen is a very reactive and short-lived species, the steady-state assumption [26] is applied,

$$\frac{d[{}^1\text{O}_2]}{dz} \overset{!}{\cong} 0 \cong r_{{}^1\text{O}_2} - (k_{\text{PO}_1} + k_{\text{PO}_y})[\text{DHAA}][{}^1\text{O}_2] - \frac{1}{\tau_\Delta}[{}^1\text{O}_2], \hspace{3em} (4.3)$$

where $r_{{}^1\text{O}_2}$ is the formation rate of singlet oxygen. Combining Equations (4.2) with Equation (4.3) yields

$$r_{\text{PO}_1} = r_{{}^1\text{O}_2} \frac{\tilde{k}_{\text{PO}_1}[DHAA]}{1 + (\tilde{k}_{\text{PO}_1} + \tilde{k}_{\text{PO}_y})[DHAA]}, \hspace{3em} (4.4a)$$

$$r_{\text{PO}_y} = r_{{}^1\text{O}_2} \frac{\tilde{k}_{\text{PO}_y}[DHAA]}{1 + (\tilde{k}_{\text{PO}_1} + \tilde{k}_{\text{PO}_y})[DHAA]}, \hspace{3em} (4.4b)$$

$$r_{\text{PO}_x} = k_{\text{PO}_x}([\text{PO}_1] + [\text{PO}_y]), \hspace{3em} (4.4c)$$

with the kinetic constants normalized to the lifetime of singlet oxygen

$$\tilde{k}_i = k_i \tau_\Delta, i \in \{\text{PO}_1, \text{PO}_y\}. \hspace{4em} (4.5)$$

The life time of singlet oxygen in toluene τ_Δ is 33.2 µs at $-20\,°C$, extrapolated from available data in the range from 5 to 90 °C [220].

Photosensitized Formation of Singlet Oxygen

In photosensitized processes, expressions for reaction rates are either empirically derived, thus having limited scope, or mechanistically motivated [221]. The mechanistic justification lies in the fact that "in a single photon absorption process, the rate of the photosensitizer activation step (primary event) is proportional to the rate of energy absorbed" [221]. The formation rate of singlet oxygen might be expressed as

$$r_{^1O_2} = \Phi_{^1O_2} L_p^a, \tag{4.6}$$

with the local volumetric rate of photon absorption L_p^a and the quantum yield of singlet oxygen $\Phi_{^1O_2}$. The latter is defined as the number of singlet oxygen molecules formed per absorbed photon.

Different mechanistic networks for the formation of singlet oxygen by DCA in various solvents have been derived in literature [211, 212]. An in-depth discussion about the networks proposed in literature can be found in Susann Triemer's dissertation [61]. Here, implications on the quantum yield by extraneous species, e.g. solvent quenching, are neglected as they are unknown and would encompass the unfavorable situation that the quantum yield does not tend to zero with vanishing oxygen concentration [211, 212, 222]. The quantum yield of singlet oxygen can then be stated as

$$\Phi_{^1O_2} = \frac{[O_2]}{k_{11}[O_2] + k_{12}}, \tag{4.7}$$

where k_{11} and k_{12} are lumped kinetic parameters that combine diverse rate constants [212]. The concentration of triplet oxygen concentration in Equation (4.7) is replaced by the concentration of dissolved oxygen as singlet oxygen occurs merely in trace quantities [102, 222].

Connecting the Reaction Kinetics to the Rate of Photon Absorption

The interaction between radiative transfer from the light source via the reaction medium to the place of reaction and reaction kinetics is visualized in Figure 4.2. The reaction rates in Equations (4.4) and (4.6) depend on the local volumetric rate of photon absorption L_p^a that results from the radiative transfer equation. The L_p^a, in turn, depends on the concentrations of the chemical species $\mathbf{c}$. A common assumption is that photons are predominantly absorbed by the photosensitizer, i.e., $\mathbf{c} = (c_{DCA})$, leading to the substantial simplification that the radiative transfer equation and
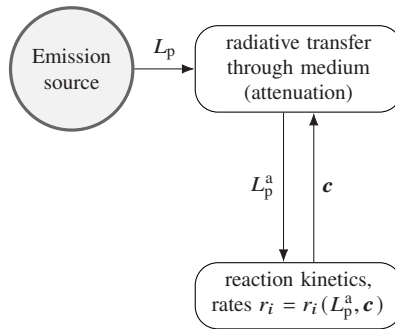
Figure 4.2: Interaction between radiative transfer and reaction kinetics; L_p: local volumetric incident photon flux, L_p^a: local volumetric rate of photon absorption, c: vector holding concentrations of present species.

the chemical kinetics are decoupled and can therefore be solved independently. However, the L_p^a remains a complex function of position and time, that is highly dependent on the individual reactor geometry, the physical properties of the participating media and the flow conditions [223].

If nontransient light intensity is assumed, an averaged L_p^a is derived from the Beer-Lambert law [224],

$$\langle L_p^a \rangle = L_p(1 - \exp\left[-\kappa c_{DCA} l_{opt}\right]), \tag{4.8}$$

with the local volumetric incident photon flux L_p, the napierian absorption coefficient of the absorbing species κ, the photosensitizer concentration c_{DCA}, and the optical path length l_{opt}. The concentration of DCA was assumed to be constant throughout the whole reactor. Please note that Equation (4.8) does not explicitly include the irradiation from two sides as the here used reactor setup would suggest. Due to the symmetric configuration of the capillary reactor, however, the superposition of the light emission from two sides is implicitly alleviated in L_p. In addition, an error resulting from this simplified description is balanced by considering the optical path length as one of the parameters to be estimated, Equation (5.7).

The local volumetric incident photon flux L_p is defined as the absolute incident photon flux q_0 related to the irradiated volume of the reaction solution V_l:

$$L_p = \frac{q_0}{V_l}. \tag{4.9}$$

In complex reactor geometries, the local rate of photon absorption might differ significantly within the reactor volume altering the local reaction rates. In this study, L_p^a was assumed to be constant. The assumption of homogeneous illumination is commonly made in microreactor modeling, resulting in good model-data fits [225]. This includes that the effect of a decreasing gas holdup due to reaction progress on the average path length [226] is neglected. The reaction kinetics are therefore related to the averaged L_p^a, which is constant over the whole reactor length.

Accordingly, the actinometric measurements used to characterize the irradiation conditions in the reactor provide an average value of the incident photon flux over the reactor length, Section 4.3.2.

4.2.2 Reactor Model

The reactor model connects the intrinsic reaction rates with the physical phenomena occurring within the reaction line, namely the specific flow conditions and mass transfer. The key assumptions for the description of the reactor behavior are stated in Table 4.1. For the sake of process characterization and process design, the gas and liquid phase as well as the mass transfer between them need to be quantified. In the following, the balance equations are derived for each phase separately based on the two-fluid model, Section 3.3.2, and subsequently the interfacial mass transfer between the gas and the liquid phase is described.

Description of Fluid Dynamics with the Two-Fluid Model

Resulting from the simplifications in Table 4.1, the material balance of a species i in the liquid phase in terms of concentration c_i along the reactor coordinate z from Equation (3.22) becomes

$$\frac{\mathrm{d}c_i}{\mathrm{d}z} = \frac{1}{u_\mathrm{l}}(\bar{r}_i + \delta_i j_{\mathrm{O}_2}), \quad \delta_i = \begin{cases} 1, & i = \mathrm{O}_2 \\ 0, & \text{else} \end{cases}, \tag{4.10}$$

where u_l is the liquid phase velocity, $\bar{r}_i$ is the net rate of reaction and j_{O_2} is the transfer of oxygen from the gas to the liquid phase. The species i is in the set $\{\mathrm{DHAA}, \mathrm{PO}_1, \mathrm{PO}_\mathrm{y}, \mathrm{PO}_\mathrm{x}, \mathrm{O}_2\}$. The delta function δ_i ensures that the oxygen transfer is solely active in the balance for dissolved oxygen.

For the gas phase, a material balance over oxygen and the total gas flow $\dot{V}_\mathrm{g}$ is considered. The former in terms of molar fraction x_{O_2}, Equation (3.27), is

$$\frac{\mathrm{d}x_{\mathrm{O}_2}}{\mathrm{d}z} = -\frac{RT}{p\dot{V}_\mathrm{g}}(1-\alpha)A j_{\mathrm{O}_2}(1-x_{\mathrm{O}_2}), \tag{4.11}$$

and the material balance over the total gas flow, Equation (3.28), reads

$$\frac{\mathrm{d}\dot{V}_\mathrm{g}}{\mathrm{d}z} = -\frac{RT}{p}(1-\alpha)A j_{\mathrm{O}_2}. \tag{4.12}$$

In Equations (4.11) and (4.12), R is the universal gas constant, T the temperature, p the total pressure, and A the known cross-sectional area of the channel.

To solve the material balances in Equations (4.10), (4.11) and (4.12), the unknown gas fraction $\alpha = \frac{A_g}{A}$, Equation (3.18), must be determined. To this end, an established simplification of the two-fluid model – the drift flux model – is used [227, 228]; for further details see SI of [108]. The drift flux model reduces the momentum and energy balance to one mixture equation in each case at the cost of losing some key characteristics of two-phase flow [128]. It may be applied to flows where the motion of the two phases are closely coupled. On the other hand, if they are only weakly locally coupled, the drift flux model can be used as well, provided that there is enough interaction time along the reactor line [128]. Its constitutive equation relates α to the known gas holdup β,

$$\alpha = \frac{1}{C_0}\beta, \tag{4.13}$$

with

$$\beta = \frac{\dot{V}_g}{\dot{V}} = \frac{\dot{V}_g}{\dot{V}_g + \dot{V}_l}. \tag{4.14}$$

The distribution factor C_0 might be taken from literature or experimentally determined. In this study, C_0 is estimated by measurement of the residence time after tracer injection.

Interfacial Oxygen Transfer

Mass transfer of oxygen from the gas into the liquid phase is modeled according to

$$j_{O_2} = k_l a([O_2]^\infty - [O_2]), \tag{4.15}$$

where $[O_2]^\infty$ is the saturation concentration of oxygen in the liquid phase and $k_l a$ is the volumetric transfer coefficient based on the specific gas-liquid interfacial surface area a. The saturation concentration is calculated by Henry's law (see SI of [108]) and is taken from literature [229]. The mass transfer coefficient $k_l a$ in Equation (4.15) is affected by several reactor-dependent and fluid properties, that are summarized in a contribution from the Taylor bubble caps and a contribution from the liquid film between reactor wall and Taylor bubble [230]. The contribution by the film was observed to be dominant [230], leading to $k_l a \propto \sqrt{D_{O_2} u_g^s / L_{UC}}/d$ with the diffusion coefficient of oxygen D_{O_2} and the length of a unit cell L_{UC} consisting of the gas bubble and the liquid slug [231]. Since no information about the geometry of the unit cell is readily available, a simple dependence of the mass transfer coefficient on the superficial gas velocity is considered:

$$k_l a = \widetilde{k_l a}\sqrt{u_g^s}, \tag{4.16}$$

introducing a constant $\widetilde{k_l a}$.

Table 4.1: Summary of key assumptions applied to describe the reactor behavior.

The relative pressure drop over the reactor is small (0.1 to 0.5 bar at 7 bar operating pressure). Consequently, the momentum balance is neglected [131].

Due to the isothermal operation of the reactor, there are no internal temperature gradients. Thus, energy balances are not considered.

The flow is one-dimensional (z axis). Hence, ideal mixing in radial direction is assumed [129, 232].

Diffusion is not considered.

The operation of the setup is in steady-state.

The liquid phase is incompressible. The density is calculated by a simple mixture density of the solvent plus the excess volume caused by the addition of DHAA.

Material exchange between the phases is based on the linear approach to mass transfer.

The gas phase can be described by an ideal gas mixture, i.e., the Taylor bubbles are well mixed.

The dissolved oxygen concentration is derived from Henry's law.

4.2.3 The Process Model: Combining the Kinetics with the Reactor Model

The integration of the chemical kinetics, Equations (4.4), and the mass transfer relation, Equation (4.15), into the material balances (4.10), (4.11) and (4.12) provides the governing equations of

the process model for both the liquid and the gas phase, yielding the state-space representation (3.5a):

$$
\frac{d[DHAA]}{dz} = \frac{\left(1 - \frac{\beta}{C_0}\right)A}{\dot{V}_l}\left(-\frac{[O_2]}{k_{11}[O_2] + k_{12}}\frac{(\tilde{k}_{PO_1} + \tilde{k}_{PO_y})[DHAA]}{1 + (\tilde{k}_{PO_1} + \tilde{k}_{PO_y})[DHAA]}\cdot\right.
$$
$$
\left. L_p(1 - \exp[-\kappa c_{DCA}l_{opt}])\right),
$$

$$
\frac{d[PO_1]}{dz} = \frac{\left(1 - \frac{\beta}{C_0}\right)A}{\dot{V}_l}\left(\frac{[O_2]}{k_{11}[O_2] + k_{12}}\frac{\tilde{k}_{PO_1}[DHAA]}{1 + (\tilde{k}_{PO_1} + \tilde{k}_{PO_y})[DHAA]}\cdot\right.
$$
$$
\left. L_p(1 - \exp[-\kappa c_{DCA}l_{opt}]) - k_{PO_x}[PO_1]\right),
$$

$$
\frac{d[PO_y]}{dz} = \frac{\left(1 - \frac{\beta}{C_0}\right)A}{\dot{V}_l}\left(\frac{[O_2]}{k_{11}[O_2] + k_{12}}\frac{\tilde{k}_{PO_y}[DHAA]}{1 + (\tilde{k}_{PO_1} + \tilde{k}_{PO_y})[DHAA]}\cdot\right.
$$
$$
\left. L_p(1 - \exp[-\kappa c_{DCA}l_{opt}]) - k_{PO_x}[PO_y]\right),
$$

$$
\frac{d[PO_x]}{dz} = \frac{\left(1 - \frac{\beta}{C_0}\right)A}{\dot{V}_l}k_{PO_x}([PO_1] + [PO_y]),
$$

$$
\frac{d[O_2]}{dz} = \frac{\left(1 - \frac{\beta}{C_0}\right)A}{\dot{V}_l}\left(-\frac{[O_2]}{k_{11}[O_2] + k_{12}}\frac{(\tilde{k}_{PO_1} + \tilde{k}_{PO_y})[DHAA]}{1 + (\tilde{k}_{PO_1} + \tilde{k}_{PO_y})[DHAA]}\cdot\right.
$$
$$
\left. L_p(1 - \exp[-\kappa c_{DCA}l_{opt}]) + \widetilde{k_la}\sqrt{u_g^s}([O_2]^\infty - [O_2])\right),
$$

$$
\frac{dx_{O_2}}{dz} = \frac{T}{p\dot{V}_g}\left(-R\frac{\beta}{C_0}A\widetilde{k_la}\sqrt{u_g^s}([O_2]^\infty - [O_2]) - \frac{p}{T}x_{O_2}\frac{d\dot{V}_g}{dz}\right),
$$

$$
\frac{d\dot{V}_g}{dz} = -\frac{T}{p}R\frac{\beta}{C_0}A\widetilde{k_la}\sqrt{u_g^s}([O_2]^\infty - [O_2]),
$$

(4.17)

with initial conditions

$$
([DHAA], [PO_1], [PO_y], [PO_x], [O_2], [x_{O_2}], [\dot{V}_g])(0)
$$
$$
= ([DHAA]_0, 0, 0, 0, [O_2]^\infty, x_{O_2,0}, \dot{V}_{g,0}).
$$

The vector of unknown model parameters of the process model, that needed to be identified, is

$$\boldsymbol{\theta} = (\widetilde{k_1 a}, k_{11}, k_{12}, \tilde{k}_{PO_1}, \tilde{k}_{PO_y}, k_{PO_x}, l_{opt}). \tag{4.18}$$

Note that the time variable t in the state equation (3.5a) is replaced by the reactor coordinate z.

4.3 Results and Discussion

In the following, the experimental results for the distribution factor in the drift-flux model, the absorption coefficient of the photosensitizer and the incident volumetric photon flux are shortly summarized. Subsequently, the reaction behavior of the photooxygenation is analyzed qualitatively on the basis of the experimental data. In the last part, the experimental data is used to identify the kinetic model parameters and assess the suitability of the previously made assumptions. The parameterized model is then applied to understand and identify the rate-determining effects in dependence on the reaction conditions. Finally, the developed process model is used to determine the most influential parameters on key quantities by a global sensitivity analysis.

4.3.1 Experimental Identification of Model Parameters

The distribution coefficient C_0 and the absorption coefficient κ of DCA at irradiation wavelength are two essential model parameters. Both were determined prior to the photooxygenation experiments and were then fixed in the model identification. The parameters have been determined by Susann Triemer at the MPI Magdeburg, and the results are solely reported in the following. For a thorough derivation and the measurement technology used, please see [108].

The determined value for the distribution factor is

$$C_0 = 1.02 \pm 0.025 \ (95\% \ \text{confidence interval}). \tag{4.19}$$

The value is close to the special case of $C_0 = 1$, that results in equal flow velocities of the liquid and the gas phase. Thus, $C_0 = 1.02$ means that only a very thin liquid film forms around the moving gas bubbles; compare with Figure 2.4.

The obtained Napierian absorption coefficient κ of 9,10-Dicyanoanthracene in Toluene is

$$\kappa = 12\,841.98\,1/(\text{mol\,cm}). \tag{4.20}$$

4.3.2 Quantification of the Incident Volumetric Photon Flux L_p

The relations between the incident volumetric photon flux L_p and both the set LED power P_{LED} and the unknown optical path length l_{opt} have been established by Susann Triemer at the MPI Magdeburg. Detailed information is given in [108] and summarized in the following.

To connect the volumetric incident photon flux with the LED-power, an LED-typical linear relation is used:

$$L_p = \tilde{L}_p \cdot P_{LED}, \tag{4.21}$$

with proportionality factor $\tilde{L}_p$.

The optical path length l_{opt} strongly influences the unknown incident photon flux L_p from the actinometric measurements, but was found to be insensitive in the performed experiments. On the other hand, the complex irradiation geometry of the applied reactor, Figure 2.3, makes it difficult to determine l_{opt} from theoretical considerations, namely wide emission angles of the LEDs, illumination from two sides, reflection within the reactor casing and Taylor flow conditions. As an alternative, the optical path length is set as an additional model parameter to be estimated from experimental data sampled during the photooxygenation of DHAA. In turn, the proportionality factor $\tilde{L}_p$ is derived from the Beer-Lambert law and actinometric measurements in the applied continuous reactor setup using ferrioxalate and with a dependence on l_{opt}:

$$\tilde{L}_p = \frac{8.893 \times 10^{-5}\,\mathrm{mol}/(\mathrm{l\,s\,LED-\%})}{1 - \exp^{-23.935/\mathrm{cm}\cdot l_{opt}}}. \tag{4.22}$$

The parameterized relation from Equations (4.21) and (4.22) is used in the model, Equations (4.17), to link the knowledge from the actinometric measurements to the photooxygenation experiments.

4.3.3 Qualitative Assessment of the Reaction Behavior of the Photooxygenation

Susann Triemer assessed the collected experimental data to infer qualitative trends of the reaction behavior on the basis of Figure 4.3 [61, 108]. The main findings are of vital importance for the interpretation of the developed process model and are therefore summarized in the following.

The concentration-time-profiles follow a mixed zero and first reaction order as proposed in the model. The decreasing recovery towards full conversion is probably attributed to rearrangement and degradation reactions of the formed hydroperoxides as observed in mechanistic studies by Brown et al. [216–218], and taken care of in the additional species PO_x, Section 4.2.1.

(**a**) Dependence on Residence Time

(**b**) Dependence on LED Power Setting

(**c**) Dependence on x_{O_2} and DCA concentration
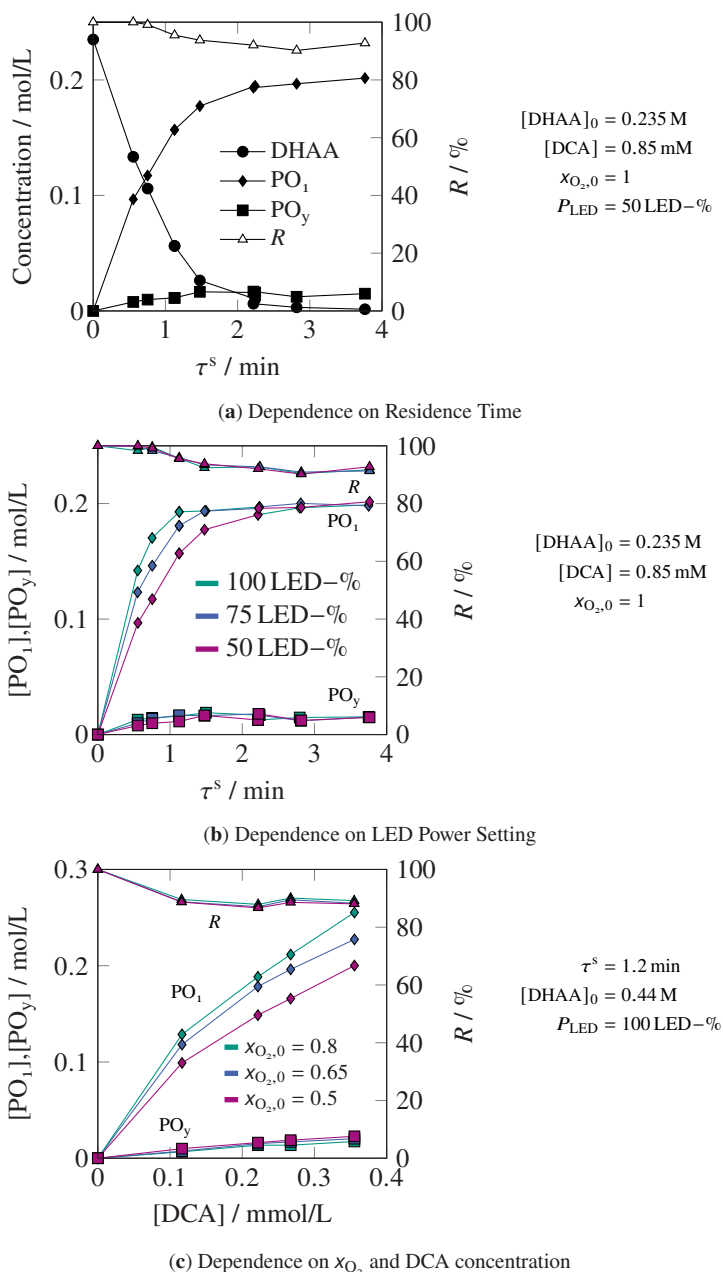
Figure 4.3: Behavior of the photooxygenation of dihydroartemisinic acid to the desired hydroperoxide PO_1 at varied reaction conditions (incl. initial concentration of DHAA): a) Concentration of DHAA, the formed hydroperoxides and the observed reactant recovery in dependence on the superficial residence time b) Dependence of PO_1 formation on provided light intensity c) Effect of varied photosensitizer concentration and gas phase composition at the inlet at constant superficial residence time. Figure is reproduced from [108].

Increasing the light intensity accelerates the reaction without impacting the final yields, Figure 4.3b. This aligns with the proposed reaction network, where the incident photon flux only affects the formation of singlet oxygen. The constant recovery with respect to light intensity suggests that the consecutive rearrangement and degradation of PO1 and POx are not dependent on radiative transfer.

According to the model structure, the reaction rate is expected to increase linearly with the incident photon flux. However, doubling the LED power from $50\,\mathrm{LED}-\%$ to $100\,\mathrm{LED}-\%$ only leads to a 1.5-fold increase in the effective initial rate of PO_1 formation, Figure 4.3b. This means that the proposed linearity is not observed in the experimental data at high irradiation intensities. This effect may be due to oxygen mass transfer, which is too slow to provide oxygen for the fast reactions under strong irradiation.

Figure 4.3c shows that varying the photosensitizer concentration and gas phase composition while keeping the superficial residence time constant only affects the reaction rate, not the total recovery. Increasing the catalyst concentration by 3-fold results in a 2-fold increase in PO1 concentration formed. This is not in complete agreement with the Beer-Lambert law for an optical path length equal to the channel diameter of 0.8 mm: An approximate 3-fold rise in light absorption would cause the same increase in the reaction rate. However, the lower increase observed in the experiments suggests that the light passes through the reactor on a longer path length, resulting in higher absorption and thus lower sensitivity on the catalyst concentration. Decreasing the O_2 content in the gas phase leads to an approximate $20\,\%$ lower yield of PO_1 under otherwise similar reaction conditions. Based on this data, it is unclear whether the significant decrease is due to a lower singlet oxygen quantum yield or slower mass transfer. A quantitative analysis based on a parameterized and validated model of the photooxygenation is required to draw a final conclusion.

4.3.4 Choice of Parameter Subset

The process model developed to describe the photooxygenation behavior contains seven unknown parameters to be identified with experimental data, Equation (4.18). Two of the parameters, the mass transfer coefficient $\widetilde{k_1a}$ and the optical path length l_{opt}, are related to the applied reactor setup. The other five parameters are kinetic rate constants, which are independent of the measurement setup.

Originally, all of the seven model parameters given in Equation (4.18) were supposed to be estimated. However, two issues led to the omission of estimating the singlet oxygen parameters k_{11} and k_{12}. First, it is well known that the mathematical structure of the quantum yield relation, Equation (4.7), impedes the practical identifiability of its parameters; despite the fact that they are both theoretically identifiable [233]. Accordingly, parameter estimation runs showed that

physically reasonable values of the quantum yield of singlet oxygen, i.e., values below 2, could not be retrieved.

To confirm this observation, a global sensitivity analysis of the model parameters on the parameter estimation objective is conducted. The results are shown in Figure 4.4. On the left side, it is clearly visible that the majority of the sensitivities is due to second-order effects, i.e., the parameters show significant interactions – a situation commonly encountered in parameter estimation. At the same time, no higher order effects above two are present as first order and second order indices add up to 1; see the summation bars in Figure 4.4a and compare with Equation (3.59). From the plot on the right side, the corresponding parameter interactions can be extracted. The parameters k_{11} and k_{12} of the quantum yield relation for singlet oxygen have overall the strongest parameter interactions, in particular among themselves, with the optical path length l_{opt}, and the kinetic parameter of the chemical reaction forming the intermediate hydroperoxide PO_1, $\tilde{k}_{PO_1}$. A potential reduction of the interactions by MBDoE did not predict to significantly disentangle the strong connection between the parameters. Thus, it becomes impractical to uniquely determine the involved parameters
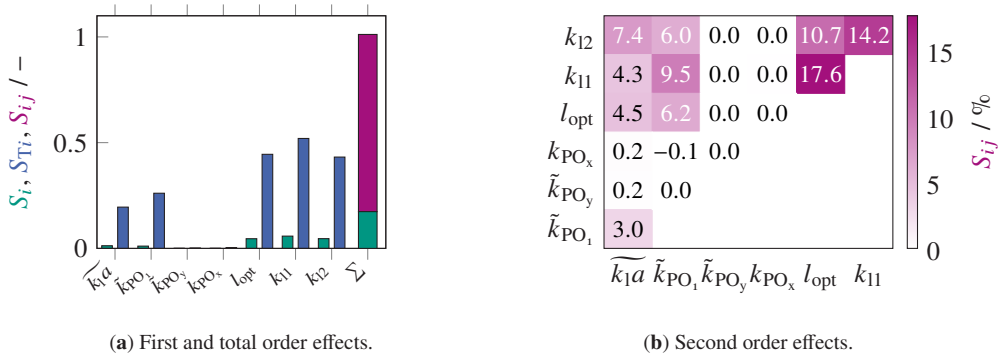

(a) First and total order effects. **(b)** Second order effects.

Figure 4.4: Influence of the primarily considered model parameters to be estimated on the parameter estimation objective, Equation 3.39, by using uniform distributions between -10 and $10\,\%$ of the nominal values. Both graphs reveal identifiability issues due to parameter interactions. The left plot suggests that higher order Sobol' indices do not play a role as first and second order indices add up to 1.

with the measurement information at hand. As discussed before, the quantum yield parameters lack the addressed practical identifiability and lead to estimated parameters that cause quantum yields larger than the maximum physical limit of 2. Consequentially, the unknown quantum yield parameters are set to literature values, taken from [212] for DCA in benzene: $k_{11} = 0.641$ and $k_{12} = 0.0119\,\text{mol/l}$. The fixing of the quantum yield parameters results in an estimation of the other model parameters with satisfying confidence.
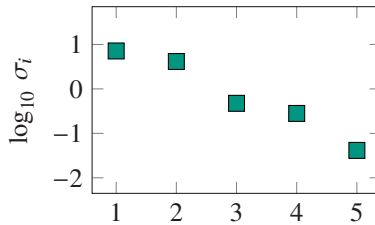
Figure 4.5: Singular value decomposition of the sensitivity matrix is used for parameter identifiability, where singular values close to zero indicate non-identifiability. The typical gap between singular values pointing towards identifiability issues cannot be observed (Section 3.5.1).

4.3.5 Identifiability of the Process Model Parameters

Five parameters to be estimated are left after fixing the kinetic parameters k_{11} and k_{12} in the quantum yield relation: The mass transfer coefficient $\widetilde{k_1 a}$, the three chemical kinetic constants $\tilde{k}_{PO_1}$, $\tilde{k}_{PO_y}$ and k_{PO_x}, and the optical path length l_{opt}. The results from the multistart approach with 60 initial points from a Latin hypercube sampling [234] suggests that the problem has only a single minimum within the investigated parameter space, as all the runs ended having the same objective value. More specifically, the estimated parameters in all runs have the same magnitude, indicating that all parameters are practically identifiable. To confirm this conjecture, inspecting the singular value decomposition of the sensitivity matrix, Section (3.5.1), and afterwards the profile likelihoods of the individual parameters gives insights. The logarithmic plot of the singular values does neither show a clear gap [159], nor is any of the singular values close enough to zero to consider it a zero singular value, Figure 4.5. The profile likelihoods (PLLs) confirm both the structural and the practical identifiability of all estimated model parameters as all PLLs have regular likelihood shapes and cross the 95 % confidence intervals, Figure 4.6. The magnitudes of the estimated parameters can therefore be reliably and physically interpreted, assuming that the model structure simulates the real process.

4.3.6 Assessment of the Estimated Model Parameters

The results of the parameter estimation and of the subsequent quantitative assessment of the derived model parameters and the model-data fit are summarized in Table 4.2. The measurement error variance estimated from regression statistics, Equation (3.40), is $\hat{\sigma}^2 = 2.73 \times 10^{-4} \, \mathrm{mol}^2/\mathrm{l}^2$. Correspondingly, the relative deviation between the predicted and measured concentration of the key intermediate PO_1 is 7.32 %. The good model-data fit is visualized in the parity plots in Figure 4.7 which show a good match between experimental results and simulated data over the whole range of investigated superficial residence times. Exemplarily, the data points appearing in Figures 4.3a are marked in Figures 4.7a, 4.7b and 4.7c accordingly. In contrast to DHAA and

Table 4.2: Goodness of fit and estimated parameter values and spreads, Equation (5.7), for the developed process model, Equations (4.17). The confidence intervals are based on the profile likelihood.

model-data fit

Symbol	unit	value	description
RSS	mol^2/l^2	0.1799	residual sum of squares
$\hat{\sigma}^2$	mol^2/l^2	2.73×10^{-4}	measurement error variance
	%	7.32	averaged relative deviation of PO_1 [†]

estimated parameters

Symbol	unit	value	COD	CI_{95}^-	CI_{95}^+
$\widetilde{k_1 a}$	$\sqrt{1/cm\,min}$	1.094	0.093	1.046	1.148
$\tilde{k}_{PO_1}$	1/mol	7.130	0.173	6.555	7.790
$\tilde{k}_{PO_y}$	1/mol	0.644	0.306	0.550	0.747
k_{PO_x}	1/min	0.0249	0.369	0.0204	0.0296
l_{opt}	cm	0.178	0.107	0.169	0.188

fixed parameters (quantum yield, Equation 4.7)

Symbol	unit	value	reference
k_{l1}	–	0.641	DCA in benzene [212]
k_{l2}	mol/l	0.0119	DCA in benzene [212]
κ	1/(mol cm)	12841.98	Section 4.3.1
C_0	–	1.02	Section 4.3.1

[†]: $\left(\sum_i^{n_{PO_1}} \left| (\tilde{y}_{PO_1,i} - y_{PO_1,i}) \right| / y_{PO_1,i} \right) / n_{PO_1}$

COD: coefficient of dispersion, $COD = (CI_{95}^+ - CI_{95}^-)/\hat{\theta}$, $\hat{\theta}$: estimated value

$CI_{95}^{+/-}$: ±95 % confidence interval

PO$_1$, the key chemical species on the route towards artemisinin, the data of PO$_y$ is less matched because for two reasons. On the one hand, the optimizer tends to favor higher concentrations per definition of the objective function, i.e., the likelihood function. On the other hand, the PO$_y$ concentrations are closer to zero, where the signal-to-noise ratio is increased.

To further assess the quality of the identified model, relative deviations of PO$_1$ over four important process parameters, namely, the initial DHAA concentration, the LED light power, the photosensitizer concentration, and the molar fraction of oxygen, are investigated, Figure 4.8. Each parameter is min-max normalized and for each quarter summary statistics are determined for the relative deviation of PO$_1$, shown as boxes and whiskers in Figure 4.8. A reliable model should show no clear trends in the summary statistics of the PO$_1$ deviation, no matter of the considered location in the design space. Otherwise, observations could point to design space regions, where the model should be used with care or needs improvement. Noticeably, the available experimental data accumulates at the parameters bounds, as specified by the widths of the boxes. Generally speaking, the boxes and whiskers in Figure 4.8 are symmetrical around the zero line with similar box and whiskers heights. Thus, it can be concluded that the existent deviations are mainly caused by measurement noise and errors that inherently occur during the measurement procedure but not by systematic model discrepancy.

Coefficient of dispersions (CODs) and the 95 % confidence intervals (CIs) for the estimated parameters are stated in Table 4.2. It can be noted that the chemical kinetic constants have larger
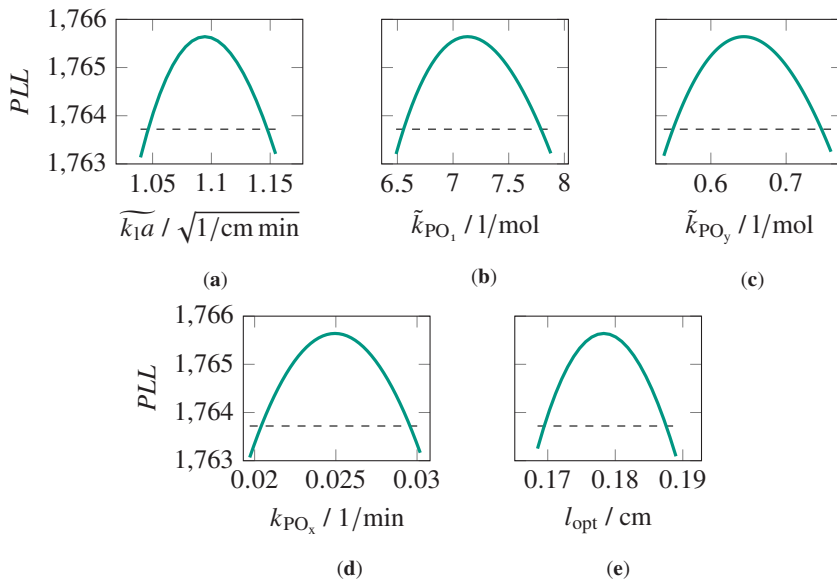

Figure 4.6: Profile likelihoods of estimated model parameters. Dashed lines mark the 95 % confidence intervals. None of the parameters shows parameter identifiability issues.

(**a**) DHAA

(**b**) PO1
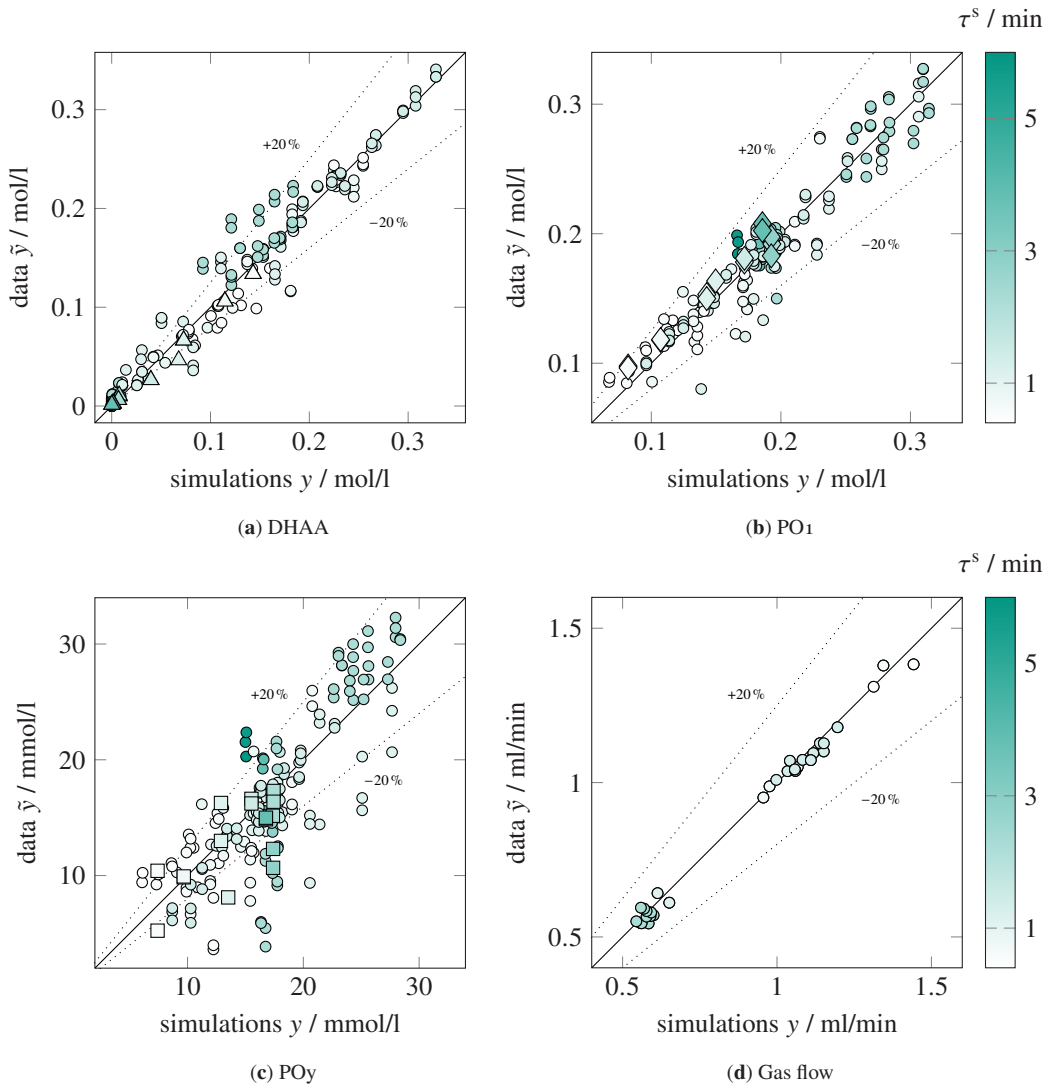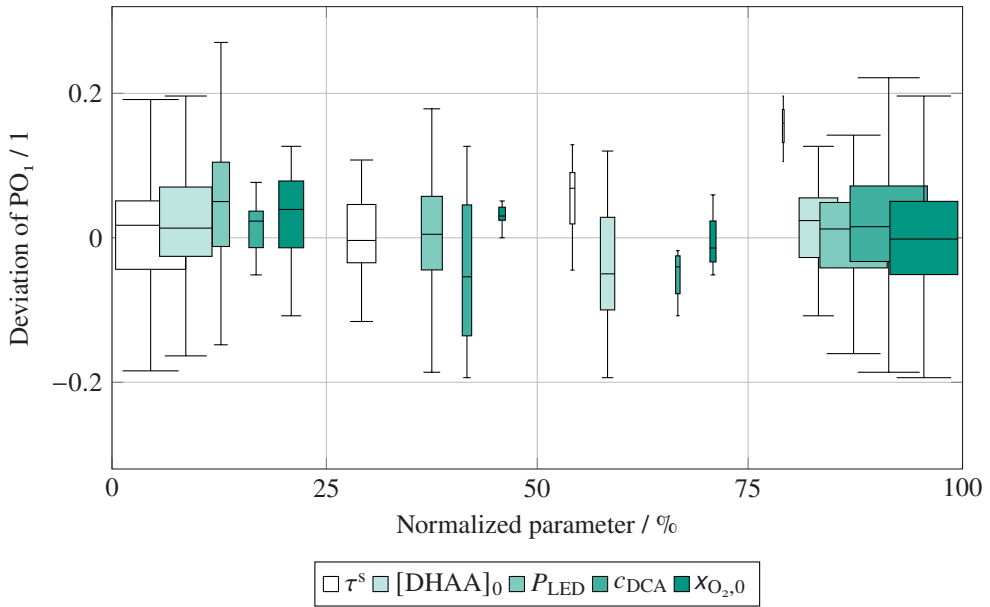
(**c**) POy

(**d**) Gas flow

Figure 4.7: Match of experimental data with simulated results based on the parameterized process model for all quantities measured at the reactor outlet. The grey scale illustrates the superficial residence time in the photoreactor of each data point. Triangle, diamond and square markers represent data from Figure 4.3a. The dashed lines mark 20 % deviations.

Figure 4.8: Relative deviation between experiment and simulation $(\tilde{y} - y)/y$ for PO_1, depicted over the investigated range of process parameter values. The widths of the boxes reflect the number of samples in each of the four sections. (The whiskers are based on 1.5 times the interquartile range. Outliers are not shown.)

Symbol	Unit	Description	Lower bound	Upper bound
τ^s	min	Theoretical residence time	0.439	5.931
$[DHAA]_0$	mol/l	Initial concentration of DHAA	0.231	0.491
P_{LED}	LED$-$%	LED light power	50	100
c_{DCA}	mmol/l	Concentration of photosensitizer DCA	0.117	0.850
$x_{O_2,0}$	mol/mol	Initial molar fraction of oxygen in gas phase	0.41	1.00

CODs and are, loosely spoken, more uncertain in their estimates than the mass transfer coefficient and the optical path length. On the whole, each of the parameters shows an acceptable spread suggesting that their expected values can be reliably used for further model-based investigation.

The rate constants for the formation of the desired hydroperoxide PO_1 and the byproducts were normed, Equation (4.5), to ease the parameter estimation process. Based on the known life time of singlet oxygen in toluene (33.2 µs at $-20\,°C$ [220]) the absolute rate constants of the reactions of DHAA with $^1O_2$ to the hydroperoxides, Equation (4.2), can be obtained:

$$k_{PO_1} = 2.15 \times 10^5 \, l/(mol\,s),$$
$$k_{PO_y} = 0.19 \times 10^5 \, l/(mol\,s).$$

Both values are in the same order of magnitude as rate constants published for other investigated ene-type reactions [102, 136, 235]. The reaction to the desired hydroperoxide is about 10-fold faster than the reaction to the byproducts. This matches with the favored selectivity of PO_1 observed in the photooxygenation experiments.

For Taylor flow fluid dynamics and mass transfer in microchannels, there are various relations for the mass transfer coefficient available that vary substantially among each other [236]. In the study case at hand, initial superficial velocities between $120\,cm/min$ and $350\,cm/min$ appear, resulting in volumetric mass transfer coefficients of approximately $12/min$ to $20/min$. These values lie within the range of $k_l a$ values predicted from correlations available in the literature [236].

Intuitively, the length of the optical path $l_{opt} = 0.178\,cm$ seems to be large at first sight as it is greater than twice the tube diameter of $0.08\,cm$. In a single circular tube geometry with perpendicular irradiation, the optical path length can be assumed to be between channel diameter d as upper boundary and the ratio A/d as lower boundary depending on the collimation of the incident light [237]. Both boundaries, however, are based on the hypothesis that light enters the tubing from one side and is lost after leaving it. In the considered photoreactor instead, two light sources are installed in a closed box of stainless steel, resulting in reflection of the light beam back to the reactor. Furthermore, as the reactor itself is symmetric (compare with Figure 2.3), leaving light beams on one side can re-enter the reactor tubing on the other side. In particular in the tube convolutions around the poles in the reactor box, optical path lengths significantly exceeding twice the tube diameter are very plausible.

Concluding, the model parameters were estimated with both acceptable uncertainty and physically meaningful magnitudes. This is for a considerable part attributed to the model-based design of experiments, that has been applied and is explained in the following Section.

4.3.7 Model-Based Design of Experiments for Improving Parameter Precision

For estimating the model parameters with low uncertainty, i.e., with narrow confidence intervals, a model-based design of experiments is performed in a last step of the iterative strategy for the identification of the process model. In this vein, the precision in the estimated model parameters from previous experiments is intended to be enhanced. The DoE optimization problem, Equation (3.65), with the objective function from Equation (3.64) is stated as:

$$
\begin{aligned}
\max_{\xi_1,\ldots,\xi_{n_{\text{DoE}}}} \quad & \det\left(\boldsymbol{IM}(\boldsymbol{\xi}_1,\ldots,\boldsymbol{\xi}_{n_{\text{DoE}}};\hat{\boldsymbol{\theta}})\right) \\
\text{s.t.} \quad & \text{Eq. (3.5a)} \\
& \text{Eq. (3.5b)} \\
& \boldsymbol{g}_{\text{ineq}}(\boldsymbol{\xi}_i),\ i \in \{1,\ldots,n_{\text{DoE}}\} \\
& \boldsymbol{\xi}_{\min} \le \boldsymbol{\xi}_i \le \boldsymbol{\xi}_{\max},\ i \in \{1,\ldots,n_{\text{DoE}}\}
\end{aligned}
\tag{4.23}
$$

with $\boldsymbol{\xi}_i$ the design variable of the ith experiment. In total for one day of operation, 12 different experiments were planned, that led to the identified process model. Besides bounds for the optimization variables as specified in the last line of Equation (4.23), the experiments were additionally constrained by practical circumstances. During the one day lasting experiment, 4 different oxygen molar fractions could be set. For each fraction, 3 different DCA concentrations were managed. Additional constraints ensured that each of the molar fractions and each of the DCA concentrations fell in distinct ranges, that were equally spaced over the experimental design space. These constraints are considered in the functions $\boldsymbol{g}_{\text{ineq}}$ in Equation (4.23). Hence, together with the liquid volumetric flow, the initial concentration of DHAA, and the LED power, Equation (5.4), there were 15 variables to optimize. For the remaining design variable, the length of the reactor, each of the possible reactor lengths was run in a separate optimization. The following bounds on the design variables were applied:

$$
\begin{pmatrix} 0.2 \\ 0.5 \\ 0.1 \\ 0.4 \\ 10 \end{pmatrix} \le
\begin{pmatrix} \dot{V}_{\text{l}} \ / \ \text{ml/min} \\ c_{\text{DCA}} \ / \ \text{mmol/l} \\ [\text{DHAA}]_0 \ / \ \text{mol/l} \\ x_{\text{O}_2,0} \ / \ - \\ P_{\text{LED}} \ / \ \text{LED}-\% \end{pmatrix} \le
\begin{pmatrix} 0.4 \\ 0.85 \\ 0.5 \\ 0.55 \\ 100 \end{pmatrix}.
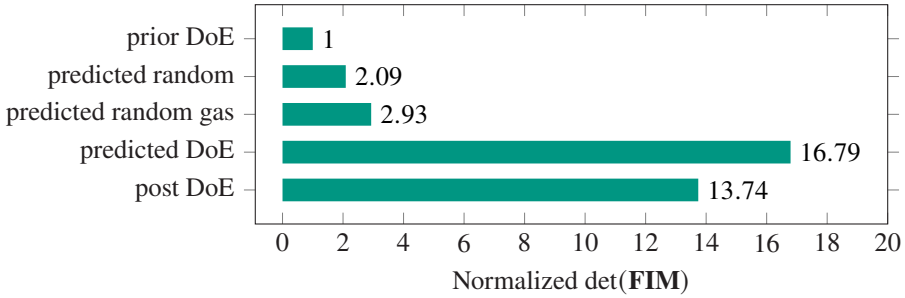\tag{4.24}
$$

Figure 4.9: Comparison of normed parametric uncertainty for non-optimized (random) and optimized (DoE) experiments. The predicted values were calculated by Equation (3.38), the others by Equation (3.37). The non-optimized experiments are randomly drawn from the existent experiments, where the corresponding bars show the mean of 20 repeated random samples. As gas measurements were introduced later during the course of the identification procedure, two mean values are given: The first is based on all existent experiments (predicted random), whereas the second solely takes the existent experiments with gas measurements into consideration (predicted random gas).

The optimized experimental conditions, resulting from solving Equation (4.23), were

$$
\begin{aligned}
L_{\mathrm{r}} &= 400\,\mathrm{cm}, \\
\dot{V}_{\mathrm{l}} &= 0.2\,\mathrm{ml/min}, \\
c_{\mathrm{DCA}} &= \{0.62, 0.73, 0.85\}\,\mathrm{mmol/l}, \\
[\mathrm{DHAA}]_0 &= 0.5\,\mathrm{mol/l}, \\
x_{\mathrm{O_2},0} &= \{0.40, 0.43, 0.45, 0.50\}, \\
P_{\mathrm{LED}} &= 100\,\mathrm{LED-\%}.
\end{aligned}
\tag{4.25}
$$

In Figure 4.9, the DoE design, Equation (4.25), is compared with possible non-optimized designs (random). It shows the normalized determinant of the FIM and indicates a considerable difference between the non-optimized and the DoE scenario, confirming the benefit of MBDoE. After the re-estimation of the model parameters, an almost 14-fold increase in the determinant could be achieved, whereas for an unplanned experiment at most a 3-fold increase would have been possible, Figure 4.9. The reduced parametric uncertainty is mostly owed to the mass transfer coefficient $\widetilde{k_1 a}$, Table 4.3. On the contrary, the uncertainty in the other parameters has not significantly changed. Note that part of the predicted uncertainty reduction, Figure 4.9 predicted DoE versus post DoE, is counteracted by an increase of the measurement variance Σ, Table 4.3, that affects the parameter covariance matrix $\boldsymbol{C}_{\theta}$, Equation (3.34). This fact partly explains why the uncertainties of the parameters $\tilde{k}_{\mathrm{PO_1}}$, $k_{\mathrm{PO_x}}$ and l_{opt} have increased, even though only marginally, if the COD is considered. However, it must be pointed out, that we intentionally have forced the design to lie within gas composition ratios where available experiments had not previously been operated, see the initial molar fraction of oxygen $x_{\mathrm{O_2},0}$ in Equation (5.4). In addition to the newly exploited operational region, the process model could fit the experimental

Table 4.3: Comparison of parameter estimation before and after DoE, including 95 % asymptotic confidence intervals.

model-data fit

		prior DoE		post DoE	
Symbol	unit	value		value	
RSS	mol^2/l^2	0.1195		0.1799	
$\hat{\sigma}^2$	mol^2/l^2	2.14×10^{-4}		2.73×10^{-4}	

estimated parameters

		prior DoE		post DoE	
Symbol	unit	value	COD	value	COD
$\widetilde{k_1 a}$	$\sqrt{1/\text{cm min}}$	1.811 ± 0.171	0.188	1.094 ± 0.0359	0.066
$\tilde{k}_{\text{PO}_1}$	l/mol	6.422 ± 0.193	0.060	7.130 ± 0.252	0.071
$\tilde{k}_{\text{PO}_y}$	l/mol	0.570 ± 0.0648	0.228	0.644 ± 0.0691	0.215
k_{PO_x}	1/min	0.0287 ± 0.00376	0.262	0.0249 ± 0.00350	0.281
l_{opt}	cm	0.171 ± 0.00370	0.043	0.178 ± 0.00457	0.051

COD: coefficient of dispersion, $COD = (CI_{95}^+ - CI_{95}^-)/\hat{\theta}$

$CI_{95}^{+/-}$: $\pm 95\,\%$ confidence interval

data sufficiently well. This supports the chosen first principles approach and the derived model structure, that make the process model to have a good accuracy of the real process behavior not only within the experimentally exploited region, but also beyond. To sum up, the MBDoE approach has performed considerably better than a random design, and significantly decreased the uncertainty in the model parameters, where the major reduction is owed to the effective mass transfer coefficient $\widetilde{k_1 a}$.

4.3.8 Remarks about the Identified Process Model

In conclusion, the model developed to describe the photooxygenation of DHAA provides a good fit with the experimental data. All model parameters are identifiable and their estimates are in plausible ranges. The required simplification on fluid dynamics and photon transfer, namely the application of the two-fluid model and the neglect of absorption rate distribution, offers a good description of the observed process behavior.

Albeit, it must be emphasized that for a reliable utilization and interpretation of the identified process model the following aspects need to be taken into account. Neglecting the distribution of the local volumetric rate of photon absorption is a strong simplification affecting the reaction system on various levels. In particular, a gradient in the absorbed photon flux will cause a non-uniform distribution of the rate of singlet oxygen production within the liquid slug, resulting in a potential diffusion limitation of the overall reaction rate. The absorbed photon flux itself is influenced by the gas holdup and photosensitizer concentration. Both quantities decrease with reaction time due to oxygen consumption and photobleaching and therefore affect the absorbed photon flux. A reliable description of the two-phase flow is essential likewise. A global sensitivity analysis of important model parameters (Section 4.3.10) shows, that the distribution parameter C_0, that links the relative motion of the different phases, Equation (4.13), is highly sensitive. A variation of C_0 in the model induces a considerable change in the simulated PO_1 concentration. Lastly, the identified model and all parameters are only valid for a temperature of $-20\,°C$. Studying the complex influence of temperature on the reaction system including the mass transfer and flow conditions is beyond the scope of this study and a task for future studies.

4.3.9 Exploitation of the Process Model to Analyze Different Operating Regimes

The identified and fully-parameterized model can now be used to understand the process behavior and identify optimal operating windows. In the following, three characteristic operating situations are illustrated that differ in the cause that limits or partially limits the process dynamics: light irradiance, substrate DHAA or mass transfer. The possible fourth operating regime – the kinetically controlled domain without any other limitation – does not occur under the investigated conditions [222].

In Figures 4.10 and 4.11, the dynamic behavior of the system's key quantities, product concentrations, gas flow rate and gas phase composition are drawn over the reactor length. The thin vertical line marks the exit of the photoreactor and thus the end of light irradiance. The discontinuities in the curves at the reactor exit are induced by a temperature jump from reactor to ambient temperature. Experimental data are plotted at the sampling position downstream to the photoreactor exit.

In the first case example, the gas phase consists solely of oxygen, as can be observed in Figure 4.10b. The volumetric gas flow decreases along the reaction line in the photoreactor since oxygen is consumed in the liquid phase due to the chemical reactions and continuously supplied from the gas phase, Figure 4.10. The negative slope of the PO_1 concentration curve after reaching its maximum concentration, Figure 4.10a, is owed to the consecutive loss reactions, Equations (4.1),

(**a**) Reaction species.
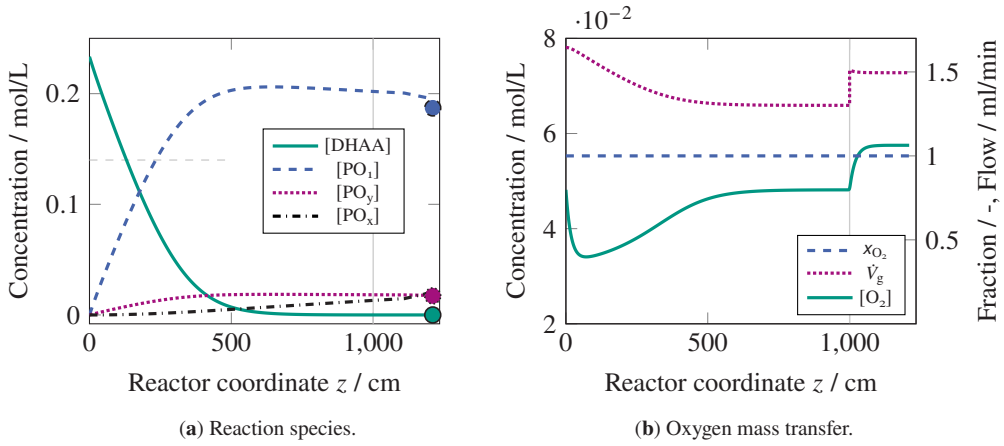

(**b**) Oxygen mass transfer.

Figure 4.10: Propagation of concentrations, oxygen molar fraction and gas flow along the reactor coordinate showing no mass transfer limitations (conditions: $[DHAA]_0 = 0.23\,mol/l$, $[DCA] = 0.85\,mmol/l$, $P_{LED} = 100\,LED-\%$, $x_{O_2,0} = 1$). The thin vertical line marks the reactor outlet. The thin dashed horizontal line in the left graph is the inflection line specifying the transition from the light-limiting to the substrate-limiting regime at a DHAA concentration of $0.14\,mol/l$.

that also continue to go on downstream of the reactor in contrast to the photo-induced reactions. The further discontinuity downstream leading to an even higher negative slope is caused by a slow down of the reaction medium due to a diameter jump of the tubing. Noteworthy is the behavior of the dissolved oxygen in Figure 4.10b. The dissolved oxygen is rapidly consumed at the inlet of the photoreactor as reaction rates are large in the beginning, see Figure 4.10a, but is recovered with decreasing reaction rate values. Obviously, mass transfer does not substantially hinder the process dynamics. In contrast, both the light-limiting and the substrate-limiting regime can be observed in Figure 4.10a. Here, a pseudo-inflection point might be determined that describes the transition between the two regimes that are often observed in photoredox catalysis [222]. At the inflection point, the reaction switches from a pseudo-zero-order reaction with the reaction rate at its maximum to a first-order reaction. Mathematically, the inflection point is defined as the half-maximum kinetic reaction rate. Accordingly, with $\frac{1}{2} \overset{!}{=} (r_{PO_1} + r_{PO_y})/r_{{}^1O_2}$ (Equation (4.4)), the light-limiting regime is controlled by

$$(\tilde{k}_{PO_1} + \tilde{k}_{PO_y})[DHAA] \gg 1 : \quad r_{PO} = \Phi_{{}^1O_2} L_p^a = r_{PO}^{max}, \tag{4.26}$$

and the substrate-limited regime by

$$(\tilde{k}_{PO_1} + \tilde{k}_{PO_y})[DHAA] \ll 1 : \quad r_{PO} = \Phi_{{}^1O_2} L_p^a (\tilde{k}_{PO_1} + \tilde{k}_{PO_y})[DHAA]. \tag{4.27}$$

In this study, the inflection point is therefore at $[DHAA] \approx 0.14\,mol/l$. In the DHAA graph in Figure 4.10a, this inflection point is passed shortly beyond the intersection between the DHAA

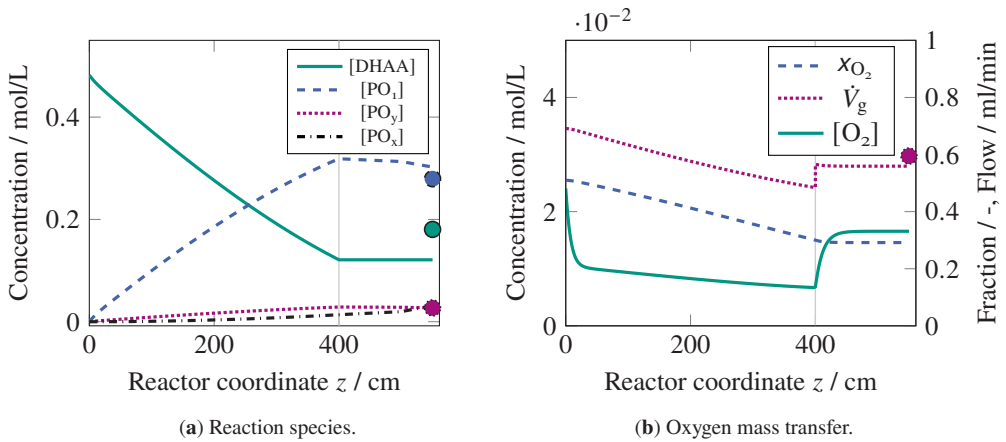(a) Reaction species. (b) Oxygen mass transfer.

Figure 4.11: Propagation of concentrations, oxygen molar fraction and gas flow along the reactor coordinate showing mass transfer limitations (conditions: $[DHAA]_0 = 0.48\,mol/l$, $[DCA] = 0.60\,mmol/l$, $P_{LED} = 100\,LED-\%$, $x_{O_2,0} = 0.51$). The thin vertical line marks the reactor outlet.

and the PO_1 curve, see the dashed horizontal line. To the left of it, it follows zero-order kinetics, and to the right of the inflection point, it approaches first order kinetics.

A complementary process characteristic is shown in Figure 4.11. In this case, the gas phase consists of both oxygen and nitrogen; see the molar concentration of oxygen in Figure 4.11b. From the curve of dissolved oxygen in Figure 4.11b, it readily can be observed that the system quickly runs into mass transfer limitations. The level of dissolved oxygen settles down to an equilibrium stage that continuously decreases as the molar fraction of oxygen in the gas phase drops and therefore correspondingly the solubility limit of oxygen that is determined by Henry's law. Note that the dissolved oxygen does not reach again the initial dissolved oxygen concentration because of the decreased molar fraction of oxygen in the gas phase and the elevated temperature beyond the photoreactor. Along the whole reactor line, the process runs above the inflection point, i.e. above $[DHAA] \approx 0.14\,mol/l$, see Figure 4.11a. This implicates that the DHAA curve in the same Figure follows pseudo-zero-order kinetics. The additional bending of the actual straight line is caused by the low availability of oxygen in the liquid phase that affects the quantum yield of singlet oxygen, Equation (4.7), and reduces the maximum reaction rate, Equation (4.26). Thus, here, the process is partially limited by mass transfer, i.e. the mass transfer rate is approximately equal to the rate of the bulk kinetics, preventing a more efficient conversion of DHAA.

Further insight of the system behavior is inferred with the help of a sensitivity study in the following Section, that reveals important parameters on the performed experiments and key quantities of the process.
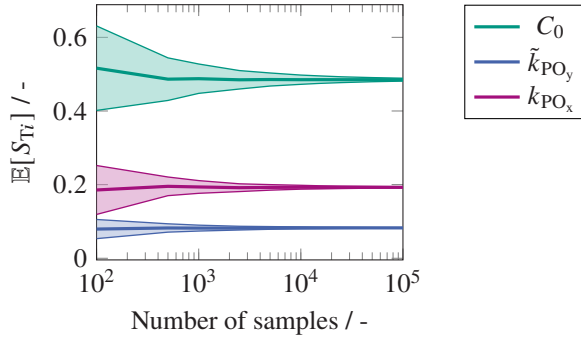
Figure 4.12: Convergence plot to determine the number of samples in the computational runs of the global sensitivity analysis. The 95 % confidence intervals were determined by bootstrapping with 1000 samples [238]. Convergence graphs for the parameters $\widetilde{k_1 a}$, $\tilde{k}_{PO_1}$, and l_{opt} are not shown for better clarity. They exhibit the same qualitative trend as the plotted graphs.

4.3.10 Global Sensitivity Study of the Process Model

Sensitivities of Model Parameters on the Performed Experiments

In the following, the influence of the estimated model parameters on all the conducted experiments is studied by applying a global sensitivity analysis (GSA), Section 3.6.2. The parameter distributions are assumed to be Gaussian, where the mean and the standard deviation are determined by their estimated values from Equation (4.19) and Table 4.2 (units are omitted):

$$
\begin{aligned}
C_0 &\sim \mathcal{N}(1.02, 1.276 \times 10^{-2}), \\
\widetilde{k_1 a} &\sim \mathcal{N}(1.094, 2.60 \times 10^{-2}), \\
\tilde{k}_{PO_1} &\sim \mathcal{N}(7.13, 0.315), \\
\tilde{k}_{PO_y} &\sim \mathcal{N}(0.644, 5.026 \times 10^{-2}), \\
k_{PO_x} &\sim \mathcal{N}(0.0249, 2.347 \times 10^{-3}), \\
l_{opt} &\sim \mathcal{N}(0.178, 4.847 \times 10^{-3}).
\end{aligned}
\tag{4.28}
$$

Prior to the GSA, a convergence study was performed to back the choice of the number of samples drawn from the parameter distributions in Equation (4.28). From the graphs in Figure 4.12 a sample size of 8000 was chosen. The results for first and total order indices on the concentrations of the hydroperoxide PO_1 and the oxygen concentration in the liquid phase $O_{2,l}$ are given in Figure 4.13. In general, all parameters show significant sensitivities, which once more backs the already established fact that the model parameters are identifiable as both hydroperoxide and gas phase measurements have been performed. Remarkably for both concentrations, the distribution factor C_0, that determines the velocity difference of the two phases, has the largest influence – in the case of PO_1 by a considerable margin. This emphasizes the need for a reliable measurement
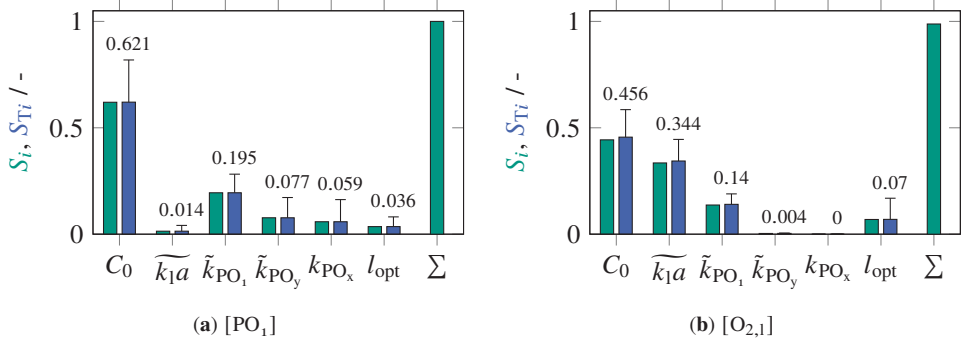
Figure 4.13: Averaged influence of estimated parameters over all performed experiments and the reactor length on a) main hydroperoxide and b) liquid oxygen concentration. Left bars are the first order Sobol' indices, Equation (3.57), and right bars are the total order Sobol' indices, Equation (3.60). The whiskers mark the standard deviation of the total order indices.

method to determine C_0, Section 4.3.1. The kinetic constant related parameters $\tilde{k}_{PO_1}$, $\tilde{k}_{PO_y}$ and k_{PO_x} have a decreasing effect as corresponding products are formed in decreasing magnitude. The zero influence of k_{PO_x} on $O_{2,1}$ is consequential as its concentration is not influenced by the loss reaction. A bit surprising is the low influence of $\widetilde{k_1a}$ on PO_1, in particular in comparison with its influence on $O_{2,1}$. The major reason might be that the conducted experiments do not primarily take place in mass-transfer limited regimes, which is confirmed later in Section 4.3.11 (see also the grey rectangle in Figure 4.19). In general, variations in the indices within different experiments are considerable, which is shown in Figure 4.14. Indeed, sensitivities of the single parameters can exhibit significant varying magnitudes between experiments. Noticeably, the optical path length l_{opt} shows clear sensitivities for the higher indexed experiments only, starting around experiment
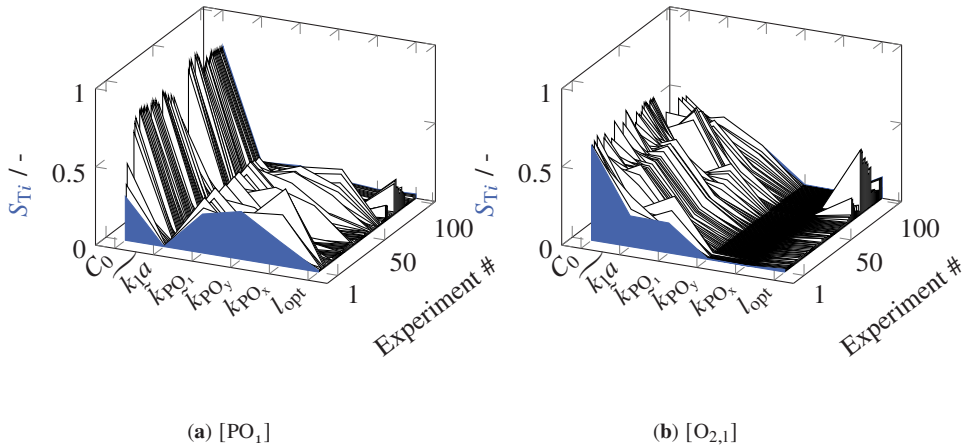

Figure 4.14: Averaged influence of estimated parameters over the reactor length on main hydroperoxide and liquid oxygen concentration for the conducted experiments. The experiments chosen to show characteristic behavior of the process, Figs. 4.10 and 4.11, are the first and last experiment, that are also colored in blue.
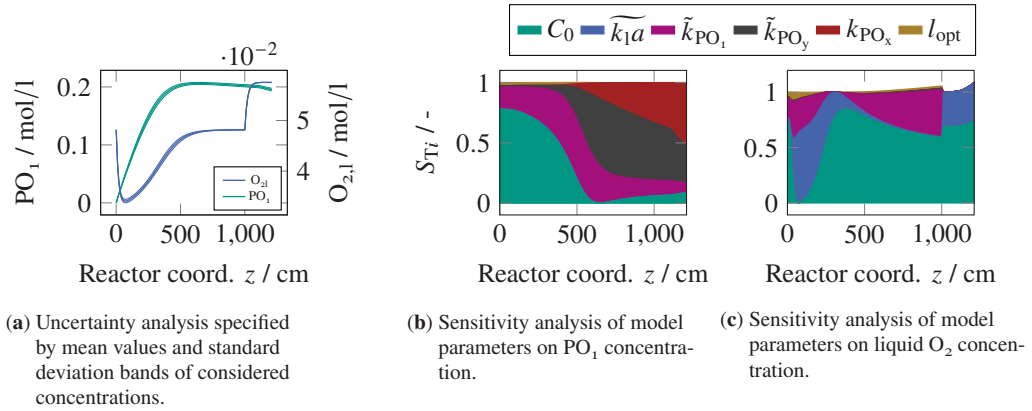
(a) Uncertainty analysis specified by mean values and standard deviation bands of considered concentrations.

(b) Sensitivity analysis of model parameters on PO_1 concentration.

(c) Sensitivity analysis of model parameters on liquid O_2 concentration.

Figure 4.15: Uncertainty and corresponding sensitivity analyses of model parameters along reactor coordinate on important liquid concentrations of the experiment in Fig. 4.10, i.e., without experiencing mass transfer limitations.

number 70 in Figure 4.14b. These experiments have been designed by MBDoEs, see Section 4.3.7 for the finally performed MBDoE. Determining a parameter value for the optical path length without the data collected from the MBDoEs would have been a non-trivial task.

In the following, a closer look at the sensitivities of the two experiments, that have already been considered previously to show characteristic process behavior, Figures 4.10 and 4.11, is taken. In general, it can be noted that the uncertainties of the considered concentrations are fairly low, Figures 4.15a and 4.16a, suggesting that reducing uncertainties in the most important inputs will not have a large absolute effect on the uncertainties of the concentrations – at least not for these two experiments. In Figure 4.15b, it is clearly visible that we are not operating in the mass-transfer limited regime as $\widetilde{k_1 a}$ shows no effect, i.e., the sensitivity effects are solely dependent on the kinetic parameters and C_0, where the sensitivity of C_0 becomes almost zero at around 600 cm when the PO_1 concentration reaches its plateau. For the $O_{2,l}$ concentration, Figure 4.15c, only $\tilde{k}_{PO_1}$ among the kinetic parameters has an influence, but that is also lost downstream of the photo reactor. This is very plausible, because the oxygen concentration has been fully restored to its equilibrium before leaving the photo reactor. Thus observing an effect of the kinetic parameters on the liquid oxygen concentration downstream of the photo reactor is simply not possible. For a determination of the kinetic parameters, it would be more beneficial to measure an extensive quantity, e.g, the gas volumetric flow. Alternatively, the experimental setup could be run in the mass transfer limited regime, as in Figure 4.16. Here, $\tilde{k}_{PO_1}$ shows an influence on the O_2 concentration also beyond the photo reactor for two reasons. First, in contrast to the scenario discussed before, the O_2 concentration is not in equilibrium at the photo reactor exit. Second, even if it was, we would still observe an effect as the gas phase was blended with nitrogen, that causes a drop in the equilibrium concentration because of a reduced oxygen partial pressure according to Henry's law, see Figure 4.16a. The operation in mass transfer-limited regime can be detected

in the sensitivity effects on the PO_1 concentration in Figure 4.16b. Contrarily to Figure 4.15b, $\widetilde{k_1 a}$ very quickly does exhibit an influence on the PO_1 concentration. Additionally, the kinetics cannot unfold their full potential as shown in Figure 4.15b.

Sensitivities of Model Parameters and Initial Concentrations on the Process Behavior

In the following, the GSA is detached from the performed experiments, and instead key process attributes are considered within the presumably valid operational space of the process model. Uncertainties are now not only assigned to the model parameters, Equation 4.28, but also to process parameters. The assigned uncertainties of the model parameters are extended therefore with:

$$
\begin{aligned}
\dot{V}_l &\sim \mathcal{U}(0.1, 0.4), \\
x_{O_2,0} &\sim \mathcal{U}(0, 1), \\
[DCA]_0 &\sim \mathcal{U}(0, 0.85 \times 10^{-3}), \\
[DHAA]_0 &\sim \mathcal{U}(0, 0.5), \\
[P_{LED}] &\sim \mathcal{U}(0, 100).
\end{aligned}
\tag{4.29}
$$

$\mathcal{U}$ is the uniform distribution, where units have been dropped as before. Note that the length of the reactor is fixed to 400 cm. First, the PO_1 and O_2 concentration over the reactor coordinate are considered, before an in-depth investigation of the PO_1 concentration at the photo reactor outlet, that determines the PO_1 yield of the process, is performed. The model parameters, that have been estimated in this Chapter, do not have significant influence on the considered concentrations with

(**a**) Uncertainty analysis specified by mean values and standard deviation bands of considered concentrations.

(**b**) Sensitivity analysis of model parameters on PO_1 concentration.

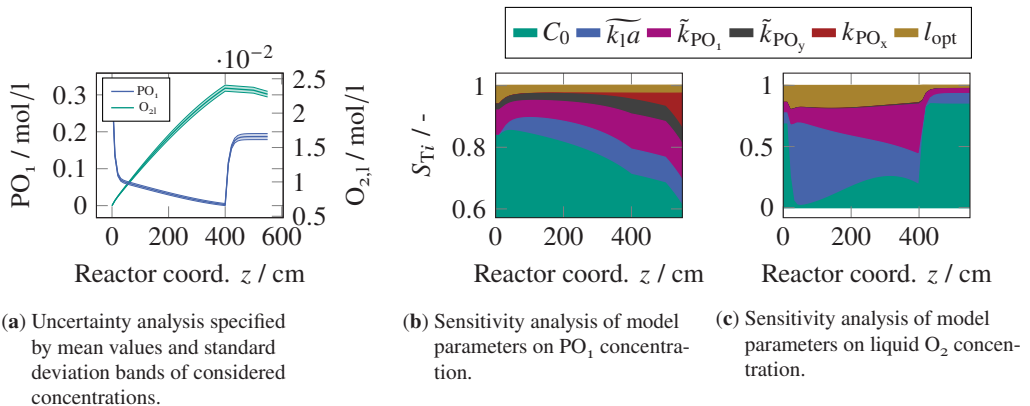(**c**) Sensitivity analysis of model parameters on liquid O_2 concentration.

Figure 4.16: Uncertainty and corresponding sensitivity analyses of model parameters along reactor coordinate on important liquid concentrations of the experiment in Figures 4.11, i.e., with occurring mass transfer limitations.
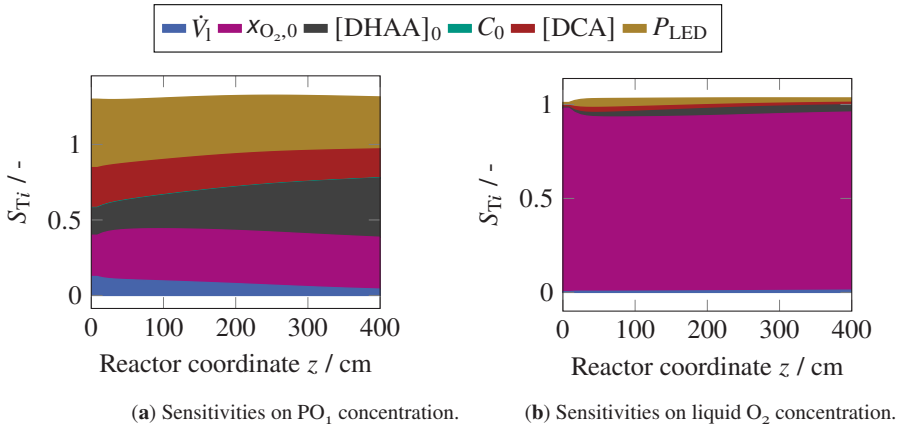
(a) Sensitivities on PO_1 concentration.

(b) Sensitivities on liquid O_2 concentration.

Figure 4.17: Global sensitivity analysis (GSA) of process parameters on selected liquid concentrations along photo reactor coordinate. Please note that, in contrast to the GSAs of the experimental runs, Figures 4.15 and 4.16, we do not consider additional tubing downstream of the photo reactor. Sensitivites below 1×10^{-3} are not shown in the plots, i.e., the sensitivities of parameters $k_1 a$, $\tilde{k}_{PO_1}$, $\tilde{k}_{PO_y}$, k_{PO_x} and l_{opt}.

C_0 having the most, yet still very little effect, Figure 4.17. In contrast, the process parameters in Equation (4.29) accumulate all the effect on the PO_1 and the liquid O_2 concentration. Interestingly, the liquid volumetric flow $\dot{V}_l$, that determines the residence time, has the least influence when compared with the other process parameters. For the PO_1 concentration, all the considered process parameters have a significant effect, Fig. 4.17a. On the contrary for the O_2 concentration, $x_{O_2,0}$ has by far the largest influence. Significant higher order effects can be postulated for the PO_1 concentration. These higher order effects are further analyzed for the PO_1 concentration at the photo reactor outlet, Figure 4.18. One fourth of the variance of the PO_1 concentration at

(a) First and total order effects.

(b) Second order effects.
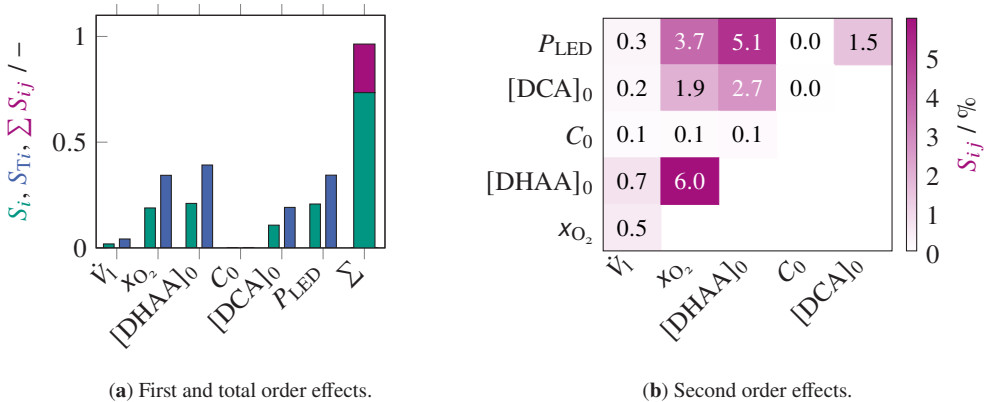
Figure 4.18: Global sensitivity analysis (GSA) of most important process parameters on the PO_1 concentration at the photo reactor outlet. Please note that, in contrast to the GSAs of the experimental runs, Figures 4.15 and 4.16, we do not consider additional tubing downstream of the photo reactor. Sensitivites below 1×10^{-3} are not shown in the plots, i.e., the sensitivities of parameters $k_1 a$, $\tilde{k}_{PO_1}$, $\tilde{k}_{PO_y}$, k_{PO_x} and l_{opt}.

the photo reactor outlet is assigned to second order indices with the rest being first order effects, Figure 4.18a, right ordinate. The largest interactions are found between the initial molar fraction of oxygen, the initial DHAA concentration and the light power, Figure 4.18b. They are followed by the DCA concentration, where $\dot{V}$ is only little coupled to other process parameters, that is of course mainly owed to its low total effect.

4.3.11 Identification of Mass Transfer Limited Regimes for the Photooxygenation of Dihydroartemisinic Acid

The analysis for the process behavior so far was linked to the applied reactor setup. The identified kinetic constants for the photooxygenation can also be used to predict suitable operation regimes for other process settings to prevent that mass transfer of oxygen limits the overall reaction rate. Such a classification can be stated with the Hatta number. Based on the two-film theory, the Hatta number relates the rate of chemical reaction in the liquid phase to the diffusion rate across the phase boundary [239]. The higher the Hatta number, the faster is the reaction in comparison to diffusion, which causes the chemical reaction to take place only at the phase boundary. Critical Hatta values are

$$Ha \geq 3, \qquad \text{strong mass transfer limitation,}$$
$$Ha \leq 0.3, \qquad \text{kinetic regime, no limitation by mass transfer.}$$

In the study case at hand, the Hatta number [100] is defined as (SI of [108])

$$Ha = \frac{1}{k_1} \sqrt{D_{O_2} L_p^a \frac{1}{k_{11}[O_2] + k_{12}} \frac{(\tilde{k}_{PO_1} + \tilde{k}_{PO_y})[DHAA]}{1 + (\tilde{k}_{PO_1} + \tilde{k}_{PO_y})[DHAA]}}. \tag{4.30}$$

The diffusion coefficient of oxygen in toluene may be taken from [240] and has a value of $2.4860 \times 10^{-9}\,\mathrm{m^2/s}$ at $-20\,°C$. The limits of the Hatta regimes are drawn as contours in Figure 4.19.

Generally speaking, with decreasing DHAA concentrations all contour lines move towards the ordinate. The conducted experiments, visualized as the grey rectangle, lie around the lower Hatta limit This matches the observations in the previous Section 4.3.9, where behaviors from dynamics partially limited by mass transfer to dynamics not limited by mass transfer have been investigated.

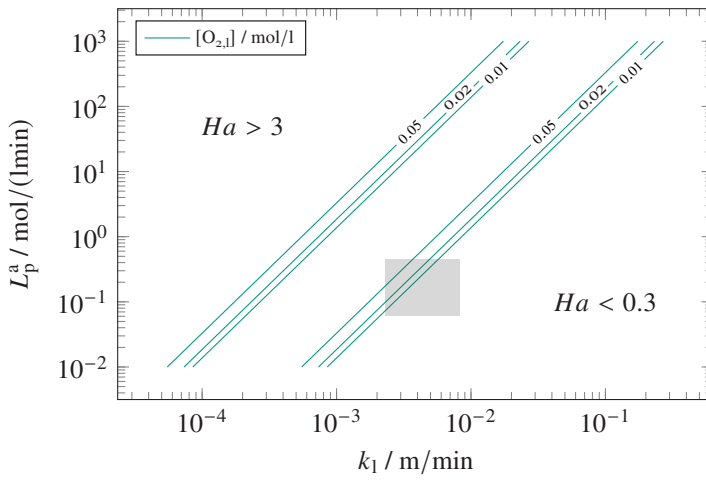**Figure 4.19:** Prediction of mass transfer limited regimes for the photooxygenation of DHAA. The Hatta number is given in dependence on the provided volumetric rate of photon absorption L_p and the mass transfer coefficient for different $O_{2,l}$ concentrations (contour lines, in mol/l) and for DHAA = 0.5 mol/l. The grey rectangle approximately covers the experimental space explored in this thesis.

5 Step 2: Acid-Catalyzed Sequence

In this Chapter, a mathematical model describing the chemical reactions in the acid-catalyzed sequence is identified from a set of different model candidates. To this end, the developed process model from the previous Chapter is utilized for the continuous experimental setup. Supportingly, data from batch experiments in a stirred tank reactor are exploited to decipher the reaction kinetics. Starting with reaction network insights from literature, an exploratory data analysis prepares the building of the reaction network candidates that exhibit different characteristics. Subsequently, the results of the model selection procedure are discussed, including the identifiability of the occurring model parameters. Here, the postulation and evaluation of the different model candidates happened in close collaboration with Susann Triemer [61]. The chosen final model candidate is used to investigate the behavior of the chemical reaction network of the acid-catalyzed sequence. Lastly, the overall identified process model, spanning the photooxygenation and the acid-catalyzed sequence, is applied in a process optimization study targeting the artemisinin yield and space-time yield. The study considers both a nominal setting and a robust one against parametric uncertainties, that are quantified during the model identification procedure.

5.1 Proposed reaction mechanism

In contrast to the photooxygenation step, the acid-catalyzed sequence to form ART from the hydroperoxide PO_1 is substantially more complex and therefore only partially understood so far. Additional complexity is introduced by the different reaction conditions, at which the reaction mechanism has been studied in literature, that might cause different intermediates, products and reaction paths. Susann Triemer has extensively researched the different postulated reaction networks for the acid-catalyzed sequence [61]; and a summary is given in this Section.

Several research groups have investigated the acid-catalyzed sequence reactions, starting with Acton and Roth [83] in 1992. Further insights have been added by Haynes and Vonwiller et al. [241–243], by Brown and Sy et al. [87, 216–218], and by Arman, Varela and Yoshimoto [244, 245]. The here proposed reaction mechanism, that includes the considered main steps and that is used for the model identification of the acid-catalyzed sequence, is shown in Figure 5.1. Along
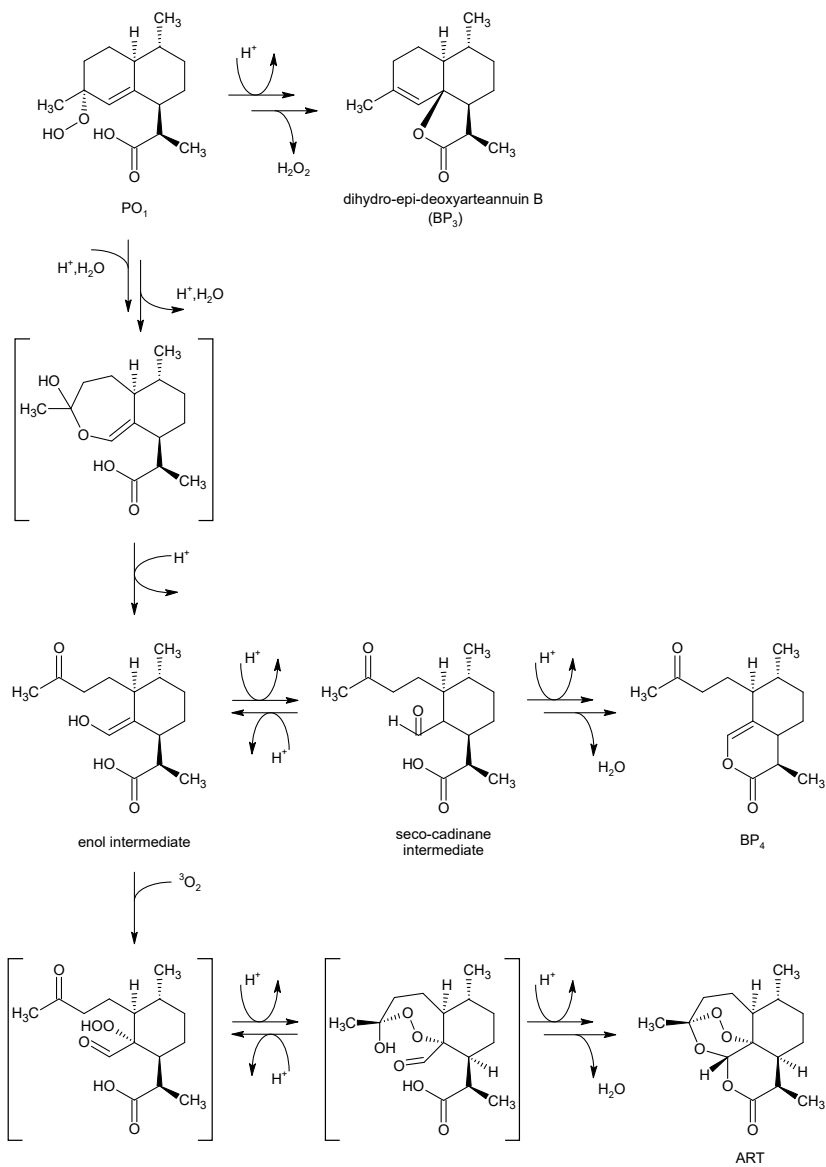
Figure 5.1: Proposed reaction mechanism for the acid-catalyzed sequence forming ART from PO_1 [216].

the reaction path to ART, PO_1 is converted, including a Hock-cleavage, to a seven-membered hemiacetal, that has not been identified in experiments though [216, 242]. Interestingly, Acton and Roth [83] reported that a trace quantity of water is needed to start this reaction. Amara et al. [246] confirmed this observation, where measurements from experiments run in dried tetrahydrofuran did not sense any ART, but solely byproducts. An acid-catalyzed loss reaction of PO_1 forms dihydro-epi-deoxyarteannuin B, which is in the model referred to as BP_3. The hemiacetal is cleaved to an enol with semi-stability, that was managed to be isolated and analyzed at less than $-20\,^\circ$C [216, 242, 243]. Adding triplet oxygen, the enol reacts further to a hydroperoxyl aldehyde, that is rearranged to a peroxy-hemiacetal. Both intermediates have been isolated when a DHAA ester was used as starting material [216, 241, 242]. The main byproduct BP_4, a lactone, is formed from the enol via a seco-cadinane intermediate [216, 242]. The peroxy-hemiacetal converts to ART in a series of irreversible reactions and under the influence of a strong Brønstedt acid [241]. Only in a heavily acidic environment ART degrades over several hours [247]. The proposed reaction mechanism along the hemiacetal and the enol is backed by experiments with labeled compounds [83, 244, 245]. The main products of the semi-synthesis from DHAA to ART are the target ART itself, and the following byproducts: arteannuin H, included in PO_x, see Section 4.1, dihydro-epi-deoxyarteannuin B (BP_3), and the lactone BP_4. Up to 80 % of used DHAA has been recovered in literature [63, 83]. Many other reaction species have been identified or postulated [216], but a complete picture of the whole reaction mechanism is unknown as in all studies (substantial) amounts of converted DHAA have not been uncovered. Considering polar solvents, it can be observed that the reaction to artemisinin is considerably sped up when a Lewis acid is used instead of a Brønstedt acid. Nonpolar solvents as toluene, dichloromethane or hexane, on the other hand, result in better yields in general [63, 246, 248], and despite the complex mechanism high yields up to 71 % for the partial synthesis can be achieved, see Table A.2 in the Appendix. Besides the potential to improve the complex photooxygenation step, the knowledge gaps regarding the reaction mechanism for the acid-catalyzed sequence, involving in particular the role of the solvent, the acidic catalyst, and the participating water make the search for an optimal process and corresponding equipment a major field of research [81, 82].

5.2　Exploratory data analysis

The available experimental data of both the continuous and the batch setup are analyzed in the following to provide assistance for the subsequent model building process. Please note that the continuous data was collected from experiments in the whole reaction line, that includes the photoreactor and the synthesis reactor in series, to form the hydroperoxide PO_1 prior to the acid-catalyzed sequence. To be able to examine the acid-catalyzed sequence in an isolated manner irrespective of this, the photoreactor was set up to reach full DHAA conversion, and the acid

was fed right before the inlet to the synthesis reactor to initiate the acid-catalyzed reactions not upstream to the synthesis reactor.

A scatter matrix including histograms of important quantities is provided in Figures 5.2 and 5.4, that are accompanied by Pearson correlations in Figures 5.3 and 5.5.   The scatter plots in the scatter matrices are numbered in gray inside each plot to guide the following discussion.

Next to the supply or non-supply of oxygen, major differences between the two data sets are the amount of dosed TFA, that is one magnitude greater for the continuous data, and the residence time. The latter is considerably larger for the batch data, i.e., up to 150 min compared to a theoretical residence time of up to roughly 16 min in the continuous case, see the first columns in Figures 5.2 and 5.4. The shown data in the scatter plots are colored according to the TFA concentration; see the bottom rows of the same Figures.

First, the continuous data visualized in Figures 5.2 and 5.3 is analyzed. As seen in the second column in Figure 5.2, high DHAA conversions of larger than 94 % are indeed achieved for all the continuous experiments. ART yields reach 54 % and 47 % within 16 min theoretical residence time for 0.125 M and 0.25 M TFA, respectively, see plot 16. Interestingly, in experiments where TFA was added before entering the photo reactor (data not shown here), the maximum ART yield is 20 % higher, i.e., 66 %, with a theoretical residence time of 22 min and 0.125 M TFA [61]. The significant difference in ART yields emphasizes the formation of potentially unknown byproducts before the acid is added. Recoveries in plot 2, on the other hand, only reach around 60 % for situations where ART has clearly reached a steady state, that is, the experiments with higher TFA concentrations, plot 16. Consequently, more than 40 % of the introduced DHAA are not identified during the applied measurement procedure, and are therefore not known. This suggests the existence of not only non-quantified byproducts, but also of at least one non-detected intermediate between the reaction path from PO_1 to ART, as the recovery significantly drops below 40 % for low residence times, plot 2 and compare with Figure 5.1. From the ^{1}H-NMR and FT-IR measurement spectra, none of the other previously reported species could be inferred, that is mainly owed to the fact that the detection of many structurally different species is limited with the used technologies [61]. Please note that the formation of the measured arteannuin H, one of the major byproducts in the semi-synthesis [61], is not considered in detail, as it is a loss product of a hydroperoxide during the photooxygenation, Chapter 4, and therefore not relevant to the conversion of PO_1 to ART. Generally speaking, BP_3 is formed in one magnitude greater than BP_4 in the continuous experiments, plots 7 and 11, respectively. More specifically, BP_4 only appears in trace quantities, causing the BP_4 data to suffer from a high signal-to-noise ratio. Patterns including BP_4 are therefore difficult to detect, with the exception of the series performed with the lowest TFA concentration, that suggests a linear correlation between the BP_4 and the ART yield, plot 21. Contrarily in the case of BP_3, a clear linear dependence on the TFA concentration is observed, plot 26. This observation is confirmed by a high Person correlation of

Figure 5.2: Scatter matrix and histograms of the available data for the acid-catalyzed sequence obtained with the continuous setup. Please note that the photoreactor was connected upstream of the synthesis reactor to form the hydroperoxide PO_1. The data points are colored according to their acid concentration, see bottom row. The conversion X is the conversion of DHAA and yields Y are based on the converted DHAA concentration. The recovery considers all recovered species. Note the following differences in this Figure and in Figure 5.4: (i) the units in the initial TFA concentration, i.e., mol/l versus mmol/l; and (ii) the time variables, i.e., the superficial residence time τ^s of the synthesis reactor versus the actual sample time t.
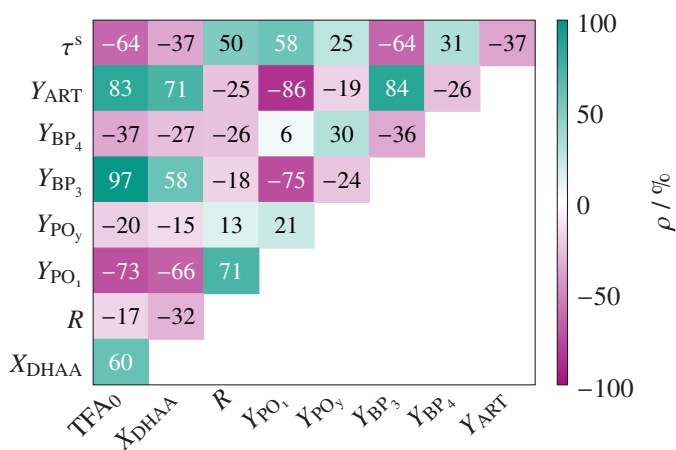
Figure 5.3: Pearson correlations [249] for continuous experimental data in Figure 5.2.

97 %, Figure 5.3. The same dependence, although not necessarily linear, can be seen for ART, plot 28. The corresponding Pearson correlation is 83 %, Figure 5.3. Remarkably, BP_3 and ART seem to be correlated likewise, plot 20, with a Pearson correlation of 84 %. From plot 7 it might be concluded that the formation of BP_3 happens very fast, as the BP_3 yields lie around a horizontal line for higher TFA concentrations after a very sharp rise at low residence times. This indicates an instantaneous appearance of BP_3, i.e., the reaction path towards BP_3 must exhibit very fast kinetics.

The complementary batch results were run six times at four different TFA concentrations, see bottom row in Figure 5.4. Please note that the reactor was flooded with nitrogen hindering the buildup of ART, that only forms in the presence of oxygen, Figure 5.1. A comparison of the batch with the continuous results yields similar concentrations for PO_1 and BP_3 at similar acid concentrations and initial conditions suggesting that results from the two setups are comparable [61]. At the same time, measurement results of the batch experiments obtained at equal TFA amounts do show discrepancies, that make drawing conclusions more difficult, see for example the BP_3 yield in plot 4 for the two similar TFA concentrations around 25 mmol/l in plot 11. The measurement uncertainties might be attributed to deviations in the addition of the acid and an initial temperature rise due to the exothermic nature of the reaction [61]. The complete decay of PO_1 takes more than 90 min at the considered TFA concentrations, plot 2. Similar to the continuous data, recoveries can significantly drop with the decay of PO_1, plot 3, below 60 %, plot 1, and start rising again as BP_4 is increasingly formed when time advances, plot 7. This again suggests that non-identified intermediates during the route towards ART appear. Contrary to the continuous case, the main byproduct is BP_4, whose concentrations are one magnitude larger than those of BP_3. Additionally, the buildup of BP_4 is delayed and not finished within the considered
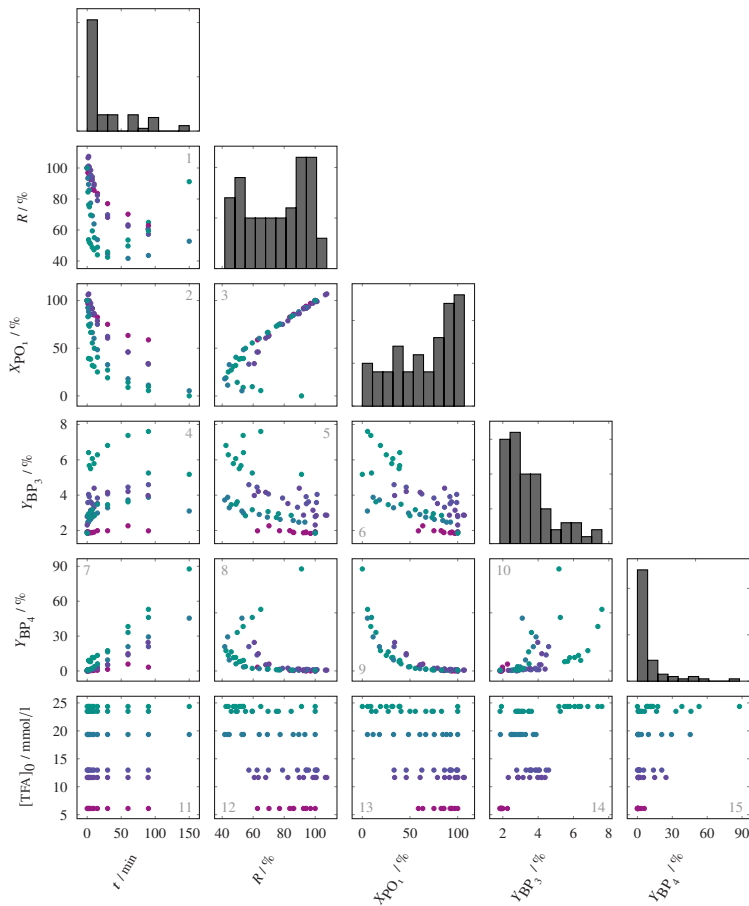
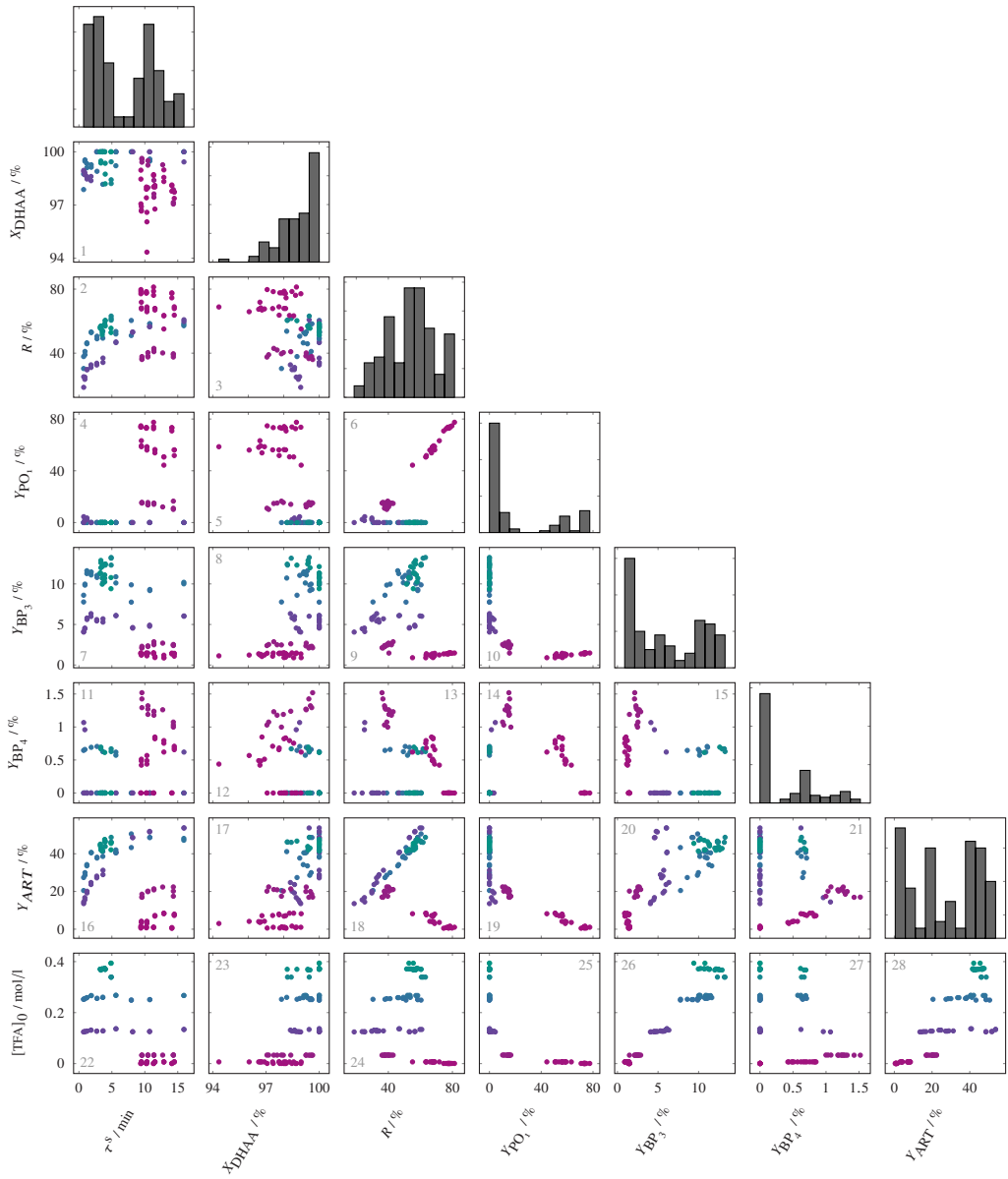**Figure 5.4:** Scatter matrix and histograms of the available data for the acid-catalyzed sequence obtained with the batch setup. The data points are colored according to their acid concentration, see bottom row. Note the following differences in this Figure and in Figure 5.2: (i) the units in the initial TFA concentration, i.e., mmol/l versus mol/l; and (ii) the time variables, i.e., the actual sample time t versus the superficial residence time τ^s.
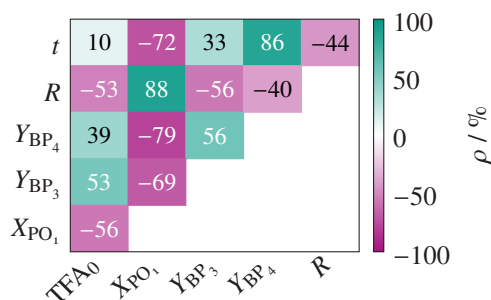
Figure 5.5: Pearson correlations [249] for batch experimental data in Figure 5.4.

reaction times, plot 7. Additionally, a strong linear dependence of BP_4 on the residence time is observed, plot 7, with a Pearson correlation of 86 %, Figure 5.5. A dependence of PO_1 and BP_4 on TFA can be observed as well, plot 13 and 15, respectively. On the other hand and in contrast to the continuous data, a dependence of BP_3 on the acid concentration cannot be concluded with certainty, plot 14. Interestingly, a distinct non-linear dependence between PO_1 and BP_4 yields can be observed, plot 9 with a Pearson correlation of -79 %, that might be even independent on the acid concentration.

Summing up, the key findings of the exploratory data analysis are:

- The batch and the continuous experiments yield similar results at similar TFA concentration and similar initial conditions.

- Residence times for the batch data are in the range of hours, and for the continuous data in the range of minutes, mainly caused by a difference of one magnitude in the TFA concentration.

- For continuous experiments reaching a steady state, around 40 % of the added DHAA cannot be recovered. This is attributed to non-identified byproducts and also at least one non-identified intermediate on the reaction path from PO_1 to ART.

- The main byproduct is BP_3 and BP_4 in the continuous and in the batch data, respectively. In both cases, the more abundant species concentration is one magnitude larger than the concentration of the other byproduct.

- TFA shows a great influence on the PO_1, BP_3 and ART concentrations in the continuous data, and on the PO_1 and BP_4 concentrations in the batch data, although less pronounced.

5.3 Building of Model Candidates

Challenges associated with the development of a complete first principles model for the acid-catalyzed sequence are multi-dimensional. One, the reaction network is of complex nature, having unknown intermediates and byproducts that take part in the process. Two, a thorough search of relevant literature yielded no established simulation model. And three, measurement information is limited, i.e., there is a relatively low number of measured species, and at the same time the measurements of the continuous setup are of steady state type with samples drawn at the very end of the reaction line only. Thus, the building of different model candidates is for the most part based on the available information about the mechanisms in literature, expert knowledge from within and outside of the participating research groups, experiences gained from the conducted experiments, and an iterative and systematic procedure for model identification
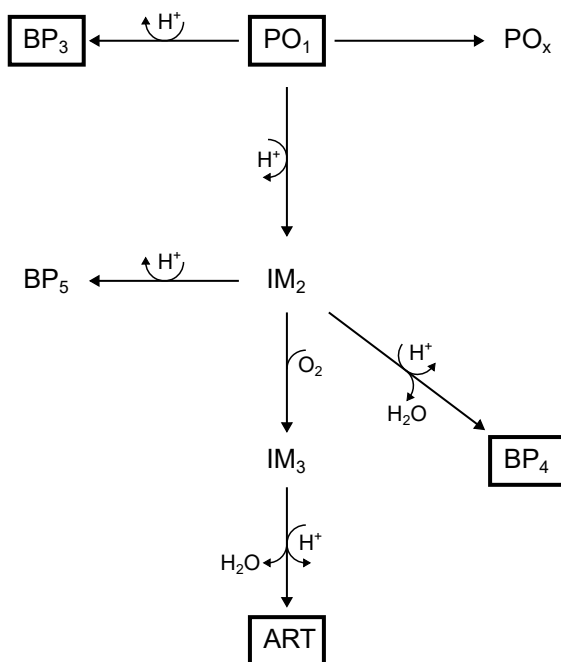
Figure 5.6: Scheme of base model candidate, i.e., model candidate 1, for the reaction network of the acid-catalyzed sequence.

according to Figure 3.3. Hence, starting from a base reaction network, several amendments and variants have been added and investigated along the course of identifying a kinetic description of the reaction network in the acid-catalyzed sequence. In the following, selected kinetic model candidates with distinct characteristics will be discussed. All tested networks are based on the following assumptions:

- The formation of ART, BP_3, BP_4 and BP_5 is irreversible. They are chemically stable under the conditions applied and do not compose.

- During the reaction to BP_3, hydrogen peroxide is formed, that does not influence the reaction kinetics and is therefore not considered.

- Each species is protonated only once. If not specified otherwise, the acid catalyst reaction order is unity, that is the rate of reaction r is proportional to the proton concentration.

- Only TFA contributes to the acidity of the reaction solution, i.e., the carboxyl group of PO_1 does not interfere.

The base model candidate is shown in Figure 5.6, and solely involves irreversible steps. PO_1 conversion has two competing paths: It either reacts to the byproduct BP_3 or to the intermediate

IM_2, with both reactions being acid-catalyzed. The series of formed species is summarized in the lumped species IM_2, that represents the central enol intermediate; compare with Figure 5.1. IM_2 is the starting point for the reactions towards both ART, BP_4, and BP_5, where the latter species is introduced to compensate the low recoveries. BP_4 is formed in an acid-catalyzed reaction step with the ejection of a water molecule. The ART formation is mapped in two steps. First, IM_2 reacts with oxygen to the intermediate IM_3, that physically represents an intermediate after the oxidation, Figure 5.1. IM_3 is then further converted to ART in an acid-catalyzed reaction under the ejection of a water molecule. In the base network, the formed water does not affect the reaction kinetics, and the proton concentration, that is set to the initial TFA concentration, stays constant over the course of the reaction.

The first variants target the dissociation equilibrium of TFA in toluene. Despite being a very strong acid in water, dissociation of TFA in the nonpolar toluene is hampered. Additionally, protonated species such as PO_1 might interfere with the dissociation equilibrium. To account for the reduced dissociation, three different options, with the equations listed in Table 5.1, are proposed. All of them hypothesize that the dissociation equilibrates significantly faster than the reactions with PO_1. Variant A assumes complete dissociation, variant B considers a dissociation equilibrium introducing the dissociation constant K, and variant C assumes that all species evolving from and including DHAA intervene in the dissociation equilibrium. The adjustment of the dissociation

Table 5.1: Different calculation methods for the dissociation equilibrium of trifluoroacetic acid (TFA) on mass action law basis. Model A assumes full dissociation. Models B and C account for an incomplete dissociation due to the nonpolarity of the solvent toluene and protonable species, introducing a dissociation constant K. The main assumption is that the dissociation equilibrates fast compared with the decay of PO_1, i.e., the equilibrium is in place before the actual reactions occur. Model B considers a simple equilibrium, where in model C it is assumed that all species evolving from and including DHAA, summarized in species S, intervene with the equilibration.

Diss.	Calculation of H^+
A	$HTFA \longrightarrow TFA^- + H^+$
	$[H^+] = [TFA]_0$
B	$HTFA \longleftrightarrow TFA^- + H^+$
	$[H^+] = -\frac{K}{2} + \sqrt{\frac{K^2}{4} + K[TFA]_0}$
C	$HTFA + S \longleftrightarrow TFA^- + SH^+$
	$[S] = [DHAA]_0, [SH^+] = [H^+]$
	$[H^+] = -\frac{K[DHAA]_0}{2} + \sqrt{\frac{K^2[DHAA]_0^2}{4} + K[TFA]_0[DHAA]_0}$

equilibrium is a consequence of the importance of a precise description of the acid-catalyzed

conversion of PO_1 to yield accurate predictions for the products ART in the continuous and BP_4 in the batch experiments. To account for this importance, the reaction orders regarding proton concentration from PO_1 to IM_2 and from PO_1 to BP_3 are added to the set of model parameters considered during parameter estimation. Thus, the rate of reactions, Equation (3.7), from the reaction scheme in Figure 5.6 are expressed as:

$$
\begin{aligned}
r_{PO_1 \cdot IM_2} &= k_{PO_1 \cdot IM_2}[H^+]^{m_{IM_2}}[PO_1] \\
r_{PO_1 \cdot BP_3} &= k_{PO_1 \cdot BP_3}[H^+]^{m_{BP_3}}[PO_1] \\
r_{PO_1 \cdot PO_x} &= k_{PO_1 \cdot PO_x}[PO_1] \\
r_{IM_2 \cdot IM_3} &= k_{IM_2 \cdot IM_3}[IM_2][O_{2,l}] \\
r_{IM_2 \cdot BP_4} &= k_{IM_2 \cdot BP_4}[H^+][IM_2] \\
r_{IM_2 \cdot BP_5} &= k_{IM_2 \cdot BP_5}[H^+][IM_2] \\
r_{IM_3 \cdot ART} &= k_{IM_3 \cdot ART}[H^+][IM_3]
\end{aligned}
\tag{5.1}
$$

with reaction orders m_{BP_3} and m_{IM_2}, and $[H^+]$ is given by the equations in Table 5.1. In certain model candidates, the reaction orders are assumed to differ by unity, i.e., $m_{BP_3} = m_{IM_2} + 1$.

Apart from a modified dissociation mechanism and variable reaction orders, the base network was extended and altered to yield different model candidates, that comprehend reasonable reaction networks, with the goal of improving the model data fit. A super structure of the developed model candidates is shown in Figure 5.7, and a corresponding table containing a first set of different model candidates in Table 5.2. In the base network, the initial protonation is considered to be rate-determining for the decay of PO_1. Alternatively, the rearrangement following the protonation might be rate-determining [250]. Here, the educt is first reversibly protonated, and following further converted to the product in a non-reversible acid-catalyzed step; see for example the path from PO_1 to IM_2 passing PO_1H^+ in Figure 5.7. The role of water, that can influence the acidity of the solution or change the reactivity of involved species by hydration, is taken into account in the species IM−hyd. Here, free water is trapped, where the equilibrium between IM_2 or IM_3 and IM−hyd shifts towards IM−hyd with increasing reaction progress, since more water becomes available. The equilibrium shifts cause the slow down of both the BP_4 and the ART formation. In a further variant, the IM_3 species may not be present, that is, ART is directly formed from IM_2. The byproduct BP_5 can be derived either from IM_2 or from IM_3. Moreover, two byproducts, BP_5 and BP_6, can be formed from the two intermediates.

Table 5.2: Core set of proposed model candidates for the acid-catalyzed reaction network, corresponding to the super structure in Figure 5.7. The font colors of the table headers match the colors of the network characteristics in the super structure Figure. The dissociation types, column 'Diss.', are given in Table 5.1. '#x' is the number of species (states) and '#θ' is the number of model parameter to be estimated, i.e., the sum of kinetic constants and variable reaction orders. The column 'Reaction orders' refers to the reaction orders regarding TFA from PO_1 to IM_2 and BP_3, respectively. All other reaction orders are unity. A check in the column 'IM_3' implies that IM_2 is participating and the orange direct route in Figure 5.7 is inactive. If there is a check in any of the columns 'IM_2 prot.', 'BP_3 prot.' or 'BP_4 eq.', the corresponding colored route in Figure 5.7 replaces the black route. In the columns 'Hydrat. position' and '$BP_{5/6}$' the starting point for the corresponding reaction is given.

| Model	#x	#θ	Diss.	Reaction orders	IM_2 prot.	BP_3 prot.	BP_4 eq.	Hydrat. position	$BP_{5/6}$ position	IM_3
1	9	7	A	1, 1	-	-	-	-	IM_2	✓
2	9	8	B	1, 1	-	-	-	-	IM_2	✓
3	9	8	C	1, 1	-	-	-	-	IM_2	✓
4	10	8	A	1, 1	✓	-	-	-	IM_2	-
5	11	9	A	1, 1	✓	-	-	-	IM_2	✓
6	10	9	A	1, 1	-	-	✓	-	IM_2	✓
7	12	11	A	1, 1	✓	✓	-	-	IM_2	✓
8	10	9	A	1, 1	-	-	-	IM_2	IM_2	✓
9		11	A	1, 1	-	-	✓	IM_2	IM_2	✓
10	13	13	A	1, 1	✓	✓	-	IM_2	IM_2	✓
11	13	13	A	1, 1	✓	✓	✓	-	IM_2	✓
12	13	15	A	1, 1	✓	✓	✓	IM_2	IM_2	✓
13	9	7	A	1, 2	-	-	-	-	IM_2	✓
14	9	8	A	$m_{IM_2}, 1$	-	-	-	-	IM_2	✓
15	9	8	A	$m_{IM_2}, m_{IM_2}+1$	-	-	-	-	IM_2	✓
16	9	8	A	$m_{IM_2}, m_{IM_2}+1$	-	-	-	-	IM_3	✓
17	9	9	B	$m_{IM_2}, m_{IM_2}+1$	-	-	-	-	IM_3	✓
18	9	9	C	$m_{IM_2}, m_{IM_2}+1$	-	-	-	-	IM_3	✓
19	11	10	A	$m_{IM_2}, m_{IM_2}+1$	✓	-	-	-	IM_2	✓
20	10	10	A	$m_{IM_2}, m_{IM_2}+1$	-	-	✓	-	IM_2	✓
21	10	10	A	$m_{IM_2}, m_{IM_2}+1$	-	-	-	IM_2	IM_2	✓
22	10	10	A	$m_{IM_2}, m_{IM_2}+1$	-	-	-	IM_3	IM_2	✓
23	10	10	A	$m_{IM_2}, m_{IM_2}+1$	-	-	-	IM_3	IM_3	✓
24	10	9	A	$m_{IM_2}, m_{IM_2}+1$	-	-	-	-	$IM_{2/3}$	✓
25	9	9	A	m_{IM_2}, m_{BP_3}	-	-	-	-	IM_2	✓
26	9	9	A	m_{IM_2}, m_{BP_3}	-	-	-	-	IM_3	✓
27	10	11	A	m_{IM_2}, m_{BP_3}	-	-	-	IM_2	IM_2	✓
28	10	11	A	m_{IM_2}, m_{BP_3}	-	-	✓	-	IM_2	✓
29	11	13	A	m_{IM_2}, m_{BP_3}	-	-	✓	IM_2	IM_2	✓
30	11	13	A	m_{IM_2}, m_{BP_3}	-	-	✓	IM_2	IM_3	✓
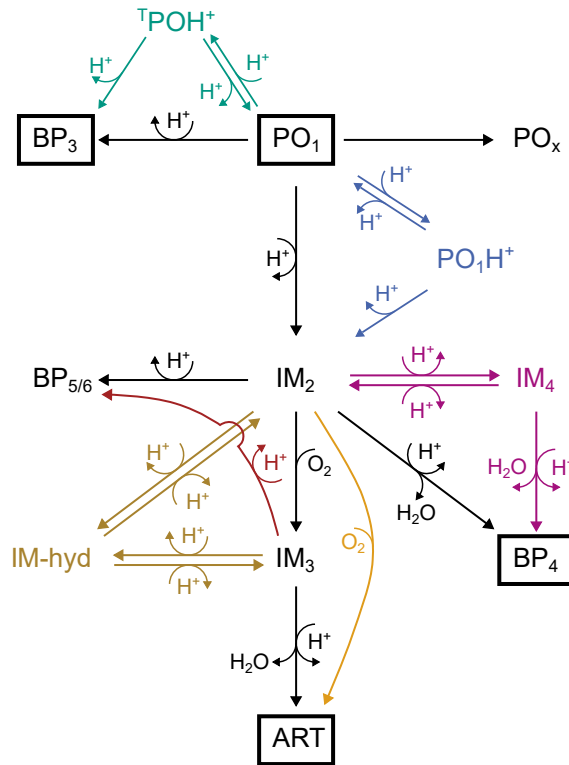
Figure 5.7: Simplified super structure for the acid-catalyzed sequence producing artemisinin from the hydroperoxide PO_1. The base network, i.e., model candidate 1, Figure 5.6, is drawn in black. Alternative routes are colored.

5.4 Methodological Procedures

5.4.1 Parameter Estimation

The continuous and batch data are both utilized during parameter estimation. As PO_1 is first converted from DHAA in the photo reactor, the ordinary least squares (OLS) approach is extended to simultaneously estimate next to the model parameters the PO_1 initial conditions of the batch experiments, referred to as extended ordinary least squares (eOLS). Furthermore, the BP_3 initial conditions are included in the eOLS method since trace quantities of BP_3 can be observed in the collected data. Thus, starting from the OLS objective function in Equation (3.39), the eOLS objective function becomes:

$$\mathcal{J}_{\text{eOLS}}(\boldsymbol{\theta}) = \sum_{j=1}^{n_y(t_k)} \sum_{k=1}^{n_t} \left(\tilde{y}_j(t_k) - y_j(t_k, \boldsymbol{\theta}) \right)^2 + \sum_{j \in \{PO_1, BP_3\}} \left(\tilde{x}_j(t=0) - x_j(t=0) \right)^2. \tag{5.2}$$

In general, the estimations were run in parallel from 25 to 60 initial starting points that were selected using Latin hypercube sampling. Typical parameter ranges during optimization had lower bounds at zero and upper bounds at 10 for the effective mass transfer coefficient $\widetilde{k_1 a}_{\mathrm{syn}}$, 5 for the kinetic constant $k_{\mathrm{PO_x}}$ of the hydroperoxide loss reactions, and 5000 for the other kinetic constants. The reaction orders were typically constrained between 0.1 and 5.0.

5.4.2 Process Optimization

Two key performance indicators of a drug production are the yield, and the space-time yield. Ideally during manufacturing, both yields are as high as possible. To obtain such optimal operating conditions, mathematical optimization can be used. Analogous to the design of experiments problem for model selection, Section 3.7, a nominal and a robust objective function are formulated, that are transformed into an optimization problem, Equation (3.65). The objective function for the robust version, that uses the same penalization scheme as in the model selection setting in Equation (3.62), is

$$\mathcal{J}_{\mathrm{rSTY}} = \lambda \mathbb{E}[STY_{\mathrm{ART}}(\boldsymbol{\xi})] + (1 - \lambda)\mathbb{V}[STY_{\mathrm{ART}}(\boldsymbol{\xi})], \tag{5.3}$$

with $\boldsymbol{\xi}$ the design vector, that holds a different number of elements according to the scenario applied. Different scenarios are considered to see the impact of reactor design and special dosing on the optimal reactor. The first scenario considers fixed lengths of the reaction line that is made up of a photooxygenation and a synthesis section, with $l_{\mathrm{photo}} = 400\,\mathrm{cm}$ and $l_{\mathrm{syn}} = 620\,\mathrm{cm}$, the most common reactor lengths used in the continuous experiments. The second scenario considers the lengths of both sections as additional design variables. In a third scenario, TFA can be fed at the photo reactor inlet, instead of dosed into the flow at the inlet of the synthesis reactor. Please bear in mind for the third scenario, that the kinetic parameters of the synthesis reactions are estimated at a $40\,^{\circ}\mathrm{C}$ difference from the photo reactor temperature. The design vector consists

then of the following quantities and corresponding design space boundaries, where the maxima cover the design space of the performed experiments:

$$
\begin{pmatrix} 0.0 \\ 0.0 \\ 0.0 \\ 0.0 \\ 0.0 \\ 0.0 \\ 0.0 \\ 0.0 \end{pmatrix} \leq \begin{pmatrix} \dot{V}_\mathrm{l} \ / \ \mathrm{ml/min} \\ c_\mathrm{DCA} \ / \ \mathrm{mmol/l} \\ [\mathrm{DHAA}]_0 \ / \ \mathrm{mol/l} \\ x_{\mathrm{O}_2,0} \ / \ 1 \\ P_\mathrm{LED} \ / \ \mathrm{LED}\text{-}\% \\ [\mathrm{TFA}]_0 \ / \ \mathrm{mol/l} \\ l_\mathrm{photo} \ / \ \mathrm{cm} \\ l_\mathrm{syn} \ / \ \mathrm{cm} \end{pmatrix} \leq \begin{pmatrix} 0.4 \\ 0.85 \\ 0.5 \\ 1.0 \\ 100 \\ 0.4 \\ 1000.0 \\ 1000.0 \end{pmatrix}. \tag{5.4}
$$

Based on the general formulations for yield, Equation 3.11, and space-time yield, Equation (3.13), the ART-related terms in the objective functions are calculated from

$$
Y_\mathrm{ART}(\boldsymbol{\xi}) = \frac{[\mathrm{ART}](\boldsymbol{\xi}, z = z_\mathrm{end})}{[\mathrm{DHAA}]_0}
$$
$$
STY_\mathrm{ART}(\boldsymbol{\xi}) = \frac{[\mathrm{ART}](\boldsymbol{\xi}, z = z_\mathrm{end})\dot{V}_\mathrm{l}(z = z_\mathrm{end})}{V}
$$

with $z_\mathrm{end} = l_\mathrm{photo} + l_\mathrm{syn}$ the reactor coordinate endpoint at the synthesis reactor outlet, V the reactor volume and the final ART concentration calculated using the identified overall process model.

For the robust setting, the space-time yield is considered, as it is crucial during production of artemisinin. TFA is considered to be dosed as the model and its parameters were identified for the same situation. The uncertain model parameters are in the same manner quantified as in the GSA, Section 5.5.7. The multi-start approach was again used for the process optimization runs, and the uncertainties were propagated with the PEM5 method, Section 3.6.1.

5.5 Results

In the following, the results for the model selection problem in the acid-catalyzed sequence, the investigation of the system behavior with the identified model, and the process optimization study are sequentially presented. For the identification of the chemical reaction network describing the acid-catalyzed sequence, the results are first analyzed for the base model, second for the previously introduced set of model candidates, and third for an extended set of model candidates. For the selection of the final model for the chemical reaction network, identifiability of the occurring

model parameters is examined and utilized for a terminal tuning of the model. The identified model is in the last part of this Chapter utilized for an analysis of the process model's behavior, and for a process optimization study targeting at the artemisinin yield and its space-time yield.

5.5.1 Performance of the Base Model

Before looking at the performance of the whole set of the different model candidates from Table 5.2, the focus is on the base model, i.e., model candidate 1, in the following. A summary of the parameter estimation is given in Table 5.3. The model-data fit is significantly worse than for the identified model of the photooxygenation, Chapter 4. The measurement error variance in the batch case is lower than in the continuous case, i.e., the continuous data is better predicted in a relative sense. The averaged relative deviation of artemisinin almost reaches 78 % – offering space for improvement. From the estimated kinetic parameter $k_{IM_2 \cdot BP_5} = 0\,l/(mol\,min)$, it follows that the byproduct reaction yielding BP_5 is not present. Satisfying parameter estimates are given for the remaining parameters with the exception of k_{PO_x} and in particular $k_{IM_2 \cdot IM_3}$, that have considerable confidence interval widths attached. The high value for $k_{IM_2 \cdot IM_3} = 205\,l/(mol\,min)$ suggests that IM_2 is converted almost instantly to IM_3 in the presence of oxygen. Corresponding parity plots for the base model are shown in Figure 5.8. In the PO_1 parity plot and for the continuous data, Figure 5.8a, the model predicts considerable amounts of PO_1 where the data is close to zero; see the data points on or very close to the abscissa. At the same time, ART concentrations are predicted too slow, Figure 5.8b. For the batch data, an opposite trend is visible: The base model does predict zero or trace quantities of PO_1, but the data shows significantly higher concentrations. Thus, the PO_1 depletion is predicted significantly too fast. For ART in Figure 5.8b, a distinct pattern is shown in its parity plot, that is, the points follow a curve. This indicates a systematic gap in the base model structure. Furthermore, the BP_3 data, Figure 5.8c, show very poor predictive capabilities of the base model over almost the entire concentration range, which clearly suggests missing characteristics of the simulated chemical reaction network. Hence, the base model is not able to predict any of the measured species in acceptable tolerances within the considered concentrations, making extensions and variants of the base model necessary.

5.5.2 Performance of the Core Model Candidates

For the set of model candidates from Table 5.2, a summary of the corresponding parameter estimation runs is given in Table 5.4. The corresponding estimated parameter values and initial conditions are given in Tables C.3, C.4 and C.5 in the Appendix. Changing the dissociation of TFA, Table 5.1, does not improve the model-data fit: The *RSS* or AIC_c values for the model candidate sets $\{1, 2, 3\}$ and $\{16, 17, 18\}$ are identical. As a first group, the extensions of the

Table 5.3: Goodness of fit and estimated parameter values and spreads for the continuous and batch process models describing the acid-catalyzed sequence with the base model, i.e., model candidate 1.

model-data fit

Symbol	unit	value	description
RSS	mol^2/l^2	0.5135	residual sum of squares
RSS_{conti}	mol^2/l^2	0.3017	
RSS_{batch}	mol^2/l^2	0.2117	
$\hat{\sigma}^2$	mol^2/l^2	8.54×10^{-4}	measurement error variance
$\hat{\sigma}^2_{conti}$	mol^2/l^2	7.54×10^{-4}	
$\hat{\sigma}^2_{batch}$	mol^2/l^2	10.53×10^{-4}	
	%	77.20	averaged relative deviation of ART[†]
	mmol/l	32.33 (28.94)	averaged absolute deviation of ART[†]

estimated parameters

Symbol	unit	value	COD	CI_{95}^-	CI_{95}^+
k_{PO_x}	1/min	6.14×10^{-4}	3.888	0.0	23.86×10^{-4}
$k_{PO_1 \cdot BP_3}$	l/(mol min)	0.349	0.393	0.282	0.419
$k_{PO_1 \cdot IM_2}$	l/(mol min)	3.17	0.148	2.945	3.415
$k_{IM_2 \cdot BP_4}$	l/(mol min)	0.441	0.353	0.368	0.524
$k_{IM_2 \cdot BP_5}$	l/(mol min)	0.0	-	-	-
$k_{IM_2 \cdot IM_3}$	l/(mol min)	205.0	6.509	95.63	1429.74
$k_{IM_3 \cdot ART}$	l/(mol min)	0.598	0.214	0.538	0.666

fixed parameters

Symbol	unit	value	reference
$\widetilde{k_1 a}_{syn}$	$\sqrt{1/cm\,min}$	1.094	fixed to estimated value in photoreactor

[†]: $\left(\sum_i^{n_{PO_1}} \left|(y_{PO_1,i}^{data} - y_{PO_1,i})\right| / y_{PO_1,i}\right)/n_{PO_1}$ (relative), $\left(\sum_i^{n_{PO_1}} \left|(y_{PO_1,i}^{data} - y_{PO_1,i})\right|\right)/n_{PO_1}$ (absolute)

Note that the relative measure is without considering the simulation points close to zero, i.e., points smaller than 0.01 mol/l.

For the absolute measure the figure for all data points is given in brackets.

COD: coefficient of dispersion, $COD = (CI_{95}^+ - CI_{95}^-)/\hat{\theta}$, $\hat{\theta}$: estimated value

$CI_{95}^{+/-}$: ±95 % confidence interval

Table 5.4: Summary of best results of parameter estimation runs for proposed core set of model candidates, Table 5.2. The number of model parameters is the number of non-zero estimated model parameters, with the original number of model parameters in brackets. Note that the rows correspond to the best estimation run in the sense of the objective function from the multi-start approach. The corresponding estimated parameter values and initial conditions are given in Tables C.3, C.4 and C.5 in the Appendix.

| ID	#θ	RSS	RSS_{conti}	RSS_{batch}	$\hat{\sigma}^2$	AIC$_c$
1	5 (7)	0.51	0.302	0.212	8.54×10^{-4}	-4230
2	6 (8)	0.51	0.302	0.212	8.54×10^{-4}	-4228
3	6 (8)	0.51	0.302	0.212	8.54×10^{-4}	-4228
4	6 (8)	0.35	0.156	0.198	5.89×10^{-4}	-4426
5	6 (9)	0.35	0.146	0.203	5.82×10^{-4}	-4457
6	7 (9)	0.49	0.282	0.213	8.23×10^{-4}	-4223
7	11 (11)	0.31	0.131	0.175	6.51×10^{-4}	-4509
8	6 (9)	0.45	0.224	0.224	7.46×10^{-4}	-4308
9	(11)	0.58	0.223	0.357	9.65×10^{-4}	-4123
10	11 (13)	0.20	0.123	0.076	3.30×10^{-4}	-4789
11	12 (13)	0.29	0.188	0.097	4.74×10^{-4}	-4571
12	14 (15)	0.20	0.124	0.078	3.36×10^{-4}	-4748
13	5 (7)	0.45	0.254	0.198	7.52×10^{-4}	-4307
14	6 (8)	0.32	0.232	0.087	5.30×10^{-4}	-4515
15	6 (8)	0.21	0.121	0.086	3.45×10^{-4}	-4773
16	7 (8)	0.17	0.081	0.088	2.81×10^{-4}	-4895
17	8 (9)	0.17	0.081	0.087	2.80×10^{-4}	-4896
18	8 (9)	0.17	0.081	0.088	2.81×10^{-4}	-4893
19	9 (10)	0.22	0.122	0.096	3.63×10^{-4}	-4738
20	8 (10)	0.21	0.121	0.086	3.45×10^{-4}	-4769
21	8 (10)	0.21	0.121	0.086	3.45×10^{-4}	-4769
22	8 (10)	0.17	0.080	0.088	2.79×10^{-4}	-4895
23	9 (10)	0.17	0.078	0.089	2.78×10^{-4}	-4899
24	7 (9)	0.17	0.081	0.088	2.81×10^{-4}	-4893
25	7 (9)	0.21	0.121	0.086	3.45×10^{-4}	-4771
26	8 (9)	0.17	0.080	0.089	2.80×10^{-4}	-4895
27	10 (11)	0.21	0.121	0.086	3.45×10^{-4}	-4741
28	9 (11)	0.21	0.121	0.086	3.45×10^{-4}	-4767
29	12 (13)	0.25	0.121	0.132	4.20×10^{-4}	-4618
30	12 (13)	0.17	0.080	0.089	2.80×10^{-4}	-4887
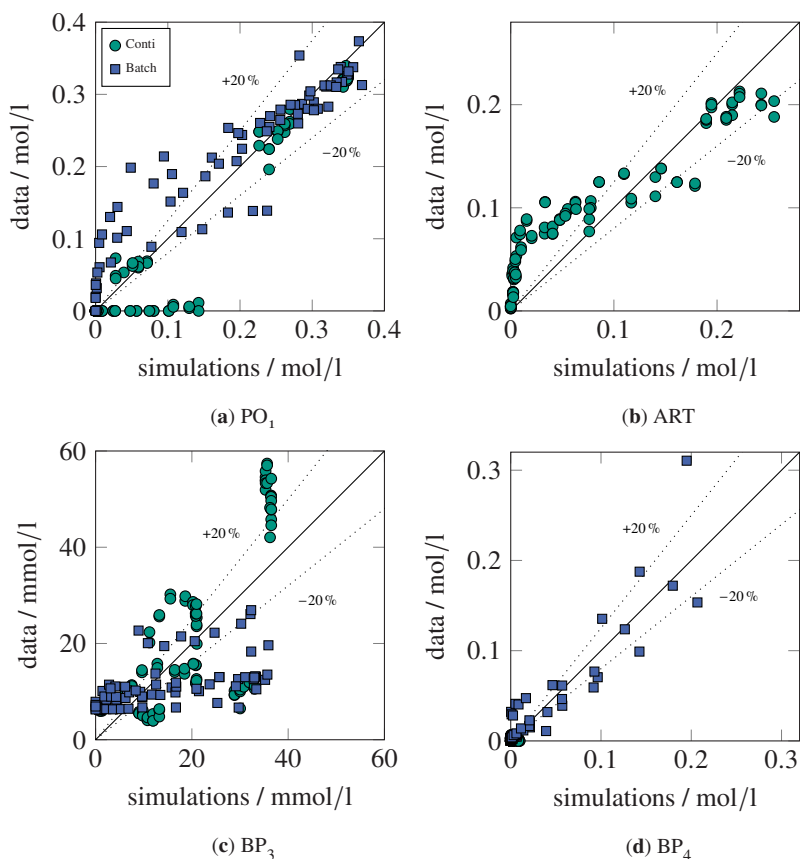
Figure 5.8: Match of experimental data with simulated results based on the parametrized process models with the base model (model candidate 1) for all quantities measured: a) PO_1, b) ART, c) BP_3, d) BP_4. The green circles correspond to the continuous and the blue squares to the batch experiments, respectively. The data of the continuous experiments was sampled at the reactor outlet, whereas the data of the batch experiments was collected in a time-resolved manner. The dashed lines mark 20 % deviations.

model candidates 4 to 12 are evaluated. They have in common that they do not consider proton reaction orders different from unity. Further, they include different schemes for protonation, equilibrium, hydration and byproducts (see colors in Figure 5.7), that are not part of the base model. Extending the base model by any or a combination of these adjustments did not necessarily lead to an improvement of the model-data fit; see for example the *RSS* values in Table 5.4. More specifically, model candidates 6 and 9, that have the BP_4 extension in common, perform worse than the base model. The largest improvement is achieved by the protonation extension of the hydroperoxide PO_1, model candidates 5, 7, and 10 to 12, emphasizing the important influence of TFA on the reaction kinetics. If additionally, the BP_3 protonation is introduced, model candidate 7, the model-data fit worsens, i.e., an *RSS* of $0.39 \, \text{mol}^2/\text{l}^2$ compared to $0.35 \, \text{mol}^2/\text{l}^2$ for model

candidate 5. The main reason for the difference is the discrepancy between the accumulation of another species between PO_1 and BP_3 on the one hand, and the extremely fast formation of BP_3 on the other hand, as can be seen for example in the corresponding scatter plot in Figure 5.2. Interestingly, integrating the hydration extension on top, model candidate 10, yields the best performing model within this group having an *RSS* as low as $0.20\,\mathrm{mol}^2/\mathrm{l}^2$. As observed before, the addition of the BP_4 equilibrium extension, model candidate 12 showed a negative effect on the predictive capability. Clearly, the key aspects beneficial for the improved model-data fit in model 10 are the variability in the acid concentration over the course of the reaction, and the possibility of a resting state by the hydration extension. As a result, model candidate 10 predicts an almost complete temporary TFA depletion in the batch experiments, and, since initial concentrations are much higher, TFA depletions of *only* more than half in the continuous experiments. Consequently, further model refinement was targeted at the acidic activity on the reaction kinetics, i.e., the alteration of the TFA reaction orders for the depletion of PO_1 towards both BP_3 and IM_2, model candidates 13 to 30. For all model candidates within this category, significant improvements are achieved, where most of them reach an *RSS* of $0.21\,\mathrm{mol}^2/\mathrm{l}^2$ or below. The orders in the model candidates 25 to 30 suggested a difference of less than 1 as set in model candidates 15 to 24, but in both cases the reaction orders of TFA lie between 2 and 3 for m_{IM_2} and 3 to 4 for m_{BP_3}. Thus, the TFA reaction orders considerably exceed 1. Such high values might be a consequence of a sequence of rate-limiting acid-catalyzed steps, i.e., multiple protonations lumped together in the simplified model candidates. Alternatively, the high reaction orders compensate physical or chemical phenomena, that are not covered by the structures of the model candidates. In many model candidates in Table 5.4, the formation of IM_3 was estimated to be very fast. That is, IM_3 is accumulated as the main intermediate and IM_2 is only formed in trace quantities in the presence of oxygen. Therefore, the byproduct formation starting from IM_3 obtains better model-data fits than the byproduct formation from IM_2, see model candidate pairs 15/16 and 25/26. This suggests the existence of an additional byproduct on the reaction path from IM_2 to ART apart from BP_4.

5.5.3 Expanding the Set of the Core Model Candidates

In further steps, the set of different model candidates from Table 5.2 was iteratively extended with the goal of improving the model-data fit. Two directions were followed. One, further structural extensions were integrated, that describe new conceivable system characteristics and might provide new insights into the system behavior. And two, starting from limitations and shortcomings of the already developed model candidates, refinements of the existent model structures were introduced, that, in the end, led to the final model candidate.
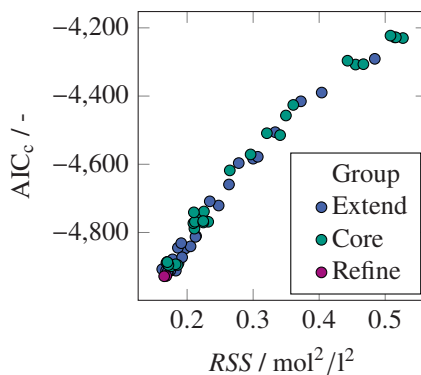
Figure 5.9: Score plot for the parameter estimation runs of all considered model candidates. The points are grouped into the first considered model candidates (*core*) from Table 5.2, model candidates with additional extensions (*extend*), Tables C.6 and C.7 in the Appendix, and model candidates with structural refinements (*refine*). Note that the points are jittered for a better view in dense regions.

The introduced extensions are not discussed in detail here as none of them is able to improve the results that are achieved in Section 5.5.2. An overview of them is given in the Appendix, Tables C.6 and C.7. Including the already established core set, the total number of model candidates then added up to almost 65. A selection of the additionally tested characteristics is given in the following:

- The position of the reaction towards BP_4 was varied along the reaction path from PO_1 to ART.

- The reaction rates of certain reactions was set to be independent on the acid concentration.

- Estimation of reaction orders on the path towards BP_4 and for the final step to ART was made possible.

- A further species IM_5 was added and formed an equilibrium with one of the other intermediates.

For a full description of the extended set, the interested reader is pointed to the Section C.3 in the Appendix.

As a summary for all model candidates, a score plot of all their parameter estimation runs is given in Figure 5.9. Despite a multitude of new variants and extensions, named as *extend* group in Figure 5.9, significant reductions in *RSS* and AIC_c values could not be achieved. This suggests that either the uncertainty in the relatively complex experimental procedure including setting up, running the experiment, taking samples, quenching, and measuring hinders further improvements; or, the set of model candidates in combination with the applied process model does not cover all physical and chemical effects that are present in the real system. The former is supported

by for example the scatter plots given in the exploratory data analysis for the batch experiments, Figure 5.4, where considerable deviations are observed for experiments with similar conditions, i.e., with similar TFA concentrations. On the other hand, traces of patterns in the parity plots of the selected model candidate, that are shown in a following Section, Figure 5.14, support the latter reason of missing physical features.

For the refinement direction, a model candidate was selected from the comprehensive set of postulated candidates. The refinements steps yielded the final model candidate that was subsequently used for a global sensitivity analysis and an overall process optimization in conjunction with the photooxygenation part to improve artemisinin yields. To this end, the AIC_c is a very good heuristic to support the decision. From Table 5.4, a small choice of model candidates reaches an AIC_c of almost -5000, with very subtle differences among the candidates. It is known that the AIC tends to overfitting, i.e., selects model candidates with a greater number of model parameters than for example the BIC [148]. Keeping the complexity of the final model candidate as low as possible, a lower number of model parameters was given more weight. Moreover, the model structure of the candidate was evaluated based on expert knowledge about the reaction mechanism. In the end, model candidate 16, having both a small number of parameters, namely 7, a good model-data fit and a low AIC_c, is considered the optimum. Here, PO_1 converts to BP_3 and IM_2 with non-unity TFA reaction orders, where the difference between the reaction orders is set to 1, see the black arrows leaving PO_1 in Figure 5.7, and Table 5.2. IM_2 is either oxygenated to IM_3, or converted to the byproduct BP_4. At IM_3, either a further byproduct BP_5 or the final product ART is formed. Model candidate 16 was then refined as explained in the following Section.

5.5.4   Refining the Selected Model Structure

Three refinements to the mechanistic structure of model candidate 16 have been performed, where the reasons for the refinements were not exclusively observed in the selected model candidate, but found in other model candidates likewise. The first refinement was inferred from interpreting the model-data fit while considering the semi-synthesis mechanism. And the two other refinements were established on the basis of identifiability problems of the present model parameters.

Considering the continuous and the batch data of the BP_4 species, Figures 5.2 and 5.4, BP_4 is almost exclusively formed in the batch experiments, with trace quantities in the continuous experiments only. On the other hand, the model candidates were generally overestimating the amount of BP_4 formed in the continuous experiments, slightly visible in the bottom left corner of Figure 5.8d, and underestimating the BP_4 formation in the batch experiments. In the batch experiments, the reaction path from IM_2 towards ART is blocked for no oxygen is present. Contrarily, in the continuous experiments, BP_4 can and is formed, even in situations where the model candidates predicted that IM_2 has a short occurrence. Hence, the results from the model

(a) Singular values.

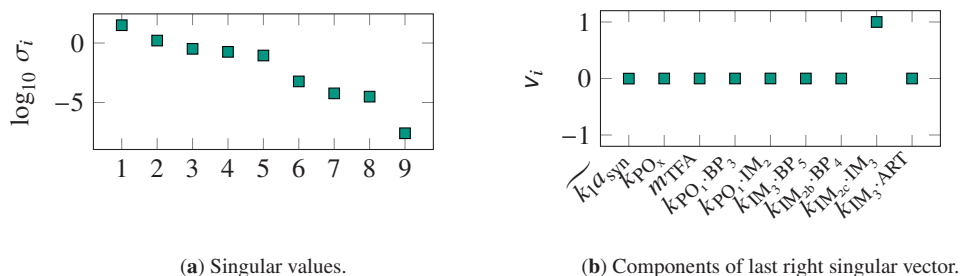(b) Components of last right singular vector.

Figure 5.10: Singular value decomposition (SVD) of the sensitivity matrix for model candidate 16 after its first refinement. The last singular value indicates non-identifiability, and the corresponding right vector points to the causing parameter $k_{IM_{2c} \cdot IM_3}$, Section 3.5.1.

selection revealed that the differing formation rates of BP_4 in the continuous and batch experiment could not be sufficiently explained by a joint model. A remedy would be to set the kinetic constant $k_{IM_2 \cdot IM_3}$ to a very high value, that is, to increase the upper limit of $k_{IM_2 \cdot IM_3}$ during parameter estimation. However, that would result in the prediction of an instant liquid oxygen depletion, that is physically not plausible. Alternatively, two different intermediates for IM_2 in the continuous and batch case, namely IM_{2c} and IM_{2b}, were introduced, that improved the model-data fit and eased the numerical simulations as the near-instant formation of IM_3 in the continuous experiments was eliminated. The introduction of two different intermediates for the same physical system is the trade-off one must accept for approximating the real system behavior by a simplified reaction scheme. Note however that the differences in the model-data fit between the original and the refined model are subtle. Hence, the original model might also be used for predictions in between the conditions applied in the batch and the continuous experiments, i.e., between short residence times, high TFA concentrations and an oxygen-only gas phase in the continuous experiments and long residence times, low TFA concentrations and absence of oxygen in the batch experiments. The refinement emphasizes the situation at hand that experimental conditions for the different set-ups were different likewise. Depending on the composition of the gas phase, either $x_{O_2} = 1$ (continuous experiments) or $x_{O_2} = 0$ (batch experiments), the accumulating intermediates in the reaction path towards ART differ.

The two remaining refinements compensate for two detected parameter identifiability issues, that all of the model candidates shared and that are explained by looking at the selected and refined model candidate 16 in the following. The plots for the singular value decomposition (SVD) approach are shown in Figure 5.10. The singular value plot on the left, Figure 5.10a, shows a clear gap between the eights and the ninth singular value indicating a non-identifiability. One might point to a second gap between the fifth and the sixth singular value. However, the previously identified gap is significantly greater, and the magnitude of the sixth singular value can still be considered non-zero ($\sigma_6 \approx 6 \times 10^{-4}$) [159]. Looking at the components of the sixth right singular vector, Figure 5.10b, it is revealed that the non-identifiability is linked to the kinetic constant

$k_{\mathrm{IM}_{2c} \cdot \mathrm{IM}_3}$. This identifiability issue is confirmed in the profile likelihood plot of the same kinetic constant, Figure 5.11b. Interestingly, continuously increasing the magnitude of $k_{\mathrm{IM}_{2c} \cdot \mathrm{IM}_3}$ results in infinitesimal improvements of the likelihood, as can be spotted in its profile likelihood, Figure 5.11b. This observation backs the previous introduction of separate IM_2 intermediates for the batch and the continuous experiments, as it suggests that the predicted IM_2 in the continuous case should at best not occur at all.

The optimization results from the multi-start approach and the profile likelihoods of the other parameters revealed a further non-identifiability that the SVD algorithm did not readily show. The second non-identifiability is attributed to the efficient mass transfer coefficient $\widetilde{k_1 a}_{\mathrm{syn}}$, that can be observed in its profile likelihood graph in Figure 5.11a. For a more in-depth analysis of the non-identifiabilities and potential dependencies among the parameters, a global sensitivity analysis (GSA) on the objective function was conducted. In Figure 5.12, the results from the GSA on the objective function with its underlying eOLS approach, are shown. Please note that the effects of the initial conditions of the batch experiments, that were equally estimated in the extended ordinary least squares approach, are not shown in the graphs. In none of the parameter estimation runs for any model candidate, identifiability issues considering the initial conditions were observed. Strikingly, the sensitivity on the objective function is almost exclusively caused by the reaction order m_{IM_2}, Figure 5.12a, i.e., the acid-dependence of the production of the first intermediate is the by far most sensitive parameter on the objective function. However, a zoomed graph, Figure 5.12b, reveals that further parameters are sensitive likewise, although for a large part based on second-order effects. Two parameters show no effect at all on the objective function, namely $\widetilde{k_1 a}_{\mathrm{syn}}$, and $k_{\mathrm{IM}_{2c} \cdot \mathrm{IM}_3}$, suggesting that the parameters are non-identifiable as concluded before from the SVD and the profile likelihood approach. The matrix plot in Figure 5.12c gives additional insight into which parameters interact with other and cause the second-order effects. Thus, the second-order effects of the reaction order m_{IM_2} and the reaction constant $k_{\mathrm{PO}_1 \cdot \mathrm{IM}_2}$ are mainly caused by an interaction among those two parameters. This is expectable as both determine the rate of IM_2 production from PO_1. Apart from the kinetic constant k_{PO_x}, that
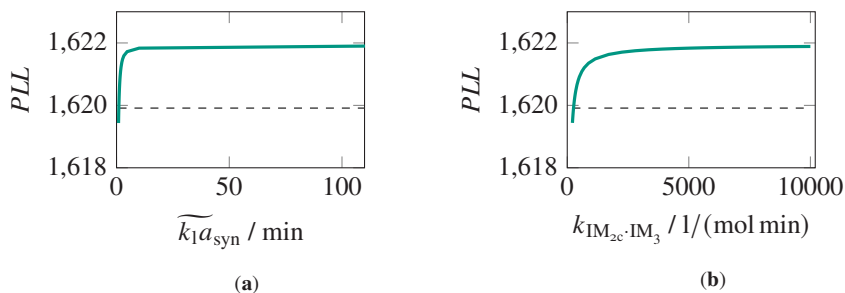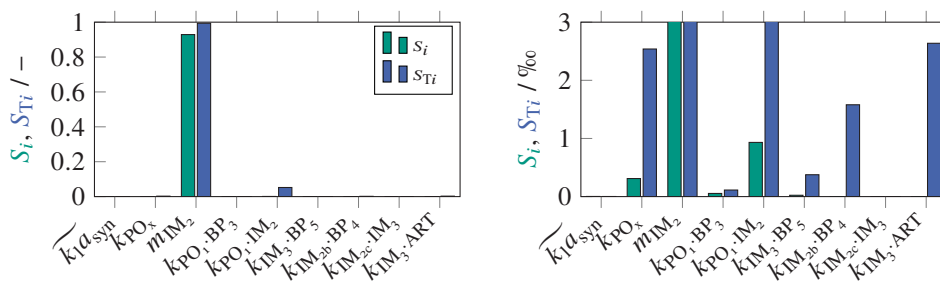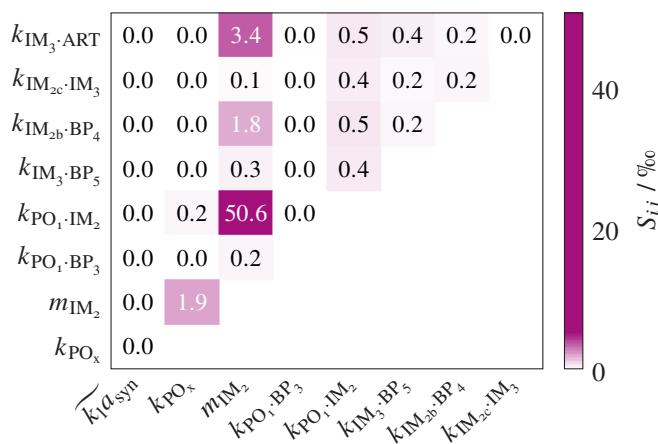

Figure 5.11: Profile likelihoods of the two non-identifiable parameters in the selected, but not refined model candidate 16.

(a) First and total order effects.

(b) First and total order effects (zoomed).

(c) Second order effects.

Figure 5.12: Influence of model parameters on the parameter estimation objective, Equation 3.39, by using uniform distributions between -10 and $10\,\%$ of the nominal values. Both graphs reveal identifiability issues for both $\widetilde{k_1 a}_{\mathrm{syn}}$ and $k_{\mathrm{IM_{2c}} \cdot \mathrm{IM_3}}$. Note that the initial conditions in the batch experiments, that have been estimated as well, are not shown here.

is part of the photooxygenation reaction network and therefore shows interaction only with the parameters involved in the main reaction pathway depleting PO_1, all kinetic parameters in the acid-catalyzed network are cross-interacting with each other. The only exception is the kinetic constant $k_{\mathrm{PO_1} \cdot \mathrm{BP_3}}$, that solely shows interaction effects with the dominant reaction order $m_{\mathrm{IM_2}}$.

The non-identifiabilities attributed to $\widetilde{k_1 a}_{\mathrm{syn}}$ and $k_{\mathrm{IM_{2c}} \cdot \mathrm{IM_3}}$ led to two further adjustments of the selected model candidate 16. In case of the mass transfer coefficient, two reasons are responsible for not being able to determine its magnitude. First, no gas phase samples were measured for the synthesis experiments in contrast to the photooxygenation experiments, Chapter 4. More importantly, the collected liquid samples are in general collected when the oxygen concentration in the liquid is equilibrated. Hence, even if the gas phase is measured, it would not be able to see
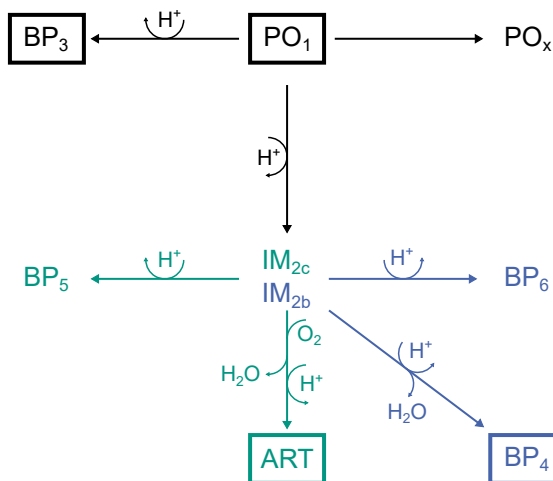
Figure 5.13: Selected reaction network for the acid-catalyzed sequence producing artemisinin from the hydroperoxide PO_1. The network consists of two sub-networks. The green sub-network is active when the gas phase consists of oxygen ($x_{O_2} = 1$, continuous experiments). The blue sub-network is active when no oxygen is present ($x_{O_2} = 0$, batch experiments).
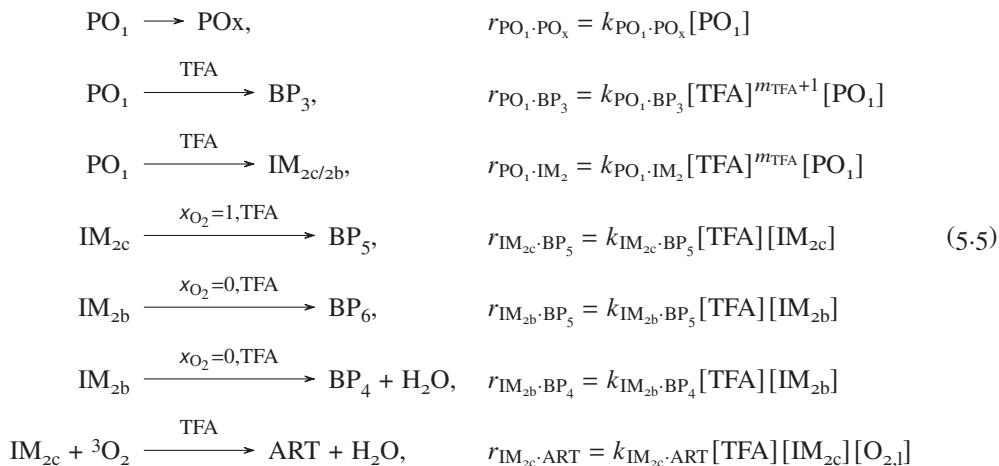
the mass transfer dynamics. The coefficient was therefore set to its estimated counterpart in the photo reactor, i.e., $\widetilde{k_1 a}_{\text{syn}} = \widetilde{k_1 a} = 1.094 \sqrt{1/\text{cm min}}$. Note that also the mass transfer coefficients in the other model candidates have been adjusted accordingly for comparison reasons.

The non-identifiability of the second parameter $k_{\text{IM}_{2c} \cdot \text{IM}_3}$ suggests that only one intermediate is accumulated in non-trace quantities. This leads to the omission of IM_3 and shortens therefore the species number of the pathway to ART by one. In contrast to $\widetilde{k_1 a}$, omitting IM_3 in the other model candidates is not necessary. The reason is that a possible estimate of $k_{\text{IM}_2 \cdot \text{IM}_3}$ at its upper limit of 5000 already gives a behavior that is close to the situation when IM_3 is omitted; see the weak increase of the profile likelihood right of 5000 min in Figure 5.11b. The omission of IM_3 also solves the problem of an unrealistic extremely rapid depletion of liquid oxygen, that occurs as a result of very high magnitudes for $k_{\text{IM}_{2c} \cdot \text{IM}_3}$, as the oxygenation was assumed to happen from IM_2 to IM_3, Figure 5.7.

5.5.5 Selected Model Candidate for the Acid-catalyzed Sequence

Following the refinement considerations in the previous Section, the selected reaction network is depicted in Figure 5.13. Key characteristic of the network is that different sub-networks are active depending on the gas phase composition. If the gas phase contains oxygen ($x_{O_2}=1$, green sub-network in Figure 5.13), the accumulating intermediate is IM_{2c}, and ART and byproduct BP_5

are formed, but no BP_4. On the other hand, if oxygen is absent ($x_{O_2}=0$, blue sub-network in Figure 5.13), the accumulating intermediate is IM_{2b}, and BP_4 and BP_6 are the only products formed. The kinetic model corresponding to the reaction network for the acid-catalyzed sequence in Figure 5.13 using mass action kinetics, Section 3.3.1, reads

$$PO_1 \longrightarrow POx, \qquad\qquad r_{PO_1 \cdot PO_x} = k_{PO_1 \cdot PO_x}[PO_1]$$

$$PO_1 \xrightarrow{\text{TFA}} BP_3, \qquad\qquad r_{PO_1 \cdot BP_3} = k_{PO_1 \cdot BP_3}[TFA]^{m_{TFA}+1}[PO_1]$$

$$PO_1 \xrightarrow{\text{TFA}} IM_{2c/2b}, \qquad\qquad r_{PO_1 \cdot IM_2} = k_{PO_1 \cdot IM_2}[TFA]^{m_{TFA}}[PO_1]$$

$$IM_{2c} \xrightarrow{x_{O_2}=1,\text{TFA}} BP_5, \qquad\qquad r_{IM_{2c} \cdot BP_5} = k_{IM_{2c} \cdot BP_5}[TFA][IM_{2c}] \qquad (5.5)$$

$$IM_{2b} \xrightarrow{x_{O_2}=0,\text{TFA}} BP_6, \qquad\qquad r_{IM_{2b} \cdot BP_5} = k_{IM_{2b} \cdot BP_5}[TFA][IM_{2b}]$$

$$IM_{2b} \xrightarrow{x_{O_2}=0,\text{TFA}} BP_4 + H_2O, \qquad r_{IM_{2b} \cdot BP_4} = k_{IM_{2b} \cdot BP_4}[TFA][IM_{2b}]$$

$$IM_{2c} + {}^3O_2 \xrightarrow{\text{TFA}} ART + H_2O, \qquad r_{IM_{2c} \cdot ART} = k_{IM_{2c} \cdot ART}[TFA][IM_{2c}][O_{2,l}]$$

Note that in the presence of oxygen ($x_{O_2}=1$, continuous case) IM_{2b} and in the absence of oxygen ($x_{O_2}=0$, batch case) IM_{2c} is inactive.

Although the kinetic constant k_{PO_x} describing the loss of hydroperoxides has been already estimated in the photooxygenation step, Section 4.3.6, it is re-estimated during the calibration of the acid-catalyzed sequence. This is necessary, since, originally, the loss of hydroperoxides in the photooxygenation considered the loss of hydroperoxides on its way from sampling to measuring. However, for the acid-catalyzed sequence, the hydroperoxide losses are not anymore as pronounced since the main hydroperoxide PO_1 immediately reacts when acid is present. Hence, connecting the kinetic model for the acid-catalyzed sequence, Equations (5.5), with the developed process model for the photooxygenation, Section 4.2.3, yields the governing differential equations for the overall process model of the semi-synthesis of artemisinin from DHAA in the continuous setup. The material balance equations for the liquid and gas phase in the whole reaction line are

$$\frac{d[DHAA]}{dz} = \frac{\left(1 - \frac{\beta}{C_0}\right)A}{\dot{V}_l}\left(-\frac{[O_2]}{k_{l1}[O_2] + k_{l2}}\frac{(\tilde{k}_{PO_1} + \tilde{k}_{PO_y})[DHAA]}{1 + (\tilde{k}_{PO_1} + \tilde{k}_{PO_y})[DHAA]}\right.$$
$$\left. L_p(1 - \exp\left[-\kappa c_{DCA}l_{opt}\right])\right),$$

$$\frac{d[PO_1]}{dz} = \frac{\left(1 - \frac{\beta}{C_0}\right) A}{\dot{V}_l} \left(\frac{[O_2]}{k_{11}[O_2] + k_{12}} \frac{\tilde{k}_{PO_1}[DHAA]}{1 + (\tilde{k}_{PO_1} + \tilde{k}_{PO_y})[DHAA]} \right.$$

$$L_p(1 - \exp[-\kappa c_{DCA} l_{opt}]) - r_{PO_1 \cdot PO_x}$$

$$\left. - r_{PO_1 \cdot BP_3} - r_{PO_1 \cdot IM_2} \right),$$

$$\frac{d[PO_y]}{dz} = \frac{\left(1 - \frac{\beta}{C_0}\right) A}{\dot{V}_l} \left(\frac{[O_2]}{k_{11}[O_2] + k_{12}} \frac{\tilde{k}_{PO_y}[DHAA]}{1 + (\tilde{k}_{PO_1} + \tilde{k}_{PO_y})[DHAA]} \right.$$

$$\left. L_p(1 - \exp[-\kappa c_{DCA} l_{opt}]) - r_{PO_1 \cdot PO_x} \right),$$

$$\frac{d[PO_x]}{dz} = \frac{\left(1 - \frac{\beta}{C_0}\right) A}{\dot{V}_l} k_{PO_x}([PO_1] + [PO_y]),$$

$$\frac{d[IM_{2c}]}{dz} = \frac{\left(1 - \frac{\beta}{C_0}\right) A}{\dot{V}_l} \left(r_{PO_1 \cdot IM_2} - r_{IM_{2c} \cdot ART} - r_{IM_{2c} \cdot BP_5} \right),$$

$$\frac{d[BP_3]}{dz} = \frac{\left(1 - \frac{\beta}{C_0}\right) A}{\dot{V}_l} r_{PO_1 \cdot BP_3},$$

$$\frac{d[BP_5]}{dz} = \frac{\left(1 - \frac{\beta}{C_0}\right) A}{\dot{V}_l} r_{IM_{2c} \cdot BP_5},$$

$$\frac{d[ART]}{dz} = \frac{\left(1 - \frac{\beta}{C_0}\right) A}{\dot{V}_l} r_{IM_{2c} \cdot ART},$$

$$\frac{d[O_2]}{dz} = \frac{\left(1 - \frac{\beta}{C_0}\right) A}{\dot{V}_l} \left(-\frac{[O_2]}{k_{11}[O_2] + k_{12}} \frac{(\tilde{k}_{PO_1} + \tilde{k}_{PO_y})[DHAA]}{1 + (\tilde{k}_{PO_1} + \tilde{k}_{PO_y})[DHAA]} \right.$$

$$L_p(1 - \exp[-\kappa c_{DCA} l_{opt}]) + \widetilde{k_1 a} \sqrt{u_g^s}([O_2]^\infty - [O_2])$$

$$\left. - r_{IM_{2c} \cdot ART} \right),$$

$$\frac{dx_{O_2}}{dz} = \frac{T}{p\dot{V}_g} \left(-R\frac{\beta}{C_0} A \widetilde{k_1 a} \sqrt{u_g^s}([O_2]^\infty - [O_2]) - \frac{p}{T} x_{O_2} \frac{d\dot{V}_g}{dz} \right),$$

$$\frac{d\dot{V}_g}{dz} = -\frac{T}{p} R\frac{\beta}{C_0} A \widetilde{k_1 a} \sqrt{u_g^s}([O_2]^\infty - [O_2]). \tag{5.6}$$

The corresponding initial conditions are

$$([\text{DHAA}], [\text{PO}_1], [\text{PO}_y], [\text{PO}_x], [\text{IM}_{2c}], [\text{BP}_5], [\text{ART}], [\text{O}_2], [x_{\text{O}_2}], [\dot{V}_g])^\top (0)$$
$$= ([\text{DHAA}]_0, 0, 0, 0, 0, 0, 0, [\text{O}_2]^\infty, x_{\text{O}_2,0}, \dot{V}_{g,0})^\top.$$

Please note that the initial conditions apply at the inlet of the photo reactor. The governing equations of the process model for the batch experiments are given in the Appendix, Section C.1. Hence, the vector of unknown model parameters of the process models for the batch and continuous setups, Equations (5.6) and (C.20), that needs to be identified, is

$$(k_{\text{PO}_x}, m_{\text{IM}_2}, k_{\text{PO}_1 \cdot \text{BP}_3}, k_{\text{PO}_1 \cdot \text{IM}_2}, k_{\text{IM}_{2b} \cdot \text{BP}_4}, k_{\text{IM}_{2c} \cdot \text{BP}_5}, k_{\text{IM}_{2b} \cdot \text{BP}_6}, k_{\text{IM}_{2c} \cdot \text{ART}})^\top. \tag{5.7}$$

Simultaneously, both the model parameters and the initial conditions of PO_1 and BP_3 for all six experiments in batch operation, Equation (C.21) in the Appendix, are estimated. Thus, in total 8 model parameters and 12 initial conditions are estimated in the extended ordinary least squares approach.

A quantitative summary of the results is given in Table 5.5. A drastic improvement of the model-data fit is observed compared to the results of the base model candidate, Table 5.3, where the *RSS* decreased from $0.5135 \, \text{mol}^2/\text{l}^2$ to $0.16 \, \text{mol}^2/\text{l}^2$. The continuous data is slightly better predicted, as the estimated measurement error variance is lower than the batch counterpart, which could be observed for all model candidates given in Table 5.2. The averaged relative deviation of ART is 13.97 %, where points smaller than simulated values of 0.01 mol/l are not considered because they would distort the calculation of the relative measure that is based on the simulated ART concentration, i.e., the simulated concentration is the denominator, Table 5.5. The parity plots of the measured versus simulated data are shown in Figure 5.14. In general the model-data fit is satisfactory considering the complexity of the considered reaction network and process characteristics, in particular for the most interesting concentration of ART, Figure 5.14b. However, some weak spots in the parity plots must be noted.

Predictions of the batch data (blue squares) are for certain data points quite poor, e.g., deviations of more than 20 % in the PO_1 concentration range up to 0.25 mol/l in Figure 5.14a. Batch data points for BP_4 also show improvements for predictions, Figure 5.14d. This is for a great part attributed to the variability of measurement results for batch experiments running on same conditions, i.e., low reproducibility, that can be seen in the Figure 5.4 used for the data analysis, and in further experimental data not shown in this work [61]. For the continuous data, at low TFA concentrations, the model predicts the depletion of PO_1 too slow. This can be seen in the ART points that lie on the ordinate in Figure 5.14b. They correspond to the points of the PO_1 concentration in Figure 5.14a below the diagonal line at around $y \approx 0.3$ mmol/l and the points of the BP_3 concentration in Figure 5.14c at $y \approx 0$ mol/l. Thus, BP_3 and ART are not formed fast

Table 5.5: Goodness of fit and estimated parameter values and spreads for the developed process model and selected and refined model candidate 16 describing the synthesis reaction network. The confidence intervals are based on the profile likelihood.

model-data fit

Symbol	unit	value	description
RSS	$\mathrm{mol}^2/\mathrm{l}^2$	0.1600	residual sum of squares
RSS_conti	$\mathrm{mol}^2/\mathrm{l}^2$	0.0748	RSS for conti experiments
RSS_batch	$\mathrm{mol}^2/\mathrm{l}^2$	0.0853	RSS for batch experiments
$\hat{\sigma}^2$	$\mathrm{mol}^2/\mathrm{l}^2$	2.66×10^{-4}	measurement error variance
$\hat{\sigma}^2_\mathrm{conti}$	$\mathrm{mol}^2/\mathrm{l}^2$	1.87×10^{-4}	$\hat{\sigma}^2$ for conti experiments
$\hat{\sigma}^2_\mathrm{batch}$	$\mathrm{mol}^2/\mathrm{l}^2$	4.24×10^{-4}	$\hat{\sigma}^2$ for batch experiments
	%	13.97	averaged relative deviation of ART[†]
	mmol/l	10.14 (11.87)	averaged absolute deviation of ART[†]

estimated parameters

Symbol	unit	value	COD	CI^-_{95}	CI^+_{95}
k_{PO_x}	1/min	0.0105	0.161	0.0096	0.0113
m_{IM_2}	-	2.646	0.013	2.629	2.664
$k_{\mathrm{PO}_1 \cdot \mathrm{BP}_3}$	$(\mathrm{l/mol})^{m_{\mathrm{IM}_2}+1}/\mathrm{min}$	424.2	0.245	373.0	477.1
$k_{\mathrm{PO}_1 \cdot \mathrm{IM}_2}$	$(\mathrm{l/mol})^{m_{\mathrm{IM}_2}}/\mathrm{min}$	880.3	0.112	833.2	931.6
$k_{\mathrm{IM}_{2b} \cdot \mathrm{BP}_6}$	$1/(\mathrm{mol\,min})$	0.0	-	-	-
$k_{\mathrm{IM}_{2c} \cdot \mathrm{BP}_5}$	$1/(\mathrm{mol\,min})$	0.682	0.206	0.614	0.755
$k_{\mathrm{IM}_{2b} \cdot \mathrm{BP}_4}$	$1/(\mathrm{mol\,min})$	0.887	0.290	0.770	1.026
$k_{\mathrm{IM}_{2c} \cdot \mathrm{ART}}$	$(\mathrm{l/mol})^2/\mathrm{min}$	30.07	0.138	28.07	32.24

fixed parameters

Symbol	unit	value	reference
$\widetilde{k_1 a}_\mathrm{syn}$	$\sqrt{1/\mathrm{cm\,min}}$	1.094	fixed to estimated value in the photoreactor

[†]: $\left(\sum_i^{n_{\mathrm{PO}_1}} \left|(\bar{y}_{\mathrm{PO}_1,i} - y_{\mathrm{PO}_1,i})\right|/y_{\mathrm{PO}_1,i}\right)/n_{\mathrm{PO}_1}$ (relative), $\left(\sum_i^{n_{\mathrm{PO}_1}} \left|(\bar{y}_{\mathrm{PO}_1,i} - y_{\mathrm{PO}_1,i})\right|\right)/n_{\mathrm{PO}_1}$ (absolute)

Note that the relative measure is without considering the simulation points close to zero, compare with Figure 5.14b.

For the absolute measure the figure for all data points is given in brackets.

COD: coefficient of dispersion, $COD = (CI^+_{95} - CI^-_{95})/\hat{\theta}$, $\hat{\theta}$: estimated value

$CI^{+/-}_{95}$: ±95 % confidence interval

(a) PO_1

(b) ART

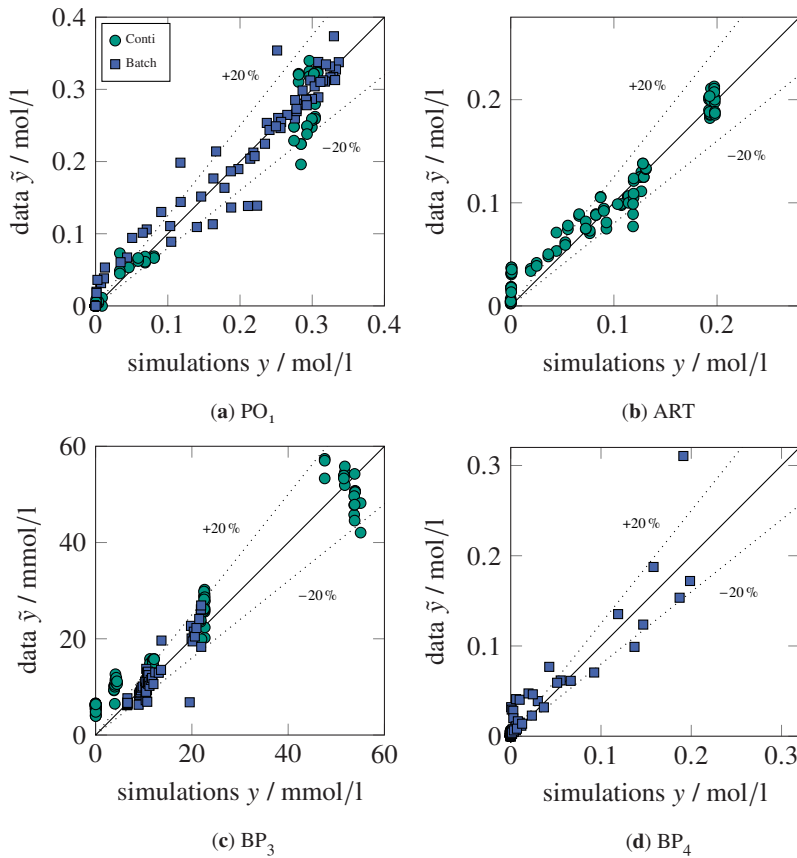**(c)** BP_3

(d) BP_4

Figure 5.14: Match of experimental data with simulated results for all quantities measured. Simulations are based on the parameterized final model, Equations (5.6) (continuous) and Equations C.1 (batch) in the Appendix. The dashed lines mark 20 % deviations.

enough, whereas PO_1 is still present in too high concentrations. For very high ART and BP_3 concentrations, the simulations predict constant concentrations, where the experimental data do not show steady state behavior; see the arrangement of parity points in a vertical manner in Figure 5.14b at $y \approx 0.2$ mmol/l, and in Figure 5.14c at $y \approx 55$ mmol/l. This is again attributed for a great part to uncertain measurements, that can be well identified in the scatter plots in Figure 5.2. Here, the data points for the highest TFA concentration in the plots of yield over theoretical residence time for BP_3 and ART (green points in plots 7 and 16), cluster and do not form curves as in the cases for lower TFA concentrations in the same plots. The same phenomenon is as well visible for lower BP_3 concentrations in Figure 5.14c, for example at $y \approx 20$ mmol/l. Once more one root cause lies in the experimental data, where measurement uncertainties for BP_3 over time seem to be considerable as shown in the BP_3 yield over theoretical residence time plot in Figure 5.2, plot 7. Hence, the observed differences between simulated and experimental data in the parity
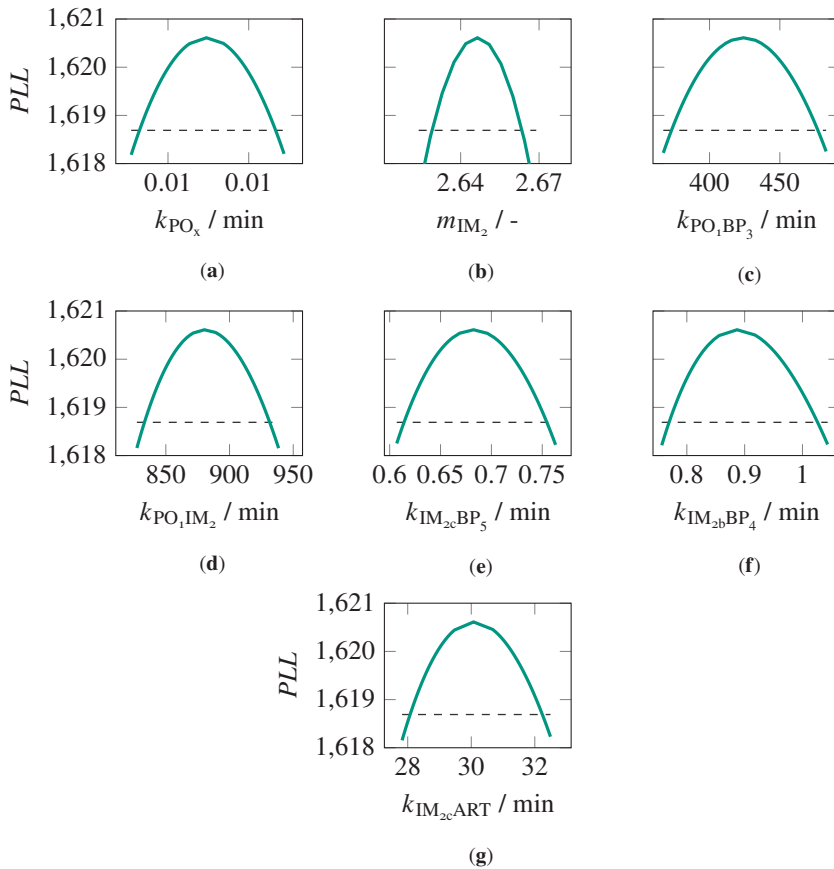
Figure 5.15: Profile likelihoods of estimated model parameters for the selected and refined model candidate 16. Dashed lines mark the 95 % confidence intervals. All PLLs cross the confidence interval line, and are therefore identifiable.

plots can be explained mostly by existent measurement uncertainty. Against this background, the overall predictive power of the process model, in particular for the ART concentration, is satisfactory. Before a deeper model-based analysis and process optimization are performed, the parameter values and their confidence intervals are assessed.

The profile likelihoods of the model parameters in Table 5.5 are shown in Figure 5.15. With the refinements of the original model structure and parameters, none of the model parameters shows identifiability issues. On the contrary, all parameters form well-shaped and narrow likelihood curves crossing the 95 % confidence interval lines. Note that the kinetic constant describing the loss reaction to byproduct BP_6 is not shown as it was estimated to be zero. The best coefficient of dispersion is obtained for the TFA reaction order, where its magnitude is considerably larger than
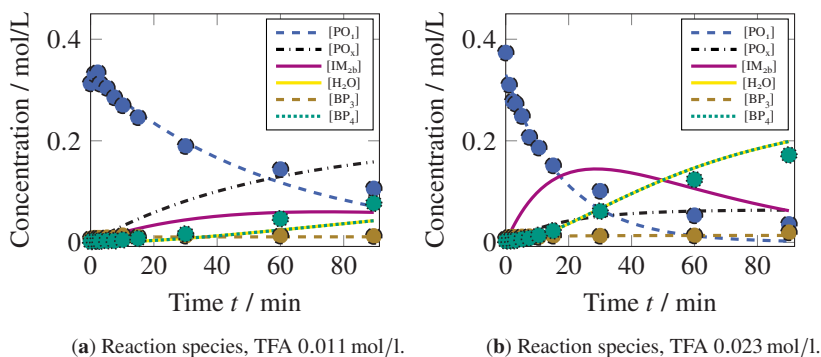
(**a**) Reaction species, TFA 0.011 mol/l.

(**b**) Reaction species, TFA 0.023 mol/l.

Figure 5.16: Time profiles of concentrations for batch experiments at different TFA concentrations. Lines are simulations, circles are experimental data points.

1, i.e., in the reaction from PO_1 to BP_3 it is 3.646 with explanations given previously in Section 5.5.2.

In the following three Sections, the identified process model is used for first, a model-based inspection of the experiments for both the continuous and the batch setup; second, a global sensitivity analysis of the overall process model on key concentrations along the reactor coordinate; and third, a process optimization focusing on the yield and the space-time yield of artemisinin.

5.5.6 Model-Based Analysis of Continuous and Batch Experiments

The process behavior is investigated in a two-step model-based analysis. First, the time-resolved trends of the species in the acid-catalyzed reaction network are analyzed on the basis of both batch and continuous data. Second, key concentrations of the continuous process are examined along the reactor coordinate.

For the operation in batch mode, time profiles of two experiments are shown for two different TFA concentrations in Figure 5.16. Predictions agree in general very well with the experimental data. A minor exception is observed for the PO_1 depletion, where predictions tend to be too fast with proceeding time. This can be observed in all batch experiments.

For the continuous experiments, results from simulations and experimental data having a TFA concentration of 0.25 mol/l are given in Figure 5.17. Overall, the match between simulated and experimental data is good. In particular, PO_1 conversion proceeds very fast according to the data, that is well matched by the model. This hinders the PO_x lumped species to form, that is in contrast to the photooxygenation experiments, where higher extents of PO_x are obtained. IM_{2c}, the major

intermediate, is very rapidly built up, and slightly less rapidly converted to ART. Despite the high rate of ART formation mass transfer limitations are not detected in Figure 5.17b, where the liquid oxygen concentration $O_{2,l}$ does not drop significantly. Figure 5.17a suggests that the model slightly underestimates the ART formation in the beginning. The same underestimation is observed for the byproduct BP_3, that has been as well observed in the previous Section, Figure 5.14.

Please note that without the introduction of a separate intermediate in the batch case (IM_{2b}) and the refinement resulting in the omission of IM_3, BP_4 was significantly overestimated in previously developed model candidates despite the short occurrence of IM_2. This observation is the major reason why two separate intermediate species in the network are required to reproduce both the continuous and the batch experimental data. In the continuous experiments on the other hand, dropping IM_3 would result in an enhanced formation of BP_4 in the continuous experiments that is not covered by the experimental data. Therefore, the different byproduct BP_5 is introduced that forms in parallel to ART capturing the non-measured and unknown species in the reaction network.

The process behavior in the continuous reactor at a low and a high TFA concentration is shown in Figure 5.18. The gray vertical lines in the Figures mark the photo reactor outlet and the synthesis reactor inlet. Note that a temperature jump from $-20\,°C$ to room temperature occurs at the photo reactor outlet (first gray vertical line), causing a rise in the gas flow and the liquid oxygen concentration. At the synthesis reactor inlet (second gray vertical line) TFA is added, that results in concentration drops of the reaction species in the liquid phase. The consequences of the different TFA concentrations are clearly visible in the graphs. PO_1 continuously converts at the low TFA concentration, Figure 5.18a, but immediately disappears at the high TFA concentration, Figure 5.18b. Accordingly, IM_{2c} does not fully convert in the former case, but is totally consumed
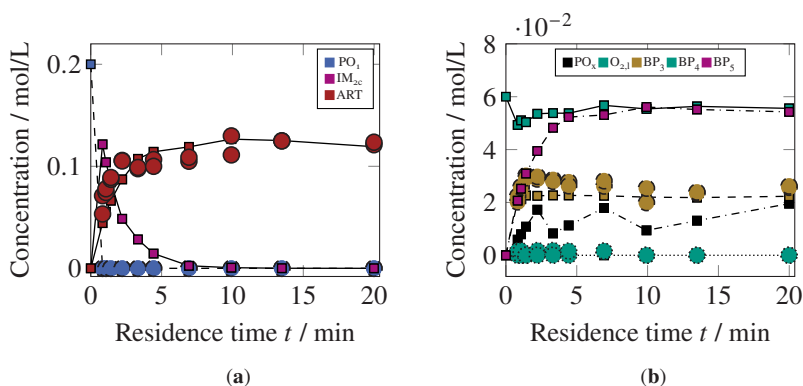

(a)

(b)

Figure 5.17: Time profiles of concentrations for continuous experiments at TFA = 0.25 mol/l. The simulations (square) and data (circle) are points at the synthesis reactor outlet. Hence, the time-resolved graphs origin from different experiments. The actual residence times were calculated from the simulations.
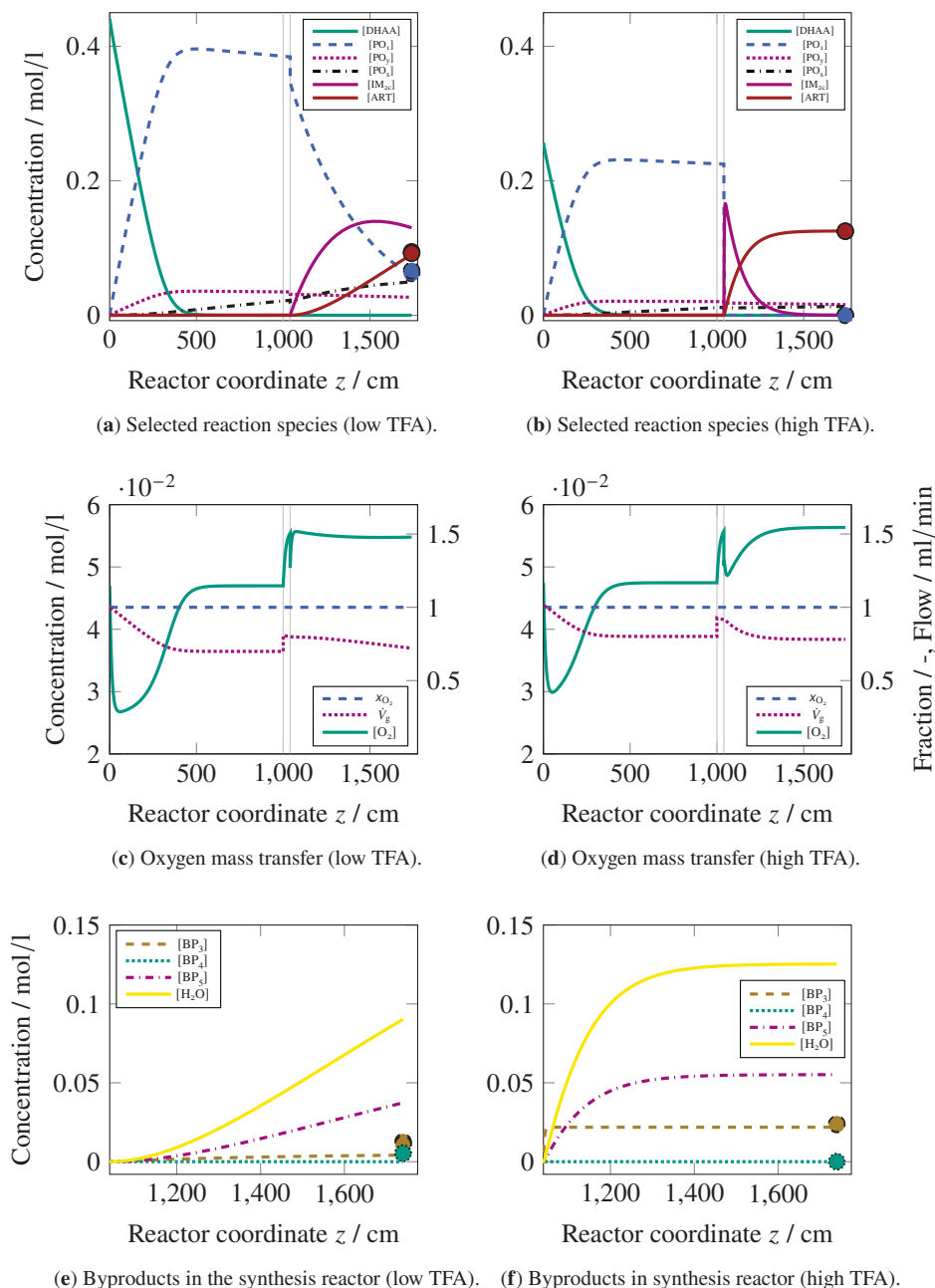
(**a**) Selected reaction species (low TFA).

(**b**) Selected reaction species (high TFA).

(**c**) Oxygen mass transfer (low TFA).

(**d**) Oxygen mass transfer (high TFA).

(**e**) Byproducts in the synthesis reactor (low TFA).

(**f**) Byproducts in synthesis reactor (high TFA).

Figure 5.18: Propagation of concentrations, oxygen molar fraction and gas flow along the reactor coordinate at low (left) and high (right) TFA concentration. Conditions: (low) $[TFA]_0$=0.033 mol/l, $[DHAA]_0$=0.44 mol/l, $[DCA]$=0.85 mmol/l, P_{LED}=97 %LED, $x_{O_2,0}$=1; (high) $[TFA]_0$=0.25 mol/l, $[DHAA]_0$=0.26 mol/l, $[DCA]$=0.85 mmol/l, P_{LED}=100 %LED, $x_{O_2,0}$=1. The first thin vertical line marks the photoreactor outlet. The second thin vertical line marks the synthesis reactor inlet. Experimental data points are plotted as circles.

in the latter case, resulting in a phase with constant concentration before leaving the reaction line. The volumetric gas flow very slowly decreases at the low TFA concentration, Figure 5.18c. The liquid oxygen concentration does therefore not show any sign of supply problems or mass transfer limitations. Even at high TFA concentrations, Figure 5.18d, the dissolved oxygen does not come close to issues related to limiting mass transfer from the gas to the liquid phase.

In total, the process behavior predicted by the developed model agrees well with the experimental data, for both low and high TFA concentrations. In contrast to the photooxygenation, the model does not show mass transfer limitations despite a fast formation of ART. In a last step of the model-based analysis of the process behavior, a global sensitivity study of all operational and uncertain model parameters is performed for fixed lengths of the photo and synthesis reactor in the following Section.

5.5.7 Global Sensitivity Analysis of the Overall Process Model

A GSA on the key concentrations PO_1, O_2 and ART is performed to analyze the influence of the most important process parameters and their interactions. Since the model parameters are as well uncertain, they are also considered in the GSA as previously done in the GSA for the photooxygenation, Section 4.3.10. The uniform distributions for the process parameters, whose limits cover the design space of the performed experiments, are

$$\dot{V}_l \sim \mathcal{U}(0.1, 0.4),$$
$$[TFA]_0 \sim \mathcal{U}(0.0, 0.4),$$
$$[DHAA]_0 \sim \mathcal{U}(0.0, 0.5),$$
$$x_{O_2} \sim \mathcal{U}(0.0, 1.0),$$
$$[DCA] \sim \mathcal{U}(0.0, 0.85 \times 10^{-3}),$$
$$P_{LED} \sim \mathcal{U}(0.0, 100.0).$$

$$(5.8)$$

The Normal distributions of the uncertain model parameters follow from the estimated parameter values, and are listed in Equation (C.22) in the Appendix. The photoreactor and the synthesis reactor are directly connected in series, and their corresponding lengths are 400 cm and 620 cm, respectively, the most common dimensions used in the performed experiments.

The sensitivities over the full reactor system are shown in Figure 5.19. The following discussion focuses on the sensitivities in the synthesis reactor, i.e., after 400 cm. For a discussion about sensitivities during the photooxygenation, see the corresponding GSA in Section 4.3.10. Analogous to the results from the GSA of the photo reactor, the model parameters have only a low impact.
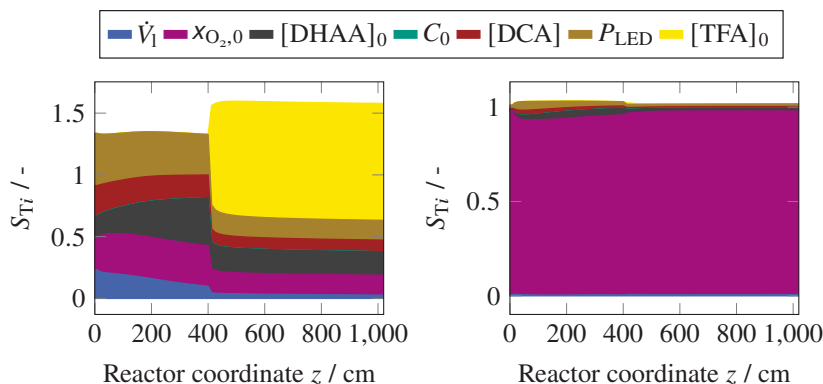
(**a**) Sensitivities on PO_1 concentration.   (**b**) Sensitivities on dissolved O_2 concentration.
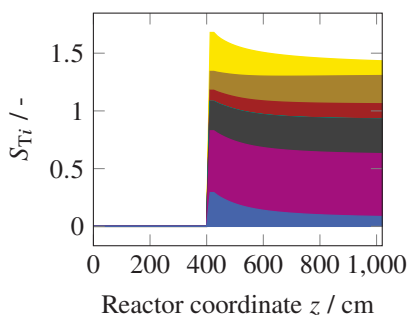
(**c**) Sensitivities on ART concentration.

Figure 5.19: Global sensitivity analysis (GSA) of process parameters on selected liquid concentrations along the reactor coordinate. The interface between photo and synthesis reactor is at 400 cm. Thus the results from the photo reactor are quantitatively equal to the GSA of the photo reactor, Figure 4.17. Sensitivities below 1×10^{-3} are not shown in the plots.

Among the model parameters, C_0 has the most influence, but is barely visible in the graphs in Figure 5.19. The largest sensitivities are therefore rooted in the process parameters, Equation (5.8).

The sensitivities on the dissolved O_2 concentration, Figure 5.19b, are almost exclusively dominated by x_{O_2}, which also causes the sum of total indices to be around unity. In contrast, the total effects on the PO_1 and ART concentration considerably exceed 1, rather approximately 1.5, suggesting that higher order effects are present. For the PO_1 concentration, Figure 5.19a, the TFA concentration is by far the most sensitive parameter. The reason is the significant importance of the acid concentration on the depletion of PO_1 that also resulted in a high reaction order during the parameter estimation. The least influential parameter on the PO_1 concentration is the volumetric

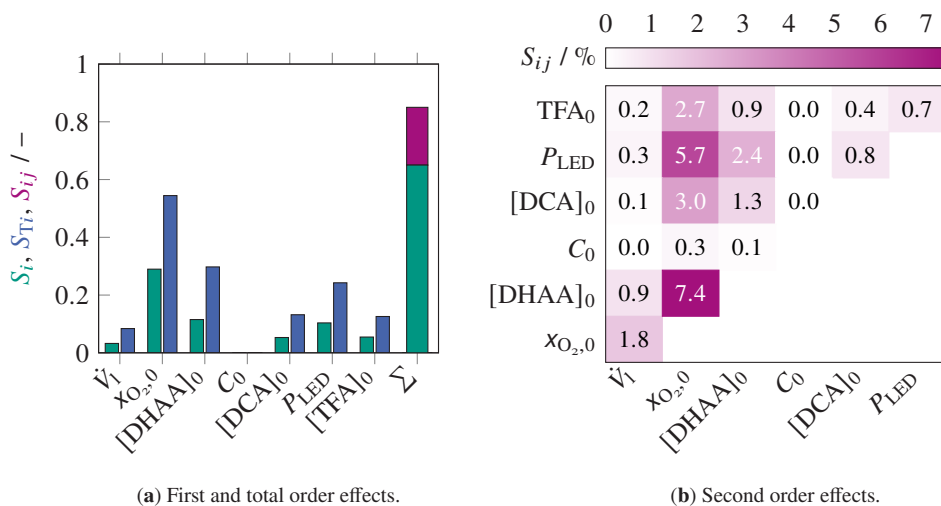(**a**) First and total order effects.   (**b**) Second order effects.

Figure 5.20: Global sensitivity analysis of most important process parameters on the ART concentration at the synthesis reaction line outlet, i.e., the sensitivities correspond to the final reactor coordinate point on the right side of Figure 5.19c. Sensitivities below 1×10^{-3} are not shown in the plots.

flow, that is linked to the fact, that all of the parameters do not change their influence along the synthesis reactor coordinate, since the depletion of PO_1 is extremely fast and happens therefore mainly at the synthesis reactor inlet. For the ART concentration the picture changes. The most influential parameter is the initial molar oxygen fraction $x_{O_2,0}$, that emphasizes the double oxygen dependence of the ART formation from DHAA to ART, see the mechanism in Figure 5.1. The relative influence of TFA decreases over the reactor coordinate because the by TFA most affected reaction, the PO_1 depletion, is most pronounced at the inlet of the synthesis reactor.

To inspect the higher order effects, sensitivities on the ART concentration at the synthesis reactor outlet are shown in Figure 5.20. In general, all of the operational parameters have higher order effects around the same magnitude as their first order ones, Figure 5.20a. Remarkably, there must be at least third order effects present, because the sum of the first and second order effects does not add up to unity, but rather to approximately 0.8. This means, there are considerable effects on the ART concentration, that are caused by the interplay between at least three process parameters. In Figure 5.20b, it can be noted that O_2 and DHAA show the largest interactions.

For an operation of the continuous reactor, the GSA shows that the main factors are the added TFA catalyst and the initial molar fraction of oxygen in the gas phase. The former significantly influences the PO_1 concentration, and the latter almost exclusively dominates the dissolved oxygen and for a great part the formed ART. Notably, the process is complex to steer as almost 40 % of the spread in the ART concentration at the reactor outlet is caused by higher order effects with a significant contribution by interactions between at least three process parameters. Considering the

same parameters and distributions as for the GSA in this Section, Equations (5.8) and (C.22), the identified process model will be applied to a model-based optimization study targeting artemisinin yields under uncertainty in the next Section.

5.5.8 Optimizing the Artemisinin Production

First, the results for the nominal settings of the process optimization, i.e., without the consideration of parametric uncertainties, in Table 5.6 are analyzed. The corresponding optimized process

Table 5.6: Results of different nominal settings for process optimization. An 'x' in the 'TFA feed' column indicates that TFA is used as feed to the photo reactor instead of being dosed at the synthesis reactor inlet. If 'Reac. design' is marked with 'x', the lengths of both the photooxygenation and the synthesis section are added to the vector of design variables. The initial DHAA concentration in the fourth column refers to its lower bound during optimization. The green font coloring specifies the target of the objective function, either the yield or the space-time yield.

#	TFA feed	Reac. design	$> [DHAA]_0$ / mol/l	Y / %	STY / mol/(l d)	Normed $\mathbb{E}[STY]$	Normed $\mathbb{V}[STY]$	τ / min
1			0.0001	53.7	0.00	0.00	0.00	23.9
2			0.2	53.5	1.64	0.07	0.00	26.9
3		x	0.0001	55.4	0.00	0.00	0.00	58.9
4		x	0.05	55.2	0.19	0.01	0.00	51.6
5		x	0.2	54.7	0.97	0.04	0.00	47.0
6		x	0.4	54.1	2.61	0.12	0.00	46.4
7	x		0.0001	61.0	0.00	0.00	0.00	31.2
8	x		0.05	60.8	0.25	0.01	0.00	38.8
9	x	x	0.0001	62.1	0.00	0.00	0.00	61.1
10	x	x	0.05	61.9	0.17	0.01	0.00	60.4
11	x	x	0.2	61.3	0.91	0.04	0.00	53.2
12			0.0001	43.3	8.61	0.39	0.13	13.8
13		x	0.0001	33.8	22.31	1.00	1.00	3.8
14	x		0.0001	47.5	8.50	0.38	0.13	14.4
15	x	x	0.0001	35.6	27.40	1.23	1.80	3.1

parameters are given in Table C.9 in the Appendix. Three different options are investigated, see Section 5.4.2: i) TFA is added at the synthesis reactor inlet with fixed reactor lengths (default); ii) the reactor lengths of the photo reactor and the synthesis reactor can be varied; iii) TFA is dosed to the feed of the photo reactor instead of added at the synthesis reactor inlet. Please note

that the rows 1 to 11 are optimizations with respect to the yield, and the trailing rows with respect to the space-time yield (compare with green background color).

The results clearly show that an optimization of the yield gives a very poor space-time yield, and is therefore of little relevance for an industrial realization. Constraining the lower bound on the initial DHAA concentration results in some increase in space-time yields, but corresponding values do not exceed 3 mol/(l d). For the default case in row 1, the ART yield is approximately 54 %. Interestingly, an increase in the lower bound of the initial DHAA concentration does not significantly decrease the yield. This can be observed for all other yield optimizations likewise. The largest improvement is achieved when the TFA mode is switched to TFA feeding, that is, TFA is fed together with the other material at the photoreactor inlet. Yields then reach around 62 %, see rows 7 to 11. This is in accordance with experiments that have been performed with TFA feeding [61], and with literature values reported [63]. On the other hand, the effect of optimizing reactor lengths is negligible, which is once more a consequence of optimizing with respect to the yield.

For the optimizations with respect to space-time yield, designing the reactor drastically increases the space-time yields from around 9 mol/(l d) to approximately 22 mol/(l d) when TFA is fed at the synthesis reactor inlet. At the same time, the ART yield drops by almost 10 percentage points to circa 34 %. Residence times are significantly lower by contrast with the optimizations targeting the ART yield. Converted to mass, 6.3 g/(ml d) ART ($M_{\mathrm{ART}} = 282.34$ g/mol) can be produced at a residence time of 3.8 min. Compared with the reported value of 3.5 g/(ml d) in a similar setup [63], this is almost a 2-fold increase. A further significant increase in space-time yield is achieved when TFA is added to the feed stream of the photo reactor and the reactor lengths are designed, resulting in an *STY* of more than 27 mol/(l d) (7.7 g/(ml d)) while maintaining a yield of 35.6 %. Hence, the option to add TFA to the feed of the photo reactor and to design the reactor lengths offers the best conditions for production operation. The corresponding optimized process parameters of case 15 rounded to two decimal places are

$$
\begin{aligned}
\dot{V}_{\mathrm{l}} &= 0.4 \, \mathrm{ml/min}, \\
[\mathrm{DCA}]_0 &= 0.85 \, \mathrm{mmol/l}, \\
P_{\mathrm{LED}} &= 100 \, \%, \\
x_{\mathrm{O_2},0} &= 1.0 \\
[\mathrm{DHAA}]_0 &= 0.5 \, \mathrm{mol/l}, \\
[\mathrm{TFA}]_0 &= 0.4 \, \mathrm{mol/l}, \\
l_{\mathrm{photo}} &= 7.45 \, \mathrm{m}, \\
l_{\mathrm{syn}} &= 0.0 \, \mathrm{m}.
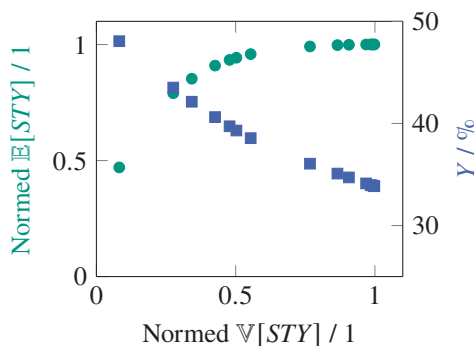\end{aligned}
\tag{5.9}
$$

Figure 5.21: Pareto optimal points of the space time yield for the robust settings (circles: space-time yield, squares: yield). Variance and expectation of the space-time yield are normalized to the optimal deterministic case, see Table 5.6. The different points are a consequence of changing λ in Equation (5.3) in the range from 1×10^{-5} to 0.1.

All process parameters apart from the reactor lengths are at their upper limits considered during optimization, and the synthesis reactor is obsolete.

To compare with the robust optimization setting, optimization case 13 is considered, because the developed process model in this Chapter has been identified from experimental runs that added TFA at the synthesis reactor inlet. The optimized process parameters of the optimization case 13 are equal to the optimized parameters in Equation (5.9) with the exceptions of the optimized reactor lengths: l_{photo}=4.88 m and l_{syn}=1.19 m. Uncertainty quantifications for the space-time yields of the nominal settings are given in the last two columns in Table 5.6, where the expected value and the variance are normalized to the reference case 13. The standard deviation of the variance of the space-time yield for the reference case is approximately 0.87 mol/(l d), that is quite narrow for a space-time yield of around 22 mmol/(l d). Once more, this underlines the robustness of the identified process model.

The results for the robust setting, i.e., the optimization under parametric uncertainty for the parameter distributions in Equation (C.22) in the Appendix, are shown in Figure 5.21. The reference case from the nominal setting can be relocated for a normed variance of unity on the abscissa, yielding a normed expected value of 1 (green point) and an ART yield of 33.8 %, compare with row 13 in the Table 5.6. Yields and space-time yields have monotonous, but opposite trends. An increase in the space-time yield, i.e., following the green points in increasing direction, comes at the cost of a reduced ART yield (blue squared) and of a larger variance (increasing abscissa values), a trend that can be observed in the Table 5.6 likewise. Naturally, the space-time yield in the robust optimization cannot exceed its counterpart in the nominal setting, that is, a normalized expectation of the space-time yield above 1 is not possible as shown in the Figure 5.21. If the variance of the space-time yield is to be reduced by half compared with the reference case 13, the space-time yield drops by 6 % and the yield increases to 39 %. The

corresponding experimental settings are again equal to the ones given in Equation (5.9) with the following deviations: l_{photo}=5.83 m and l_{syn}=1.48 m. A further decrease in uncertainty of the space-time yield results in an increase of the reactor lengths and a lowering of all other experimental settings apart from the initial molar oxygen fraction that stays constant, see Table C.10 in the Appendix.

5.6 Conclusion

The reaction network of the acid-catalyzed sequence is based on several simplifications, and was developed for purified dihydroartemisinic acid in toluene catalyzed by 9,10-dicyanoanthracene and trifluoroacetic acid. The identified kinetic constants are valid only at the investigated temperature of 20 °C. To increase the predictive power of the identified process model, a more thorough understanding of the reaction mechanisms in the acid-catalyzed sequence is required. As the developed model and the model-based analysis have shown, the influence of the acidic environment plays a crucial part. The model assumes that the acid completely dissolves in the solvent, keeping a constant concentration over the course of the reactions. However, interactions that alter the acid activity are possible, and probably likely. The formation of water might on the one hand influence reaction kinetics and on the other hand bind H^+ ions, thereby removing them from the organic to a separate aqueous phase. The dissolution equilibrium of H^+ in toluene will provide valuable insight into the acid activity of TFA in the solvent. The interference of other present species with H^+ was modeled by simple approaches, and despite having shown no improvements in the model-data fit, a more mechanistic approach in this dimension might also be beneficial. The extension to other temperature areas will not solely give additional insight, but might be helpful for the identification of the occurring kinetics and the associated model parameters. In contrast to the photooxygenation experiments, nitrogen has not been present in the gas phase. Conclusions drawn from the developed model for different gas phase compositions must be handled with care. Experiments with varying gas phase compositions are therefore necessary, in particular runs with pure nitrogen should be targeted to suppress part of the reaction network, similar as happened in the batch experiments. Gas phase measurements are a further add-on, in particular if the volumetric gas flow is measured in dynamic mode.

To facilitate process design and optimization, a reliable process model is a valuable tool. For the semi-synthesis of artemisinin from dihydroartemisinic acid, a process model was identified, that explains the major physical interactions with good predictive power as a result of the applied systematic model identification strategy. In the photooxygenation step, deviations between the experimental data and the model predictions for the main hydroperoxide PO_1 were 7.3 % on average, where a wide range of critical process parameters was investigated. The assumptions

incorporated in the developed process model can explain the main process characteristics. However, one must be aware of its strong simplifications: (i) the application of the drift flux model neglecting local effects at the two-phase interface, (ii) the omission of both a momentum and an energy balance, and (iii) assuming a spatially independent rate of photon absorption, that resulted in a large value for the optical path length. The developed model was used for the identification of different operating regimes, limited by either absorbed photon flux, substrate concentration, or mass transfer.

In the acid-catalyzed sequence, different model candidates for the reaction network were proposed, where between 24 to 76 % of the reaction products formed could be identified in the experiments. Major finding from the model selection problem was that the acid concentration plays a key role. Model candidates including either high H^+ reaction orders or intermediate steps with H^+ consumption could satisfactorily reproduce the experimental data. The selected final model has high H^+ reaction orders exceeding 2 and different intermediates for an oxygen-rich and an oxygen-absent atmosphere. Relative deviation for artemisinin is 14 % on average. A sensitivity analysis confirmed the importance of the role of the acid catalyst, and indicated that the initial molar fraction of oxygen is another very important process factor. Process optimizations resulted in ART yields around 55 % and in an ART space-time yield of 22 mmol/(l min) (6.3 g/(ml d)) in the applied reactor setup.

6 Differential Flatness for Model Identification

Established methods for model identification reveal limitations when confronted with high non-linearities, significant uncertainties, or the automatic identification of a model from a set of candidates. In particular, the widely used comparison of measurement data with predicted model outcomes by integration of the underlying system of differential equations works well in many application cases, see Chapters 4 and 5, but might lead to sub-optimal or misleading results in identification tasks. Based on these experiences, novel approaches to model identification are an active research field. In this Chapter, a promising alternative for model identification is proposed, that is based on an inverse modeling approach utilizing the concept of differential flatness. The problem of selecting a model from a set of different model candidates for a pharma-related biocatalytic reaction network is considered. After an introduction about the current state of research considering enhanced methods for model identification, the mathematical fundamentals for inverse modelling and differential flatness are presented. Following, the study case is introduced and the differential flatness strategy for the model selection problem is put into action. Here, a nominal situation is compared to a setting under parametric uncertainty – with and without model-based design of experiments.

Contents of this chapter including Tables and Figures have been published in [110].

6.1 Introduction

The model-based design of experiments (MBDoE) approach frequently aims for optimal control actions, Section 3.7, where commonly used numerical methods give rise to nonlinear programming problems that need substantial amounts of computational time and efficient solvers [251]. Moreover, robustification against model parameter uncertainties further complicates the problem, as statistical quantities must be considered when solving the underlying optimization problem. In addition to the actual MBDoE optimization framework and data acquisition, recent studies have shown that a well-posed parameter identification and model selection problem is equally important [45, 169, 252]. In this context, the consideration of input residuals in parameter estimation

beyond the classical approach of output residuals has drawn attention in the literature [45, 169, 253–255]. The idea of assigning errors to all variables, i.e., including the independent variables, dates back to the 1940s [256], where the term total least squares for linear systems was coined in 1979 [257, 258]. In many engineering problems as in pharmaceutical synthesis, independent variables in general exhibit randomness, that should therefore be taken care of during parameter estimation [253]. Moreover, it can be shown that the existence of errors in model inputs can cause a biased least squares estimator [256].

Several of the developed strategies have in common that they release themselves from integrating the model dynamics, but propose functional relations for the model predictions or controls and constrain these relations by the model dynamics. Reasons are manifold, e.g., parallel parameter estimation and data reconciliation [256], avoidance of numerical integration [254], or conversion to optimization formulations that can be solved by efficient algorithms [206]. A well-established representative is collocation within the framework of dynamic optimization, where the original problem is transferred to a large non-linear programming (NLP) problem that can be efficiently solved with available large-scale NLP solvers [45, 47]. McAuley and co-workers have proposed the use of B-splines in an extended version of principal differential analysis (PDA) to fit B-spline curves to the observed data, called iteratively refined PDA (iPDA) [46]. Currently, neural networks are gaining attention, where the model predictions are replaced by neural networks resulting in physics-informed neural networks (PINNs) [44]. In contrast to collocation, iPDA, and PINNs, the application of an inverse model inherently considers the model dynamics, that makes it able to precisely back-calculate the inputs of the model for a given system trajectory.

For an effective solution to the robust model selection problem, an inverse modeling technique by using the differential flatness concept [259] is implemented in this Chapter. In systems theory, differential flatness implies that analytical expressions of the system's states and controls exist that are functions of so-called flat outputs and their derivatives. Hence, by implementing a differential flatness strategy to solve an MBDoE problem, solving differential and sensitivity equations numerically is avoided as required by standard control vector parameterization strategies for model selection. Moreover, differential flatness enables straightforward feed-forward control, and eases optimization problems by smoothing objective functions and providing analytic gradient and hessian functions [49, 50]. Please also note that while optimizing the flat output trajectory, the number of continuous optimization variables is reduced to the number of flat outputs, i.e., an additional reduction of computational costs as compared to standard nonlinear programming techniques with control and state variable discretization [205]. Methods based on differential flatness have been heavily used in research and industry – primarily in the design of open-loop controllers and the planning of state trajectories in (electro)mechanical systems [260]. In the case of the MBDoE technique, strategies exploiting differential flatness have barely been considered [253, 254, 261, 262], and, following a thorough search of the relevant literature, have not been applied

to model selection problems under uncertainty before, Figure 6.1. Thus, this study addresses two open research challenges: (i) to apply the flatness concept to multi-model problems, and (ii) to integrate parameter uncertainties into the flatness-based optimization problem for robust model selection. In detail, the aim is to discard inappropriate model candidates from a set of competing model hypotheses. To this end, it first must be shown that the considered model candidates satisfy the differential flatness condition, and second an optimization problem under uncertainty has to be solved that makes use of the flatness property. For the sake of illustration, a biocatalytic process from a carboligation reaction system is considered that forms an essential precursor in the synthesis of natural products and pharmaceuticals [263]. Please note that carbon-carbon bond-forming reactions are the backbone of numerous high-value molecules in industrial organic synthesis. However, biocatalytic production of the related bulk and fine chemicals and active pharmaceutical ingredients is insufficiently explored today. Therefore, the application of enzymes in organic synthesis is currently an important research topic to exploit the significant potential of improving manufacturing processes in the chemical and pharmaceutical industry under the agenda of green chemistry [264, 265]. An essential problem with all mathematical models and model-based design concepts, including MBDoE, is the uncertainty in model parameters. To ensure reliable inferences, parametric uncertainty should be taken into account in the MBDoE approach [29, 168–170]. In general, probability-based concepts have attracted considerable attention in robust optimization. In the literature, between classical and Bayesian settings for handling model predictive errors as a potential consequence of uncertain model parameters can be distinguished. In the former, the strategies have in common that the model output differences in the objective function are weighted by an error covariance matrix of the model prediction to avoid experimental regions where model predictions are poor [121, 266–268]. One drawback of these strategies is that the prediction error covariance matrix is calculated from local sensitivities, where designs of experiments for local sensitivities might provide misleading information compared to designs based on global sensitivities [166], see Sections 3.5.1 and 3.6. On the other hand, Bayesian model selection with consideration of parametric uncertainties requires the determination of computationally expensive integrals [148, 172], Section 3.6.1. In this context, an efficient and effective rule to determine statistical moments circumventing a local approximation, namely the point estimate method (PEM), is proposed, that diminishes this computational burden. The PEM has been introduced in Section 3.6.1.

6.2 Inverse Modeling

As opposed to solving the ODE system (Equation (3.5a)) in a forward manner to conventionally exploit the outputs y given the inputs u, inverse modeling aims at reconstructing the inputs u for given outputs y [27, 269]. Please note that the process of inverse simulation is not to be confused
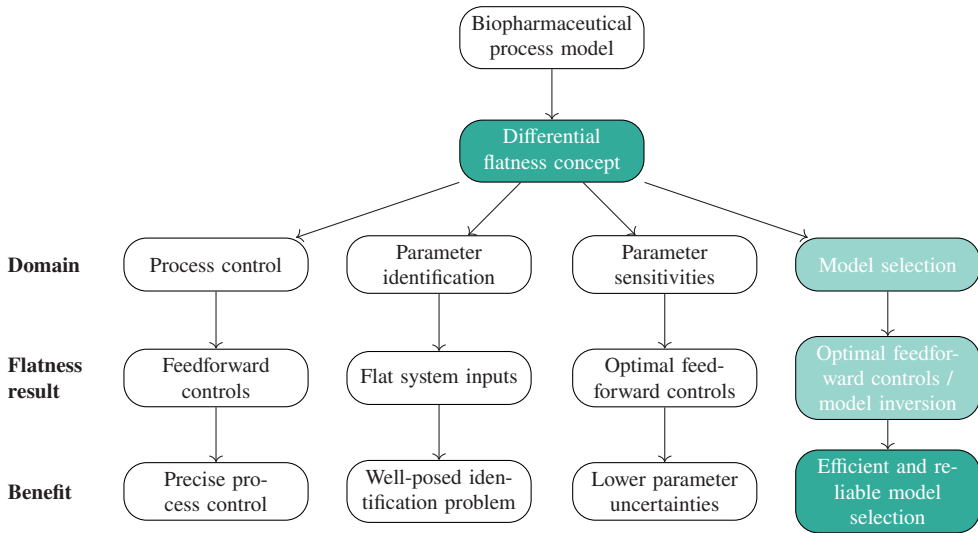
Figure 6.1: Possible applications for the application of differential flatness strategies. The vast majority of differential flatness approaches has been used for process control and trajectory planning. To our knowledge, the in this thesis developed model-based design of experiments strategy, that exploits differential flatness, (blue colored route), has not been applied before in literature.

with inverse problems, where in the latter the goal is to estimate unknown model parameters $\hat{\theta}$ [27]. The different principles of forward simulation, inverse modeling, and the inverse problem of parameter identification are visualized in Figure 6.2.

In addition to numerical inversion approaches as model inversion- or inverse simulation-based techniques [270], algebraic methods have been proposed for inverse modeling [50], among which strategies based on differential flatness are important representatives.

6.2.1 Differential Flatness

In systems theory, within the context of algebraic model inversion techniques and aiming at feedforward control problems, differential flatness was introduced by Fliess et al. [259] in 1992.
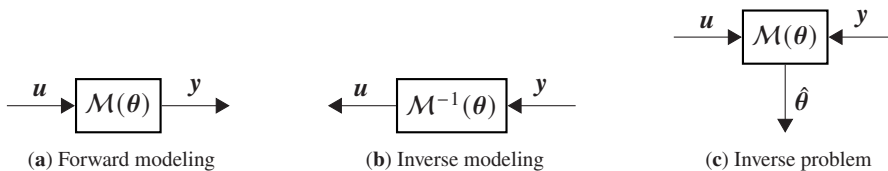

Figure 6.2: Illustration of the different principles of a standard process simulation configuration (**a**), the inverse modeling setting to reconstruct system inputs (**b**), and the inverse problem for parameter identification (**c**).

A (non-)linear process model (Equations (3.5a) and (3.5c)) is called differentially flat or shortly flat if there exists an output vector

$$\boldsymbol{\gamma} = \boldsymbol{h}^{\text{flat}}(\boldsymbol{x}, \boldsymbol{u}, \dot{\boldsymbol{u}}, \ldots, \boldsymbol{u}^{(s)}, \boldsymbol{\theta}), \tag{6.1}$$

with a finite value $s \in \mathbb{N}$ and the smooth mapping function $\boldsymbol{h}^{\text{flat}} : \mathbb{R}^{n_x} \times (\mathbb{R}^{n_u})^{s+1} \times \mathbb{R}^{n_\theta} \to \mathbb{R}^q$, referred to as a flat output which fulfills the following conditions:

1. The states and the controls can be described as a function of the flat output and its derivatives:

$$\boldsymbol{x} = \boldsymbol{\Psi}_x(\boldsymbol{\gamma}, \dot{\boldsymbol{\gamma}}, \ldots, \boldsymbol{\gamma}^{(r)}, \boldsymbol{\theta}), \tag{6.2}$$
$$\boldsymbol{u} = \boldsymbol{\Psi}_u(\boldsymbol{\gamma}, \dot{\boldsymbol{\gamma}}, \ldots, \boldsymbol{\gamma}^{(r+1)}, \boldsymbol{\theta}), \tag{6.3}$$

with the smooth mapping functions $\boldsymbol{\Psi}_x : (\mathbb{R}^{n_u})^{r+1} \times \mathbb{R}^{n_\theta} \to \mathbb{R}^{n_x}$ and $\boldsymbol{\Psi}_u : (\mathbb{R}^{n_u})^{r+2} \times \mathbb{R}^{n_\theta} \to \mathbb{R}^{n_u}$.

2. The dimensions of the control and the flat output vector are equal:

$$\dim \boldsymbol{\gamma} = \dim \boldsymbol{u}. \tag{6.4}$$

Here, $r \in \mathbb{N}$ specifies the number of occurring derivatives. Generally speaking, r is not known beforehand, apart from single-input single-output (SISO) systems, where $r = n - 1$ [271]. There is an infinite number of flat output candidates, and often, they are a function of the states only [271]—similar to the fact that the real output function of a dynamic system is, in many cases, exclusively a function of the states.

Flat outputs might have no direct physical meaning, or they might be identical to measurable quantities; then also referred to as flat inputs [272]. Moreover, between local and global flatness must be distinguished, where for the local form, the differential flatness is valid only for a restricted domain bound by occurring singularities [273]. For certain kinds of singularities, a globally flat system can be designed following a superposition concept. To this end, individual local model inversion domains are created from different local flat outputs where the union of the local domains provides a global framework for the flatness-based model inversion [273]. Alternatively, a transformation approach exists to bypass points of a singularity [274]. In addition to differential flatness of ODE systems, flatness-based methods are also being used for discrete-time systems and partial differential equations (PDEs); see [275–277], and references within. Application scenarios based on differential flatness cover predominantly (electro)mechanical problems, but also process technologies like heat exchangers [278], crystallizers [279] or (bio)reactors [276, 280], lithium-ion batteries [281], and more.

In general, the class of dynamic systems, that are differentially flat by their definitions, i.e., their states and controls can be recovered according to the conditions of differential flatness, is limited. For example, all controllable linear or state feedback linearizable systems are differentially flat [282]. An overview of differentially flat and non-flat mechanical systems is given in [282]. In contrast, industrial chemical processes having many states and few controls are usually not flat [283]. However, differentially non-flat dynamic systems can be in general made differentially flat [283]. A straightforward approach is to increase the number of control variables, that is, to add fictive control variables to the dynamic systems' real controls. This intuitive strategy exploits the tendency of a dynamic systems becoming differentially flat with an increasing number of controls [284]. The drawback of this method is that the fictive control variables have to be forced to vanish in the considered optimization problem, i.e., additional constraints are introduced. This endeavor is numerically very challenging and strongly depends on the underlying differential equations of the dynamic system under study [283].

6.2.2 Flat Output Identification

To implement a flatness-based concept, two key challenges exist: First, determining if a system is differentially flat, and second, constructing a flat output alternatively. There is no general method for either of those challenges. However, exceptions exist, and include systems that are linearizable by static feedback control, which are flat by definition. Considering a linear system, controllability conditions differential flatness and vice versa [274]. Methods of determining flat outputs and the mapping function h^{flat}, respectively, are currently being researched, and the interested reader is referred to [260, 285, 286] and the references therein. Moreover, the construction of so-called flat inputs (i.e., reconstructed inputs based on the given output function (Equation (3.5c))) was shown for SISO systems and a limited set of multi-input and multi-output (MIMO) cases [287].

Alternatively, in systems theory, valuable information about system characterization based on the interaction of inputs, system states and outputs can also be extracted from graph theory [50, 288, 289]. Typically, observability or controllability measures are derived for (non)linear state-space models using directed graphs (digraphs) [290–292]. A digraph $D = [V, E]$ with $n_x + n_u + n_y$ vertices $v_i \in V$ and edges $e \in E$ can be constructed from adjacency matrices A_u, A_x, and A_y of the process model for the inputs, system states, and outputs, respectively. The $a_{i,j}$-th element of A_x or A_u is set to 1 if derivatives $\frac{\partial f_{x,i}(\boldsymbol{x},\boldsymbol{u})}{\partial x_j}$ or $\frac{\partial f_{x,i}(\boldsymbol{x},\boldsymbol{u})}{\partial u_j}$ exist, respectively, and to 0 if this is not the case. If these derivatives exist (i.e., $\partial f_{x,i}/\partial x_j \neq 0$ or $\partial f_{x,i}/\partial u_j \neq 0$), then there is an edge from vertex v_j to vertex v_i. Analogously, the adjacency matrix for the outputs $\boldsymbol{y}$ and the output function $\boldsymbol{f}_y(\boldsymbol{x}, \boldsymbol{u})$ can be defined. Regarding the flatness property, in the paper by Csercsik et al. [289], an algorithm for flatness analysis of MIMO systems is introduced that uses an *explicit expressibility graph*. Please note that from a given digraph, the explicit expressibility graph is

formed with reversed edge directions, with the outputs replaced by the flat outputs, and with the self-loop system states dependencies omitted. The following theorem then gives a necessary condition for differential flatness based on the adjacency matrices A_u, A_x, and A_y [289].

Theorem 1 *For a prospective set of flat output-input pairs, m pairwise disjoint paths must exist in the explicit expressibility graph, the union of which covers each vertex of the graph.*

In summary, existing construction methods are often restrictive and require cumbersome calculations. In practice, for the identification of flat outputs (Equation (6.1)) a sequential strategy including an expert guessing for a flat output candidate followed by a subsequent validation step in terms of Equations (6.2)-(6.4) has proven favorable. This trial-and-error approach is facilitated by two facts. First, numerous technical systems are indeed flat systems. Second, frequently, comparable to Lyapunov functions in control theory, informative flat outputs have physical signification [271]. Once the flat output configuration is identified, the flat output functions y^{flat} must be parameterized using for instance spline functions.

6.2.3 Basis Splines

The flat outputs γ have to be parameterized while limited by the fact that they have to satisfy solutions of the dynamic system (Equations (3.5a) and (3.5c)). For flat outputs, basis functions from a large set of possibilities, ranging from simple polynomials to more complex functions, can be chosen. Basis splines, i.e., piece-wise polynomial functions also known as B-splines, offer great freedom of action, are flexible and well-studied, and libraries for their usage are implemented in many different programming languages [293]. The classical application of splines is the approximation and interpolation of data points.

A flat output based on B-splines is defined by

$$\gamma(t) = \sum_{i=1}^{l} \tilde{\theta}_i B_{i,k}(t), \tag{6.5}$$

where $B_{i,k}$ are B-splines of order k on l collocation points, and $\tilde{\theta}$ is a coefficient vector, whose elements are referred to as meta-parameters to distinguish them from model parameters θ, Equation (3.1). Please note that the meta-parameters $\tilde{\theta}_i$ constitute the decision variables in the flatness-based optimal experimental design framework for model selection, which is introduced in the following Section.

6.3 Flatness-Based Robust Design of Experiments for Model Selection

In contrast to the MBDoE problems in Chapter 4, the proposed flatness-based approach for the MBDoE literally operates in an inverse manner. Optimized flat output trajectories maximize the difference between the model outputs of the competing model candidates. The related controls u and the initial states x_0 are reconstructed from the flat model $\mathcal{M}^{-1}$ and have to be identical for all model candidates and their optimized flat outputs γ. Using the Euclidean distance as a discrepancy measure between model outputs and assuming M model candidates, the original optimal control problem given in Equation (3.65) becomes

$$
\begin{aligned}
\max_{\gamma} \quad & \int_{t_0}^{t_{\mathrm{f}}} \sum_{i=1}^{M-1} \sum_{j=i+1}^{M} \Big[y_i(\gamma_i, \dot{\gamma}_i, \dots, \gamma_i^{(r_i)}) \\
& \qquad - y_j(\gamma_j, \dot{\gamma}_j, \dots, \gamma_j^{(r_j)}) \Big]^2 \, \mathrm{d}t \\
\text{s.t.} \quad & \Delta u(\gamma) = 0, \\
& \Delta x_0(\gamma) = 0, \\
& g_{\mathrm{eq}}(\gamma) = 0, \\
& g_{\mathrm{ineq}}(\gamma) \leq 0,
\end{aligned}
\tag{6.6}
$$

with $\gamma = \{\gamma_1, \dots, \gamma_M\}$ the set of all the model candidates' flat outputs. The inputs, states and outputs in the optimization formulation are expressed according to Equations (3.5c), (6.2), and (6.3). The differences between the recalculated inputs and the initial states for all M model candidates are measured by the delta function $\Delta(\cdot)$ that might be the Euclidean distance alike. Since the flat outputs are of functional form, time-dependent empirical basis functions $\gamma_i = \gamma_i(\tilde{\theta}_i, t) \; \forall \, i \in \{1, \dots, M\}$ with meta-parameters $\tilde{\theta}_i$ have to be specified; see also Section 6.2.3. The optimal control problem stated in Equation (3.65) is readily transformed in an algebraic nonlinear optimization problem as the system inputs and outputs are available in closed form, where the need for integrating the underlying ODE system and the need for control and or state vector parameterization are dropped.

For the robust formulation of the nominal optimization problem, Equation (6.6), a penalty term as in Equation 3.62 is introduced. The term penalizes the propagated uncertainty that is quantified by the variances $\mathbb{V}$ of the models' inputs u. In this vein, the calculated overlap, Equation (3.43),

is expected to decrease as the confidence bands of the trajectories tighten. The optimization problem for a flatness-based robust design of experiments for model selection is then stated as

$$
\begin{aligned}
\max_{\tilde{\boldsymbol{\theta}}} \quad & \sum_{k=0}^{T}\left(\lambda \sum_{i=1}^{M-1} \sum_{j=i+1}^{M}\left(\mathbb{E}[\boldsymbol{y}_i(\tilde{\boldsymbol{\theta}}_i, t_k)] - \mathbb{E}[\boldsymbol{y}_j(\tilde{\boldsymbol{\theta}}_j, t_k)]\right)^2\right. \\
& \left.(1-\lambda) \sum_{i=1}^{M} \mathbb{V}[\boldsymbol{u}_i(\tilde{\boldsymbol{\theta}}_i, t_k)]\right)
\end{aligned}
\tag{6.7}
$$

$$
\begin{aligned}
\text{s.t.} \quad & \Delta\mathbb{E}[\boldsymbol{u}(\tilde{\boldsymbol{\theta}}, t_k)] = 0, \\
& \Delta\mathbb{E}[\boldsymbol{x}_0(\tilde{\boldsymbol{\theta}}, t_k)] = 0, \\
& \boldsymbol{g}_{\text{eq}}(\tilde{\boldsymbol{\theta}}, t_k) = 0, \\
& \boldsymbol{g}_{\text{ineq}}(\tilde{\boldsymbol{\theta}}, t_k) \leq 0.
\end{aligned}
$$

Please note that the expectations and variances are taken with respect to the uncertain model parameters $\boldsymbol{\theta}$. In contrast, the decision variables of the optimization problem are the meta-parameters $\tilde{\boldsymbol{\theta}}$ present in the basis functions for the flat outputs, i.e., the control vectors of the B-spline curves, Equation (6.5). As previously in the nominal optimization problem, Equation (6.6), the robust formulation is a programming problem for which all occurring functions are algebraically available. Thus, the nominal version, Equation (6.6), and the robust version, Equation (6.7), are readily stated as an NLP without any use of parameterization methods. Furthermore, the possibility of deriving functions for exact gradients is given as opposed to the application of automatic differentiation or finite differences methods. A flow chart for the proposed robust MBDoE strategy using differential flatness is given in Figure 6.3.

6.4 Case Study

Biocatalytic reactions appear in numerous syntheses of natural products and active pharmaceutical ingredients. For example, chiral hydroxy ketones are important building blocks in the pharmaceutical industry and can be produced from aldehydes via enzymatic carboligation [263]. A lack of mechanistic kinetic models for biocatalytic carboligation and simultaneous inactivation of the benzaldehyde lyase was studied in [294] using MBDoE, where the model quality of the different model candidates was analyzed using the Akaike information criterion (AIC). Motivated by the biocatalytic carboligation of ketones from aldehydes, in this simulation study, two models simulating the enzymatic step from benzaldehyde to benzoin are considered [263]. The enzymatic reaction network follows Michaelis-Menten kinetics with the additional assumption that the reaction towards the enzyme-substrate complex ES_2 is irreversible, Table 6.1. In detail, enzyme E and substrate S form the enzyme-substrate complex ES_2 that reacts in a last step to
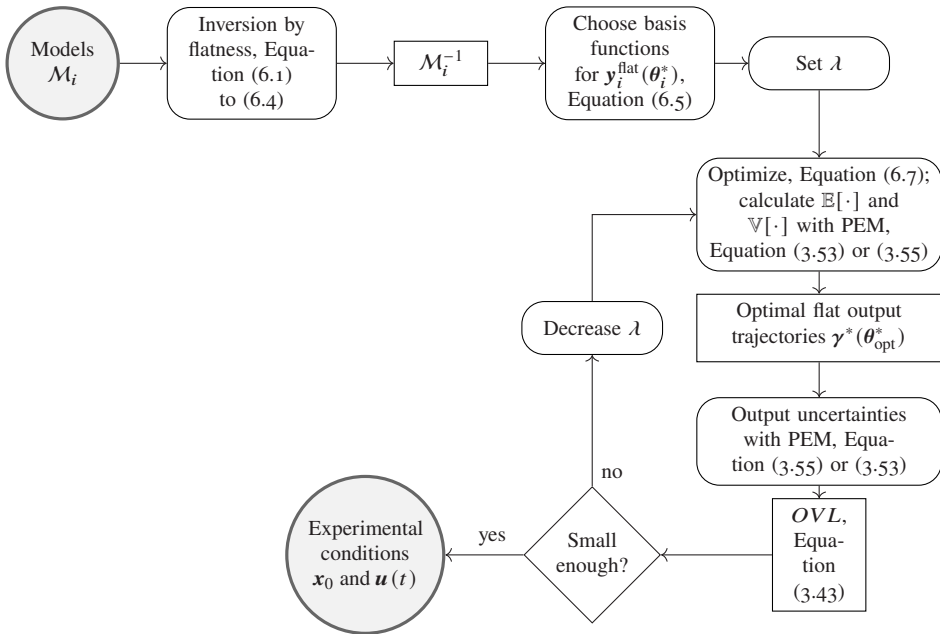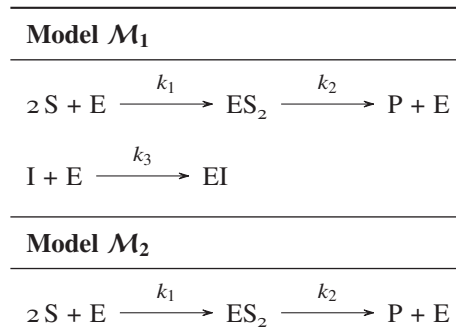
Figure 6.3: Robust MBDoE strategy.

Table 6.1: Reaction schemes of models $\mathcal{M}_1$ and $\mathcal{M}_2$.

Model $\mathcal{M}_1$

$$2\,S + E \xrightarrow{\;k_1\;} ES_2 \xrightarrow{\;k_2\;} P + E$$

$$I + E \xrightarrow{\;k_3\;} EI$$

Model $\mathcal{M}_2$

$$2\,S + E \xrightarrow{\;k_1\;} ES_2 \xrightarrow{\;k_2\;} P + E$$

product P, thereby releasing the bound enzyme again. The two proposed models differ in that way, that model candidate $\mathcal{M}_1$ exemplifies irreversible inhibition of the enzyme E by an inhibitor I, e.g., a second substrate, a typical situation in enzyme networks [295]. In contrast, model candidate $\mathcal{M}_2$ represents the uninhibited situation. Please note that the occurrence of inhibition could be straightforwardly verified in experiments if the substrate and the inhibiting substance can be added separately.

If elementary reactions are assumed, Section 3.3.1, and the inhibitor I is expected to be constant via proper control actions over the experimental run, the corresponding fed batch models are

$$
\mathcal{M}_1 = \begin{cases}
\frac{\mathrm{d[S]}}{\mathrm{d}t} & = -2k_1[\mathrm{S}]^2[\mathrm{E}] + u_\mathrm{S} \\
\frac{\mathrm{d[ES_2]}}{\mathrm{d}t} & = k_1[\mathrm{S}]^2[\mathrm{E}] - k_2[\mathrm{ES_2}] \\
\frac{\mathrm{d[E]}}{\mathrm{d}t} & = -k_1[\mathrm{S}]^2[\mathrm{E}] + k_2[\mathrm{ES_2}] - k_3[\mathrm{I}][\mathrm{E}] + u_\mathrm{E} \\
\frac{\mathrm{d[P]}}{\mathrm{d}t} & = k_2[\mathrm{ES_2}]
\end{cases},
$$

$$
\mathcal{M}_2 = \begin{cases}
\frac{\mathrm{d[S]}}{\mathrm{d}t} & = -2k_1[\mathrm{S}]^2[\mathrm{E}] + u_\mathrm{S} \\
\frac{\mathrm{d[ES_2]}}{\mathrm{d}t} & = k_1[\mathrm{S}]^2[\mathrm{E}] - k_2[\mathrm{ES_2}] \\
\frac{\mathrm{d[E]}}{\mathrm{d}t} & = -k_1[\mathrm{S}]^2[\mathrm{E}] + k_2[\mathrm{ES_2}] + u_\mathrm{E} \\
\frac{\mathrm{d[P]}}{\mathrm{d}t} & = k_2[\mathrm{ES_2}]
\end{cases}.
$$

$$(6.8)$$

Here, the states x_i for $i \in \{\mathrm{S}, \mathrm{E}, \mathrm{ES_2}, \mathrm{P}\}$ are written in concentration notation for better readability. It follows that both the substrate and the enzyme can be dosed over the course of the experiment, see the model inputs u_S and u_E in the Equation (6.8), respectively. Please note that in model $\mathcal{M}_1$, the differential equations of the inhibitor I, which is assumed to be constant, and the loss product EI are not specified, as information about their time behavior does not influence the other differential equations, and therefore, is not relevant to the problem at hand. The measured concentrations are the concentrations of the substrate and the final product; that is, $y = (x_\mathrm{S}, x_\mathrm{P})^\top$. The kinetic constants, that have been previously determined from experimental data, have the following expected values: For model $\mathcal{M}_1$ $(k_1, k_2, k_3) = (0.215\,\mathrm{L}^2/(\mathrm{mmol}^2\,\mathrm{min}), 91.475\,\mathrm{min}^{-1}, 0.019\,\mathrm{L}/(\mathrm{mmol}\,\mathrm{min}))$, and for model $\mathcal{M}_2$ $(k_1, k_2) = (0.204\,\mathrm{L}^2/(\mathrm{mmol}^2\,\mathrm{min}), 103.344\,\mathrm{min}^{-1})$. The variances of the normally distributed parameters k_1, k_2 and k_3 equal 5 % of their expected values in the absence of parameter dependencies.

6.5 Results

For the case study given in Section 6.4, the differential flatness property is analyzed, and then, discriminating input controls based on the proposed MBDoE approach are designed, making use of the differential flatness concept. The effect of model parameter uncertainties is studied as well, and the robust MBDoE approach is applied as an appropriate countermeasure.

6.5.1 Differential Flatness Property

The flat outputs for both models are derived following heuristic methods to 1) obtain a flat output candidate according to Equation (6.1) and 2), with the help of graph theory, to show that the candidate fulfills the differential flatness conditions given Equations (6.2)–(6.4). Drawing the directed graphs (digraphs) for model $\mathcal{M}_1$ and model $\mathcal{M}_2$, we observe that they look alike. The corresponding adjacency matrices are

$$
A_u = \begin{array}{c} x_S \\ x_{ES_2} \\ x_E \\ x_P \end{array}
\begin{array}{cc} u_S & u_E \end{array}
\begin{pmatrix} 1 & 0 \\ 0 & 0 \\ 0 & 1 \\ 0 & 0 \end{pmatrix},
\quad
A_x = \begin{array}{c} x_S \\ x_{ES_2} \\ x_E \\ x_P \end{array}
\begin{array}{cccc} x_S & x_{ES_2} & x_E & x_P \end{array}
\begin{pmatrix} 1 & 0 & 1 & 0 \\ 1 & 1 & 1 & 0 \\ 1 & 1 & 1 & 0 \\ 0 & 1 & 0 & 0 \end{pmatrix},
\quad
A_y = \begin{array}{c} y_S \\ y_P \end{array}
\begin{array}{cccc} x_S & x_{ES_2} & x_E & x_P \end{array}
\begin{pmatrix} 1 & 0 & 0 & 0 \\ 0 & 0 & 0 & 1 \end{pmatrix},
$$

and the resulting digraph is shown in Figure 6.4a. The digraph is composed of 8 vertices, $\mathcal{V} = \{u_S, u_E\} \cup \{x_S, x_{ES_2}, x_E, x_P\} \cup \{y_S, y_P\}$, and 13 edges corresponding to the non-zero entries in the adjacency matrices A_u, A_x, and A_y. The self-loops of $\{x_S, x_{ES_2}, x_E\} \in \mathcal{V}$ are related to the non-zero diagonal elements of A_x.

The control vector dimension in both models is 2. Therefore, to comply with condition given in Equation (6.4), the dimension of the flat output vector must be 2 as well. Inspecting the system of differential equations in Equation (6.8) one might observe that x_P does not appear on the right side of any of the differential equations. The corresponding node in the digraph, see Figure 6.4a, represents a dead end (i.e., no edge from $x_P \in \mathcal{V}$ to $\{x_S, x_{ES_2}, x_E\} \in \mathcal{V}$), and therefore, must be part of the flat output. Obviously, the second element of the flat output vector should be chosen from the concentrations left as they have direct physical meaning for the study case at hand. We consider the flat output candidate

$$
\gamma = \begin{pmatrix} \gamma_1 \\ \gamma_2 \end{pmatrix} = \begin{pmatrix} x_S \\ x_P \end{pmatrix}
\tag{6.9}
$$

(a) Digraph for model $\mathcal{M}_1$ and $\mathcal{M}_2$.

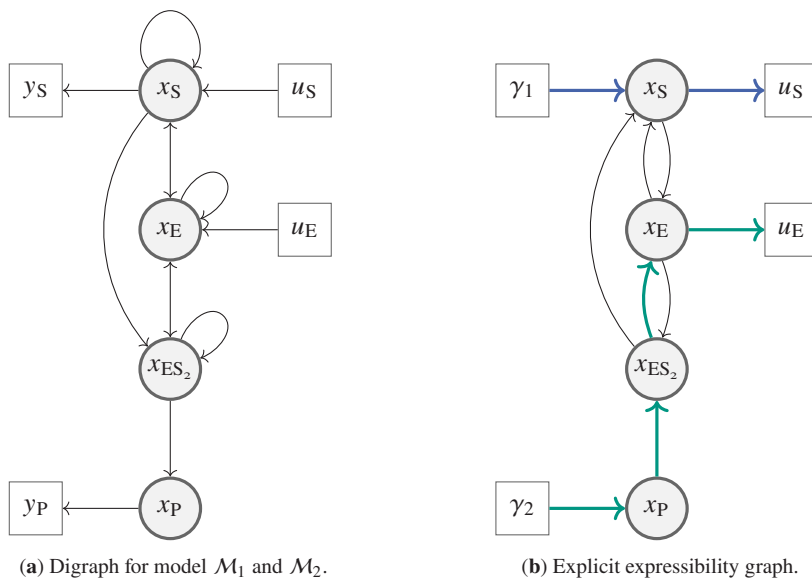(b) Explicit expressibility graph.

Figure 6.4: Digraph and explicit expressibility graph to study the differential flatness property.

that evidently satisfies Equation (6.1).

The explicit expressibility graph, which can be readily obtained from the digraph, is shown in Figure 6.4b. Please note that in comparison to the digraph, Figure 6.4a, the self-loops are omitted, and the edge directions are reversed. In Figure 6.4b, two disjoint paths are drawn that cover all vertices related to the inputs, system states, and flat outputs. Therefore, the flat output vector, Equation (6.9), is supposed to form a differentially flat system which we will confirm using its definition in the following. From the ODE system, after several reformulations and substitutions, we obtain the inverse models:

$$
\mathcal{M}_1^{-1} =
\begin{cases}
x_S & = \gamma_1 \\[2mm]
x_{ES_2} & = \frac{\dot\gamma_2}{k_2} \\[2mm]
x_E & = \frac{\frac{\ddot\gamma_2}{k_2} + \dot\gamma_2}{k_1 \gamma_1^2} \\[2mm]
x_P & = \gamma_2 \\[2mm]
u_S & = \dot\gamma_1 + 2\gamma_1^2 \frac{\frac{\ddot\gamma_2}{k_2} + \dot\gamma_2}{\gamma_1^2} \\[2mm]
u_E & = \frac{\frac{\ddot\gamma_2}{k_2} + \dot\gamma_2}{k_1 \gamma_1^2} + \frac{\frac{\ddot\gamma_2}{k_2} + \dot\gamma_2}{k_1 \gamma_1^2} \left(-2\frac{\dot\gamma_1}{k_1 \gamma_1^3} + k_1 \gamma_1^2 + k_3 [I] \right) - k_2 \frac{\dot\gamma_2}{k_2}
\end{cases}
\tag{6.10}
$$

and

$$
\mathcal{M}_2^{-1} = \begin{cases}
x_{\text{S}} & = \gamma_1 \\[4pt]
x_{\text{ES}_2} & = \dfrac{\dot{\gamma}_2}{k_2} \\[8pt]
x_{\text{E}} & = \dfrac{\frac{\ddot{\gamma}_2}{k_2} + \dot{\gamma}_2}{k_1 \gamma_1^2} \\[10pt]
x_{\text{P}} & = \gamma_2 \\[6pt]
u_{\text{S}} & = \dot{\gamma}_1 + 2\gamma_1^2 \dfrac{\frac{\ddot{\gamma}_2}{k_2} + \dot{\gamma}_2}{\gamma_1^2} \\[12pt]
u_{\text{E}} & = \dfrac{\frac{\ddot{\gamma}_2}{k_2} + \ddot{\gamma}_2}{k_1 \gamma_1^2} + \dfrac{\frac{\ddot{\gamma}_2}{k_2} + \dot{\gamma}_2}{k_1 \gamma_1^2} \left(-2\dfrac{\dot{\gamma}_1}{k_1 \gamma_1^3} + k_1 \gamma_1^2 \right) - k_2 \dfrac{\dot{\gamma}_2}{k_2}
\end{cases} \qquad . \qquad (6.11)
$$

The inverse model, Equation (6.10), with its flat output, Equation (6.9), satisfies the set containing all three conditions for differential flatness, Equations (6.2) to (6.4). Accordingly, the inverse model of model $\mathcal{M}_2$, Equation (6.11), fulfills the conditions for differential flatness. Thus, both models are differentially flat models. For prescribed trajectories $\gamma_1^* = x_{\text{S}}^*$ and $\gamma_2^* = x_{\text{P}}^*$, the necessary experimental conditions for the controls are readily available by differentiation; for an example, see [261].

6.5.2 Non-Optimized Experimental Design

The non-optimized experimental design is considered first, i.e., the initial situation before any optimization iteration. Please note that batch operation is assumed, and thus, the controls u_{S} and u_{E} are zero and not explicitly shown in the following. This represents a simple experiment in which only the initial concentrations of the substrate and the enzyme are altered. Plots for the measured states and the measured states with confidence bands are shown in Figure 6.6 on the left side and on the right side, respectively.

For the nominal case in Figure 6.5a, it is impossible to distinguish the two models from each other, even if the experimental data were close to one of the models. In Figure 6.5b, it is well observable that the uncertainties in the measured states given as confidence intervals are low. To better compare the results with the expected results from the optimization part, the overlap measure in Equation (3.43) is normalized to the overlap of the non-optimized design in Figure 6.5b; that is, $OVL_{\text{N}} = 1.0$.
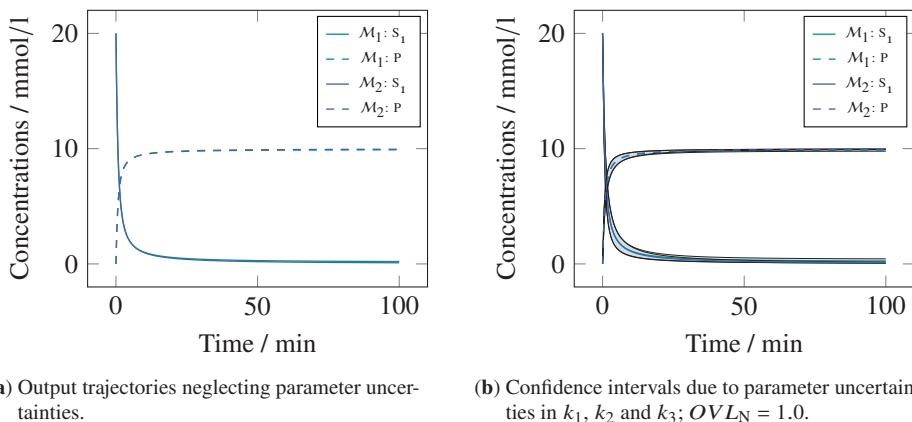
(**a**) Output trajectories neglecting parameter uncertainties.

(**b**) Confidence intervals due to parameter uncertainties in k_1, k_2 and k_3; $OVL_N = 1.0$.

Figure 6.5: Measured states before applying the MBDoE approach.

6.5.3 Optimized Experimental Design without Uncertainty: The Nominal Case

Before optimizing, suitable B-spline types must be chosen. In contrast to the classical application of splines in approximation or interpolation of available data, they are used to express smooth control and state trajectories along the time axis, and are created from their definition as opposed to a fitting process. Thus, common problems experienced in spline approximation and interpolation, like cusps and loops [296], are less likely to occur. From the different methods for splines, we choose the *uniform* method where the data points are uniformly distributed over the domain range [293]. Furthermore, for each element of the flat output vectors, a B-spline curve of order 6 with 12 control points and clamped end conditions was used, resulting in a 48-dimensional decision space for the optimization problem. In the first optimization step, the classical deterministic optimization by setting $\lambda = 1$ in the setting is followed, Equation (6.7). In contrast to the the non-optimized design in Section 6.5.2, the controls u_S and u_E are now considered variable over time, i.e., a fed batch situation is assumed. The optimization results for the measured states of the nominal case are shown in Figure 6.6a, again, without uncertainty and with uncertainty vis-à-vis. The corresponding control curves are displayed in Figure 6.7 on the left side.

In the plot without propagated uncertainties, Figure 6.6a, it is clearly visible that the expected values of the measured states are significantly driven apart. On the other hand, a look at the plot on the right reveals that (1) the uncertainties have substantially enlarged compared to the initial situation, and (2) the confidence bands of both models overlap noticeably. The overlap values are given in Table 6.2. The overlap has decreased versus the initial situation, i.e., it is 6 percentage points lower compared to before the optimization. However, in performed simulations ending up in other local minima, that are not shown here, the optimization results worsened in the sense of
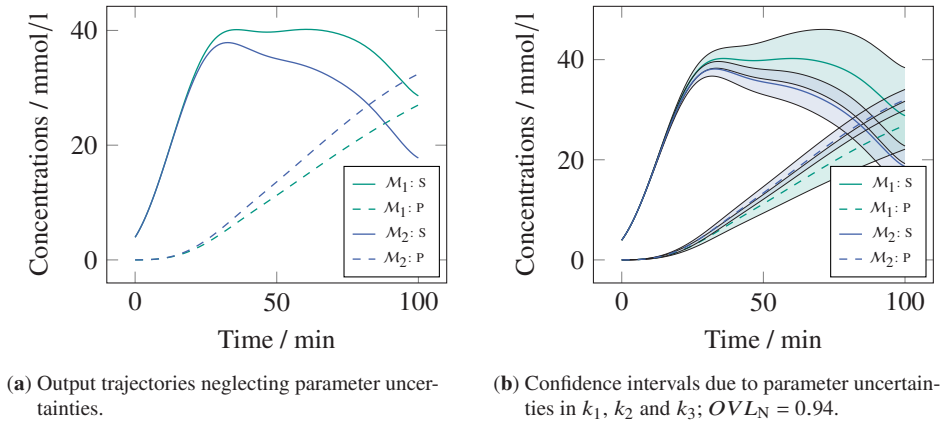
(**a**) Output trajectories neglecting parameter uncertainties.

(**b**) Confidence intervals due to parameter uncertainties in k_1, k_2 and k_3; $OVL_N = 0.94$.

Figure 6.6: Measured states for the nominal design.

a larger overlap value if the nominal optimization state was compared with the non-optimized. In this context, the question arises if the overlap can be further decreased and thus the feasibility to identify the right model be increased by inherently taking care of the parametric uncertainties in the optimization setting. Therefore, the optimization is robustified in the following by considering the variances in the objective function as described in Section 3.6.1.

6.5.4 Robust Experimental Design

For the robust MBDoE setting, Equation (6.7), the weight factor is set to $\lambda = 0.5$; that is, the Euclidean distance of the flat outputs of model $\mathcal{M}_1$ and $\mathcal{M}_2$ as well as the resulting uncertainties in the recalculated model inputs are equally weighted. Compared with the nominal optimization, the computational time to reach satisfying convergence increases multiple times despite the low number of sampling points that the PEM is using. In particular, when PEM5 is employed, the computational time increases considerably due to the higher sample number; see Equations (3.54) and (3.56).

The optimal controls for the substrate and enzyme of both the nominal and the robust setting are drawn in Figure 6.7. Please note that the realization of the profiles in a laboratory setup is constrained by the available pump devices. These constraints could be included in the robust MBDoE framework, Equation (6.7), but the technical realization of these input controls is beyond the scope of this study. Albeit, the main observations are shortly summarized in the following. In both settings, the dosing of enzyme is four magnitudes lower than the dosing of the substrate, and the dosing rates vary in the same ranges for both substrate and enzyme. Furthermore, the dosing rates of substrate follow similar patterns in the nominal and the robust design.
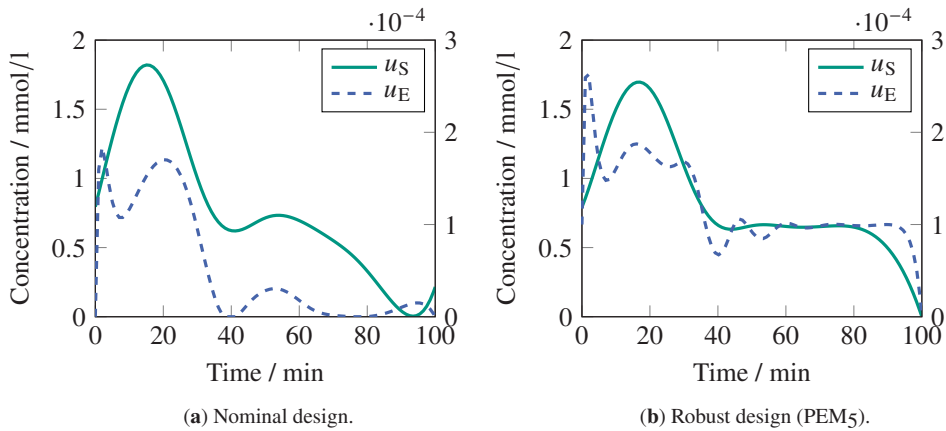
(**a**) Nominal design.

(**b**) Robust design (PEM5).

Figure 6.7: Optimized input controls (u_1: y-axis on the left, u_2: y-axis on the right).

The concentration curves for the resulting states of the robust flatness-based design are shown in Figure 6.8. Interestingly, the trajectories for the expected values in the left subfigure clearly drift apart, but less strongly than in the nominal optimization case, see Figure 6.6a. Considering 100 equally spaced points, the norms of the model output distances in the robust case are roughly half as large as in the nominal case. However, the presumption that the overlap has decreased can be confirmed when looking at the overlap values in Table 6.2. The overlap value has decreased by 19 percentage points and by 13 percentage points when compared with the initial situation and the nominal optimization, respectively. The propagated uncertainties can be extracted from the graphs shown in Figure 6.9 for the nominal and robust design where the variances for both outputs of model 1 are considerably lower when the nominal case on the left is compared with the robust one on the right. Furthermore, the approximation of the propagated uncertainty using the PEM
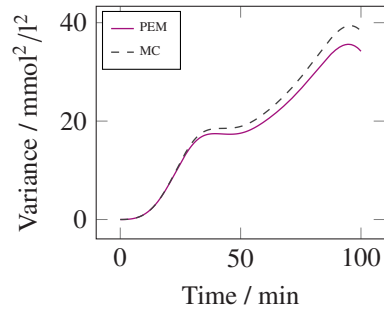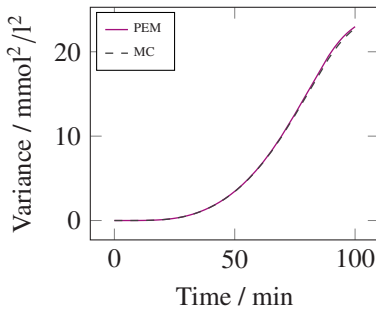

(**a**) Output trajectories neglecting parameter uncertainties.

(**b**) Confidence intervals due to parameter uncertainties.
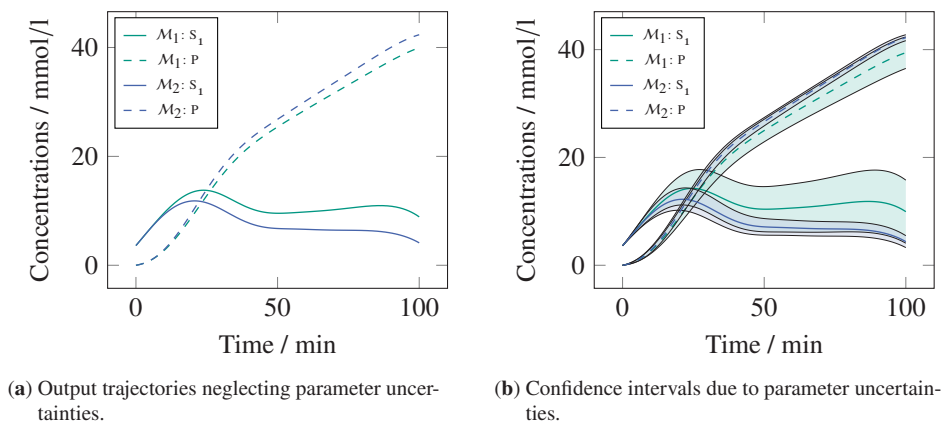
Figure 6.8: Measured states for the robust flatness-based design.

Table 6.2: Results for the overlap.

Design	**None**	**Nominal**	**Robust**	
			PEM3	PEM5
OVL_N	1.0	0.94	0.81	0.80
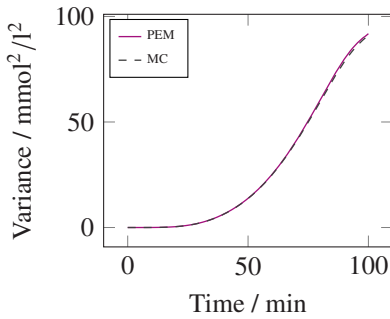
(**a**) Nominal design, y_1.

(**b**) Robust design, y_1.

(**c**) Nominal design, y_2.
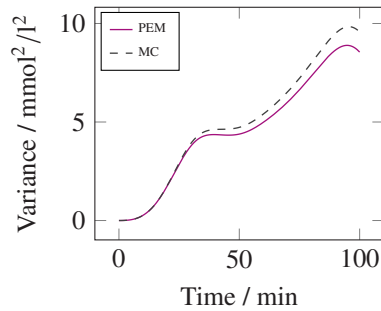
(**d**) Robust design, y_2.

Figure 6.9: Variances of model outputs for model $\mathcal{M}_1$.

is sufficiently good, as the results are in proximity to the Monte Carlo simulations performed with 10^4 samples. Thus, the inclusion of the propagated uncertainty as a penalty in the objective function has delivered the desired outcome. Prospectively, a different choice of λ or the drawing of a Pareto front might further decrease the overlap between the two model outcomes.

6.6 Conclusion

A novel approach to the model-based design of experiments for model selection using the differential flatness property of the systems was extended by robustifying the optimization problem against parametric uncertainty. In comparison with commonly used methods for model discrimination, the resulting optimal control problem does not require approximation methods for solving the underlying system of differential equations as both controls and states can be derived analytically in differentially flat systems without numerical integration. Likewise, parameterization of the controls and potentially the states is obsolete for we directly arrive at a nonlinear programming problem. Moreover, analytic gradients to the optimization solver can be provided with ease, even for highly nonlinear systems. The robustification strategy comprised the consideration of propagated uncertainties; that is, the variances of the reconstructed model inputs were added as a penalty term in the objective function. The corresponding uncertainty quantification was performed using the point estimate method, a computationally cheap but reasonably accurate method compared with standard Monte Carlo simulations for uncertainty quantification. The strategy was applied to a nonlinear enzymatic reaction using B-splines as the parameterization technique for expressing the flat outputs, and thus, optimal experimental input controls for the subsequent experiment were obtained. It was shown, that a nominal optimization without the consideration of parameter uncertainties might result in unreliable optimal controls, i.e., not leading to the possibility of selecting one model over another after having performed the subsequent experiment. In contrast, if parametric uncertainties were inherently considered in the optimal experimental design problem, more reliable MBDoE results were identified. This emphasizes the importance of including the quantification of uncertainties over classic deterministic optimization where the differential flatness concept shows promising characteristics for advanced system identification strategies in terms of precise parameter estimates and reliable model selection.

In general, the application of the developed strategy based on differential flatness would be as well possible to the developed process model for the artemisinin semi-synthesis from Chapters 4 and 5. However, the process model has an increased number of states (10) and at the same time no controls, making it differentially non-flat. The transfer to a differentially flat system would cause the parameter estimation and model selection tasks to be extraordinarily challenging. A first step could be the consideration of other parameterization techniques for the flat outputs than B-splines; e.g., neural networks, as they are known to have excellent approximation capabilities that satisfy the *Universal approximation theorem*.

7   Conclusions and Future Directions

Artemisinin-based combination therapies are key in the fight against malaria. Today, the primary source of artemisinin (ART) is extraction from the plant *Artemisia annua L.*, resulting in a high and very volatile ART market price. The semi-synthesis of ART from dihydroartemisinic acid (DHAA), a late-stage precursor of ART and an extraction byproduct, is a potential option to increase ART yields obtained from the plant and thereby decrease and stabilize ART market prices.

In this work, a mathematical process model describing the semi-synthesis of ART from DHAA in a continuous two-phase flow reactor was developed, that was subsequently used for a model-based analysis of the system under study. The challenge of identifying the model was impeded by, first, a complex interplay of flow, mass transfer, radiative and reaction phenomena; second, a lack of knowledge considering the underlying reaction network; and third, scarce measurement data. Streamlined with the Quality by design (QbD) initiative in the pharmaceutical industry, a systematic approach within the framework of Process Systems Engineering (PSE), that in particular consisted of model-based design of experiments (MBDoE), methods to test parameter identifiability and sensitivity analyses, was therefore followed. The reactor model was described by the two-fluid model, which was connected with simplified equations for the mass, photon transfer, and the chemical kinetics, based on thoroughly discussed assumptions.

For the photooxygenation step of the semi-synthesis, the parameterized model predicted the experimental data for the hydroperoxide of interest, i.e., PO_1, with a deviation of 7.3 %. It was shown that the two parameters describing the quantum yield needed to be fixed to literature values from a similar reaction system because of very strong parameter interactions. A final parameter estimation step, whose experimental data resulted from a MBDoE, reduced the parameter uncertainties significantly, and yielded a robust process model with identifiable parameters as confirmed by a combined sensitivity and uncertainty analysis. One characteristic feature of the process model is the consideration of the optical path length as a model parameter to be estimated, that yielded an effective path length and made the application of a simple description of the radiative transfer possible.

For the acid-catalyzed sequence, the second step in the semi-synthesis of ART from DHAA starting with the hydroperoxide PO_1, a kinetic model for the underlying reaction network was

identified from a set of different model candidates, that is, a model selection problem was solved. It could be shown that the dependence of the PO_1 conversion on the acid concentration must be non-linear, which was achieved by altering the reaction orders of the acid in the two corresponding reactions. Applying the kinetic model candidates to a series of batch experiments revealed that ART in the continuous experiments and the major byproduct in the batch experiments must accumulate via different intermediates. This observation might be a consequence of having run the experiments in different TFA concentration ranges for the batch and the continuous setups. A lumped byproduct species was introduced that accounted for the non-measured and unknown species in the reaction network. The best identified model structure from both batch and continuous experimental data predicted the ART concentration with an averaged relative deviation of nearly 14 % for simulated ART concentrations above 0.01 mol/l. A greater part of the deviation, that is twice as large as in the photooxygenation, could be attributed to measurement uncertainty. In an exploratory data analysis, it could be shown that the experimental data featured considerable variation. The identification of the best candidate also included the removal and fixing of non-identifiable parameters, that, in the end, led to an identifiable and robust model structure as confirmed by a global sensitivity study and a follow-up process optimization. In the latter task, the developed overall process model was applied in a mathematical optimization problem to improve ART and ART space time yields in a nominal and a robust setting considering parametric uncertainty. The yields showed only a slight worsening when the initial DHAA concentration was increased to 0.4 mol/l, resulting in a yield of roughly 54 %. A considerable increase to around 62 % was observed when TFA was not dosed at the synthesis reactor inlet, but fed together with DHAA. Analogously, space time yields of 22.3 mol/(l d) (6.3 g/(ml d)) and 27.4 mol/(l d) (7.7 g/(ml d)) were achieved in the differing cases, where the runs considering parametric uncertainty showed that variances in the yields are small, emphasizing once more the robustness of the developed process model.

In summary, the developed process model simulates the continuous partial synthesis of ART from DHAA in a two-phase tube reactor, while considering the complexity of the occurring phenomena, ranging from fluid motion, two-phase mass transfer over light irradiation to chemical kinetics, with good predictive capability. The model balances the phenomenological complexity with a manageable mathematical complexity, leading to a robust process model that is straightforward to use and therefore serves as a valuable tool in optimizing the whole process chain for the production of ART and for process control. Hence, the model is a good starting point for industrial players to support the generation of valuable process understanding and to optimize the ART production using the proposed co-strategy, i.e., running the partial synthesis in tandem with ART extraction. In this vein, the ART market price and its volatility are potentially reduced and a contribution is made in the important fight against one of the deadliest diseases on earth. Furthermore, the identification strategy and the straightforward modeling approaches developed

in this work provide a blueprint for similar complex processes with the availability of only scarce measurement data, in particular for the growing field of photo flow chemistry.

On the other hand, a successful industrial implementation would benefit from deeper research in both, system understanding of the process behavior, and the modeling approach and identification strategy. In the former, the following three major directions crystallize: improving the understanding of the reaction mechanism, enhancing the measurement capabilities, and coupling of extraction and partial synthesis with the purification of ART. In the photooxygenation, a more profound insight into the radiative heat transfer inside the three-dimensional casing and the tubing will give rise to a more effective design of the photo reactor and a more precise description of the irradiation phenomena. In the acid-catalyzed sequence, a better understanding of the reaction mechanisms is crucial to improve the predictability of the kinetic model. An improved picture of unknown byproducts and intermediates helps to break down the reaction mechanism. Importantly, the decisive effect of the acidic catalyst on the specific reaction steps during the conversion of PO_1 to ART must be uncovered. A first step into this direction is to conduct continuous experiments in the absence of oxygen to reproduce the conditions in the batch experiments and to exclude the additional complexity introduced by oxygen. Likewise, additional experiments in the setups with similar acid concentrations would strengthen the validity of drawn conclusions about the reaction network. In parallel, precise gas measurements, that are sampled in non-stationary operation, will similarly increase the process understanding. All actions related to improving the mechanistic understanding come with the cost of intensified and advanced measurement technology. For example, in-situ measurements would solve multiple problems by providing a time-resolved tracking of the reaction progress and making sample workup and quenching unnecessary, where the latter introduced significant uncertainty into the experimental data. In addition, the water concentration during the synthesis needs to be determined to quantify the effect of water in the reaction network. Considering other temperatures could lead to a more reliable process model and the same time increase its applicability. To test the developed process model on different catalysts and feed stocks, in particular the actual plant extract, would give insights on its generalizability. Having analyzed the partial synthesis, the reactors can be connected to the extraction and purification units, and the process be utilized to analyze the coupled process chain.

On the modeling aspect, a comparison of the developed process model with a more complete description of the two-phase fluid behavior inside the tubing will yield a better estimation of the model's validity and its potential shortcomings. This necessitates the implementation of advanced measurement technology. The availability of a larger set of experimental data will enable the application of more recent approaches in model selection, focusing on autonomous discovery of reaction networks using for example neural networks [297] or the SINDy algorithm [298]. Likewise, a more precise and individual consideration of the observed measurement uncertainties would be a good next step to improve and robustify the developed process model.

Challenging model selection problems of pharma-related processes with considerable complexity and non-linearities as the acid-catalyzed sequence of the semi-synthesis to ART frequently appear. In contrast to the data-intensive possibilities mentioned in the previous paragraph, a promising alternative to the forward simulation approach followed for the semi-synthesis is the use of inverse models. To this end, an inverse modeling technique based on differential flatness, a system property widely used in control theory, was transferred to model selection problems and applied to a biocatalytic carboligation forming benzoin, a representative for the pharmaceutically important building block of hydroxy ketones. Contrarily to commonly used methods for model selection, states and controls of a differentially flat system can be derived analytically without the need for approximations as in numerical integration or parameterization strategies. That also enables the provision of analytic gradients to the optimization solver. Analogous to the robust setting for process optimization of the semi-synthesis, parametric uncertainties were considered in the model selection problem by applying the point estimate method. The variances of the reconstructed model inputs were added as a penalty term in the objective function. The nominal and robust strategies utilizing the differential flatness property were successfully applied to the enzymatic reaction, where B-splines parameterized the flat outputs, yielding optimal MBDoEs.

The two different strategies revealed that the consideration of parametric uncertainties leads to more reliable MBDoE results, that is, it is more likely in the nominal case to end up with optimal controls, that do not necessarily lead to the possibility of selecting one model candidate over another. The results emphasize the importance of including the quantification of uncertainties over classic deterministic optimization. The differential flatness concept shows promising characteristics for advanced system identification strategies in terms of precise parameter estimates and reliable model selection. An interesting new application of differential flatness might be its use for the calculation of parameter sensitivities, that has not been looked into so far. Ongoing research efforts consider rules and algorithms to a more automatized detection of the differential flatness property and the finding of flat outputs. In parallel, a generalizing study about applicability and practicality of the use of differential flatness for originally non-differentially flat systems is recommended. In particular, pharmaceutical syntheses frequently have many states and few controls and are therefore usually differentially non-flat. Note however that any system can be transferred into a differentially flat system. This also holds for the developed process model for the artemisinin semi-synthesis, that is differentially non-flat and that makes this transfer with its 10 states and zero controls extremely challenging. A look at alternative flat output parameterizations to B-splines would be a good first step into this direction. In particular machine learning models such as neural networks shall be a good starting point as they provide excellent approximation capabilities. Positive results would potentially increase the utilization of differentially flat systems beyond their classical implementations in control theory, where the beneficial characteristics of differentially flat systems have received great approval and contributed to their success story.

Bibliography

[1] Rasmuson, A. *Mathematical Modeling in Chemical Engineering*. United Kingdom ; New York: Cambridge University Press, 2014. ISBN: 978-1-107-04969-7.

[2] Pistikopoulos, E. N., Barbosa-Povoa, A., Lee, J. H., Misener, R., Mitsos, A., Reklaitis, G. V., Venkatasubramanian, V., You, F., and Gani, R. "Process Systems Engineering – The Generation Next?" In: *Computers & Chemical Engineering* 147 (Apr. 2021). DOI: 10.1016/j.compchemeng.2021.107252.

[3] U.S. Food and Drug Administration. *Guidance for Industry PAT - A Framework for Innovative Pharmaceutical Development, Manufacturing, and Quality Assurance*. 2004.

[4] U.S. Food and Drug Administration. *Pharmaceutical CGMPS for the 21st Century – A Risk-Based Approach (Final Report)*. Sept. 2004.

[5] Yu, L. X. "Pharmaceutical Quality by Design: Product and Process Development, Understanding, and Control". In: *Pharmaceutical Research* 25.4 (Apr. 2008), pp. 781–791. DOI: 10.1007/s11095-007-9511-1.

[6] Scopus® scientific database. Feb. 6, 2022. URL: https://www.scopus.com.

[7] Tomba, E., Facco, P., Bezzo, F., and Barolo, M. "Latent Variable Modeling to Assist the Implementation of Quality-by-Design Paradigms in Pharmaceutical Development and Manufacturing: A Review". In: *International Journal of Pharmaceutics* 457.1 (Nov. 2013), pp. 283–297. DOI: 10.1016/j.ijpharm.2013.08.074.

[8] International Council for Harmonisation of Technical Requirements for Pharmaceuticals for Human Use. *ICH Guideline Q8 (R2) – Pharmaceutical Development*. Aug. 2009. DOI: 10.1163/ej.9789004163300.i-1081.897.

[9] International Council for Harmonisation of Technical Requirements for Pharmaceuticals for Human Use. *ICH Q8, Q9, & Q10 Questions and Answers – Appendix: Q&As from Training Sessions (Q8, Q9, & Q10 Points to Consider)*. Aug. 2022.

[10] Chatterjee, S., Moore, C. M. V., and Nasr, M. M. "An Overview of the Role of Mathematical Models in Implementation of Quality by Design Paradigm for Drug Development and Manufacture". In: *Comprehensive Quality by Design for Pharmaceutical Product Development and Manufacture*. Ed. by Reklaitis, G. V.,

Seymour, C., and García-Munoz, S. Hoboken, NJ, USA: John Wiley & Sons, Inc., Sept. 8, 2017, pp. 9–24. ISBN: 978-1-119-35618-9 978-0-470-94237-6. DOI: `10.1002/9781119356189.ch2`.

[11]   Destro, F. and Barolo, M. "A Review on the Modernization of Pharmaceutical Development and Manufacturing - Trends, Perspectives, and the Role of Mathematical Modeling". In: *International Journal of Pharmaceutics* (Mar. 2022), p. 121715. DOI: `10.1016/j.ijpharm.2022.121715`.

[12]   Sarkis, M., Bernardi, A., Shah, N., and Papathanasiou, M. M. "Emerging Challenges and Opportunities in Pharmaceutical Manufacturing and Distribution". In: *Processes* 9.3 (Mar. 3, 2021), p. 457. DOI: `10.3390/pr9030457`.

[13]   Schenkendorf, R., Gerogiorgis, D., Mansouri, S., and Gernaey, K. "Model-Based Tools for Pharmaceutical Manufacturing Processes". In: *Processes* 8.1 (Jan. 1, 2020), p. 49. DOI: `10.3390/pr8010049`.

[14]   Djuris, J. and Djuric, Z. "Modeling in the Quality by Design Environment: Regulatory Requirements and Recommendations for Design Space and Control Strategy Appointment". In: *International Journal of Pharmaceutics* 533.2 (Nov. 2017), pp. 346–356. DOI: `10.1016/j.ijpharm.2017.05.070`.

[15]   Rantanen, J. and Khinast, J. "The Future of Pharmaceutical Manufacturing Sciences". In: *Journal of Pharmaceutical Sciences* 104.11 (Nov. 2015), pp. 3612–3638. DOI: `10.1002/jps.24594`.

[16]   Gernaey, K. V., Cervera-Padrell, A. E., and Woodley, J. M. "A Perspective on PSE in Pharmaceutical Process Development and Innovation". In: *Computers & Chemical Engineering* 42 (July 2012), pp. 15–29. DOI: `10.1016/j.compchemeng.2012.02.022`.

[17]   Walz, O., Marks, C., Viell, J., and Mitsos, A. "Systematic Approach for Modeling Reaction Networks Involving Equilibrium and Kinetically-Limited Reaction Steps". In: *Computers & Chemical Engineering* 98 (Mar. 2017), pp. 143–153. DOI: `10.1016/j.compchemeng.2016.12.014`.

[18]   Berger, R. J., Stitt, E. H., Marin, G. B., Kapteijn, F., and Moulijn, J. A. "Eurokin. Chemical Reaction Kinetics in Practice". In: *CATTECH* 5.1 (2001), pp. 36–60. DOI: `10.1023/A:1011928218694`.

[19]   Marquardt, W. "Model-Based Experimental Analysis of Kinetic Phenomena in Multi-Phase Reactive Systems". In: *Chemical Engineering Research and Design* 83.6 (June 2005), pp. 561–573. DOI: `10.1205/cherd.05086`.

[20]   Dewyer, A. L., Argüelles, A. J., and Zimmerman, P. M. "Methods for Exploring Reaction Space in Molecular Systems". In: *WIREs Computational Molecular Science* 8.2 (Mar. 2018). DOI: `10.1002/wcms.1354`.

[21] Susnow, R. G., Dean, A. M., Green, W. H., Peczak, P., and Broadbelt, L. J. "Rate-Based Construction of Kinetic Models for Complex Systems". In: *The Journal of Physical Chemistry A* 101.20 (May 1, 1997), pp. 3731–3740. DOI: `10.1021/jp9637690`.

[22] Taylor, C. J., Booth, M., Manson, J. A., Willis, M. J., Clemens, G., Taylor, B. A., Chamberlain, T. W., and Bourne, R. A. "Rapid, Automated Determination of Reaction Models and Kinetic Parameters". In: *Chemical Engineering Journal* 413 (June 2021), p. 127017. DOI: `10.1016/j.cej.2020.127017`.

[23] Michalik, C., Brendel, M., and Marquardt, W. "Incremental Identification of Fluid Multi-Phase Reaction Systems". In: *AIChE Journal* 55.4 (Apr. 2009), pp. 1009–1022. DOI: `10.1002/aic.11738`.

[24] López C., D. C., Barz, T., Körkel, S., and Wozny, G. "Nonlinear Ill-Posed Problem Analysis in Model-Based Parameter Estimation and Experimental Design". In: *Computers & Chemical Engineering* 77 (June 2015), pp. 24–42. DOI: `10.1016/j.compchemeng.2015.03.002`.

[25] Balsa-Canto, E., Banga, J., and Alonso, A. "Computational Procedures for Optimal Experimental Design in Biological Systems". In: *IET Systems Biology* 2.4 (July 1, 2008), pp. 163–172. DOI: `10.1049/iet-syb:20070069`.

[26] Levenspiel, O. *Chemical Reaction Engineering*. 3rd ed. New York: Wiley, 1999. ISBN: 978-0-471-25424-9.

[27] Walter, E. and Pronzato, L. *Identification of Parametric Models from Experimental Data*. Communications and Control Engineering. London: Springer, 1997. ISBN: 978-3-540-76119-8.

[28] Villaverde, A. F., Pathirana, D., Fröhlich, F., Hasenauer, J., and Banga, J. R. "A Protocol for Dynamic Model Calibration". In: *Briefings in Bioinformatics* 23.1 (Jan. 17, 2022), bbab387. DOI: `10.1093/bib/bbab387`.

[29] Abt, V., Barz, T., Cruz, N., Herwig, C., Kroll, P., Möller, J., Pörtner, R., and Schenkendorf, R. "Model-Based Tools for Optimal Experiments in Bioprocess Engineering". In: *Current Opinion in Chemical Engineering* 22 (Dec. 2018), pp. 244–252. DOI: `10.1016/j.coche.2018.11.007`.

[30] Quaglio, M., Fraga, E. S., and Galvanin, F. "Model-Based Design of Experiments in the Presence of Structural Model Uncertainty: An Extended Information Matrix Approach". In: *Chemical Engineering Research and Design* 136 (Aug. 2018), pp. 129–143. DOI: `10.1016/j.cherd.2018.04.041`.

[31] Raue, A., Kreutz, C., Maiwald, T., Klingmüller, U., and Timmer, J. "Addressing Parameter Identifiability by Model-Based Experimentation". In: *IET Systems Biology* 5.2 (Mar. 1, 2011), pp. 120–130. DOI: `10.1049/iet-syb.2010.0061`.

[32]   Kreutz, C. and Timmer, J. "Systems Biology: Experimental Design". In: *FEBS Journal* 276.4 (Feb. 2009), pp. 923–942. DOI: `10.1111/j.1742-4658.2008.06843.x`.

[33]   Franceschini, G. and Macchietto, S. "Model-Based Design of Experiments for Parameter Precision: State of the Art". In: *Chemical Engineering Science* 63.19 (Oct. 2008), pp. 4846–4872. DOI: `10.1016/j.ces.2007.11.034`.

[34]   Vallerio, M., Telen, D., Cabianca, L., Manenti, F., Impe, J. V., and Logist, F. "Robust Multi-Objective Dynamic Optimization of Chemical Processes Using the Sigma Point Method". In: *Chemical Engineering Science* 140 (Feb. 2016), pp. 201–216. DOI: `10.1016/j.ces.2015.09.012`.

[35]   Razavi, S. et al. "The Future of Sensitivity Analysis: An Essential Discipline for Systems Modeling and Policy Support". In: *Environmental Modelling & Software* 137 (Mar. 2021), p. 104954. DOI: `10.1016/j.envsoft.2020.104954`.

[36]   Xie, X., Schenkendorf, R., and Krewer, U. "Efficient Sensitivity Analysis and Interpretation of Parameter Correlations in Chemical Engineering". In: *Reliability Engineering & System Safety* 187 (July 2019), pp. 159–173. DOI: `10.1016/j.ress.2018.06.010`.

[37]   Saltelli, A., Ratto, M., Andres, T., Campolongo, F., Cariboni, J., Gatelli, D., Saisana, M., and Tarantola, S. *Global Sensitivity Analysis. The Primer*. Chichester, UK: John Wiley & Sons, Ltd, Dec. 18, 2007. ISBN: 978-0-470-72518-4 978-0-470-05997-5. DOI: `10.1002/9780470725184`.

[38]   Maußner, J. and Freund, H. "Optimization under Uncertainty in Chemical Engineering: Comparative Evaluation of Unscented Transformation Methods and Cubature Rules". In: *Chemical Engineering Science* 183 (June 2018), pp. 329–345. DOI: `10.1016/j.ces.2018.02.002`.

[39]   Schuëller, G. and Jensen, H. "Computational Methods in Optimization Considering Uncertainties – An Overview". In: *Computer Methods in Applied Mechanics and Engineering* 198.1 (Nov. 2008), pp. 2–13. DOI: `10.1016/j.cma.2008.05.004`.

[40]   Grossmann, I. E. and Sargent, R. W. H. "Optimum Design of Chemical Plants with Uncertain Parameters". In: *AIChE Journal* 24.6 (Nov. 1978), pp. 1021–1028. DOI: `10.1002/aic.690240612`.

[41]   Ding, J., Tarokh, V., and Yang, Y. "Model Selection Techniques: An Overview". In: *IEEE Signal Processing Magazine* 35.6 (Nov. 2018), pp. 16–34. DOI: `10.1109/MSP.2018.2867638`.

[42]   Grossmann, I. E., Apap, R. M., Calfa, B. A., García-Herreros, P., and Zhang, Q. "Recent Advances in Mathematical Programming Techniques for the Optimization of Process Systems under Uncertainty". In: *Computers & Chemical Engineering* 91 (Aug. 2016), pp. 3–14. DOI: `10.1016/j.compchemeng.2016.03.002`.

[43]   Toni, T., Welch, D., Strelkowa, N., Ipsen, A., and Stumpf, M. P. "Approximate Bayesian Computation Scheme for Parameter Inference and Model Selection in Dynamical Systems". In: *Journal of The Royal Society Interface* 6.31 (Feb. 6, 2009), pp. 187–202. DOI: `10.1098/rsif.2008.0172`.

[44]   Lu, L., Meng, X., Mao, Z., and Karniadakis, G. E. "DeepXDE: A Deep Learning Library for Solving Differential Equations". In: *SIAM Review* 63.1 (Jan. 2021), pp. 208–228. DOI: `10.1137/19M1274067`.

[45]   Wang, Y., Biegler, L. T., Patel, M., and Wassick, J. "Parameters Estimation and Model Discrimination for Solid-Liquid Reactions in Batch Processes". In: *Chemical Engineering Science* (May 2018). DOI: `10.1016/j.ces.2018.05.040`.

[46]   Varziri, M., Poyton, A., McAuley, K., McLellan, P., and Ramsay, J. "Selecting Optimal Weighting Factors in iPDA for Parameter Estimation in Continuous-Time Dynamic Models". In: *Computers & Chemical Engineering* 32.12 (Dec. 2008), pp. 3011–3022. DOI: `10.1016/j.compchemeng.2008.04.005`.

[47]   Biegler, L. T. "An Overview of Simultaneous Strategies for Dynamic Optimization". In: *Chemical Engineering and Processing: Process Intensification* 46.11 (Nov. 2007), pp. 1043–1053. DOI: `10.1016/j.cep.2006.06.021`.

[48]   Fliess, M., Lévine, J., Martin, P., and Rouchon, P. "On Differentially Flat Nonlinear Systems". In: *IFAC Proceedings Volumes* 25.13 (June 1992), pp. 159–163. DOI: `10.1016/S1474-6670(17)52275-2`.

[49]   Schenkendorf, R. "Optimal Experimental Design for Paramter Identification and Model Selection". PhD thesis. Otto-von-Guericke-Universität Magdeburg, 2014.

[50]   Wey, T. *Nichtlineare Regelungssysteme: ein differentialalgebraischer Ansatz.* 1st ed. Stuttgart: Teubner, 2002. ISBN: 978-3-519-00395-3.

[51]   World Health Organization. *World Malaria Report 2021.* Geneva: World Health Organization, 2021. ISBN: 978-92-4-004049-6.

[52]   World Health Organization. *World Malaria Report 2015.* World Health Organization, 2015. ISBN: 978-92-4-156515-8.

[53]   Peplow, M. "Synthetic Malaria Drug Meets Market Resistance". In: *Nature* 530 (2016), pp. 389–390.

[54]   World Health Organization. *WHO Briefing on Malaria Treatment Guidelines and Artemisinin Monotherapies.* 2006, p. 28.

[55] ACTwatch Group, Tougher, S., Hanson, K., and Goodman, C. "What Happened to Anti-Malarial Markets after the Affordable Medicines Facility-malaria Pilot? Trends in ACT Availability, Price and Market Share from Five African Countries under Continuation of the Private Sector Co-Payment Mechanism". In: *Malaria Journal* 16.1 (Dec. 2017), p. 173. DOI: `10.1186/s12936-017-1814-z`.

[56] World Health Organization. *Global Malaria Diagnostic and Artemisinin Treatment Commodities Demand Forecast*. Forecast Report. World Health Organization (Unitaid), 2018.

[57] Martino, E., Tarantino, M., Bergamini, M., Castelluccio, V., Coricello, A., Falcicchio, M., Lorusso, E., and Collina, S. "Artemisinin and Its Derivatives; Ancient Tradition Inspiring the Latest Therapeutic Approaches against Malaria". In: *Future Medicinal Chemistry* 11.12 (June 2019), pp. 1443–1459. DOI: `10.4155/fmc-2018-0337`.

[58] Cheong, D. H., Tan, D. W., Wong, F. W., and Tran, T. "Anti-Malarial Drug, Artemisinin and Its Derivatives for the Treatment of Respiratory Diseases". In: *Pharmacological Research* 158 (Aug. 2020), p. 104901. DOI: `10.1016/j.phrs.2020.104901`.

[59] Pushpakom, S. et al. "Drug Repurposing: Progress, Challenges and Recommendations". In: *Nature Reviews Drug Discovery* 18.1 (Jan. 2019), pp. 41–58. DOI: `10.1038/nrd.2018.168`.

[60] Lévesque, F. and Seeberger, P. H. "Continuous-Flow Synthesis of the Anti-Malaria Drug Artemisinin". In: *Angewandte Chemie International Edition* 51.7 (Feb. 13, 2012), pp. 1706–1709. DOI: `10.1002/anie.201107446`.

[61] Triemer, S. "Reactive Transformation of Extraction Byproducts: Enhanced Production of the Antimalarial Artemisinin". PhD thesis. Magdeburg: Otto-von-Guericke-Universität Magdeburg, 2023. DOI: `10.25673/103427`. This work is licensed under CC BY-SA 4.0.

[62] Lapkin, A. A., Plucinski, P. K., and Cutler, M. "Comparative Assessment of Technologies for Extraction of Artemisinin". In: *Journal of Natural Products* 69.11 (Nov. 1, 2006), pp. 1653–1664. DOI: `10.1021/np060375j`.

[63] Kopetzki, D., Lévesque, F., and Seeberger, P. H. "A Continuous-Flow Process for the Synthesis of Artemisinin". In: *Chemistry - A European Journal* 19.17 (Apr. 22, 2013), pp. 5450–5456. DOI: `10.1002/chem.201204558`.

[64] Ferreira, J. F. S. and Luthria, D. L. "Drying Affects Artemisinin, Dihydroartemisinic Acid, Artemisinic Acid, and the Antioxidant Capacity of *Artemisia Annua* L. Leaves". In: *Journal of Agricultural and Food Chemistry* 58.3 (Feb. 10, 2010), pp. 1691–1698. DOI: `10.1021/jf903222j`.

[65]   Triemer, S., Gilmore, K., Vu, G. T., Seeberger, P. H., and Seidel-Morgenstern, A. "Literally Green Chemical Synthesis of Artemisinin from Plant Extracts". In: *Angewandte Chemie International Edition* 57.19 (May 4, 2018), pp. 5525–5528. DOI: `10.1002/anie.201801424`.

[66]   Politano, F. and Oksdath-Mansilla, G. "Light on the Horizon: Current Research and Future Perspectives in Flow Photochemistry". In: *Organic Process Research & Development* 22.9 (Sept. 21, 2018), pp. 1045–1062. DOI: `10.1021/acs.oprd.8b00213`.

[67]   Czechowski, T., Weathers, P. J., Brodelius, P. E., Brown, G. D., and Graham, I. A. "Editorial: Artemisinin—From Traditional Chinese Medicine to Artemisinin Combination Therapies; Four Decades of Research on the Biochemistry, Physiology, and Breeding of Artemisia Annua". In: *Frontiers in Plant Science* 11 (Sept. 18, 2020), p. 594565. DOI: `10.3389/fpls.2020.594565`.

[68]   Ferreira, J., Laughlin, J. C., Delabays, N., and de Magalhães, P. "Cultivation and Genetics of *Artemisia Annua* L. for Increased Production of the Antimalarial Artemisinin". In: *Plant Genetic Resources* 3.2 (Aug. 2005), pp. 206–229. DOI: `10.1079/PGR200585`.

[69]   Delabays, N., Simonnet, X., and Gaudin, M. "The Genetics of Artemisinin Content in Artemisia Annua L. and the Breeding of High Yielding Cultivars". In: *Current Medicinal Chemistry* 8.15 (Dec. 1, 2001), pp. 1795–1801. DOI: `10.2174/0929867013371635`.

[70]   Bhakuni, R. S., Jain, D. C., Sharms, R. P., and Kumar, S. "Secondary Metabolites of Artemisia Annua and Their Biological Activity". In: *Current Science* 80.1 (2001), p. 15.

[71]   Wani, K. I., Choudhary, S., Zehra, A., Naeem, M., Weathers, P., and Aftab, T. "Enhancing Artemisinin Content in and Delivery from Artemisia Annua: A Review of Alternative, Classical, and Transgenic Approaches". In: *Planta* 254.2 (Aug. 2021), p. 29. DOI: `10.1007/s00425-021-03676-3`.

[72]   Ferreira, J. F. S., Benedito, V. A., Sandhu, D., Marchese, J. A., and Liu, S. "Seasonal and Differential Sesquiterpene Accumulation in Artemisia Annua Suggest Selection Based on Both Artemisinin and Dihydroartemisinic Acid May Increase Artemisinin in Planta". In: *Frontiers in Plant Science* 9 (Aug. 13, 2018), p. 1096. DOI: `10.3389/fpls.2018.01096`.

[73]   Brown, G. D. "The Biosynthesis of Artemisinin (Qinghaosu) and the Phytochemistry of Artemisia Annua L. (Qinghao)". In: *Molecules* 15.11 (Oct. 28, 2010), pp. 7603–7698. DOI: `10.3390/molecules15117603`.

[74] Liu, K., Zuo, H., Li, G., Yu, H., and Hu, Y. "Global Research on Artemisinin and Its Derivatives: Perspectives from Patents". In: *Pharmacological Research* 159 (Sept. 2020), p. 105048. DOI: `10.1016/j.phrs.2020.105048`.

[75] Paddon, C. J. and Keasling, J. D. "Semi-Synthetic Artemisinin: A Model for the Use of Synthetic Biology in Pharmaceutical Development". In: *Nature Reviews Microbiology* 12.5 (May 2014), pp. 355–367. DOI: `10.1038/nrmicro3240`.

[76] Kjær, A., Verstappen, F., Bouwmeester, H., Ivarsen, E., Fretté, X., Christensen, L. P., Grevsen, K., and Jensen, M. "Artemisinin Production and Precursor Ratio in Full Grown Artemisia Annua L. Plants Subjected to External Stress". In: *Planta* 237.4 (Apr. 2013), pp. 955–966. DOI: `10.1007/s00425-012-1811-y`.

[77] Wallaart, T. E., Pras*, N., Beekman and, A. C., and Quax, W. J. "Seasonal Variation of Artemisinin and Its Biosynthetic Precursors in Plants of Artemisia Annua of Different Geographical Origin: Proof for the Existence of Chemotypes". In: *Planta Medica* 66.1 (Feb. 2000), pp. 57–62. DOI: `10.1055/s-2000-11115`.

[78] Ferreira, J. F. S. "Nutrient Deficiency in the Production of Artemisinin, Dihydroartemisinic Acid, and Artemisinic Acid in *Artemisia Annua* L." In: *Journal of Agricultural and Food Chemistry* 55.5 (Mar. 1, 2007), pp. 1686–1694. DOI: `10.1021/jf063017v`.

[79] Zhu, C. and Cook, S. P. "A Concise Synthesis of (+)-Artemisinin". In: *Journal of the American Chemical Society* 134.33 (Aug. 22, 2012), pp. 13577–13579. DOI: `10.1021/ja3061479`.

[80] Schmid, G. and Hofheinz, W. "Total Synthesis of Qinghaosu". In: *Journal of the American Chemical Society* 105.3 (Feb. 1983), pp. 624–625. DOI: `10.1021/ja00341a054`.

[81] Kung, S. H., Lund, S., Murarka, A., McPhee, D., and Paddon, C. J. "Approaches and Recent Developments for the Commercial Production of Semi-synthetic Artemisinin". In: *Frontiers in Plant Science* 9 (Jan. 31, 2018), p. 87. DOI: `10.3389/fpls.2018.00087`.

[82] Corsello, M. A. and Garg, N. K. "Synthetic Chemistry Fuels Interdisciplinary Approaches to the Production of Artemisinin". In: *Natural Product Reports* 32.3 (2015), pp. 359–366. DOI: `10.1039/C4NP00113C`.

[83] Acton, N. and Roth, R. J. "On the Conversion of Dihydroartemisinic Acid into Artemisinin". In: *The Journal of Organic Chemistry* 57.13 (June 1992), pp. 3610–3614. DOI: `10.1021/jo00039a020`.

[84] Roth, R. J. and Acton, N. "A Facile Semisynthesis of the Antimalarial Drug Qinghaosu". In: *Journal of Chemical Education* 68.7 (July 1991), p. 612. DOI: `10.1021/ed068p612`.

[85]   Roth, R. J. and Acton, N. "A Simple Conversion of Artemisinic Acid into Artemisinin".
        In: *Journal of Natural Products* 52.5 (Sept. 1989), pp. 1183–1185. DOI:
        10.1021/np50065a050.

[86]   Paddon, C. J. et al. "High-Level Semi-Synthetic Production of the Potent Antimalarial
        Artemisinin". In: *Nature* 496.7446 (Apr. 2013), pp. 528–532. DOI:
        10.1038/nature12051.

[87]   Brown, G. D. and Sy, L.-K. "In Vivo Transformations of Dihydroartemisinic Acid in
        Artemisia Annua Plants". In: *Tetrahedron* 60.5 (Jan. 2004), pp. 1139–1159. DOI:
        10.1016/j.tet.2003.11.070.

[88]   Martin, V. J. J., Pitera, D. J., Withers, S. T., Newman, J. D., and Keasling, J. D.
        "Engineering a Mevalonate Pathway in Escherichia Coli for Production of Terpenoids".
        In: *Nature Biotechnology* 21.7 (July 2003), pp. 796–802. DOI: 10.1038/nbt833.

[89]   Tsuruta, H., Paddon, C. J., Eng, D., Lenihan, J. R., Horning, T., Anthony, L. C.,
        Regentin, R., Keasling, J. D., Renninger, N. S., and Newman, J. D. "High-Level
        Production of Amorpha-4,11-Diene, a Precursor of the Antimalarial Agent Artemisinin,
        in Escherichia Coli". In: *PLoS ONE* 4.2 (Feb. 16, 2009). Ed. by Gregson, A., e4489.
        DOI: 10.1371/journal.pone.0004489.

[90]   Ro, D.-K. et al. "Production of the Antimalarial Drug Precursor Artemisinic Acid in
        Engineered Yeast". In: *Nature* 440.7086 (Apr. 13, 2006), pp. 940–943. DOI:
        10.1038/nature04640.

[91]   Turconi, J., Griolet, F., Guevel, R., Oddon, G., Villa, R., Geatti, A., Hvala, M.,
        Rossen, K., Göller, R., and Burgard, A. "Semisynthetic Artemisinin, the Chemical Path
        to Industrial Production". In: *Organic Process Research & Development* 18.3 (Mar. 21,
        2014), pp. 417–422. DOI: 10.1021/op4003196.

[92]   Peplow, M. "Looking for Cheaper Routes to Malaria Medicines – Efforts to Produce
        Low-Cost Synthetic Artemisinin Gain Momentum with Help from Gates Foundation".
        In: *Chemical & Engineering News* (2018).

[93]   Singh, D. et al. "Amalgamation of Synthetic Biology and Chemistry for
        High-Throughput Nonconventional Synthesis of the Antimalarial Drug Artemisinin".
        In: *Organic Process Research & Development* 21.4 (Apr. 21, 2017), pp. 551–558. DOI:
        10.1021/acs.oprd.6b00414.

[94]   Schwertz, G., Zanetti, A., de Oliveira, M. N., Fernandez, M. A. G., Amara, Z., and
        Cossy, J. "Chemo- and Diastereoselective Hydrosilylation of Amorphadiene toward the
        Synthesis of Artemisinin". In: *The Journal of Organic Chemistry* 85.15 (Aug. 7, 2020),
        pp. 9607–9613. DOI: 10.1021/acs.joc.0c00617.

[95]   Gomez Fernandez, M. A., Nascimento de Oliveira, M., Zanetti, A., Schwertz, G.,
         Cossy, J., and Amara, Z. "Photochemical Hydrothiolation of Amorphadiene and Formal
         Synthesis of Artemisinin via a Pummerer Rearrangement". In: *Organic Letters* 23.15
         (Aug. 6, 2021), pp. 5593–5598. DOI: `10.1021/acs.orglett.1c00636`.

[96]   Burgard, A., Gieshoff, T., Peschl, A., Hörstermann, D., Keleschovsky, C., Villa, R.,
         Michelis, S., and Feth, M. P. "Optimisation of the Photochemical Oxidation Step in the
         Industrial Synthesis of Artemisinin". In: *Chemical Engineering Journal* 294 (June
         2016), pp. 83–96. DOI: `10.1016/j.cej.2016.02.085`.

[97]   Plumb, K. "Continuous Processing in the Pharmaceutical Industry". In: *Chemical
         Engineering Research and Design* 83.6 (June 2005), pp. 730–738. DOI:
         `10.1205/cherd.04359`.

[98]   Lee, S. L., O'Connor, T. F., Yang, X., Cruz, C. N., Chatterjee, S., Madurawe, R. D.,
         Moore, C. M. V., Yu, L. X., and Woodcock, J. "Modernizing Pharmaceutical
         Manufacturing: From Batch to Continuous Production". In: *Journal of Pharmaceutical
         Innovation* 10.3 (Sept. 2015), pp. 191–199. DOI: `10.1007/s12247-015-9215-8`.

[99]   Aroh, K. C. and Jensen, K. F. "Efficient Kinetic Experiments in Continuous Flow
         Microreactors". In: *Reaction Chemistry & Engineering* 3.1 (2018), pp. 94–101. DOI:
         `10.1039/C7RE00163K`.

[100]   Su, Y., Straathof, N. J. W., Hessel, V., and Noël, T. "Photochemical Transformations
         Accelerated in Continuous-Flow Reactors: Basic Concepts and Applications". In:
         Chemistry - A European Journal 20.34 (Aug. 18, 2014), pp. 10562–10589. DOI:
         `10.1002/chem.201400283`.

[101]   Aillet, T., Loubiere, K., Dechy-Cabaret, O., and Prat, L. "Accurate Measurement of the
         Photon Flux Received Inside Two Continuous Flow Microphotoreactors by
         Actinometry". In: *International Journal of Chemical Reactor Engineering* 12.1 (Jan. 1,
         2014), pp. 257–269. DOI: `10.1515/ijcre-2013-0121`.

[102]   Loponov, K. N., Lopes, J., Barlog, M., Astrova, E. V., Malkov, A. V., and Lapkin, A. A.
         "Optimization of a Scalable Photochemical Reactor for Reactions with Singlet Oxygen".
         In: *Organic Process Research & Development* 18.11 (Nov. 21, 2014), pp. 1443–1454.
         DOI: `10.1021/op500181z`.

[103]   Mascia, S. et al. "End-to-End Continuous Manufacturing of Pharmaceuticals: Integrated
         Synthesis, Purification, and Final Dosage Formation". In: *Angewandte Chemie
         International Edition* 52.47 (Nov. 18, 2013), pp. 12359–12363. DOI:
         `10.1002/anie.201305429`.

[104]   Lehr, A., Janiga, G., Seidel-Morgenstern, A., and Thévenin, D. "CFD Simulation of a Solid-Liquid Counter-Current Screw Extractor". In: *Computer Aided Chemical Engineering*. Vol. 48. Elsevier, 2020, pp. 223–228. ISBN: 978-0-12-823377-1. DOI: 10.1016/B978-0-12-823377-1.50038-0.

[105]   Kopetzki, D., McQuade, D. T., Seeberger, P. H., and Gilmore, K. "Method and Apparatus for the Synthesis of Dihydroartemisinin and Artemisinin Derivatives". European pat. 2 826 779 A1. 2015.

[106]   Gilmore, K., Kopetzki, D., Lee, J. W., Horváth, Z., McQuade, D. T., Seidel-Morgenstern, A., and Seeberger, P. H. "Continuous Synthesis of Artemisinin-Derived Medicines". In: *Chem. Commun.* 50.84 (2014), pp. 12652–12655. DOI: 10.1039/C4CC05098C.

[107]   Horváth, Z., Horosanskaia, E., Lee, J. W., Lorenz, H., Gilmore, K., Seeberger, P. H., and Seidel-Morgenstern, A. "Recovery of Artemisinin from a Complex Reaction Mixture Using Continuous Chromatography and Crystallization". In: *Organic Process Research & Development* 19.6 (June 19, 2015), pp. 624–634. DOI: 10.1021/acs.oprd.5b00048.

[108]   Triemer, S., Schulze, M., Wriedt, B., Schenkendorf, R., Ziegenbalg, D., Krewer, U., and Seidel-Morgenstern, A. "Kinetic Analysis of the Partial Synthesis of Artemisinin: Photooxygenation to the Intermediate Hydroperoxide". In: *Journal of Flow Chemistry* 11.3 (2021), pp. 641–659. DOI: 10.1007/s41981-021-00181-2. This article is an open access article distributed under CC BY 4.0.

[109]   Münzberg, S., Vu, T. G., and Seidel-Morgenstern, A. "Generalizing Countercurrent Processes: Distillation and Beyond". In: *Chemie Ingenieur Technik* 90.11 (Nov. 2018), pp. 1769–1781. DOI: 10.1002/cite.201800132.

[110]   Schulze, M. and Schenkendorf, R. "Robust Model Selection: Flatness-Based Optimal Experimental Design for a Biocatalytic Reaction". In: *Processes* 8.2 (2020), pp. 233–238. DOI: 10.3390/pr8020190. This article is an open access article distributed under CC BY 4.0.

[111]   Takamatsu, T. "The Nature and Role of Process Systems Engineering". In: *Computers & Chemical Engineering* 7.4 (Jan. 1983), pp. 203–218. DOI: 10.1016/0098-1354(83)80012-X.

[112]   Ponton, J. "Process Systems Engineering: Halfway through the First Century". In: *Chemical Engineering Science* 50.24 (Dec. 1995), pp. 4045–4059. DOI: 10.1016/0009-2509(96)81832-X.

[113]   Klatt, K.-U. and Marquardt, W. "Perspectives for Process Systems Engineering—Personal Views from Academia and Industry". In: *Computers & Chemical Engineering* 33.3 (Mar. 2009), pp. 536–550. DOI: 10.1016/j.compchemeng.2008.09.002.

[114] Emenike, V. N., Xie, X., Schenkendorf, R., Spiess, A. C., and Krewer, U. "Robust Dynamic Optimization of Enzyme-Catalyzed Carboligation: A Point Estimate-Based Back-off Approach". In: *Computers & Chemical Engineering* 121 (2019), pp. 232–247. DOI: `10.1016/j.compchemeng.2018.10.006`.

[115] Kroll, P., Hofer, A., Ulonska, S., Kager, J., and Herwig, C. "Model-Based Methods in the Biopharmaceutical Process Lifecycle". In: *Pharmaceutical Research* 34.12 (Dec. 2017), pp. 2596–2613. DOI: `10.1007/s11095-017-2308-y`.

[116] Pörtner, R., Barradas, O. P., Frahm, B., and Hass, V. "16 - Advanced Process and Control Strategies for Bioreactors". In: *Current Developments in Biotechnology and Bioengineering*. Ed. by Larroche, C., Sanromán, M. Á., Du, G., and Pandey, A. Elsevier, 2017, pp. 463–493. ISBN: 978-0-444-63663-8. DOI: `10.1016/B978-0-444-63663-8.00016-1`.

[117] Asprey, S. and Macchietto, S. "Statistical Tools for Optimal Dynamic Model Building". In: *Computers & Chemical Engineering* 24.2-7 (July 2000), pp. 1261–1267. DOI: `10.1016/S0098-1354(00)00328-8`.

[118] Nelles, O. *Nonlinear System Identification: From Classical Approaches to Neural Networks and Fuzzy Models*. Berlin; London: Springer, 2011. ISBN: 978-3-642-08674-8.

[119] James, G., Witten, D., Hastie, T., Tibshirani, R., and Taylor, J. *An Introduction to Statistical Learning: With Applications in Python*. Springer Texts in Statistics. Cham: Springer International Publishing, 2023. ISBN: 978-3-031-38746-3 978-3-031-38747-0. DOI: `10.1007/978-3-031-38747-0`.

[120] Burnham, K. P., Anderson, D. R., and Burnham, K. P. *Model Selection and Multimodel Inference: A Practical Information-Theoretic Approach*. 2nd ed. New York: Springer, 2002. ISBN: 978-0-387-95364-9.

[121] Stamati, I., Logist, F., Akkermans, S., Fernández, E. N., and Impe, J. V. "On the Effect of Sampling Rate and Experimental Noise in the Discrimination between Microbial Growth Models in the Suboptimal Temperature Range". In: *Computers & Chemical Engineering* 85 (2016), pp. 84–93. DOI: `10.1016/j.compchemeng.2015.10.005`.

[122] Telen, D., Logist, F., Van Derlinden, E., and Van Impe, J. "Approximate Robust Optimal Experiment Design in Dynamic Bioprocess Models". In: *2012 20th Mediterranean Conference on Control & Automation (MED)*. 2012 20th Mediterranean Conference on Control & Automation (MED 2012). Barcelona, Spain: IEEE, July 2012, pp. 157–162. ISBN: 978-1-4673-2531-8 978-1-4673-2530-1 978-1-4673-2529-5. DOI: `10.1109/MED.2012.6265631`.

[123] Skanda, D. and Lebiedz, D. "An Optimal Experimental Design Approach to Model Discrimination in Dynamic Biochemical Systems". In: *Bioinformatics* 26.7 (Apr. 1, 2010), pp. 939–945. DOI: `10.1093/bioinformatics/btq074`.

[124] Ljung, L. *System Identification: Theory for the User*. 2nd ed. Prentice Hall Information and System Sciences Series. Upper Saddle River, NJ: Prentice Hall PTR, 1999. ISBN: 978-0-13-656695-3.

[125] Seidel-Morgenstern, A. "Analysis and Experimental Investigation of Catalytic Membrane Reactors". In: *Integrated Chemical Processes*. Ed. by Sundmacher, K., Kienle, A., and Seidel-Morgenstern, A. Weinheim, FRG: Wiley-VCH Verlag GmbH & Co. KGaA, Nov. 3, 2005, pp. 359–389. ISBN: 978-3-527-60573-6 978-3-527-30831-6. DOI: 10.1002/3527605738.ch12.

[126] Jakobsen, H. A. *Chemical Reactor Modeling: Multiphase Reactive Flows*. Second edition. Cham: Springer, 2014. ISBN: 978-3-319-05091-1.

[127] Bendiksen, K. H., Maines, D., Moe, R., and Nuland, S. "The Dynamic Two-Fluid Model OLGA: Theory and Application". In: *SPE Production Engineering* 6.02 (May 1, 1991), pp. 171–180. DOI: 10.2118/19451-PA.

[128] Ishii, M. and Hibiki, T. *Thermo-Fluid Dynamics of Two-Phase Flow*. New York, N.Y: Springer Science+Business Media, 2006. ISBN: 978-0-387-28321-0 978-0-387-29187-1.

[129] Gupta, R., Fletcher, D., and Haynes, B. "Taylor Flow in Microchannels: A Review of Experimental and Computational Work". In: *The Journal of Computational Multiphase Flows* 2.1 (Mar. 2010), pp. 1–31. DOI: 10.1260/1757-482X.2.1.1.

[130] Wörner, M. "Numerical Modeling of Multiphase Flows in Microfluidics and Micro Process Engineering: A Review of Methods and Applications". In: *Microfluidics and Nanofluidics* 12.6 (May 2012), pp. 841–886. DOI: 10.1007/s10404-012-0940-8.

[131] Kreutzer, M. T., Kapteijn, F., and Moulijn, J. A. "Fast Gas–Liquid–Solid Reactions in Monoliths: A Case Study of Nitro-Aromatic Hydrogenation". In: *Catalysis Today* (2005), p. 8.

[132] Cao, B. and Luo, L. "Modeling of Gas Liquid Taylor Flow in Capillaries by Using a Two Fluid Model". In: *Ind. Eng. Chem. Res.* (2012), p. 8.

[133] Peixoto, R. A. and Bullard, C. W. "A Simulation and Design Model for Capillary Tube - Suction Line Heat Exchangers". In: International Refigeration and Air Conditioning Conference. 1994, p. 7.

[134] Xu, B. and Bansal, P. "Non-Adiabatic Capillary Tube Flow: A Homogeneous Model and Process Description". In: *Applied Thermal Engineering* 22.16 (Nov. 2002), pp. 1801–1819. DOI: 10.1016/S1359-4311(02)00110-2.

[135] Zareh, M., Khayat, M., and Fouladi, H. "Numerical Simulation of Two Phase Refrigerant Flow through Non-Adiabatic Capillary Tubes Using Drift Flux Model". In: *Journal of Mechanical Science and Technology* 32.1 (Jan. 2018), pp. 381–389. DOI: 10.1007/s12206-017-1238-2.

[136]   Zhang, W., Hibiki, T., and Mishima, K. "Correlations of Two-Phase Frictional Pressure Drop and Void Fraction in Mini-Channel". In: *International Journal of Heat and Mass Transfer* (2010), p. 13.

[137]   Sandler, S. I. *Chemical, Biochemical, and Engineering Thermodynamics*. 4th ed. Hoboken, N.J: John Wiley, 2006. ISBN: 978-0-471-66174-0.

[138]   Maria, G. "A Review of Algorithms and Trends in Kinetic Model Identification for Chemical and Biochemical Systems". In: *Chemical and Biochemical Engineering Quarterly* 18.3 (2004), pp. 195–222.

[139]   Loskot, P., Atitey, K., and Mihaylova, L. "Comprehensive Review of Models and Methods for Inferences in Bio-Chemical Reaction Networks". In: *Frontiers in Genetics* 10 (June 14, 2019), p. 549. DOI: 10.3389/fgene.2019.00549.

[140]   Wakefield, J. *Bayesian and Frequentist Regression Methods*. Springer Series in Statistics. New York, NY: Springer New York, 2013. ISBN: 978-1-4419-0924-4 978-1-4419-0925-1. DOI: 10.1007/978-1-4419-0925-1.

[141]   Kay, S. M. *Fundamentals Of Statistical Signal Processing: Estimation Theory*. 1993.

[142]   Aldrich, J. "R.A. Fisher and the Making of Maximum Likelihood 1912-1922". In: *Statistical Science* 12.3 (Sept. 1, 1997). DOI: 10.1214/ss/1030037906.

[143]   Fisher, R. A. "On the Mathematical Foundations of Theoretical Statistics". In: *Philosophical Transactions of the Royal Society of London A* 222.594-604 (Jan. 1922), pp. 309–368. DOI: 10.1098/rsta.1922.0009.

[144]   Efron, B. and Hinkley, D. V. "Assessing the Accuracy of the Maximum Likelihood Estimator: Observed versus Expected Fisher Information". In: *Biometrika* 65.3 (1978), pp. 457–483. DOI: 10.1093/biomet/65.3.457.

[145]   Verheijen, P. J. "Model Selection: An Overview of Practices in Chemical Engineering". In: *Computer Aided Chemical Engineering* 16 (2003), pp. 85–104.

[146]   Doherty, P. F., White, G. C., and Burnham, K. P. "Comparison of Model Building and Selection Strategies". In: *Journal of Ornithology* 152.S2 (Feb. 2012), pp. 317–323. DOI: 10.1007/s10336-010-0598-5.

[147]   Lorenz, S., Diederichs, E., Telgmann, R., and Schütte, C. "Discrimination of Dynamical System Models for Biological and Chemical Processes: Discrimination of Dynamical System Models". In: *Journal of Computational Chemistry* 28.8 (June 2007), pp. 1384–1399. DOI: 10.1002/jcc.20674.

[148]   Schöniger, A., Wöhling, T., Samaniego, L., and Nowak, W. "Model Selection on Solid Ground: Rigorous Comparison of Nine Ways to Evaluate Bayesian Model Evidence". In: *Water Resources Research* 50.12 (Dec. 2014), pp. 9484–9513. DOI: 10.1002/2014WR016062.

[149] Rao, M. M. and Swift, R. J. *Probability Theory with Applications*. 2nd ed. Mathematics and Its Applications v. 582. New York: Springer, 2006. ISBN: 978-0-387-27730-1 978-0-387-27731-8.

[150] McLean, K. A. P. and McAuley, K. B. "Mathematical Modelling of Chemical Processes-Obtaining the Best Model Predictions and Parameter Estimates Using Identifiability and Estimability Procedures". In: *The Canadian Journal of Chemical Engineering* 90.2 (Apr. 2012), pp. 351–366. DOI: `10.1002/cjce.20660`.

[151] Janzén, D. L. I., Bergenholm, L., Jirstrand, M., Parkinson, J., Yates, J., Evans, N. D., and Chappell, M. J. "Parameter Identifiability of Fundamental Pharmacodynamic Models". In: *Frontiers in Physiology* 7 (Dec. 5, 2016). DOI: `10.3389/fphys.2016.00590`.

[152] Hines, K. E., Middendorf, T. R., and Aldrich, R. W. "Determination of Parameter Identifiability in Nonlinear Biophysical Models: A Bayesian Approach". In: *Journal of General Physiology* 143.3 (Mar. 1, 2014), pp. 401–416. DOI: `10.1085/jgp.201311116`.

[153] Miao, H., Xia, X., Perelson, A. S., and Wu, H. "On Identifiability of Nonlinear ODE Models and Applications in Viral Dynamics". In: *SIAM Review* 53.1 (Jan. 2011), pp. 3–39. DOI: `10.1137/090757009`.

[154] Chis, O.-T., Banga, J. R., and Balsa-Canto, E. "Structural Identifiability of Systems Biology Models: A Critical Comparison of Methods". In: *PLoS ONE* 6.11 (Nov. 22, 2011). Ed. by Jaeger, J., e27755. DOI: `10.1371/journal.pone.0027755`.

[155] Bellu, G., Saccomani, M. P., Audoly, S., and D'Angiò, L. "DAISY: A New Software Tool to Test Global Identifiability of Biological and Physiological Systems". In: *Computer Methods and Programs in Biomedicine* 88.1 (Oct. 2007), pp. 52–61. DOI: `10.1016/j.cmpb.2007.07.002`.

[156] Ligon, T. S., Fröhlich, F., Chiş, O. T., Banga, J. R., Balsa-Canto, E., and Hasenauer, J. "GenSSI 2.0: Multi-Experiment Structural Identifiability Analysis of SBML Models". In: *Bioinformatics* 34.8 (Apr. 15, 2018). Ed. by Wren, J., pp. 1421–1423. DOI: `10.1093/bioinformatics/btx735`.

[157] Guillaume, J. H. et al. "Introductory Overview of Identifiability Analysis: A Guide to Evaluating Whether You Have the Right Type of Data for Your Modeling Purpose". In: *Environmental Modelling & Software* 119 (Sept. 2019), pp. 418–432. DOI: `10.1016/j.envsoft.2019.07.007`.

[158] Jacquez, J. A. and Perry, T. "Parameter Estimation: Local Identifiability of Parameters". In: *American Journal of Physiology-Endocrinology and Metabolism* 258.4 (Apr. 1, 1990), E727–E736. DOI: `10.1152/ajpendo.1990.258.4.E727`.

[159]   Stigter, J. D., Joubert, D., and Molenaar, J. "Observability of Complex Systems: Finding the Gap". In: *Scientific Reports* 7.1 (Dec. 2017). DOI: `10.1038/s41598-017-16682-x`.

[160]   Miao, H., Dykes, C., Demeter, L. M., Cavenaugh, J., Park, S. Y., Perelson, A. S., and Wu, H. "Modeling and Estimation of Kinetic Parameters and Replicative Fitness of HIV-1 from Flow-Cytometry-Based Growth Competition Experiments". In: *Bulletin of Mathematical Biology* 70.6 (Aug. 2008), pp. 1749–1771. DOI: `10.1007/s11538-008-9323-4`.

[161]   Joshi, M., Seidel-Morgenstern, A., and Kremling, A. "Exploiting the Bootstrap Method for Quantifying Parameter Confidence Intervals in Dynamical Systems". In: *Metabolic Engineering* 8.5 (Sept. 2006), pp. 447–455. DOI: `10.1016/j.ymben.2006.04.003`.

[162]   Balsa-Canto, E., Alonso, A. A., and Banga, J. R. "An Iterative Identification Procedure for Dynamic Modeling of Biochemical Networks". In: *BMC Systems Biology* 4.1 (Dec. 2010), p. 11. DOI: `10.1186/1752-0509-4-11`.

[163]   Raue, A., Kreutz, C., Maiwald, T., Bachmann, J., Schilling, M., Klingmüller, U., and Timmer, J. "Structural and Practical Identifiability Analysis of Partially Observed Dynamical Models by Exploiting the Profile Likelihood". In: *Bioinformatics* 25.15 (Aug. 1, 2009), pp. 1923–1929. DOI: `10.1093/bioinformatics/btp358`.

[164]   Simpson, M. J., Browning, A. P., Warne, D. J., Maclaren, O. J., and Baker, R. E. "Parameter Identifiability and Model Selection for Sigmoid Population Growth Models". In: *Journal of Theoretical Biology* 535 (Feb. 2022), p. 110998. DOI: `10.1016/j.jtbi.2021.110998`.

[165]   Meeker, W. Q. and Escobar, L. A. "Teaching about Approximate Confidence Regions Based on Maximum Likelihood Estimation". In: *The American Statistician* 49.1 (1995), pp. 48–53.

[166]   Schenkendorf, R., Xie, X., Rehbein, M., Scholl, S., and Krewer, U. "The Impact of Global Sensitivities and Design Measures in Model-Based Optimal Experimental Design". In: *Processes* 6.4 (Mar. 21, 2018), p. 27. DOI: `10.3390/pr6040027`.

[167]   Xie, X. and Schenkendorf, R. "Robust Optimization of a Pharmaceutical Freeze-Drying Process under Non-Gaussian Parameter Uncertainties". In: *Chemical Engineering Science* 207 (Nov. 2019), pp. 805–819. DOI: `10.1016/j.ces.2019.06.023`.

[168]   Galvanin, F., Barolo, M., Bezzo, F., and Macchietto, S. "A Backoff Strategy for Model-Based Experiment Design under Parametric Uncertainty". In: *AIChE Journal* (2009), NA–NA. DOI: `10.1002/aic.12138`.

[169]   Barz, T., C., D. C. L., Bournazou, M. N. C., Körkel, S., and Walter, S. F. "Real-Time Adaptive Input Design for the Determination of Competitive Adsorption Isotherms in Liquid Chromatography". In: *Computers & Chemical Engineering* 94 (2016), pp. 104–116. DOI: `10.1016/j.compchemeng.2016.07.009`.

[170]   Jost, F., Sager, S., and Le, T. "A Feedback Optimal Control Algorithm with Optimal Measurement Time Points". In: *Processes* 5.4 (Feb. 28, 2017), p. 10. DOI: `10.3390/pr5010010`.

[171]   Xiangzhong, X. "Sensitivity Analysis and Robust Design of Pharmaceutical Manufacturing Processes". PhD thesis. TU Braunschweig, 2020.

[172]   Brunetti, C. and Linde, N. "Impact of Petrophysical Uncertainty on Bayesian Hydrogeophysical Inversion and Model Selection". In: *Advances in Water Resources* 111 (Jan. 2018), pp. 346–359. DOI: `10.1016/j.advwatres.2017.11.028`.

[173]   Lerner, U. N. "Hybrid Bayesian Networks for Reasoning about Complex Systems". PhD thesis. California, USA: Stanford University, 2002.

[174]   Xie, X., Zhang, Z., Hu, Y., and Cheng, H. "A Mechanistic Kinetic Model for Singlet Oxygen Mediated Self-Sensitized Photo-Oxidation of Organic Pollutants in Water". In: *Chemical Engineering Journal* 334 (Feb. 2018), pp. 1242–1251. DOI: `10.1016/j.cej.2017.11.070`.

[175]   Xie, X. and Schenkendorf, R. "Robust Process Design in Pharmaceutical Manufacturing under Batch-to-Batch Variation". In: *Processes* 7.8 (Aug. 3, 2019), p. 509. DOI: `10.3390/pr7080509`.

[176]   Turányi, T. "Sensitivity Analysis of Complex Kinetic Systems. Tools and Applications". In: *Journal of Mathematical Chemistry* 5.3 (Sept. 1990), pp. 203–248. DOI: `10.1007/BF01166355`.

[177]   Lakerveld, R., Benyahia, B., Braatz, R. D., and Barton, P. I. "Model-Based Design of a Plant-Wide Control Strategy for a Continuous Pharmaceutical Plant". In: *AIChE Journal* 59.10 (Oct. 2013), pp. 3671–3685. DOI: `10.1002/aic.14107`.

[178]   Saltelli, A., Aleksankina, K., Becker, W., Fennell, P., Ferretti, F., Holst, N., Li, S., and Wu, Q. "Why so Many Published Sensitivity Analyses Are False: A Systematic Review of Sensitivity Analysis Practices". In: *Environmental Modelling & Software* 114 (Apr. 2019), pp. 29–39. DOI: `10.1016/j.envsoft.2019.01.012`.

[179]   Borgonovo, E. and Plischke, E. "Sensitivity Analysis: A Review of Recent Advances". In: *European Journal of Operational Research* 248.3 (Feb. 2016), pp. 869–887. DOI: `10.1016/j.ejor.2015.06.032`.

[180]   Iooss, B. and Lemaître, P. "A Review on Global Sensitivity Analysis Methods". In: *Uncertainty Management in Simulation-Optimization of Complex Systems*. Ed. by Dellino, G. and Meloni, C. Vol. 59. Boston, MA: Springer US, 2015, pp. 101–122. ISBN: 978-1-4899-7546-1 978-1-4899-7547-8. DOI: `10.1007/978-1-4899-7547-8_5`.

[181]   Pianosi, F., Beven, K., Freer, J., Hall, J. W., Rougier, J., Stephenson, D. B., and Wagener, T. "Sensitivity Analysis of Environmental Models: A Systematic Review with Practical Workflow". In: *Environmental Modelling & Software* 79 (May 2016), pp. 214–232. DOI: `10.1016/j.envsoft.2016.02.008`.

[182]   Sudret, B., Marelli, S., and Wiart, J. "Surrogate Models for Uncertainty Quantification: An Overview". In: *2017 11th European Conference on Antennas and Propagation (EUCAP)*. IEEE, 2017, pp. 793–797.

[183]   Oakley, J. E. and O'Hagan, A. "Probabilistic Sensitivity Analysis of Complex Models: A Bayesian Approach". In: *Journal of the Royal Statistical Society: Series B (Statistical Methodology)* 66.3 (Aug. 2004), pp. 751–769. DOI: `10.1111/j.1467-9868.2004.05304.x`.

[184]   Snowden, T. J., van der Graaf, P. H., and Tindall, M. J. "Methods of Model Reduction for Large-Scale Biological Systems: A Survey of Current Methods and Trends". In: *Bulletin of Mathematical Biology* 79.7 (July 2017), pp. 1449–1486. DOI: `10.1007/s11538-017-0277-2`.

[185]   Sobol', I. M. "Sensitivity Estimates for Nonlinear Mathematical Models". In: *Mathematical Modelling and Computational Experiments* 4 (1993), pp. 407–414.

[186]   Saltelli, A., Annoni, P., Azzini, I., Campolongo, F., Ratto, M., and Tarantola, S. "Variance Based Sensitivity Analysis of Model Output. Design and Estimator for the Total Sensitivity Index". In: *Computer Physics Communications* 181.2 (Feb. 2010), pp. 259–270. DOI: `10.1016/j.cpc.2009.09.018`.

[187]   Saltelli, A. and Tarantola, S. "On the Relative Importance of Input Factors in Mathematical Models: Safety Assessment for Nuclear Waste Disposal". In: *Journal of the American Statistical Association* 97.459 (Sept. 2002), pp. 702–709. DOI: `10.1198/016214502388618447`.

[188]   Lebrun, R. and Dutfoy, A. "Do Rosenblatt and Nataf Isoprobabilistic Transformations Really Differ?" In: *Probabilistic Engineering Mechanics* 24.4 (Oct. 2009), pp. 577–584. DOI: `10.1016/j.probengmech.2009.04.006`.

[189]   Xie, X., Ohs, R., Spieß, A., Krewer, U., and Schenkendorf, R. "Moment-Independent Sensitivity Analysis of Enzyme-Catalyzed Reactions with Correlated Model Parameters". In: *IFAC-PapersOnLine* 51.2 (2018), pp. 753–758. DOI: `10.1016/j.ifacol.2018.04.004`.

[190] Li, G., Rabitz, H., Yelvington, P. E., Oluwole, O. O., Bacon, F., Kolb, C. E., and Schoendorf, J. "Global Sensitivity Analysis for Systems with Independent and/or Correlated Inputs". In: *The Journal of Physical Chemistry A* 114.19 (May 20, 2010), pp. 6022–6032. DOI: `10.1021/jp9096919`.

[191] Flassig, R. J. and Sundmacher, K. "Optimal Design of Stimulus Experiments for Robust Discrimination of Biochemical Reaction Networks". In: *Bioinformatics* 28.23 (Dec. 1, 2012), pp. 3089–3096. DOI: `10.1093/bioinformatics/bts585`.

[192] Galvanin, F., Ballan, C. C., Barolo, M., and Bezzo, F. "A General Model-Based Design of Experiments Approach to Achieve Practical Identifiability of Pharmacokinetic and Pharmacodynamic Models". In: *Journal of Pharmacokinetics and Pharmacodynamics* 40.4 (Aug. 2013), pp. 451–467. DOI: `10.1007/s10928-013-9321-5`.

[193] Barz, T., Arellano-Garcia, H., and Wozny, G. "Handling Uncertainty in Model-Based Optimal Experimental Design". In: *Industrial & Engineering Chemistry Research* 49.12 (June 16, 2010), pp. 5702–5713. DOI: `10.1021/ie901611b`.

[194] Montgomery, D. C. *Design and Analysis of Experiments*. Eighth edition. Hoboken, NJ: John Wiley & Sons, Inc, 2013. ISBN: 978-1-118-14692-7.

[195] Möller, J., Kuchemüller, K. B., Steinmetz, T., Koopmann, K. S., and Pörtner, R. "Model-Assisted Design of Experiments as a Concept for Knowledge-Based Bioprocess Development". In: *Bioprocess and Biosystems Engineering* 42.5 (May 2019), pp. 867–882. DOI: `10.1007/s00449-019-02089-7`.

[196] Telen, D., Nimmegeers, P., and Impe, J. V. "Uncertainty in Optimal Experiment Design: Comparing an Online versus Offline Approaches". In: *IFAC-PapersOnLine* 51.2 (2018), pp. 771–776. DOI: `10.1016/j.ifacol.2018.04.007`.

[197] Schwaab, M., Luiz Monteiro, J., and Carlos Pinto, J. "Sequential Experimental Design for Model Discrimination". In: *Chemical Engineering Science* 63.9 (May 2008), pp. 2408–2419. DOI: `10.1016/j.ces.2008.01.032`.

[198] Chen, B. H. and Asprey, S. P. "On the Design of Optimally Informative Dynamic Experiments for Model Discrimination in Multiresponse Nonlinear Situations". In: *Industrial & Engineering Chemistry Research* 42.7 (Apr. 2003), pp. 1379–1390. DOI: `10.1021/ie0203025`.

[199] Mélykúti, B., August, E., Papachristodoulou, A., and El-Samad, H. "Discriminating between Rival Biochemical Network Models: Three Approaches to Optimal Experiment Design". In: *BMC systems biology* 4.1 (2010), p. 38.

[200] Kikuchi, C. P., Ferré, T. P. A., and Vrugt, J. A. "On the Optimal Design of Experiments for Conceptual and Predictive Discrimination of Hydrologic System Models". In: *Water Resources Research* 51.6 (June 2015), pp. 4454–4481. DOI: `10.1002/2014WR016795`.

[201]   Vanlier, J., Tiemann, C. A., Hilbers, P. A., and van Riel, N. A. "Optimal Experiment Design for Model Selection in Biochemical Networks". In: *BMC Systems Biology* 8.1 (2014), p. 20. DOI: `10.1186/1752-0509-8-20`.

[202]   Burnham, K. P., Anderson, D. R., and Huyvaert, K. P. "AIC Model Selection and Multimodel Inference in Behavioral Ecology: Some Background, Observations, and Comparisons". In: *Behavioral Ecology and Sociobiology* 65.1 (Jan. 2011), pp. 23–35. DOI: `10.1007/s00265-010-1029-6`.

[203]   Stegmaier, J., Skanda, D., and Lebiedz, D. "Robust Optimal Design of Experiments for Model Discrimination Using an Interactive Software Tool". In: *PLoS ONE* 8.2 (Feb. 4, 2013). Ed. by Pappalardo, F., e55723. DOI: `10.1371/journal.pone.0055723`.

[204]   Pronzato, L. "Optimal Experimental Design and Some Related Control Problems". In: *Automatica* 44.2 (2008), pp. 303–325.

[205]   Biegler, L. T. *Nonlinear Programming: Concepts, Algorithms, and Applications to Chemical Processes*. MOS-SIAM Series on Optimization. SIAM, 2010. ISBN: 978-0-89871-702-0.

[206]   Biegler, L. T. and Grossmann, I. E. "Retrospective on Optimization". In: *Computers & Chemical Engineering* 28.8 (July 2004), pp. 1169–1192. DOI: `10.1016/j.compchemeng.2003.11.003`.

[207]   Nocedal, J. and Wright, S. J. *Numerical Optimization*. 2nd ed. Springer Series in Operations Research. New York: Springer, 2006. ISBN: 978-0-387-30303-1.

[208]   Wächter, A. and Biegler, L. T. "On the Implementation of an Interior-Point Filter Line-Search Algorithm for Large-Scale Nonlinear Programming". In: *Mathematical Programming* 106.1 (Mar. 2006), pp. 25–57. DOI: `10.1007/s10107-004-0559-y`.

[209]   K Mogensen, P. and N Riseth, A. "Optim: A Mathematical Optimization Package for Julia". In: *Journal of Open Source Software* 3.24 (Apr. 4, 2018), p. 615. DOI: `10.21105/joss.00615`.

[210]   Bezanson, J., Edelman, A., Karpinski, S., and Shah, V. B. "Julia: A Fresh Approach to Numerical Computing". In: *SIAM Review* 59.1 (Jan. 2017), pp. 65–98. DOI: `10.1137/141000671`.

[211]   Araki, Y., Dobrowolski, D. C., Goyne, T. E., Hanson, D. C., Jiang, Z. Q., Lee, K. J., and Foote, C. S. "Chemistry of Singlet Oxygen. 47. 9,10-Dicyanoanthracene-sensitized Photooxygenation of Alkyl-Substituted Olefins". In: *Journal of the American Chemical Society* 106.16 (Aug. 1984), pp. 4570–4575. DOI: `10.1021/ja00328a045`.

[212]   Kanner, R. C. and Foote, C. S. "Singlet Oxygen Production from Singlet and Triplet States of 9,10-Dicyanoanthracene". In: *Journal of the American Chemical Society* 114.2 (Jan. 1992), pp. 678–681. DOI: `10.1021/ja00028a040`.

[213] Dobrowolski, D. C., Ogilby, P. R., and Foote, C. S. "Chemistry of Singlet Oxygen. 39. 9,10-Dicyanoanthracene-sensitized Formation of Singlet Oxygen". In: *The Journal of Physical Chemistry* 87.13 (June 1983), pp. 2261–2263. DOI: `10.1021/j100236a001`.

[214] Scurlock, R. D. and Ogilby, P. R. "Production of Singlet Oxygen (1Δg O2) by 9,10-Dicyanoanthracene and Acridine: Quantum Yields in Acetonitrile". In: *Journal of Photochemistry and Photobiology A: Chemistry* 72.1 (May 1993), pp. 1–7. DOI: `10.1016/1010-6030(93)85077-L`.

[215] Breitmaier, E. and Jung, G. *Organische Chemie: Grundlagen, Verbindungsklassen, Reaktionen, Konzepte, Molekülstruktur, Naturstoffe, Syntheseplanung, Nachhaltigkeit*. 7. ed. Georg Thieme Verlag, 2012. ISBN: 978-3-13-541507-9.

[216] Sy, L.-K. and Brown, G. D. "The Mechanism of the Spontaneous Autoxidation of Dihydroartemisinic Acid". In: *Tetrahedron* 58.5 (Jan. 2002), pp. 897–908. DOI: `10.1016/S0040-4020(01)01193-0`.

[217] Sy, L.-K., Brown, G. D., and Haynes, R. "A Novel Endoperoxide and Related Sesquiterpenes from Artemisia Annua Which Are Possibly Derived from Allylic Hydroperoxides". In: *Tetrahedron* 54.17 (Apr. 1998), pp. 4345–4356. DOI: `10.1016/S0040-4020(98)00148-3`.

[218] Sy, L.-K., Ngo, K.-S., and Brown, G. D. "Biomimetic Synthesis of Arteannuin h and the 3,2-Rearrangement of Allylic Hydroperoxides". In: *Tetrahedron* 55.52 (Dec. 1999), pp. 15127–15140. DOI: `10.1016/S0040-4020(99)00987-4`.

[219] Triemer, S. "Experimentelle und theoretische Untersuchung der photokatalytischen Oxidation von Dihydroartemisininsäure zu Artemisinin". MA thesis. Magdeburg: Otto von Guericke University Magdeburg, 2016.

[220] Bregnhøj, M., Westberg, M., Jensen, F., and Ogilby, P. R. "Solvent-Dependent Singlet Oxygen Lifetimes: Temperature Effects Implicate Tunneling and Charge-Transfer Interactions". In: *Physical Chemistry Chemical Physics* 18.33 (2016), pp. 22946–22961. DOI: `10.1039/C6CP01635A`.

[221] Muñoz-Batista, M. J., Ballari, M. M., Kubacka, A., Alfano, O. M., and Fernández-García, M. "Braiding Kinetics and Spectroscopy in Photo-Catalysis: The Spectro-Kinetic Approach". In: *Chemical Society Reviews* 48.2 (2019), pp. 637–682. DOI: `10.1039/C8CS00108A`.

[222] Bloh, J. Z. "A Holistic Approach to Model the Kinetics of Photocatalytic Reactions". In: *Frontiers in Chemistry* 7 (Mar. 14, 2019), p. 128. DOI: `10.3389/fchem.2019.00128`.

[223] Modest, M. F. *Radiative Heat Transfer*. third. New York: Academic Press, 2013. ISBN: 978-0-12-386944-9.

[224] Parnis, J. M. and Oldham, K. B. "Beyond the Beer–Lambert Law: The Dependence of Absorbance on Time in Photochemistry". In: *Journal of Photochemistry and Photobiology A: Chemistry* 267 (Sept. 2013), pp. 6–10. DOI: `10.1016/j.jphotochem.2013.06.006`.

[225] Meir, G., Leblebici, M. E., Fransen, S., Kuhn, S., and Van Gerven, T. "Principles of Co-axial Illumination for Photochemical Reactions: Part 1. Model Development". In: *Journal of Advanced Manufacturing and Processing* 2.2 (Apr. 2020). DOI: `10.1002/amp2.10044`.

[226] Roibu, A., Van Gerven, T., and Kuhn, S. "Photon Transport and Hydrodynamics in Gas-Liquid Flows. Part 1: Characterization of Taylor Flow in a Photo Microreactor". In: *ChemPhotoChem* (June 4, 2020), cptc.202000065. DOI: `10.1002/cptc.202000065`.

[227] Nicklin, D. "Two-Phase Bubble Flow". In: *Chemical Engineering Science* 17.9 (Sept. 1962), pp. 693–702. DOI: `10.1016/0009-2509(62)85027-1`.

[228] Zuber, N. and Findlay, J. A. "Average Volumetric Concentration in Two-Phase Flow Systems". In: *Journal of Heat Transfer* 87.4 (Nov. 1, 1965), pp. 453–468. DOI: `10.1115/1.3689137`.

[229] Wu, X., Deng, Z., Yan, J., Zhang, Z., Zhang, F., and Zhang, Z. "Experimental Investigation on the Solubility of Oxygen in Toluene and Acetic Acid". In: *Industrial & Engineering Chemistry Research* 53.23 (June 11, 2014), pp. 9932–9937. DOI: `10.1021/ie5014772`.

[230] Van Baten, J. and Krishna, R. "CFD Simulations of Mass Transfer from Taylor Bubbles Rising in Circular Capillaries". In: *Chemical Engineering Science* 59.12 (June 2004), pp. 2535–2545. DOI: `10.1016/j.ces.2004.03.010`.

[231] Vandu, C., Liu, H., and Krishna, R. "Mass Transfer from Taylor Bubbles Rising in Single Capillaries". In: *Chemical Engineering Science* 60.22 (Nov. 2005), pp. 6430–6437. DOI: `10.1016/j.ces.2005.01.037`.

[232] Angeli, P. and Gavriilidis, A. "Hydrodynamics of Taylor Flow in Small Channels: A Review". In: *Proceedings of the Institution of Mechanical Engineers, Part C: Journal of Mechanical Engineering Science* 222.5 (May 1, 2008), pp. 737–751. DOI: `10.1243/09544062JMES776`.

[233] Holmberg, A. "On the Practical Identifiability of Microbial Growth Models Incorporating Michaelis-Menten Type Nonlinearities". In: *Mathematical Biosciences* 62.1 (Nov. 1982), pp. 23–43. DOI: `10.1016/0025-5564(82)90061-X`.

[234]   Bates, S., Sienz, J., and Toropov, V. "Formulation of the Optimal Latin Hypercube Design of Experiments Using a Permutation Genetic Algorithm". In: *45th AIAA/ASME/ASCE/AHS/ASC Structures, Structural Dynamics & Materials Conference*. 45th AIAA/ASME/ASCE/AHS/ASC Structures, Structural Dynamics & Materials Conference. Palm Springs, California: American Institute of Aeronautics and Astronautics, Apr. 19, 2004. ISBN: 978-1-62410-079-6. DOI: `10.2514/6.2004-2011`.

[235]   Griesbeck, A. G., Adam, W., Bartoschek, A., and El-Idreesy, T. T. "Photooxygenation of Allylic Alcohols: Kinetic Comparison of Unfunctionalized Alkenes with Prenol-Type Allylic Alcohols, Ethers and Acetates". In: *Photochem. Photobiol. Sci.* 2.8 (2003), pp. 877–881. DOI: `10.1039/B302255B`.

[236]   Haase, S., Murzin, D. Y., and Salmi, T. "Review on Hydrodynamics and Mass Transfer in Minichannel Wall Reactors with Gas–Liquid Taylor Flow". In: *Chemical Engineering Research and Design* 113 (Sept. 2016), pp. 304–329. DOI: `10.1016/j.cherd.2016.06.017`.

[237]   Roibu, A., Fransen, S., Leblebici, M. E., Meir, G., Van Gerven, T., and Kuhn, S. "An Accessible Visible-Light Actinometer for the Determination of Photon Flux and Optical Pathlength in Flow Photo Microreactors". In: *Scientific Reports* 8.1 (Dec. 2018), p. 5421. DOI: `10.1038/s41598-018-23735-2`.

[238]   Wehrens, R., Putter, H., and Buydens, L. M. "The Bootstrap: A Tutorial". In: *Chemometrics and Intelligent Laboratory Systems* 54.1 (Dec. 2000), pp. 35–52. DOI: `10.1016/S0169-7439(00)00102-7`.

[239]   Bourne, J. R. "Mixing and the Selectivity of Chemical Reactions". In: *Organic Process Research & Development* 7.4 (July 2003), pp. 471–508. DOI: `10.1021/op020074q`.

[240]   Schumpe, A. and Luehring, P. "Oxygen Diffusivities in Organic Liquids at 293.2 K". In: *Journal of Chemical & Engineering Data* 35.1 (Jan. 1990), pp. 24–25. DOI: `10.1021/je00059a007`.

[241]   Haynes, R. K. and Vonwiller, S. C. "Catalysed Oxygenation of Allylic Hydroperoxides Derived from Qinghao (Artemisinic) Acid. Conversion of Qinghao Acid into Dehydroginghaosu (Artemisitene) and Qinghaosu (Artemisinin)". In: *Journal of the Chemical Society, Chemical Communications* 6 (1990), p. 451. DOI: `10.1039/c39900000451`.

[242]   Vonwiller, S. C., Warner, J. A., Mann, S. T., and Haynes, R. K. "Copper(II) Trifluoromethanesulfonate-Induced Cleavage Oxygenation of Allylic Hydroperoxides Derived from Qinghao Acid in the Synthesis of Qinghaosu Derivatives: Evidence for the Intermediacy of Enols". In: *Journal of the American Chemical Society* 117.45 (Nov. 1995), pp. 11098–11105. DOI: `10.1021/ja00150a009`.

[243] Haynes, R. K. and Vonwiller, S. C. "From Qinghao, Marvelous Herb of Antiquity, to the Antimalarial Trioxane Qinghaosuand Some Remarkable New Chemistry". In: *Accounts of Chemical Research* 30.2 (Feb. 1, 1997), pp. 73–79. DOI: `10.1021/ar950058w`.

[244] Varela, K., Arman, H. D., and Yoshimoto, F. K. "Synthesis of [3,3-^{2}H$_2$]-Dihydroartemisinic Acid to Measure the Rate of Nonenzymatic Conversion of Dihydroartemisinic Acid to Artemisinin". In: *Journal of Natural Products* 83.1 (Jan. 24, 2020), pp. 66–78. DOI: `10.1021/acs.jnatprod.9b00686`.

[245] Varela, K., Arman, H. D., and Yoshimoto, F. K. "Synthesis of [15,15,15-^{2}H$_3$]-Dihydroartemisinic Acid and Isotope Studies Support a Mixed Mechanism in the Endoperoxide Formation to Artemisinin". In: *Journal of Natural Products* 84.7 (July 23, 2021), pp. 1967–1984. DOI: `10.1021/acs.jnatprod.1c00246`.

[246] Amara, Z., Bellamy, J. F. B., Horvath, R., Miller, S. J., Beeby, A., Burgard, A., Rossen, K., Poliakoff, M., and George, M. W. "Applying Green Chemistry to the Photochemical Route to Artemisinin". In: *Nature Chemistry* 7.6 (June 2015), pp. 489–495. DOI: `10.1038/nchem.2261`.

[247] Hui, S.-M., Ngo, K.-S., and Brown, G. D. "Epimerization in Acid Degradation Products of Artemisinin". In: *Journal of the Chemical Society, Perkin Transactions 1* 22 (1997), pp. 3435–3442. DOI: `10.1039/a702714a`.

[248] Lee, D. S., Amara, Z., Clark, C. A., Xu, Z., Kakimpa, B., Morvan, H. P., Pickering, S. J., Poliakoff, M., and George, M. W. "Continuous Photo-Oxidation in a Vortex Reactor: Efficient Operations Using Air Drawn from the Laboratory". In: *Organic Process Research & Development* 21.7 (July 21, 2017), pp. 1042–1050. DOI: `10.1021/acs.oprd.7b00153`.

[249] Bard, Y. *Nonlinear Parameter Estimation*. New York: Academic Press, 1974. ISBN: 978-0-12-078250-5.

[250] Beller, M., Renken, A., and Santen, R. A. van, eds. *Catalysis: From Principles to Applications*. Weinheim, Germany: Wiley-VCH Verlag GmbH & Co. KGaA, 2012. ISBN: 978-3-527-32349-4.

[251] Biral, F., Bertolazzi, E., and Bosetti, P. "Notes on Numerical Methods for Solving Optimal Control Problems". In: *IEEJ Journal of Industry Applications* 5.2 (2016), pp. 154–166.

[252] Rodrigues, D., Billeter, J., and Bonvin, D. "Maximum-Likelihood Estimation of Kinetic Parameters via the Extent-Based Incremental Approach". In: *Computers & Chemical Engineering* (May 2018). DOI: `10.1016/j.compchemeng.2018.05.024`.

[253] Liu, J., Mendoza, S., Li, G., and Fathy, H. "Efficient Total Least Squares State and Parameter Estimation for Differentially Flat Systems". In: IEEE, July 2016, pp. 5419–5424. ISBN: 978-1-4673-8682-1. DOI: `10.1109/ACC.2016.7526519`.

[254] Schenkendorf, R. and Mangold, M. "Parameter Identification for Ordinary and Delay Differential Equations by Using Flat Inputs". In: *Theoretical Foundations of Chemical Engineering* 48.5 (Sept. 2014), pp. 594–607. DOI: `10.1134/S0040579514050224`.

[255] Gau, C.-Y. and Stadtherr, M. A. "Reliable Nonlinear Parameter Estimation Using Interval Analysis: Error-in-Variable Approach". In: *Computers & Chemical Engineering* 24.2-7 (July 2000), pp. 631–637. DOI: `10.1016/S0098-1354(00)00363-X`.

[256] Kim, I.-W., Liebman, M. J., and Edgar, T. F. "Robust Error-in-Variables Estimation Using Nonlinear Programming Techniques". In: *AIChE Journal* 36.7 (July 1990), pp. 985–993. DOI: `10.1002/aic.690360703`.

[257] Markovsky, I. and Van Huffel, S. "Overview of Total Least-Squares Methods". In: *Signal Processing* 87.10 (Oct. 2007), pp. 2283–2302. DOI: `10.1016/j.sigpro.2007.04.004`.

[258] Golub, G. H. and Van Loan, C. "Total Least Squares". In: *Smoothing Techniques for Curve Estimation*. Ed. by Gasser, T. and Rosenblatt, M. Vol. 757. Berlin, Heidelberg: Springer Berlin Heidelberg, 1979, pp. 69–76. ISBN: 978-3-540-09706-8 978-3-540-38475-5. DOI: `10.1007/BFb0098490`.

[259] Fliess, M., Lévine, J., Martin, P., and Rouchon, P. "Sur les systèmes non linéaires différentiellement plats". In: *CR Acad. Sci. Paris* (1992), pp. 619–624.

[260] Franke, M. and Robenack, K. "On the Computation of Flat Outputs for Nonlinear Control Systems". In: *Control Conference (ECC), 2013 European*. IEEE, 2013, pp. 167–172.

[261] Schulze, M. and Schenkendorf, R. "Flatness-Based Design of Experiments for Model Selection". In: *IFAC-PapersOnLine* 51.15 (2018), pp. 233–238. DOI: `10.1016/j.ifacol.2018.09.140`.

[262] Schenkendorf, R., Reichl, U., and Mangold, M. "Parameter Identification of Time-Delay Systems: A Flatness Based Approach". In: *IFAC Proceedings Volumes* 45.2 (2012), pp. 165–170.

[263] Hildebrand, F., Kühl, S., Pohl, M., Vasic-Racki, D., Müller, M., Wandrey, C., and Lütz, S. "The Production of (*R*)-2-Hydroxy-1-Phenyl-Propan-1-One Derivatives by Benzaldehyde Lyase from *Pseudomonas Fluorescens* in a Continuously Operated Membrane Reactor". In: *Biotechnology and Bioengineering* 96.5 (Apr. 1, 2007), pp. 835–843. DOI: `10.1002/bit.21189`.

[264] vSvarc, A., Findrik Blavzević, Z., Vasić-Ravcki, Đ., Szekrenyi, A., Fessner, W.-D., Charnock, S. J., and Vrsalović Presevcki, A. "2-Deoxyribose-5-phosphate Aldolase from *Thermotoga Maritima* in the Synthesis of a Statin Side-chain Precursor: Characterization, Modeling and Optimization". In: *Journal of Chemical Technology & Biotechnology* 94.6 (June 2019), pp. 1832–1842. DOI: 10.1002/jctb.5956.

[265] Hampel, S. et al. "Structural and Mutagenesis Studies of the Thiamine-Dependent, Ketone-Accepting YerE from *Pseudomonas Protegens*". In: *ChemBioChem* 19.21 (Nov. 2, 2018), pp. 2283–2292. DOI: 10.1002/cbic.201800325.

[266] Buzzi-Ferraris, G. and Forzatti, P. "A New Sequential Experimental Design Procedure for Discriminating among Rival Models". In: *Chemical Engineering Science* 38.2 (1983), pp. 225–232. DOI: 10.1016/0009-2509(83)85004-0.

[267] Donckels, B. M., De Pauw, D. J., De Baets, B., Maertens, J., and Vanrolleghem, P. A. "An Anticipatory Approach to Optimal Experimental Design for Model Discrimination". In: *Chemometrics and Intelligent Laboratory Systems* 95.1 (Jan. 2009), pp. 53–63. DOI: 10.1016/j.chemolab.2008.08.002.

[268] Violet, L., Loubière, K., Rabion, A., Samuel, R., Hattou, S., Cabassud, M., and Prat, L. "Stoichio-Kinetic Model Discrimination and Parameter Identification in Continuous Microreactors". In: *Chemical Engineering Research and Design* 114 (Oct. 2016), pp. 39–51. DOI: 10.1016/j.cherd.2016.07.025.

[269] Lu, L., Murray-Smith, D. J., and Thomson, D. "Issues of Numerical Accuracy and Stability in Inverse Simulation". In: *Simulation Modelling Practice and Theory* 16.9 (Oct. 2008), pp. 1350–1364. DOI: 10.1016/j.simpat.2008.07.003.

[270] Lu, L. "Inverse Modelling and Inverse Simulation for System Engineering and Control Applications". PhD thesis. University of Glasgow, 2007.

[271] Adamy, J. *Nichtlineare Systeme und Regelungen*. Berlin, Heidelberg: Springer Vieweg, 2014. ISBN: 978-3-642-45012-9 978-3-642-45013-6. DOI: 10.1007/978-3-642-45013-6.

[272] Waldherr, S. and Zeitz, M. "Conditions for the Existence of a Flat Input". In: *International Journal of Control* 81.3 (2008), pp. 439–443.

[273] Kaminski, Y. J., Lévine, J., and Ollivier, F. "Intrinsic and Apparent Singularities in Differentially Flat Systems, and Application to Global Motion Planning". In: *Systems & Control Letters* 113 (Mar. 2018), pp. 117–124. DOI: 10.1016/j.sysconle.2018.01.013.

[274] Rigatos, G. G. "Differential Flatness Theory and Flatness-Based Control". In: *Nonlinear Control and Filtering Using Differential Flatness Approaches*. Vol. 25. Cham: Springer International Publishing, 2015, pp. 47–101. ISBN: 978-3-319-16419-9 978-3-319-16420-5. DOI: 10.1007/978-3-319-16420-5_2.

[275] Fliess, M., Sira-Ramírez, H., and Marquez, R. "Regulation of Non-Minimum Phase Outputs: A Flatness Based Approach". In: *Perspectives in Control*. Ed. by Normand-Cyrot, D. D. Springer London, 1998, pp. 143–163. ISBN: 978-1-4471-1278-5 978-1-4471-1276-1. DOI: 10.1007/978-1-4471-1276-1_11.

[276] Andrej, J. and Meurer, T. "Flatness-Based Constrained Optimal Control of Reaction-Diffusion Systems". In: *2018 Annual American Control Conference (ACC)*. 2018 Annual American Control Conference (ACC). Milwaukee, WI: IEEE, June 2018, pp. 2539–2544. ISBN: 978-1-5386-5428-6. DOI: 10.23919/ACC.2018.8431201.

[277] Kolar, B., Diwold, J., and Schoberl, M. "Necessary and Sufficient Conditions for Difference Flatness". In: *IEEE Transactions on Automatic Control* 68.3 (Mar. 2023), pp. 1715–1721. DOI: 10.1109/TAC.2022.3151615.

[278] Wagner, M. O., Meurer, T., and Kugi, A. "Trajectory Planning for Semilinear PDEs Modeling a Countercurrent Heat Exchanger". In: *IFAC Proceedings Volumes* 43.14 (Sept. 2010), pp. 593–598. DOI: 10.3182/20100901-3-IT-2016.00269.

[279] Vollmer, U. and Raisch, J. "Control of Batch Crystallization—A System Inversion Approach". In: *Chemical Engineering and Processing: Process Intensification* 45.10 (Oct. 2006), pp. 874–885. DOI: 10.1016/j.cep.2006.01.012.

[280] Mahadevan, R., Agrawal, S. K., and Doyle III, F. J. "Differential Flatness Based Nonlinear Predictive Control of Fed-Batch Bioreactors". In: *Control Engineering Practice* 9.8 (2001), pp. 889–899.

[281] Liu, J., Li, G., and Fathy, H. K. "An Extended Differential Flatness Approach for the Health-Conscious Nonlinear Model Predictive Control of Lithium-Ion Batteries". In: *IEEE Transactions on Control Systems Technology* 25.5 (Sept. 2017), pp. 1882–1889. DOI: 10.1109/TCST.2016.2624143.

[282] Murray, R. M., Rathinam, M., and Sluis, W. "Differential Flatness of Mechanical Control Systems: A Catalog of Prototype Systems". In: *ASME International Mechanical Engineering Congress and Exposition*. 1995.

[283] Oldenburg, J. and Marquardt, W. "Flatness and Higher Order Differential Model Representations in Dynamic Optimization". In: *Computers & Chemical Engineering* 26.3 (Mar. 2002), pp. 385–400. DOI: 10.1016/S0098-1354(01)00752-9.

[284] Sira-Ramírez, H. and Agrawal, S. K. *Differentially Flat Systems*. CRC Press, May 2004. ISBN: 978-0-8247-5470-9.

[285] Kolar, B., Kaldmäe, A., Schöberl, M., Kotta, Ü., and Schlacher, K. "Construction of Flat Outputs of Nonlinear Discrete-Time Systems in a Geometric and an Algebraic Framework". In: *IFAC-PapersOnLine* 49.18 (2016), pp. 796–801. DOI: `10.1016/j.ifacol.2016.10.263`.

[286] Victor, S., Melchior, P., Lévine, J., and Oustaloup, A. "Flat Output Computation for Fractional Linear Systems: Application to a Thermal System". In: *IFAC Proceedings Volumes* 47.3 (2014), pp. 2891–2896. DOI: `10.3182/20140824-6-ZA-1003.01911`.

[287] Waldherr, S. and Zeitz, M. "Flat Inputs in the MIMO Case". In: *IFAC Proceedings Volumes* 43.14 (2010), pp. 695–700.

[288] Richard, P., Buisson, J., and Cormerais, H. "Analysis of Flatness Using Bond Graphs and Bicausality". In: *IFAC Proceedings Volumes* 35.1 (2002), pp. 25–30. DOI: `10.3182/20020721-6-ES-1901.00254`.

[289] Csercsik, D., Szederkényi, G., and Hangos, K. M. "Determining Flat Outputs of MIMO Nonlinear Systems Using Directed Graphs". In: CONTROLO 2008, 8th Portuguese Conference on Automatic Control. Villa Real, Portugal, 2008, p. 6.

[290] Schizas, C. and Evans, F. "A Graph Theoretic Approach to Multivariable Control System Design". In: *Automatica* 17.2 (Mar. 1981), pp. 371–377. DOI: `10.1016/0005-1098(81)90054-6`.

[291] Reinschke, K. J. *Multivariable Control: A Graph-theoretic Approach*. De Gruyter, Dec. 31, 1988. ISBN: 978-3-11-248058-8. DOI: `10.1515/9783112480588`.

[292] Dion, J.-M., Commault, C., and van der Woude, J. "Generic Properties and Control of Linear Structured Systems: A Survey". In: *Automatica* 39.7 (July 2003), pp. 1125–1144. DOI: `10.1016/S0005-1098(03)00104-3`.

[293] De Boor, C. *A Practical Guide to Splines*. Applied Mathematical Sciences 27. New York: Springer-Verlag, 2001.

[294] Ohs, R., Leipnitz, M., Schöpping, M., and Spiess, A. C. "Simultaneous Identification of Reaction and Inactivation Kinetics of an Enzyme-catalyzed Carboligation". In: *Biotechnology Progress* 34.5 (Sept. 2018), pp. 1081–1092. DOI: `10.1002/btpr.2656`.

[295] Rogers, A. and Gibon, Y. "Enzyme Kinetics: Theory and Practice". In: *Plant Metabolic Networks*. Ed. by Schwender, J. New York, NY: Springer New York, 2009, pp. 71–103. ISBN: 978-0-387-78744-2 978-0-387-78745-9. DOI: `10.1007/978-0-387-78745-9_4`.

[296] Fang, J.-J. and Hung, C.-L. "An Improved Parameterization Method for B-spline Curve and Surface Interpolation". In: *Computer-Aided Design* 45.6 (June 2013), pp. 1005–1028. DOI: `10.1016/j.cad.2013.01.005`.

[297]   Ji, W. and Deng, S. "Autonomous Discovery of Unknown Reaction Pathways from Data by Chemical Reaction Neural Network". In: *The Journal of Physical Chemistry A* (Jan. 20, 2021), acs.jpca.0c09316. DOI: `10.1021/acs.jpca.0c09316`.

[298]   Brunton, S. L., Proctor, J. L., and Kutz, J. N. "Discovering Governing Equations from Data by Sparse Identification of Nonlinear Dynamical Systems". In: *Proceedings of the National Academy of Sciences* 113.15 (Apr. 12, 2016), pp. 3932–3937. DOI: `10.1073/pnas.1517384113`.

[299]   World Health Organization. *World Health Statistics 2020: Monitoring Health for the SDGs, Sustainable Development Goals*. Vol. 98. World Health Organization, Nov. 1, 2020.

[300]   World Health Organization. *Global Health Estimates 2019 Summary Tables*. 2020.

[301]   World Health Organization. *World Malaria Report 2020: 20 Years of Global Progress and Challenges*. Geneva: World Health Organization, 2020.

[302]   World Health Organization. *World Health Statistics 2021: Monitoring Health for the SDGs, Sustainable Development Goals*. Geneva: World Health Organization, 2021. ISBN: 978-92-4-002705-3.

[303]   Hogan, A. B. et al. "Potential Impact of the COVID-19 Pandemic on HIV, Tuberculosis, and Malaria in Low-Income and Middle-Income Countries: A Modelling Study". In: *The Lancet Global Health* 8.9 (Sept. 2020), e1132–e1141. DOI: `10.1016/S2214-109X(20)30288-6`.

[304]   Phillips, M. A., Burrows, J. N., Manyando, C., van Huijsduijnen, R. H., Van Voorhis, W. C., and Wells, T. N. C. "Malaria". In: *Nature Reviews Disease Primers* 3.1 (Dec. 21, 2017), p. 17050. DOI: `10.1038/nrdp.2017.50`.

[305]   Fischer, L., Gültekin, N., Kaelin, M. B., Fehr, J., and Schlagenhauf, P. "Rising Temperature and Its Impact on Receptivity to Malaria Transmission in Europe: A Systematic Review". In: *Travel Medicine and Infectious Disease* 36 (July 2020), p. 101815. DOI: `10.1016/j.tmaid.2020.101815`.

[306]   World Health Organization. *World Malaria Report 2019*. Geneva: World Health Organization, 2019. ISBN: 978-92-4-004049-6. This work is licensed under CC BY-NC-SA 3.0 IGO.

[307]   World Health Organization. *Global Technical Strategy for Malaria 2016-2030 - 2021 Update*. Geneva: World Health Organization, 2021. ISBN: 978-92-4-004049-6.

[308]   World Health Organization. *Artemisinin Resistance and Artemisinin-Based Combination Therapy Efficacy*. 2018.

[309] Eastman, R. T. and Fidock, D. A. "Artemisinin-Based Combination Therapies: A Vital Tool in Efforts to Eliminate Malaria". In: *Nature Reviews Microbiology* 7.12 (Dec. 2009), pp. 864–874. DOI: `10.1038/nrmicro2239`.

[310] World Health Organization. *Q&A - Malaria: Artemisinin Resistance*. 2022. URL: `https://www.who.int/news-room/questions-and-answers/item/artemisinin-resistance`.

[311] Maiga, F. O. et al. "Artemisinin-Based Combination Therapy for Uncomplicated Plasmodium Falciparum Malaria in Mali: A Systematic Review and Meta-Analysis". In: *Malaria Journal* 20.1 (Dec. 2021), p. 356. DOI: `10.1186/s12936-021-03890-0`.

[312] Tu, Y. "Artemisinin-A Gift from Traditional Chinese Medicine to the World (Nobel Lecture)". In: *Angewandte Chemie International Edition* 55.35 (Aug. 22, 2016), pp. 10210–10226. DOI: `10.1002/anie.201601967`.

[313] Christensen, S. B. "Natural Products That Changed Society". In: *Biomedicines* 9.5 (Apr. 26, 2021), p. 472. DOI: `10.3390/biomedicines9050472`.

[314] Youyou, T. "The Development of the Antimalarial Drugs with New Type of Chemical Structure–Qinghaosu and Dihydroqinghaosu". In: Southeast Asian J Trop Med Public Health 35.2 (2004), p. 2.

[315] Menard, D. and Dondorp, A. "Antimalarial Drug Resistance: A Threat to Malaria Elimination". In: *Cold Spring Harbor Perspectives in Medicine* 7.7 (July 2017), a025619. DOI: `10.1101/cshperspect.a025619`.

[316] Arya, A., Kojom Foko, L. P., Chaudhry, S., Sharma, A., and Singh, V. "Artemisinin-Based Combination Therapy (ACT) and Drug Resistance Molecular Markers: A Systematic Review of Clinical Studies from Two Malaria Endemic Regions – India and Sub-Saharan Africa". In: *International Journal for Parasitology: Drugs and Drug Resistance* 15 (Apr. 2021), pp. 43–56. DOI: `10.1016/j.ijpddr.2020.11.006`.

[317] Balikagala, B. et al. "Evidence of Artemisinin-Resistant Malaria in Africa". In: *New England Journal of Medicine* 385.13 (Sept. 23, 2021), pp. 1163–1171. DOI: `10.1056/NEJMoa2101746`.

[318] Datoo, M. S. et al. "Efficacy of a Low-Dose Candidate Malaria Vaccine, R21 in Adjuvant Matrix-M, with Seasonal Administration to Children in Burkina Faso: A Randomised Controlled Trial". In: *The Lancet* 397.10287 (May 2021), pp. 1809–1818. DOI: `10.1016/S0140-6736(21)00943-0`.

[319] BionTech. *BioNTech gibt Update zu Entwicklungsplänen für nachhaltige Lösungen gegen Infektionskrankheiten auf dem afrikanischen Kontinent*. 2021. URL: `https://investors.biontech.de/de/news-releases/news-release-details/biontech-gibt-update-zu-entwicklungsplaenen-fuer-nachhaltige`.

[320] Novartis. *Novartis Reaches Milestone Delivery of 1 Billion Courses of Antimalarial Treatment*. Novartis. 2021. URL: `https://www.novartis.com/news/media-releases/novartis-reaches-milestone-delivery-1-billion-courses-antimalarial-treatment` (visited on 07/26/2022).

[321] Van der Pluijm, R. W. et al. "Triple Artemisinin-Based Combination Therapies versus Artemisinin-Based Combination Therapies for Uncomplicated Plasmodium Falciparum Malaria: A Multicentre, Open-Label, Randomised Clinical Trial". In: *The Lancet* 395.10233 (Apr. 2020), pp. 1345–1360. DOI: `10.1016/S0140-6736(20)30552-3`.

[322] Randrianarivo, S., Rasolohery, C., Rafanomezantsoa, S., Randriamampionona, H., Haramaty, L., Rafanomezantsoa, R. M., and Andrianasolo, E. H. "(-)-6-Epi-Artemisinin, a Natural Stereoisomer of (+)-Artemisinin in the Opposite Enantiomeric Series, from the Endemic Madagascar Plant Saldinia Proboscidea, an Atypical Source". In: *Molecules* 26.18 (Sept. 12, 2021), p. 5540. DOI: `10.3390/molecules26185540`.

[323] Numonov, S., Sharopov, F., Salimov, A., Sukhrobov, P., Atolikshoeva, S., Safarzoda, R., Habasi, M., and Aisa, H. "Assessment of Artemisinin Contents in Selected Artemisia Species from Tajikistan (Central Asia)". In: *Medicines* 6.1 (Jan. 31, 2019), p. 23. DOI: `10.3390/medicines6010023`.

[324] Arnold, W. *Heilpflanzen - Pilze - W. Arnold*. URL: `https://www.awl.ch/` (visited on 07/19/2022).

[325] Muangphrom, P., Seki, H., Fukushima, E. O., and Muranaka, T. "Artemisinin-Based Antimalarial Research: Application of Biotechnology to the Production of Artemisinin, Its Mode of Action, and the Mechanism of Resistance of Plasmodium Parasites". In: *Journal of Natural Medicines* 70.3 (July 2016), pp. 318–334. DOI: `10.1007/s11418-016-1008-y`.

[326] Haynes, R. "From Artemisinin to New Artemisinin Antimalarials: Biosynthesis, Extraction, Old and New Derivatives, Stereochemistry and Medicinal Chemistry Requirements". In: *Current Topics in Medicinal Chemistry* 6.5 (Mar. 1, 2006), pp. 509–537. DOI: `10.2174/156802606776743129`.

[327] Nahar, L., Guo, M., and Sarker, S. D. "A Review on the Latest Advances in Extraction and Analysis of Artemisinin". In: *Phytochemical Analysis* 31.1 (Jan. 2020), pp. 5–14. DOI: `10.1002/pca.2873`.

[328] Lapkin, A. A., Peters, M., Greiner, L., Chemat, S., Leonhard, K., Liauw, M. A., and Leitner, W. "Screening of New Solvents for Artemisininextraction Process Using Ab Initio Methodology". In: *Green Chem.* 12.2 (2010), pp. 241–251. DOI: 10.1039/B922001A.

[329] Lapkin, A. A. "Green Extraction of Artemisinin from *Artemisia Annua* L". In: *Green Extraction of Natural Products*. Ed. by Chemat, F. and Strube, J. Weinheim, Germany: Wiley-VCH Verlag GmbH & Co. KGaA, Feb. 6, 2015, pp. 333–356. ISBN: 978-3-527-67682-8 978-3-527-33653-1. DOI: 10.1002/9783527676828.ch10.

[330] Martinez-Correa, H. A., Bitencourt, R. G., Kayano, A. C. A., Magalhães, P. M., Costa, F. T., and Cabral, F. A. "Integrated Extraction Process to Obtain Bioactive Extracts of Artemisia Annua L. Leaves Using Supercritical CO2, Ethanol and Water". In: *Industrial Crops and Products* 95 (Jan. 2017), pp. 535–542. DOI: 10.1016/j.indcrop.2016.11.007.

[331] Arumugham, T., K, R., Hasan, S. W., Show, P. L., Rinklebe, J., and Banat, F. "Supercritical Carbon Dioxide Extraction of Plant Phytochemicals for Biological and Environmental Applications – A Review". In: *Chemosphere* 271 (May 2021), p. 129525. DOI: 10.1016/j.chemosphere.2020.129525.

[332] Laboukhi-Khorsi, S., Daoud, K., and Chemat, S. "Efficient Solvent Selection Approach for High Solubility of Active Phytochemicals: Application for the Extraction of an Antimalarial Compound from Medicinal Plants". In: *ACS Sustainable Chemistry & Engineering* 5.5 (May 1, 2017), pp. 4332–4339. DOI: 10.1021/acssuschemeng.7b00384.

[333] Tzeng, T., Lin, Y., Jong, T., and Chang, C. "Ethanol Modified Supercritical Fluids Extraction of Scopoletin and Artemisinin from Artemisia Annua L." In: *Separation and Purification Technology* 56.1 (Aug. 1, 2007), pp. 18–24. DOI: 10.1016/j.seppur.2007.01.010.

[334] ElSohly, H. N., Croom, E. M., El-Feraly, F. S., and El-Sherei, M. M. "A Large-Scale Extraction Technique of Artemisinin from Artemisia Annua". In: *Journal of Natural Products* 53.6 (Nov. 1990), pp. 1560–1564. DOI: 10.1021/np50072a026.

[335] Pilkington, J. L., Preston, C., and Gomes, R. L. "Comparison of Response Surface Methodology (RSM) and Artificial Neural Networks (ANN) towards Efficient Extraction of Artemisinin from Artemisia Annua". In: *Industrial Crops and Products* 58 (July 2014), pp. 15–24. DOI: 10.1016/j.indcrop.2014.03.016.

[336] Zhang, H., Zhang, L., Hu, X., Zhou, Y., Ding, C., Yang, R., Wang, X., and Li, D. "Optimization of Ultrasound-Assisted Extraction of Artemisinin from *Artemisia Annua* L. by Response Surface Methodology". In: *Separation Science and Technology* 49.5 (Mar. 24, 2014), pp. 673–681. DOI: 10.1080/01496395.2013.862545.

[337]   Misra, H., Mehta, D., Mehta, B. K., and Jain, D. C. "Microwave-Assisted Extraction Studies of Target Analyte Artemisinin from Dried Leaves of *Artemisia Annua* L." In: *Organic Chemistry International* 2013 (Mar. 14, 2013), pp. 1–6. DOI: `10.1155/2013/163028`.

[338]   Kohler, M., Haerdi, W., Christen, P., and Veuthey, J.-L. "Extraction of Artemisinin and Artemisinic Acid from Artemisia Annua L. Using Supercritical Carbon Dioxide". In: *Journal of Chromatography A* 785.1-2 (Oct. 1997), pp. 353–360. DOI: `10.1016/S0021-9673(97)00403-2`.

[339]   Krieger, J., Smeilus, T., Kaiser, M., Seo, E.-J., Efferth, T., and Giannis, A. "Total Synthesis and Biological Investigation of (-)-Artemisinin: The Antimalarial Activity of Artemisinin Is Not Stereospecific". In: *Angewandte Chemie International Edition* 57.27 (July 2, 2018), pp. 8293–8296. DOI: `10.1002/anie.201802015`.

[340]   Galloway, W. R., Isidro-Llobet, A., and Spring, D. R. "Diversity-Oriented Synthesis as a Tool for the Discovery of Novel Biologically Active Small Molecules". In: *Nature Communications* 1.1 (Dec. 2010), p. 80. DOI: `10.1038/ncomms1081`.

[341]   Tang, X., Demiray, M., Wirth, T., and Allemann, R. K. "Concise Synthesis of Artemisinin from a Farnesyl Diphosphate Analogue". In: *Bioorganic & Medicinal Chemistry* 26.7 (Apr. 2018), pp. 1314–1319. DOI: `10.1016/j.bmc.2017.03.068`.

[342]   Elsherbini, M., Allemann, R. K., and Wirth, T. ""Dark" Singlet Oxygen Made Easy". In: *Chemistry – A European Journal* 25.54 (Sept. 25, 2019), pp. 12486–12490. DOI: `10.1002/chem.201903505`.

[343]   Liu, X., Ding, W., and Jiang, H. "Engineering Microbial Cell Factories for the Production of Plant Natural Products: From Design Principles to Industrial-Scale Production". In: *Microbial Cell Factories* 16.1 (Dec. 2017), p. 125. DOI: `10.1186/s12934-017-0732-7`.

[344]   Westfall, P. J. et al. "Production of Amorphadiene in Yeast, and Its Conversion to Dihydroartemisinic Acid, Precursor to the Antimalarial Agent Artemisinin". In: *Proceedings of the National Academy of Sciences* 109.3 (Jan. 17, 2012), E111–E118. DOI: `10.1073/pnas.1110740109`.

[345]   Wu, L., Abreu, B. L., Blake, A. J., Taylor, L. J., Lewis, W., Argent, S. P., Poliakoff, M., Boufroura, H., and George, M. W. "Multigram Synthesis of Trioxanes Enabled by a Supercritical CO_2 Integrated Flow Process". In: *Organic Process Research & Development* 25.8 (Aug. 20, 2021), pp. 1873–1881. DOI: `10.1021/acs.oprd.1c00111`.

[346] Kong, C. J., Fisher, D., Desai, B. K., Yang, Y., Ahmad, S., Belecki, K., and Gupton, B. F. "High Throughput Photo-Oxidations in a Packed Bed Reactor System". In: *Bioorganic & Medicinal Chemistry* 25.23 (Dec. 2017), pp. 6203–6208. DOI: `10.1016/j.bmc.2017.07.004`.

[347] Thomson, C. G., Lee, A.-L., and Vilela, F. "Heterogeneous Photocatalysis in Flow Chemical Reactors". In: *Beilstein Journal of Organic Chemistry* 16 (June 26, 2020), pp. 1495–1549. DOI: `10.3762/bjoc.16.125`.

[348] Feng, L. et al. "Porphyrinic Metal–Organic Frameworks Installed with Brønsted Acid Sites for Efficient Tandem Semisynthesis of Artemisinin". In: *ACS Catalysis* 9.6 (June 7, 2019), pp. 5111–5118. DOI: `10.1021/acscatal.8b04960`.

[349] Akaike, H. "A New Look at the Statistical Model Identification". In: *IEEE Transactions on Automatic Control* 19.6 (Dec. 1974), pp. 716–723. DOI: `10.1109/TAC.1974.1100705`.

[350] Sobol', I. "Global Sensitivity Indices for Nonlinear Mathematical Models and Their Monte Carlo Estimates". In: *Mathematics and Computers in Simulation* 55.1-3 (Feb. 2001), pp. 271–280. DOI: `10.1016/S0378-4754(00)00270-6`.

[351] Janon, A., Klein, T., Lagnoux, A., Nodet, M., and Prieur, C. "Asymptotic Normality and Efficiency of Two Sobol Index Estimators". In: *ESAIM: Probability and Statistics* 18 (2014), pp. 342–364. DOI: `10.1051/ps/2013040`.

[352] Saltelli, A. "Making Best Use of Model Evaluations to Compute Sensitivity Indices". In: *Computer Physics Communications* 145.2 (May 2002), pp. 280–297. DOI: `10.1016/S0010-4655(02)00280-1`.

[353] Khorashadi Zadeh, F., Nossent, J., Sarrazin, F., Pianosi, F., van Griensven, A., Wagener, T., and Bauwens, W. "Comparison of Variance-Based and Moment-Independent Global Sensitivity Analysis Approaches by Application to the SWAT Model". In: *Environmental Modelling & Software* 91 (May 2017), pp. 210–222. DOI: `10.1016/j.envsoft.2017.02.001`.

[354] Vassiliadis, V. S., Sargent, R. W. H., and Pantelides, C. C. "Solution of a Class of Multistage Dynamic Optimization Problems. 1. Problems without Path Constraints". In: *Industrial & Engineering Chemistry Research* 33.9 (Sept. 1994), pp. 2111–2122. DOI: `10.1021/ie00033a014`.

[355] Vassiliadis, V. S., Sargent, R. W. H., and Pantelides, C. C. "Solution of a Class of Multistage Dynamic Optimization Problems. 2. Problems with Path Constraints". In: *Industrial & Engineering Chemistry Research* 33.9 (Sept. 1994), pp. 2123–2133. DOI: `10.1021/ie00033a015`.

List of Figures

List of Tables

Appendix

A   Background on Malaria and Artemisinin

A.1   Malaria – a Global Threat

Plasmodium parasites, that are transmitted to humans through the bites of infected female *Anopheles* mosquitoes, cause malaria. Its incubation period is around 10 to 15 days. First symptoms are fever, headache and chills. Because of mild first symptoms, malaria might be difficult to recognize, but quickly progresses to a severe illness and death within one day if left untreated. Several *Plasmodium* parasites can transmit malaria. The most dangerous parasite species, that is responsible for more than 95 % of the Malaria cases since 2015 is *P. falciparum*, with *P. vivax* being second [51]. In 2020, despite being both preventable and treatable, there were more than 240 million estimated malaria cases on the globe, which make malaria the fourth top cause of deaths world-wide considering selected infectious and parasitic diseases [299, 300]. Estimated figures are 409 000 [301] and 558 000 [51] in 2019, and 627 000 fatalities in 2020 [51]. It is merely surpassed by HIV/AIDS, 675 000 deaths in 2019 [300], tuberculosis, 1 208 000 deaths in 2019 [300], and by the recently appeared COVID-19 disease with 1 800 000 deaths in 2020 [302]. Over the past 20 years malaria incidences and mortality rates have continuously fallen. But their their decreasing paces slowed down lately, as shown in Figures A.1a and A.1b. Moreover, in 2020, figures have risen again, which at least can partly be explained by the COVID-19 pandemic, where prevention activities and health services for other diseases have been cut back [303].

Globe-wide, Figure A.1c, malaria is in particular prevalent in low-income countries, and more specifically in nations of sub-Saharan Africa. The fatalities related to malaria occur by a considerable margin in the WHO African region[1] (WHO: World Health Organization), Figure A.1b. The list of fatalities in 2020 is led by Nigeria, 31.9 %, Democratic Republic of the Congo, 13.2 %, United Republic of Tanzania, 4.1 %, Mozambique, 3.8 %, and Uganda, 3.5 % [51]. Despite being mainly determined by climate and ecology, malaria heavily burdens the poorest – those least able to afford preventative measures and medical treatment – and results in a vicious circle with

---

[1]   The WHO African region roughly covers sub-Saharan Africa, excluding Somalia and including Algeria [301].

(**a**) Cases (solid) and incidence (dashed) in selected regions [51].

(**b**) Fatalities (solid) and mortality (dashed) in selected regions [51].

(**c**) Incidence in countries in 2018, adapted from [306].
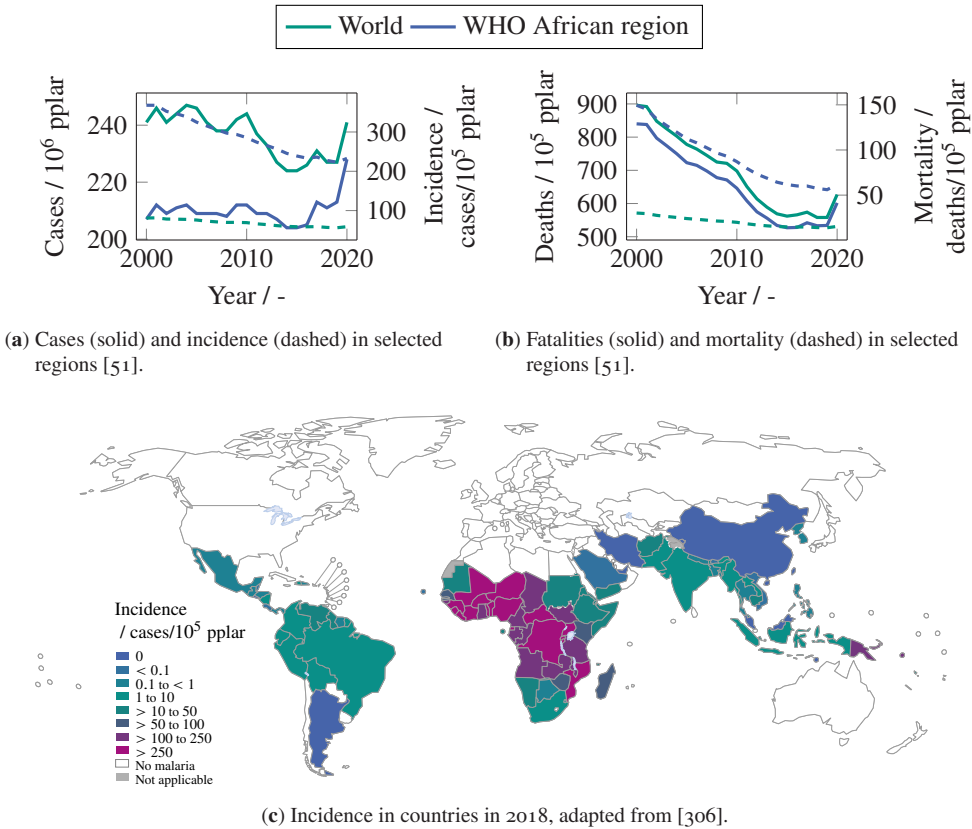
Figure A.1: Key figures related to malaria across the globe (pplar: people at risk).

enormous socioeconomic costs [304]. Historically, malaria has also been present in Germany and other countries in Europe, but disappeared for many reasons including agricultural changes, socioeconomic improvements and intervention efforts [305]. However, a reappearance of malaria in Europe in the future is not unlikely, not least due to climatic changes [305]. Alarmingly, 77 % of the total malaria deaths in 2020 are attributed to children aged under five years, where the share has decreased from 87 % in 2000 [51]. This makes malaria the top cause of deaths globally among children aged under five years for selected infectious and parasitic diseases in 2019 [300], with a recently updated total share of 7.8 % in this vulnerable group in 2020 [51]. Furthermore, malaria infections during pregnancy do not solely increase risk of death for the fetus, the newborn and the mother, but can significantly decrease the quality of life of the adolescent human being as well due to life-long effects of malaria [304].

A.2   Artemisinin as Key Drug in the Fight against Malaria

Two of the four main goals laid out by the WHO *Global technical strategy for malaria 2016-2030* are the reduction of both the incidence and the mortality rate of malaria by 90 % in 2030 compared to 2015 [307]. To achieve these goals, three pillars and two supporting elements were defined, where the first pillar is to ensure access to malaria prevention, diagnosis and treatment, and the first supporting element harnessing innovation and expanding research [307]. In practice, today's malaria management is a combination of vector control approaches, like insecticide spraying and the use of insecticide-treated bed nets, and drugs for both treatment and prevention [304]. The most effective medication against uncomplicated *P. falciparum* malaria are artemisinin-based combination therapies (ACTs), that are consequently recommended by WHO as the first- and second-line treatment for *P. falciparum* malaria and as well for chloroquine-resistant *P. vivax* malaria [308]. ACTs contain two different active ingredients: A fast-acting artemisinin derivative, that is more bioavailable for humans than artemisinin, and a longer-acting antimalarial partner drug with a different mode of action, i.e., having a longer half-life to clear remaining parasites [309]. The WHO currently recommends six different ACTs[2] and two injectable treatments[3], that should be followed by an ACT, for severe malaria [310]. In the WHO African Region, where ACT was launched between 2001 and 2004 [311], the first-line treatments for *P. falciparum* malaria include artemether-lumefantrine (AL), artesunate-amodiaquine (AS-AQ), artesunate-pyronaridine (AS-PY) and dihydroartemisinin-piperaquine (DHA-PPQ) [51]. ACTs have replaced Quinine-based medications chloroquine and mefloquine, that lost efficacy because of widespread resistancies in *Plasmodium* strains [311]. The decrease of the malaria-associated incidence and mortality between 2000 and 2015 by 37 % and 60 %, respectively, was attributed by the WHO with 21 % to ACTs [304]. The other two interventions were insecticide-treated bed nets, 69 %, and indoor residual insecticide spraying, 10 % [304].

The success of artemisinin in the fight against malaria facilitated the Nobel Prize in Physiology or Medicine 2015 that was awarded in half to Tu Youyou "for her discoveries concerning a novel therapy against Malaria" [312]. Project 523 with Tu Youyou as manager was launched in May 1967 by Mao Zedong at request of North Vietnam's Ho Chi Minh. The goal of the project was to find a new drug for chloroquine-resistant malaria in order to reduce casualties among soldiers in the Vietnam civil war. Tu Youyou turned to traditional Chinese medicine, where the plant *Artemisia annua*, quinghao in Chinese, also known as sweet wormwood, was used in several recipes against fever. In an ancient Chinese book written in 340 AD, she found a method for extracting artemisinin, in Chinese quinghaosu, meaning the active ingredient in quinghao, without

---

[2]   Artesunate-amodiaquine; artesunate-mefloquine; artesunate-pyronaridine; artesunate+sulfadoxine-pyrimethamine; artemether-lumefantrine; dihydroartemisinin-piperaquine.

[3]   Artesunate; artemether.
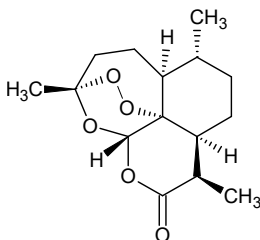
Figure A.2: Molecular structure of artemisinin (ART).

heating up the plant, and obtained thereby a very potent parasite killer [313, 314]. In the 1990s early trials of ACTs have been conducted, and in 2001 the WHO recommendation for the usage of ACTs as first-line treatment was published. Unfortunately, and probably before the widespread use of ACTs following the WHO recommendation, an artemisinin resistance by a mutation in the K13 parasite gene has been showing up. The resistance shows clear evidence in the Greater Mekong subregion (GMS), and scattered evidence in eastern Africa, in particular in Uganda and Rwanda [310, 315, 316]. In the GMS, several ACTs lost efficacy, that was accelerated by parallel resistancies against the artemisinin partner drugs [310, 315]. In Africa on the other hand, only a few studies have reported ACT treatment failures so far, but their development is likely to be inevitable [310, 317]. In parallel to the development of medication, the WHO recommendation, that the first malaria vaccine (RTS,S, trade name: Mosquirix), can be used for the prevention of *P. falciparum* malaria in children with moderate to high transmission, gives new hope for reaching the ambitious WHO goals for malaria until 2030 [51]. Furthermore, another vaccine (R21) shows efficacies above 75 %, that are significantly higher than the 56 % efficacy over 12 months in African children reported with RTS,S [318]. In the same vein, the company BioNTech, that has become renown in a short time for the development and success of its COVID-19 vaccine, is focusing on developing a further vaccine for malaria, that is based on the very same mRNA technology, and wants to start a clinical study until the end of 2022 [319]. Moreover, new antimalarial APIs are in the pipelines of pharmaceutical companies [320], and clinical trials with triple artemisin-based combination therapies (TACTs), incorporating a second partner drug, are under investigation [321].

A.3 Artemisinin and its Production Routes

Artemisia is a genus of plants among which several species have been found to produce the secondary metabolite artemisinin [322, 323], a sesquiterpene lactone with a peroxide constituent, Figure A.2. Its most prominent representative *Artemisia annua* is native to Asia, probably China, but can be found today in numerous other countries on all six populated continents [68], Figure A.3. Today, the *Artemisia annua* plant is the sole global source of artemisinin [67], that is

(**a**) *Artemisia annua*[4].   (**b**) *Artemisia annua* in blossom[4].   (**c**) Dried leaves of *Artemisia annua*.
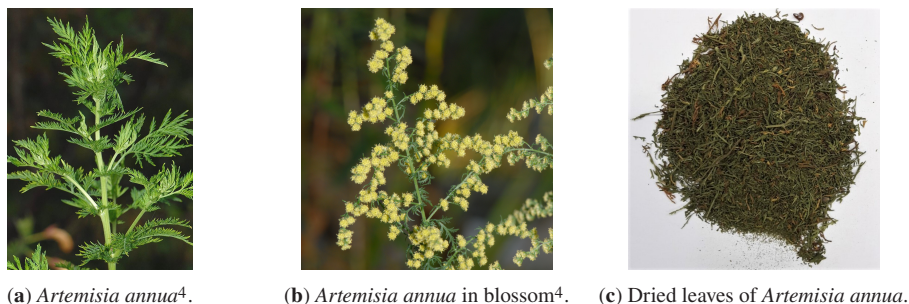
Figure A.3: *Artemisia annua* plant. Picture of dried leaves is reprinted from [61].

obtained by extraction, with main cultivation areas in China, Vietnam and East Africa [68]. The weight content of ART in wild and cultivated types is low and, depending on climatic conditions and chemotype, widely ranges from 0.01 to 1.5 % based on dry matter [69–72], with unpublished reports of 2 % [68]. Most often the leaves of the plant are considered, although ART content in the flowers might be higher [73].

The low ART weight content in the *A. annua* plant and the stimuli described in Section 1.2 are responsible for extensive research in artemisinin and its derivatives [74]. Next to extraction from its natural source, the production of ART can be categorized into two further approaches: Total syntheses from readily available and cheap chemical stocks, and semi- or partial syntheses, that either start with extraction byproducts or with species from heterologous production, Figure A.4. Research is in particular focused on enhancing production *in vivo* and *in vitro* of artemisinin or artemisinin precursors [71, 325], where between four different strategies might be differentiated: plant breeding technologies, gene overexpression in the biosynthetic pathway, direct or indirect upregulation of artemisinin biosynthesis, and heterologous production [325]. Albeit, at the same time, process-related improvements and technologies have been researched, both for extraction [326, 327] and for (bio)synthetic routes starting at ART precursors. The different production routes of artemisinin, i.e., extraction, partial synthesis, and total synthesis, are drawn in Figure A.4.

A.3.1   Extraction and Purification

The period from planting *A. annua* to extracting ART spans almost one year, for harvesting takes 4 to 7 months [326]. Dried leaf yields per hectare vary from 3 to 5 tonnes [326]. After drying, sequential extraction steps of the dried leaves at 30 to 60 °C are applied with, traditionally,

---

4   Pictures by courtesy of Werner Arnold, © Werner Arnold [324].
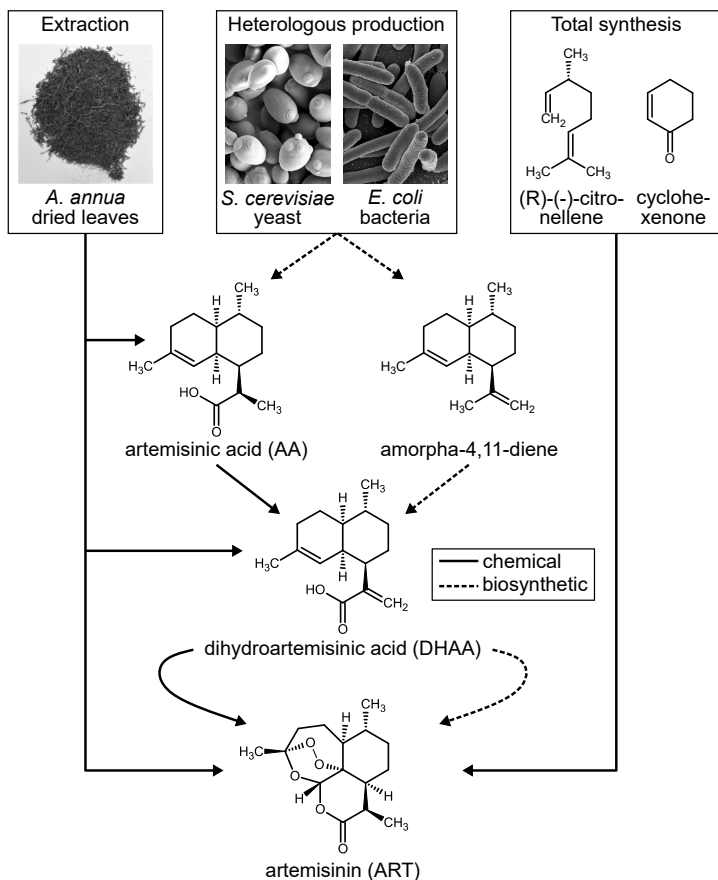
Figure A.4: Possible production routes of artemisinin, with direct extraction being the standard technology in industry today. Alternatives are total syntheses from readily available and cheap chemical stocks, and semi-syntheses, that either start with extraction byproducts or with species from heterologous production[5]. Reproduced and adapted with permission from [65].

hazardous hydrocarbon solvents like petroleum ether, hexane, or toluene [62].   In large-scale processes, crude extract efficiencies are within 62 to 70 % [62]. Following extraction, multi-stage crystallization and normal-phase liquid chromatography are utilized to purify the ART containing liquor [62]. Overall process yields for direct extraction by most prominent hydrocarbons typically lie around 60 % [328]. The low yields are owed to the decreased concentration gradient in the extract mixture when reaching equilibrium, insufficient mixing, decomposition of ART when

---

extraction temperature is increased, and difficult recovery [328, 329]. The latter is caused by structurally similar components in the leaves and efficient solubility enhancers in the non-usable parts of the extract. Nevertheless, direct extraction is the predominant technology to industrially gain ART from the plant, with percolation and Soxhlet-extraction used less frequently, because direct extraction has low capital cost, is technically simple, and widely applicable [62, 329].

Research efforts have been undertaken to replace the hazardous solvents with greener solvents, to improve the extraction process or to change extraction technology. Here, focuses lie on supercritical fluid extraction, mostly using supercritical CO_2, and both ultrasound- and microwave-assisted extraction [327, 330, 331]. A further promising research project is the use of a counter-current screw extractor that exhibits high mass transfer and approaches optimal concentration gradients [104, 109]. For instance, in [332], the authors used Hansen solubility parameters to extract ART from *A. annua* and determined an extraction efficiency of 65 % on dried biomass after a single batch, using the green solvent alternative isopropanol. With supercritical CO_2 extraction, corresponding extraction efficiencies might be high, in particular when used with a co-solvent [333], but they are not necessarily higher than more traditional extraction procedures with hexane [330]. In [62], a yield of 82 % is mentioned. Yields for artemisinin extraction reported in literature are listed in Table A.1.

A.4 Partial Synthesis

Today, the *Artemisia annua* plant is the sole global source of artemisinin [67], that is obtained by extraction, with main cultivation areas in China, Vietnam and East Africa [68]. The weight content of ART in wild and cultivated types is low and, depending on climatic conditions and chemotype, widely ranges from 0.01 to 1.5 % based on dry matter [69–72], with unpublished reports of 2 % [68]. Most often the leaves of the plant are considered, although ART content in the flowers might be higher [73].

The low ART weight content in the *A. annua* plant and the stimuli described in Section 1.2 are responsible for extensive research in artemisinin and its derivatives [74]. Next to extraction from its natural source, the production of ART can be categorized into two further approaches: Total syntheses from readily available and cheap chemical stocks, and semi- or partial syntheses, that either start with extraction byproducts or with species from heterologous production, see Figure A.4.

The total synthesis of artemisinin is a very complicated and expensive endeavor due to its molecular structure with several asymmetric carbon atoms and a relatively unstable endoperoxide intermediate [79]. A first total synthesis approach was published by Schmid and Hofheinz from LaRoche in 1983. They obtained ART from iso-pulegol in eleven steps and with a yield of

Table A.1: Yields of artemisin (ART) for different extraction technologies and total synthesis strategies from selected references.

Extraction			
Reference	ART recovery		Remarks
(semi-)batch	/ %[1]	/ mg/g (leaves)	
Lapkin et al. (2010) [328]	≈ 60	–	Process yields of industrial extraction by hydrocarbons (mostly PE, and hexane).
ElSohly et al. (1990) [334]	–	1.2	Soxhlet extraction in hexane with reflux, 48 h.
Pilkington, Preston, and Gomes (2014) [335]	76	13.26	Extraction with PE, optimized by DoE, 45 °C for 8 h, two cycles; ART content 1.37 %.
Laboukhi-Khorsi, Daoud, and Chemat (2017) [332]	62	6.19	Hansen solubility parameters in isopropanol; ART content 1 %.
Zhang et al. (2014) [336]	–	7.8	UAE, 68 °C for 30 min.
Misra et al. (2013) [337]	–	7.3	MAE, 120 sec, two cycles.
Martinez-Correa et al. [330]		5.49	Ethanol extraction at 25 °C for 42 h.
Martinez-Correa et al. [330]		5.47	sCO$_2$ at 40 MPa and 60 °C.
Kohler et al. (1997) [338]	–	7	sCO$_2$ with methanol as co-solvent for 20 min.
Tzeng et al. (2007) [333]	–	11.26	sCO$_2$ with ethanol as co-solvent for 2 h.
Total synthesis			
Reference	Starting material	ART yield / %	Remarks
Schmid and Hofheinz (1983) [80]	iso-pulegol	< 5	11 steps.
Zhu and Cook (2012) [79]	cyclohexenone	8	
Krieger et al. (2018) [339]	R-(-)-citronellene	15	

PE: petroleum ether, DoE: design of experiments, UAE: ultrasound-assisted extraction, MB: methylene blue,
MAE: microwave-assisted extraction, sCO$_2$: supercritical carbon dioxide, TFA: trifluoroacetic acid
TPP: tetraphenylporphyrin, THF: tetrahydrofuran
[1]: based on ART content in dried biomass

less than 5 % [80]. A recent approach aims at diversity-oriented synthesis [340] for the isolated production of ART isomers from commercially available citronellene that makes the manufacture of stereospecific ART derivatives possible [339]. Another research group at the Cardiff University used an analogue of farnesyl diphosphate, an intermediate in the artemisinin biosynthesis towards amorphadiene (AD), Figure A.4, and converted it in a single step to an DHAA aldehyde, that is further transformed to ART in a continuous setup [341, 342]. An overview of ART yields from total synthesis approaches reported in literature is given in Table A.1.

On the other hand, partial syntheses from artemisinin precursors are potential and cost-effective alternatives [81, 82]. Fundamental studies about the semi-synthetic pathway from AA to ART were published by Acton and Roth beginning in 1989 [83–85], Figure A.5. In a first step, AA is hydrogenated to DHAA, where only the (R)-11 epimer has the correct stereochemistry found
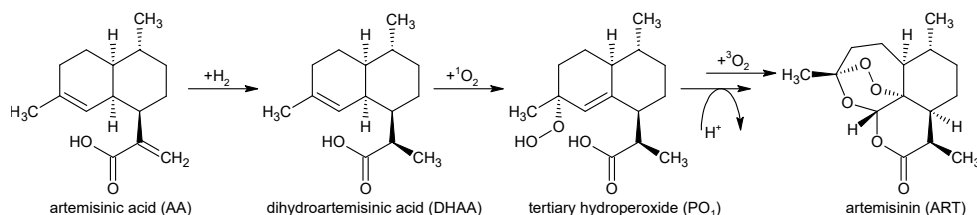
Figure A.5: Simplified semi-synthetic path from artemisinic acid (AA) to artemisin (ART) based on the fundamental works by Acton and Roth [83–85].

in ART [86]. However, other isomers of artemisinin have been isolated that show biological activity likewise [322, 339]. Following, DHAA is oxygenated to the dihydroartemisinic acid hydroperoxide PO_1 in a stereoselective ene-type reaction caused by singlet oxygen. In a final acid-catalyzed sequence with several steps including an in-situ chemical oxidation, the final molecule ART is formed.

Specifically, Roth and Acton [84] converted in methanol dissolved AA to DHAA in a water bath cooled vessel in a time frame exceeding 2 h. The DHAA was then photooxygenated at 0 °C in under 30 min using a high-intensity street lamp with acetone as solvent and 0.125 mol/l methylene blue as photosensitizer. The formed hydroperoxide was dissolved in either petroleum ether or hexane, dosed with a drop of TFA and converted to ART in air at room temperature within 4 days, resulting in an ART yield of 30 %.

For the production of ART precursors with a focus on AD and AA [325], researchers have turned to biotechnology [343]. In 2003, Keasling and co-workers engineered *Escherichia coli* bacteria to produce AD [88, 89], a biosynthetic precursor of ART, Figure A.4. Alternatively, in a major break-through by Keasling and colleagues, AA was produced in engineered *S. cerevisiae* yeast [90]. Historically, the former was replaced by the latter simply because of higher AA concentrations in the yeast cells [75]. AD can be converted to AA or DHAA by enzymatic oxidation [75] or to DHAA by a chemical process [93, 344], see Figure A.4.

Based on the preparatory work by Acton and Roth and the studies about AA production in yeast, the semi-synthesis of ART has been attempted to be industrialized by the companies Amyris and Sanofi [86, 91]. At Amyris, *S. cerevisiae* was engineered and grown on inexpensive carbon substrates using extractive fermentation that resulted in an AA yield of 25 g/l [86]. In the first step of the chemical semi-synthesis, AA was dissolved in toluene and Wilkinson's catalyst, i.e., a rhodium complex, was added. The vessel was pressurized to 25 bar with hydrogen after evacuation. AA is thereby completely converted, and DHAA was gained with a 90 % selectivity of the epimer of interest. Following, an esterification of DHAA was performed to prevent DHAA from converting to side products because of the acidic conditions. In the subsequent acid-catalyzed conversion to ART, the singlet oxygen was chemically produced by a metal-salt induced disproportionation of concentrated hydrogen peroxide. ART yields for this semi-synthesis were

between 40 and 45 %, with a final isolation by chromatography that reduced the overall process yield to 19 % [91]. However, the chemical conversion from AA to ART was not suitable for scale-up, a prerequisite for a successful industrialization [92]. Amyris is still working on ART [92], and in 2017, they reported a semi-synthesis starting with AD instead of AA as it is produced in a 2-fold higher molar yield, obtaining pure ART with a yield of 60 % [93]. To utilize the cheaper and less advanced intermediate AD, it was also investigated in very recent publications, where the published processes aim at forming a DHAA aldehyde from AD [94, 95].

Sanofi took up the idea of Amyris, developed from 2008 to 2013 another industrial production process, and built a plant in Garessio, Italy, that produced 35 t of ART in 2013 and was supposed to output almost 60 t a year in 2014 [91]. However, it has stopped operating in 2015 mainly due to low ART market prices [53, 57]. In the hydrogenation step, they exchanged the expensive and impractical Wilkinson's catalyst, which, at the same time, resulted in an increased selectivity of 95 % and a full conversion as in the Amyris process. Similar to the Amyris process, they used a DHAA derivative, i.e., an anhydride of DHAA, to prevent loss reactions. Contrary to the Amyris counterpart, Sanofi used a photochemically induced process for the generation of singlet oxygen, thereby mimicking the biosynthetic pathway. They applied tetraphenylporphyrin (TPP) as photosensitizer and added trifluoroacetic acid (TFA) in dichloromethane before entering the photo reactor. In this vein, the final acid-catalyzed cyclizations to ART and the generation of the DHAA hydroperoxide happened in one reactor. The overall Sanofi process yield is 55 %, a significant improvement to the Amyris process. After its shutdown in 2015, Sanofi sold the factory in Garessio to Huvepharma in Hungary, that, according to its CEO, produced 20 t of semi-synthetic ART in 2017 [92]. In 2016, Burgard et al. [96] from Sanofi published an improvement to their process. The energy-intensive mercury lamps were replaced by LED modules and the omission of the derivatization step to the DHAA anhydride was investigated. The replacement with LED lamps resulted in a yield of 50 % and a total reaction time of 8 h. Additionally, using DHAA instead of its derivative gave yields between 47 to 59 % for different measurement campaigns and batches, and a maximum yield of 62 % for diastomeric pure DHAA.

Other biotech companies, that have received grants in the near past, are Manus Bio for engineering E. coli to produce AA, and Phyton Biotech to research if ART can be directly produced by fermenting cells from the *A. annua* plant itself [92].

A.5   Continuous Manufacturing of Artemisinin

Both the Amyris and the Sanofi process are run in batch and semibatch reactors, as it is standard in the pharmaceutical industry until today. Batch processes are not very well understood on a micro-scale, have low yields, are difficult to scale-up, and therefore inherently hinder a good product quality [97]. Continuous processes in turn, as established in the chemical industry, offer

considerable potential in improving efficiency, safety, material consumption, scale-up, process understanding, monitoring and control, and in finding new synthetic routes, leading ultimately to increased product quality and economic benefits, for both development and manufacturing [98]. Relating to the process in this work, the photooxygenation of DHAA to PO_1 requires efficient irradiation of the reactant solution and sufficient supply of oxygen to achieve good yields within an acceptable time frame. Likewise, sufficient supply of oxygen is needed in the acid-catalyzed section. Milli-scaled flow reactors in Taylor flow mode offer high surface area between gas and liquid phase and efficient irradiation of the substrate due to the small channel depths. Flow microreactors are therefore suitable for the production of artemisinin using the here considered partial synthesis route, not least as multiple phases and photoreactions are involved. Besides the manufacturing perspective, the same advantages of continuous flow microreactors are beneficial for the study of kinetic reactions alike [99–102]. On the other hand, the regulatory Quality-by-design and Process Analytical Technology initiatives by the U.S. Food and Drug Administration stimulate innovations such as continuous manufacturing processes [98]; see the work by Mascia et al. [103] for an end-to-end continuous pharmaceutical process example.

The research groups of Seeberger and Seidel-Morgenstern have been developing a continuous process for the production of artemisinin and derivatives, starting from extraction, across synthesis up to purification [60, 63, 65, 104–109]. For the synthesis part, the pathway starting from DHAA is extensively explored, and led to a significant reduction in residence times to several minutes for the production of ART because of the use of milliscaled flow reactors. Next to the provision of DHAA from heterologous production, the authors suggest to utilize the DHAA content of the plant itself, compare with Figure A.4. Converting DHAA to ART is conducted in a single flow reactor with three different sections [63]. The first section comprised the photoreactor, the trailing two sections temperature-controlled regions for the acid-catalyzed synthesis. The conversion from DHAA to ART proceeds along the pathway that is shown in Figure A.6. DHAA reacts with singlet oxygen, that is formed photochemically using either Tetraphenylporphyrin (TPP) [60] or dicyanoanthracene (DCA) [63] as photosensitizer, in an ene-type reaction to the desired hydroperoxide PO_1, besides other hydroperoxides [63]. Next, by terminal protonation with trifluoroacetic acid (TFA), a Hock cleavage is induced that converts PO_1 to the enol. With the addition of triplet oxygen, the enol reacts to the enol hydroperoxide, that further reacts to the final product ART under acidic conditions.

In a first attempt with TPP and TFA in dichloromethane and a mercury lamp, a by chromatography purified ART yield of 39 % was achieved with a total residence time in the reaction lines of only 4.5 min [60]. Later, the more chemically-stable DCA replaced TPP, toluene replaced dichloromethane, and an LED module replaced the mercury lamp [63]. The selectivity of the photooxygenation was increased by setting the reaction temperature to $-20\,°C$, and an ART yield of 65 % was achieved resulting in a space-time yield of 3.5 g/(ml d). Following a temperature

Figure A.6: Semi-synthetic path from dihydroartemisinic acid (DHAA) to artemisin (ART) [60].

screening of both the photo reactor and the reaction line temperature, a maximum ART yield of 69 % was achieved [63]. In contrast to the utilization of synthetically produced photosensitizers, Triemer et al. [65] showed that in a similar setup the DHAA-containing crude plant extract can be directly used to produce artemisinin in similar yields, i.e., 67 %, where the present chlorophylls act as natural photosensitizers.

Current research directions aim at replacing solvents, catalysts, and photosensitizers with greener and cheaper materials. For instance, the usually applied nonpolar solvents are often toxic and highly flammable, but are first choice because polar solvents show worse selectivity for ART [63]. At the University of Nottingham, they used solid catalysts in a fixed-bed photoreactor as dual-function catalysts, i.e., the heterogeneous catalysts have an acidic base material and an immobilized photocatalyst phase. Toluene and liquid CO_2 mixed with oxygen, where the high pressure of 18 MPa enables high O_2 solubility, flows through the photoreactor giving a yield of 51 % based on DHAA [246]. A second strategy in the same article uses tetrahydrofuran in water with a water-soluble ionic photosensitizer and TFA as acid catalyst, that resulted in a yield of 66 % and a space-time yield of 3.4 g/(ml d), but was run in batch mode. Another modification was the development of a vortex reactor, that is able to efficiently suck in ambient air while the vortices generate rapid mixing and high mass transfer between the phases [248]. The use of supercritical CO_2 for the production of hydroperoxides in a flow process has been investigated likewise [345]. A further use of heterogeneous catalysis with immobilized rose bengal can be found in [346], but strategies based on heterogeneous catalysis are often challenging due to low irradiation efficiencies caused by the light-hindering solid material [347]. Albeit, Feng et al.

[348] published a record ART yield of 71 % based on DHAA. They implemented Brønsted acid sites into metal-organic frameworks (MOFs) enabling high surface areas, where porphyrinic units and trapped sulfuric acid formed the dual-function recyclable catalyst. The MOF catalyst and DHAA were dispersed in dichloromethane with bubbling O_2 and irradiated by LED lamps over a period of 6 h in a batch reactor.

From selected literature, an overview of yields for the partial synthesis is given in Table A.2.

Table A.2: Yields of artemisin (ART) for partial synthesis approaches from selected references. For other production routes, i.e., extraction and total synthesis, see Table A.1.

Reference	ART yields / % (basis)		Remarks
(semi-)batch	crude	process	
Roth and Acton (1991) [84]	30 (AA)	–	Photooxygenation in ice-water cooled acetone solution incl. MB, using a street lamp; air-oxidation of hydroperoxide in PE or hexane with TFA in about one day.
Paddon et al. (2013) [86], Amyris	40 – 45 (AA), 43 – 48³ (DHAA)	19 [91] (AA), 21² (DHAA)	Photooxygenation of DHAA ester via group VI metal salt-induced disproportionation of concentrated hydrogen peroxide; conversion of hydroperoxide to ART with benzenesulfonic acid and suspended copper(II)/Dowex resin in methylene chloride and bubbling dry air, cooled in an ice bath.
Kopetzki, Lévesque, and Seeberger (2013) [63]	69, 76, 81 (PO_1)	-	Conversion of PO_1 to ART; solvents: dichloromethane, cyclohexane, toluene; TFA, batch with bubbling oxygen.
Turconi et al. (2014) [91], Sanofi	–	55 (AA), 58² (DHAA)	One-pot photooxygenation of DHAA anhydride and conversion to ART in dichloromethane with TPP and TFA using mercury vapor lamps, −10 to −15 °C.
Amara et al. (2015) [246]	66 (DHAA)		THF in water (60 : 40) with a water-soluble ionic photosensitizer and TFA as acid catalyst, space-time yield 3.4 g/(ml d).
Burgard et al. (2016) [96]	62 (DHAA)		TFA and TPP in dichloromethane and bubbling air; LED module with total reaction time 13 h; diastomeric pure DHAA.
Feng et al. (2019) [348]	71 (DHAA)		Dual function recyclable solid catalyst, 6 h irradiation by LED lamps in dichloromethane with bubbling O_2.
continuous			
Lévesque and Seeberger (2012) [60]	46 (PO_1), 39 (DHAA)		TFA and TPP in dichloromethane using a mercury lamp at room temperature, residence time in photo reactor about 2 min, in reaction line 2.5 min.
Kopetzki, Lévesque, and Seeberger (2013) [63]	69 (DHAA)		Photoreactor temp. at −20 °C, reaction line temp. at 20 °C; DHAAconv. 99 %, selectivity 69 %, 0.5 M TFA in toluene, DHAA 0.5 M, DCA 2.5 mM, using LED lamps. Space-time yield: 3.5 g/(ml d).
Amara et al. (2015) [246]	51 (DHAA)		Dual-function solid catalyst, TPP with Amberlyst-15 support, toluene and liquid CO_2 mixed with oxygen (18 MPa).
Triemer et al. (2018) [65]	67 (DHAA)		Photoreactor temp. at −20 °C, reaction line temp. at 20 °C; crude extract with 0.5 M DHAA, 0.25 M TFA, chlorophylls, using LED lamps.

PE: petroleum ether, DoE: design of experiments, UAE: ultrasound-assisted extraction, MB: methylene blue,

MAE: microwave-assisted extraction, sCO_2: supercritical carbon dioxide, TFA: trifluoroacetic acid

TPP: tetraphenylporphyrin, THF: tetrahydrofuran

²: back-calculated based on yield and selectivity data given in [91]

³: assuming 99 % yield of DHAA, compare with yields in [91]

B   Mathematical Methodologies

B.1   Background on Likelihood Theory

In practice, estimators are searched that have zero bias and minimum variance, referred to as minimum variance unbiased estimators (MVUEs). MVUEs do not always exist and even if existing, they might not necessarily be found [141]. To assert an MVUE, a lower limit on the covariance matrix of an unbiased estimator for a parameter vector $\boldsymbol{\theta}^\star$ can be postulated with the Cramér-Rao lower bound (CRLB) [141]:

$$\boldsymbol{C}_\theta \geq -\left(\mathbb{E}\left[\left. \frac{\partial^2 \, \mathrm{pdf}(\tilde{\boldsymbol{y}}|\boldsymbol{\theta})}{\partial\boldsymbol{\theta}\partial\boldsymbol{\theta}^\mathsf{T}} \right|_{\theta^\star} \right] \right)^{-1} . \tag{B.1}$$

The CRLB, Equation (B.1), requires the regularity conditions $\mathbb{E}\left[\frac{\partial \, \mathrm{pdf}(\tilde{\boldsymbol{y}}|\boldsymbol{\theta})}{\partial\boldsymbol{\theta}} \right] = 0 \; \forall\boldsymbol{\theta}$ to hold [141]. Thus, an evaluation of the CRLB boundary case, Equation (B.1), quantifies if an estimator is a MVUE, or how far it is away from an MVUE. The problems of the potential non-existence of and the search for an MVUE calls for alternative and practical estimators in the sense that they can be straightforwardly evaluated and possess beneficial statistical properties. The most popular alternative is the maximum likelihood estimator (MLE), that is a central part of likelihood theory. For his pioneering and extensive work in likelihood theory in the beginning of the 20$^{\text{th}}$ century, Ronald A. Fisher is considered its founder [142, 143], although maximum likelihood estimates have been used prior to his work [142]. The MLE is considered to be asymptotically optimal, as it is unbiased with an approximate Normal distribution and has minimum variance for large enough data sets, i.e., it is asymptotically an MVUE [141]. The MLE is attained by maximizing the likelihood function $\mathcal{L}$, that is underlain by a PDF. For example, based on the Normal PDF in Equation (3.4), the logarithmic likelihood function for the additive noise model, Figure 3.2a, with independently distributed Normal error terms and zero means, is:

$$\log\mathcal{L}(\boldsymbol{\theta},\boldsymbol{\sigma}|\tilde{\boldsymbol{y}},\mathcal{M}) = -\frac{1}{2}\sum_{j=1}^{n_y(t_k)}\sum_{k=1}^{n_t}\left[\log(2\pi\sigma_j^2(t_k)) + \left(\frac{\tilde{y}_j(t_k) - y_j(t_k,\boldsymbol{\theta})}{\sigma_j(t_k)} \right)^2 \right], \tag{B.2}$$

where it is considered, that different samples at time points t_k might have different numbers of data points $n_y(t_k)$. The total number of data points is then $N = \sum_{j=1}^{n_y(t_k)}\sum_{k=1}^{n_t} 1$. The assumption of Gaussian errors is justified with the *Central limit theorem*, stating that summing up independent random variables, regardless their distributions, yields approximately a Normal distribution. Thus, for inference about the model parameters $\boldsymbol{\theta}$ and the standard deviations $\boldsymbol{\sigma}$, data $\tilde{\boldsymbol{y}}$ and a statistical model must be given. To calculate confidence intervals for the model parameters $\boldsymbol{\theta}$ from the MLE, Equation (3.29), we make use of the asymptotic properties of the MLE, i.e., we

evaluate the CRLB, Equation (B.1), at its limiting case. In honor of Fisher, the expectation on the right hand side in Equation (B.1) is termed the Fisher information matrix (FIM):

$$\mathbf{FIM} = -\mathbb{E}\left[\left.\frac{\partial^2 \, \mathrm{pdf}(\tilde{y}|\boldsymbol{\theta})}{\partial \boldsymbol{\theta} \partial \boldsymbol{\theta}^{\mathsf{T}}}\right|_{\boldsymbol{\theta}^{\star}}\right]. \tag{B.3}$$

The parameter covariance matrix can thus be approximated from the inverse of the FIM:

$$\boldsymbol{C}_{\theta} \approx \mathbf{FIM}^{-1}. \tag{B.4}$$

The $(1 - \phi)100\%$ asymptotic confidence interval for a parameter θ_i is then evaluated as follows:

$$\hat{\theta}_i \pm z_{1-\phi/2}\sqrt{C_{\theta,ii}}, \tag{B.5}$$

with z the $1 - \phi/2$ quantile of $Z \sim \mathcal{N}(0, 1)$. In the case of independent Gaussian errors, Equation (3.32), the FIM can be calculated as [141]:

$$\mathbf{FIM} \stackrel{\mathcal{N}}{=} \left[\underbrace{\left.\frac{\partial \boldsymbol{y}(\boldsymbol{\theta})}{\partial \boldsymbol{\theta}}\right|_{\boldsymbol{\theta}^{\star}}}_{\boldsymbol{SM}}\right]^{\mathsf{T}} \boldsymbol{\Sigma}^{-1} \left.\frac{\partial \boldsymbol{y}(\boldsymbol{\theta})}{\partial \boldsymbol{\theta}}\right|_{\boldsymbol{\theta}^{\star}}, \tag{B.6}$$

with $\boldsymbol{\Sigma}$ the measurement covariance matrix, and $\boldsymbol{SM} = \partial \boldsymbol{y}/\partial \boldsymbol{\theta}$ the sensitivity matrix of the model parameters. The FIM in Equation (3.36) generally cannot be evaluated due to lack of knowledge about the true parameter value $\boldsymbol{\theta}^{\star}$. In practice, the FIM is therefore approximated in Equation (3.35) or Equation (3.36) by utilizing the MLE. In the former case, the FIM follows from the log likelihood function, Equation (3.32) [141]:

$$\mathbf{FIM} \approx -\left.\frac{\partial^2 \log \mathcal{L}(\boldsymbol{\theta})}{\partial \boldsymbol{\theta} \partial \boldsymbol{\theta}^{\mathsf{T}}}\right|_{\hat{\boldsymbol{\theta}}_{\mathrm{MLE}}}. \tag{B.7}$$

Alternatively, the FIM can be determined from the parameter sensitivities, Equation (3.36):

$$\mathbf{FIM} \approx [\boldsymbol{SM}|_{\hat{\boldsymbol{\theta}}_{\mathrm{MLE}}}]^{\mathsf{T}} \boldsymbol{\Sigma}^{-1} \boldsymbol{SM}|_{\hat{\boldsymbol{\theta}}_{\mathrm{MLE}}}. \tag{B.8}$$

Hence, the second alternative is especially helpful if data is not or not yet present. Accordingly, the FIM in Equation (3.37) is usually termed the observed FIM, and the FIM in Equation (3.38) is referred to as expected FIM. For a discussion about differences in the expected and the observed FIM, the interested reader is pointed to [144].

B.2 Derivation of Akaike Information Criterion

The AIC follows from information and likelihood theory. The Kullback-Leibler information (KLI) is

$$I_{KL}(f_0, f) = \int f_0(\boldsymbol{x}) \log \left(\frac{f_0(\boldsymbol{x})}{f(\boldsymbol{x}|\boldsymbol{\theta})} \right) d\boldsymbol{x}, \tag{B.9}$$

and denotes the information lost when f is used to approximate f_0 [120]. The KLI is heuristically also interpreted as the distance between two probability density functions f and f_0, although it is not a symmetric measure. Considering f_0 to be the truth representing the physical system to be modeled, calculation of I_{KL} for all postulated process model candidates would provide a decision support for selecting the best model candidate in the sense of Kullback-Leibler information. For it is not possible to evaluate the truth f_0, a relative distance based on the KLI is introduced by rewriting Equation (B.9):

$$I_{KL}(f_0, f) = \underbrace{\int f_0(\boldsymbol{x}) \log \left(f_0(\boldsymbol{x}) \right) d\boldsymbol{x}}_{=C} - \underbrace{\int f_0(\boldsymbol{x}) \log \left(f(\boldsymbol{x}|\boldsymbol{\theta}) \right) d\boldsymbol{x}}_{=\mathbb{E}_{f_0}[\log(f(\boldsymbol{x}|\boldsymbol{\theta}))]} \tag{B.10}$$

$$I_{KL}(f_0, f) - C = -\mathbb{E}_{f_0}[\log(f(\boldsymbol{x}|\boldsymbol{\theta}))],$$

with C a constant, that has the same magnitude across all model candidates. The relative KLI on the right hand side of the second line in Equation (B.10) is still unknown and estimated parameters have not been considered so far. Akaike showed that the evaluation of a relative expected Kullback-Leibler distance is approximately possible from the MLE calling it the Akaike information criterion (AIC) [120, 349]:

$$AIC = -2\mathcal{L}(\hat{\boldsymbol{\theta}}_{MLE}) + 2K, \tag{B.11}$$

with K the number of estimated parameters, that is in general not equal to the number of estimated process model parameters. The corrected AIC is

$$AIC_c = AIC + \frac{2K(K+1)}{N - K - 1}, \tag{B.12}$$

where its use is recommended for N/K ratios below 40 [120]. From Equation (3.41), it is obvious that the AIC inherently considers the bias-variance trade-off, Equation (3.3), by penalizing the goodness-of-fit measure, i.e., the log likelihood value at the MLE, through the number of estimated parameters K. The quite technical derivation of the AIC can be found in the original article [349] or in [120]. Note that the AIC is a relative measure and therefore must be interpreted as such, where AIC values ranging from large negative values to values as high as $304,000$ have been observed [120].

B.3 Derivation of Sobol' Method via Hoeffding Decomposition

The relation (3.59) can be derived from a decomposition of the original model function f, Equation (3.1), that was derived by Sobol' [185], that also forms the basis of his main idea to calculate the sensitivity indices. From here on it is assumed without loss of generality that the input domain is a n_u-dimensional unit hypercube with uniformly distributed inputs. The decomposition, also known as Hoeffding or Hoeffding-Sobol' decomposition, is

$$
\begin{aligned}
f(\boldsymbol{U}) &= f_0 + \sum_{s=1}^{n_u} \sum_{i_1 < \cdots < i_s}^{n_u} f_{i_1 \cdots i_s}(U_{i_1}, \ldots, U_{i_s}) \\
&= f_0 + \sum_{i=1}^{n_u} f_i(U_i) + \sum_{i=1}^{n_u} \sum_{j>i}^{n_u} f_{ij}(U_i, U_j) + \cdots + f_{12 \cdots n_u}(U_1, U_2, \ldots, U_{n_u})
\end{aligned}
\tag{B.13}
$$

with $1 \le i_1 < \cdots < i_s \le n_u$ and having 2^{n_u} terms on the right hand side. The Hoeffding composition becomes unique if the following conditions hold [185]:

$$
\int_0^1 f_{i_1 \cdots i_s}(u_{i_1}, \ldots, u_{i_s}) \, \mathrm{d}u_k = 0 \quad \text{for} \quad k = i_1, \ldots, i_s.
\tag{B.14}
$$

The decomposition (B.13) is then also referred to as ANOVA representation [350]. A direct consequence is that the terms on the right hand side of Equation (B.13) are pairwise orthogonal:

$$
\int f_{i_1 \cdots i_m} f_{j_1 \cdots j_n} \, \mathrm{d}\boldsymbol{u} = 0, \quad \text{if } (i_1, \ldots, i_m) \ne (j_1, \ldots, j_n),
\tag{B.15}
$$

because at least one index will not be repeated and therefore its interval will be zero, Equation (B.14). Note that the dependencies are dropped here for the sake of brevity. If assuming that $f(\boldsymbol{U})$ is square integrable, it follows that all the $f_{i_1 \cdots i_s}$ terms are square integrable as well, and the variance decomposition is obtained:

$$
\begin{aligned}
\int f^2(\boldsymbol{u}) \mathrm{d}\boldsymbol{u} - f_0^2 &= \sum_{s=1}^{n_u} \sum_{i_1 < \cdots < i_s}^{n_u} \int f_{i_1 \cdots i_s}^2 \, \mathrm{d}u_{i_1} \cdots \mathrm{d}u_{i_s} \\
\mathbb{V}[Y] &= \sum_{i}^{n_u} V_i + \sum_{i}^{n_u} \sum_{j>i}^{n_u} V_{ij} + \sum_{i}^{n_u} \sum_{j>i}^{n_u} \sum_{k>j}^{n_u} V_{ijk} + \cdots + V_{123 \ldots n_u},
\end{aligned}
\tag{B.16}
$$

with partial variances

$$V_i = \int_0^1 f_i^2 \, \mathrm{d}u_i = \mathbb{V}[f_i]$$
$$V_{ij} = \int f_{ij}^2 \, \mathrm{d}u_i \mathrm{d}u_j = \mathbb{V}[f_{ij}]. \tag{B.17}$$
$$\vdots$$

To understand the last equalities, a look at the definition of the variance gives insight:

$$\mathbb{V}[f_{i_1 \cdots i_s}] = \mathbb{E}[f_{i_1 \cdots i_s}^2] - \mathbb{E}[f_{i_1 \cdots i_s}]^2$$
$$= \mathbb{E}[f_{i_1 \cdots i_s}^2] - \underbrace{\int f_{i_1 \cdots i_s} \, \mathrm{d}u_{i_1} \cdots \mathrm{d}u_{i_s}}_{\overset{\text{(B.14)}}{=} 0}$$
$$= \mathbb{E}[f_{i_1 \cdots i_s}^2] = \int f_{i_1 \cdots i_s}^2 \, \mathrm{d}u_{i_1} \cdots \mathrm{d}u_{i_s}$$

It is clear that each partial variance measures solely the influence that is caused by the given index or by the combination of the given indices due to the basic idea of the performed decomposition, Equation (B.13). Dividing Equation (B.16) by $\mathbb{V}[Y]$ yields the summation relation of the Sobol' sensitivity indices, Equation (3.59).

B.4   Computation of Sobol' Indices

For the computation of the Sobol' indices, Monte Carlo methods with tailored sampling strategies are used [186, 351]. I the following the estimators for the first and total order indices from [186] and for the second order indices from [352] are described. All of the estimators have in common that they start with two independent sample matrices A and B with sizes $N \times n_u$, and N the number of simulations. A third matrix $A_B^{(i)}$ for each parameter is created where all columns are

from A apart from the ith column, that is from A. Analogously, for the second order indices, a fourth matrix $B_A^{(i)}$ is required. The sensitivity indices are then calculated as

$$S_i \mathbb{V}[Y] = \frac{1}{N} \sum_{k=1}^{N} f(B)_k \left(f(A_B^{(i)})_k - f(A)_k \right),$$

$$S_{\mathrm{T}i} \mathbb{V}[Y] = \frac{1}{2N} \sum_{k=1}^{N} \left(f(A)_k - f(A_B^{(i)})_k \right)^2,$$

$$S_{ij} \mathbb{V}[Y] = \frac{1}{N} \sum_{k=1}^{N} f(B_A^{(i)})_k f(A_B^{(j)})_k - f(A)_k f(B)_k$$

$$- (S_i + S_j)\mathbb{V}[Y].$$

(B.18)

with the total variance given by the uncorrected sample variance, Equation (3.50b),

$$\mathbb{E}[Y] = \frac{1}{2N} \sum_{k=1}^{N} f(A)_k + f(B)_k$$

$$\mathbb{V}[Y] = \frac{1}{2N} \sum_{k=1}^{N} (f(A)_k - \mathbb{E}[Y])^2 + (f(B)_k - \mathbb{E}[Y])^2$$

(B.19)

The sampling and design of the four matrices, that are quasi-random sequences, is given in [352] and [186]. For very small sensitivity indices, negative values might appear due to computational inaccuracies [37]. Khorashadi Zadeh et al. [353] proposed to introduce a dummy parameter, that does not exist in the model, but is added to the input vector to estimate the occurring inaccuracies. Indices that do not exceed the index of the dummy parameter should not be considered sensitive.

B.5 Solving Optimal Control Problems

Solving the dynamic optimization problem, Equation (3.65), can be performed following two different discretization strategies of the time-dependent functions in Equation (3.65): *Optimize then Discretize*, also called the *indirect* or *variational approach*, or *Discretize then Optimize*, its *direct* counterpart. The first strategy focuses on the solution of the first-order optimality conditions for the OCP, resulting in a boundary value problem (BVP). The difficulties associated with solving BVPs led to research activities dealing with the conversion of the OCP to constrained, finite-dimensional problems to exploit state-of-the-art large-scale *nonlinear program* (NLP) solvers [205]. Methods applying NLP solvers can be classified further into sequential and simultaneous strategies. In the sequential approach referred to as *single shooting*, the control vector is parameterized, and the resulting NLP problem is solved using control vector parameterization

(CVP) methods [354, 355]. In contrast, the simultaneous approach *multiple shooting* divides the OCP into smaller subproblems requiring next to CVP initial states in the individual problems and serves as a bridge to the *direct transcription* approach, where all variables, i.e., states and controls, are discretized [205]. The discretization of the states and controls is usually realized using collocation and control parameterization techniques that lead to complex optimization problems for which efficient solvers and great computational power are needed [251].

C   Step 2: Acid-Catalyzed Sequence

C.1   Governing Equations of Batch Experiments

The reactor used in the batch experiments is modeled as a continuous stirred tank reactor (CSTR) [26]. Based on the reaction network in Equation (5.5) and under the absence of oxygen, the governing equations of the batch experiments are

$$
\begin{aligned}
\frac{d[PO_1]}{dt} &= -k_{PO_x}[PO_1] - k_{PO_1 \cdot BP_3}[PO_1][H^+]^{m_{IM_2}+1} - k_{PO_1 \cdot IM_2}[PO_1][H^+]^{m_{IM_2}}, \\
\frac{d[IM_{2b}]}{dt} &= k_{PO_1 \cdot IM_2}[PO_1][H^+]^{m_{IM_2}} - k_{IM_{2b} \cdot BP_4}[IM_{2c}][H^+], \\
\frac{d[BP_4]}{dt} &= k_{IM_{2b} \cdot BP_4}[IM_{2b}][H^+], \\
\frac{d[BP_3]}{dt} &= k_{PO_1 \cdot BP_3}[PO_1][H^+]^{m_{IM_2}+1}, \\
\frac{d[BP_6]}{dz} &= k_{IM_{2b} \cdot BP_6}[IM_{2b}][H^+].
\end{aligned}
\tag{C.20}
$$

The corresponding initial conditions are

$$
\begin{aligned}
([PO_1], &[IM_{2b}], [BP_4], [BP_3], [BP_6])^\top(0) \\
&= ([PO_1]_0, 0, 0, [BP_3]_0, 0)^\top.
\end{aligned}
\tag{C.21}
$$

C.2   Estimated Model Parameters and Initial Conditions for the Core Set of Model Candidates

The estimated model parameters and the estimated values of the initial conditions of the core set of model candidates, Table 5.2, are listed in Tables C.3, C.4 and C.5.

C.3   Model Candidates for Acid-Catalyzed Sequence

The core set of the model candidates for the acid-catalyzed sequence in Table 5.2 was extended with further combinations of the super structure not investigated so far, or with additional variants to the super structure, that is shown in Figure 5.7. A summary of the extension set of model candidates is given in Table C.6. The additional features of the extended model candidates are:

Table C.3: First part of estimated model parameters of the different model candidates for the synthesis reaction network. For the second part, see Table C.4. Values are rounded to three significant figures and a maximum number of three decimals. With the exception of k_{PO_x}, a threshold of 5×10^{-4} is applied, below which the values are tabulated as 0.

#	k_{PO_x} 1×10^{-3}/min	k_{PO,IM_2} mol/(l min)	k_{IM_2,IM_3} mol/(l min)	$k_{IM_2,ART}$ mol/(l min)	$k_{IM_3,ART}$ mol/(l min)	K_{TFA} 1	m_{IM_2} -	m_{BP_3} -	k_{PO,BP_3} mol/(l min)	k_{IM_2,BP_4} mol/(l min)	k_{IM_2,BP_5} mol/(l min)
1	0.614	3.17	205		0.598					0.441	0
2	0.614	3.17	205		0.598	5000			0.349	0.441	0
3	0.614	3.17	205		0.598	5000			0.349	0.441	0
4	11.2	0.234		175					26.0	1.54	0
5	9.98	0.262	5000		5000				249	1.28	0
6	0.771	3.13	81.9		0.902				0.353		0
7	7.51	4960	69.0		12.5					1.42	0.49
8	0.449	3.13	942		2.4				0.06	0.574	0
9	5.36	2.87	2280		2.66				0.298		0
10	5.42	2.47	1570		14.2				0.31	15.1	
11	5.15	1910	435		3.11				0.008		7.34
12	4.93	9.99	1500		6.16				0.013		0
13	0.801	3.40	432		0.716				0.008		0
14	10.0	835	5000		0.493		2.61		2.37	0.391	0
15	10.7	985	5000		0.786		2.67		0.043	0.718	0
16	9.92	318	5000		1.46		2.37		634	0.858	0
17	10.2	495	5000		1.60	1.23	2.49		159	0.732	
18	9.92	318	5000		1.46	4990	2.37		300	0.804	
19	9.47	155	2500		0.804		2.11		159	0.733	
20	10.7	985	5000		0.786		2.67		104	0.76	0.003
21	10.7	981	5000		0.787		2.67		634		0
22	9.85	311	5000		1.63		2.36		632	0.86	0
23	9.88	293	5000		1.82		2.35		157	0.716	
24	9.92	318	5000		1.46		2.37		145	0.721	
25	10.7	986	5000		0.786		2.67	3.68	641	0.733	0
26	9.90	304	5000		1.51		2.36	3.08	112	0.858	0
27	10.7	982	5000		0.786		2.67	3.68	639	0.742	
28	10.7	986	5000		0.786		2.67	3.68	641	0.86	
29	9.20	72.6	490		365		1.98	2.25	13.7		0
30	9.90	304	5000		1.51		2.36	3.08	112		0

Table C.4: Second part of estimated model parameters of the different model candidates for the synthesis reaction network. For the first part, see Table C.3. Values are rounded to three significant figures and a maximum number of three decimals. A threshold of 5×10^{-4} is applied, below which the values are tabulated as 0.

#	$k_{PO_3,BP_3,f}$ mol/(l min)	$k_{PO_3,BP_3,r}$ mol/(l min)	$k_{PO_3,IM_2,f}$ mol/(l min)	$k_{PO_3,IM_2,r}$ mol/(l min)	$k_{IM_2,IM_4,f}$ mol/(l min)	$k_{IM_2,IM_4,r}$ mol/(l min)	k_{IM_4,BP_4} mol/(l min)	k_{IM_3,BP_5} mol/(l min)	k_{IM_3,BP_6} mol/(l min)	$k_{hyd,f}$ mol/(l min)	$k_{hyd,r}$ mol/(l min)
1											
2											
3											
4			145	0							
5			1410	0							
6					101	0	0.377				
7	7.89	0.129	22.7	3910						5000	0
8										5000	0
9					6.57	0	0.919			5000	0.183
10	3.35	0.005	35.7	1.14							
11	1.50	0.006	39.0	4990	10.7	5000	5000				
12	1.70	0.008	409	312	36.8	5000	963			5000	0.065
13											
14											
15											
16								0.59			
17								0.644			
18								0.59			
19			4600	5000							
20					1.72	5000	5000				
21										128	3360
22										3.84	0.036
23								0.571		11.3	1.27
24									0.59		
25											
26								0.612			
27										120	3360
28					1.72	5000	5000				
29					2.18	5000	5000			5000	0.263
30					1.48	5000	5000	0.612		0.005	3330

209

Table C.5: Estimated initial conditions of PO_1 and BP_3 of the six considered batch experiments for the different model candidates of the synthesis reaction network. Values are rounded to three significant figures and a maximum number of three decimals. A threshold of 1×10^{-6} mol/l is applied, below which the values are tabulated as 0.

#	$[PO_1]_{0,1}$ mol/l	$[BP_3]_{0,1}$ mmol/l	$[PO_1]_{0,2}$ mol/l	$[BP_3]_{0,2}$ mmol/l	$[PO_1]_{0,3}$ mol/l	$[BP_3]_{0,3}$ mmol/l	$[PO_1]_{0,4}$ mol/l	$[BP_3]_{0,4}$ mmol/l	$[PO_1]_{0,5}$ mol/l	$[BP_3]_{0,5}$ mmol/l	$[PO_1]_{0,6}$ mol/l	$[BP_3]_{0,6}$ mmol/l
1	0.282	4.51	0.357	0	0.322	0	0.339	0	0.369	0	0.365	0
2	0.282	4.51	0.357	0	0.322	0	0.339	0	0.369	0	0.365	0
3	0.282	4.51	0.357	0	0.322	0	0.339	0	0.369	0	0.365	0
4	0.245	2.84	0.362	0.454	0.319	0	0.322	0	0.356	0	0.333	0
5	0.246	2.17	0.362	0	0.314	0	0.325	0	0.358	0	0.338	0
6	0.284	4.14	0.357	0	0.323	0	0.344	0	0.370	0	0.367	0
7	0.271	2.05	0.362	0.041	0.328	0	0.342	0	0.365	0	0.356	0
8	0.283	6.58	0.356	0	0.321	0.055	0.347	0	0.367	0	0.367	0
9	0.300	7.19	0.380	0.339	0.340	1.34	0.365	0	0.380	0.688	0.380	0
10	0.303	16.4	0.355	5.77	0.338	9.05	0.364	5.99	0.368	9.05	0.382	8.99
11	0.323	14.2	0.363	5.19	0.352	7.89	0.383	3.90	0.382	7.96	0.400	7.09
12	0.318	16.3	0.360	5.68	0.348	8.89	0.378	5.81	0.377	8.89	0.399	8.75
13	0.281	18.1	0.357	6.19	0.322	9.63	0.340	7.51	0.369	9.49	0.365	9.08
14	0.258	18.5	0.337	5.25	0.295	8.69	0.314	7.00	0.334	8.38	0.338	9.44
15	0.253	19.1	0.337	6.55	0.293	10.5	0.309	8.66	0.332	10.4	0.332	10.3
16	0.254	19.5	0.337	6.55	0.295	10.5	0.312	8.85	0.334	10.4	0.334	10.6
17	0.252	19.3	0.337	6.55	0.294	10.5	0.310	8.72	0.333	10.3	0.332	10.4
18	0.254	19.5	0.337	6.55	0.295	10.5	0.312	8.85	0.334	10.4	0.334	10.6
19	0.257	18.2	0.342	6.52	0.300	10.3	0.314	8.33	0.341	10.2	0.336	9.91
20	0.253	19.1	0.337	6.55	0.293	10.5	0.309	8.66	0.332	10.4	0.332	10.3
21	0.253	19.1	0.337	6.55	0.293	10.5	0.31	8.66	0.332	10.4	0.332	10.3
22	0.255	19.4	0.337	6.54	0.295	10.5	0.312	8.83	0.334	10.4	0.335	10.6
23	0.254	19.5	0.337	6.55	0.295	10.5	0.312	8.85	0.334	10.4	0.334	10.6
24	0.254	19.5	0.337	6.55	0.295	10.5	0.312	8.85	0.334	10.4	0.334	10.6
25	0.253	19.2	0.337	6.55	0.293	10.5	0.309	8.69	0.332	10.4	0.332	10.3
26	0.254	18.1	0.337	6.49	0.295	10.1	0.312	7.80	0.334	10.0	0.334	9.23
27	0.253	19.2	0.337	6.55	0.293	10.5	0.31	8.69	0.332	10.4	0.332	10.3
28	0.253	19.2	0.337	6.55	0.293	10.5	0.309	8.69	0.332	10.4	0.332	10.3
29	0.257	13.5	0.339	5.86	0.299	7.98	0.323	3.36	0.339	7.98	0.342	4.21
30	0.254	18.1	0.337	6.49	0.295	10.1	0.312	7.80	0.334	10.0	0.334	9.23

Table C.6: First part of the extended set of proposed model candidates for the acid-catalyzed reaction network, with additional variants to the super structure shown in Figure 5.7. The font colors of the table columns match the colors of the network characteristics in the same Figure. The dissociation type of all candidates in the extension set is "A", see Table 5.1. The reaction orders, separated by commas, are the orders for the reactions from PO_1 to IM_2, from PO_1 to BP_3, from IM_3 to ART, and from IM_2 to BP_4. In the last case, forward and reverse reaction orders are estimated if the BP_4 is formed through an equilibrium step.

ID	#x	#θ	Reaction orders	IM_2 prot.	BP_3 prot.	BP_4 eq.	BP_4 pos.	Hyd. pos.	$BP_{5/6/7}$ pos.	IM_3	IM_5 pos.	ART pos.
31	11	11	1,1,1	eq.	eq.	-	IM_2	-	IM_2	✓	-	-
32	10	10	$m_{IM_2}, m_{IM_2}+1,1$	-	-	-	IM_3	IM_3	IM_3	✓	-	-
33	10	9	$m_{IM_2}, m_{IM_2}+1,1$	-	-	-	IM_2	-	"$IM_{2/3}$ (hyd.) "	✓	-	-
34	12	12	$m_{IM_2}, m_{IM_2}+1,1$	-	-	✓	IM_2	-	"$IM_{2/3/4}$ (hyd.) "	✓	-	-
35	9	8	$m_{IM_2}, m_{IM_2}+1,1$	-	-	-	IM_2	-	IM_3 (w/o TFA)	✓	-	-
36	10	9	$m_{IM_2}, m_{IM_2}+1,1$	-	-	-	IM_2	-	$IM_{2/3}$ (w/o TFA)	✓	-	-
37	11	11	$m_{IM_2}, m_{IM_2}+1,1$	-	-	✓	IM_2	-	$IM_{2/3}$ (w/o TFA)	✓	-	-
38	10	11	$m_{IM_2}, m_{IM_2}+1, m_{ART}$	-	-	-	$IM2$	IM_3	IM_3	✓	-	-
39	12	12	$m_{IM_2},1,1$	✓	-	-	IM_2	IM_2	IM_2	✓	-	-
40	10	11	$m_{IM_2}, m_{BP_3},1$	-	-	-	IM_2	IM_2	IM_2	✓	-	-
41	11	13	$m_{IM_2}, m_{BP_3},1$	-	-	-	IM_2	-	IM_2	✓	IM_3	IM_3
42	12	15	$m_{IM_2}, m_{BP_3},1$	-	-	✓	IM_2	-	IM_2	✓	IM_3	IM_3
44	10	10	$m_{IM_2}, m_{IM_2}+1,1$	-	-	-	IM_2	-	IM_3	✓	IM_3	IM_5
45	11	11	$m_{IM_2}, m_{IM_2}+1,1$	-	-	-	IM_2	-	$IM_{3/5}$	✓	IM_3	IM_5
46	10	11	$m_{IM_2}, m_{BP_3},1$	-	-	-	IM_2	-	IM_3	✓	IM_3	IM_3
47	10	11	$m_{IM_2}, m_{BP_3},1$	-	-	-	IM_2	-	IM_3	✓	IM_3	IM_5
48	11	12	$m_{IM_2}, m_{BP_3},1$	-	-	-	IM_2	-	$IM_{3/5}$	✓	IM_3	IM_5

Table C.7: Second part of the extended set of proposed model candidates for the acid-catalyzed reaction network, Table C.6.

ID	#x	#θ	Reaction orders	IM₂ prot.	BP₃ prot.	BP₄ eq.	BP₄ pos.	Hyd. pos.	BP₅/₆/₇ pos.	IM₃	IM₅ pos.	ART pos.
49	12	12	$m_{IM_2}, m_{IM_2}+1, 1, 1$	-	-	-	IM_2	-	$IM_{2/3/5}$	eq.	$IM_3\ (O_2)$	IM_5
50	12	13	$m_{IM_2}, m_{IM_2}+1, 1, m_{BP_4}$	-	-	-	IM_2	-	$IM_{2/3/5}$	eq.	$IM_3\ (O_2)$	IM_5
51	13	14	$m_{IM_2}, m_{IM_2}+1, 1, 1$	-	-	✓	IM_2	-	$IM_{2/3/5}$	eq.	$IM_3\ (O_2)$	IM_5
52	13	12	$m_{IM_2}, m_{IM_2}+1, 1, 1$	-	-	-	IM_2	-	$IM_{2/3/5}$	eq. (rev. w/o TFA)	$IM_3\ (O_2)$	IM_5
53	10	10	$m_{IM_2}, m_{IM_2}+1, 1, 1$	-	-	-	IM_2	-	$IM_{2/3/5}$	eq. (rev. w/o TFA)	-	$IM_3\ (O_2,\ \text{w/o TFA})$
54	10	10	$m_{IM_2}, m_{IM_2}+1, 1, 1$	-	-	-	IM_2	-	$IM_{2/3/5}$	eq. (rev. w/o TFA)	-	$IM_3\ (O_2,\ \text{TFA})$
55	9	9	$m_{IM_2}, m_{IM_2}+1, 1, 1$	-	-	✓	IM_2	-	IM_2	-	-	$IM_2\ (O_2,\ \text{w/o TFA})$
56	9	11	$m_{IM_2}, m_{IM_2}+1, 1, m_{BP_4}^{f/r}$	-	-	✓	IM_2	-	IM_2	-	-	$IM_2\ (\text{TFA})$
57	9	9	$m_{IM_2}, m_{IM_2}+1, 1, 1$	-	-	✓	IM_2	-	IM_2	-	-	$IM_2\ (\text{TFA})$
58	9	10	$m_{IM_2}, m_{IM_2}+1, 1, m_{BP_4}$	-	-	-	IM_2	-	IM_2	-	IM_2	$IM_2\ (\text{w/o TFA})$
59	9	11	$m_{IM_2}, m_{IM_2}+1, 1, m_{BP_4}^{f/r}$	-	-	✓	IM_2	-	IM_2	-	-	$IM_2\ (\text{w/o TFA})$
60	9	10	$m_{IM_2}, m_{IM_2}+1, 1, m_{BP_4}$	-	-	-	IM_2	-	IM_2	-	IM_2	$IM_2\ (\text{TFA})$
61	10	11	$m_{IM_2}, m_{IM_2}+1, m_{IM_3}, m_{BP_4}$	-	-	-	IM_2	-	$IM_{2/3}$	✓	-	$IM_3\ (O_2,\ \text{w/o TFA})$
62	10	11	$m_{IM_2}, m_{IM_2}+1, m_{IM_3}, m_{BP_4}$	-	-	-	IM_2	-	$IM_{2/3}$	✓	-	$IM_3\ (O_2,\ \text{TFA})$
63	10	9	$m_{IM_2}, m_{IM_2}+1, 1, m_{BP_4}$	-	-	-	IM_2	-	$IM_{2/2}$	-	-	$IM_2\ (\text{w/o TFA})$
64	10	9	$m_{IM_2}, m_{IM_2}+1, 1, m_{BP_4}$	-	-	-	IM_2	-	$IM_{2/2}$	-	-	$IM_2\ (\text{TFA})$

- An equilibrium step from PO_1 to BP_3 is possible as an alternative to the protonation step. The column "BP_3 prot." then has an "eq." entry.

- The reaction pathway towards BP_4 might also branch off at IM_3, instead of IM_2, denoted in the "BP_4 pos." column.

- Reactions to byproducts can also be hydration reactions, that is, they are dependent on the water concentration in first order. This is marked with "(hyd.)" in the $BP_{5/6/7}$ column.

- There might exist a third byproduct, BP_7.

- Reactions can be independent on the TFA concentration, denoted by "(w/o TFA)".

- Reaction orders can additionally be estimated for the reaction to ART (m_{ART}), and to BP_4 (m_{BP_4}). If BP_4 is formed via an equilibrium step, the forward and reverse orders are both estimated ($m_{BP_4}^{f/r}$).

- An additional intermediate can appear, IM_5. It acts either as an equilibrium resting state, whose forward and reverse reactions are acid-catalyzed, or as a further intermediate on the reaction path way towards ART. The first one is active when in the columns "IM_5 pos." and "ART pos." different species are mentioned. And the second one is active when the mentioned species in both columns are the same.

- Species IM_2 and IM_3 can form equilibrium, denoted by "eq." in the "IM_3" column. The reverse reaction, i.e., from IM_3 to IM_2 might be independent on TFA, specified as "(rev. w/o TFA)" in the IM_3 column.

- The reaction that involves the consumption of oxygen might be moved from starting at IM_2 to IM_3, denoted by "(O_2)".

- If in the reaction forming ART, oxygen in consumed, it is specified in brackets, if the reaction is TFA dependent, "(TFA)", or not, "(w/o TFA)"

The results for the extension set of model candidates are given in Table C.8.

Table C.8: Summary of best results of parameter estimation runs for extension set of model candidates, Tables C.6 and C.7. The number of model parameters is the number of non-zero estimated model parameters, with the original number of model parameters in brackets. Note that the rows correspond to the best estimation run in the sense of the objective function from the multi-start approach.

ID	#θ	RSS	RSS_{conti}	RSS_{batch}	$\hat{\sigma}^2$	AIC_c
31	8 (11)	0.37	0.210	0.162	6.19×10^{-4}	−4415
32	9 (10)	0.39	0.070	0.320	6.48×10^{-4}	−4390
33	7 (9)	0.17	0.080	0.088	2.80×10^{-4}	−4896
34	10 (12)	0.17	0.080	0.088	2.80×10^{-4}	−4890
35	7 (8)	0.18	0.097	0.086	3.05×10^{-4}	−4847
36	7 (9)	0.18	0.097	0.086	3.05×10^{-4}	−4845
37	9 (11)	0.18	0.097	0.086	3.05×10^{-4}	−4841
38	9 (11)	0.17	0.078	0.089	2.77×10^{-4}	−4897
39	10 (12)	0.32	0.105	0.214	5.31×10^{-4}	−4506
40	9 (11)	0.21	0.121	0.086	3.45×10^{-4}	−4767
41	10 (13)	0.16	0.072	0.089	2.69×10^{-4}	−4912
42	12 (15)	0.16	0.072	0.089	2.69×10^{-4}	−4908
44	9 (10)	0.17	0.081	0.088	2.81×10^{-4}	−4891
45	10 (11)	0.17	0.081	0.088	2.81×10^{-4}	−4889
46	10 (11)	0.16	0.073	0.089	2.71×10^{-4}	−4912
47	10 (11)	0.17	0.080	0.089	2.80×10^{-4}	−4891
48	11 (12)	0.17	0.080	0.089	2.80×10^{-4}	−4889
49	9 (12)	0.17	0.081	0.088	2.82×10^{-4}	−4886
50	11 (13)	0.16	0.074	0.086	2.66×10^{-4}	−4918
51	11 (14)	0.17	0.081	0.088	2.82×10^{-4}	−4882
52	9 (12)	0.16	0.074	0.087	2.68×10^{-4}	−4917
53	8 (10)	0.25	0.134	0.115	4.14×10^{-4}	−4659
54	8 (10)	0.19	0.090	0.104	3.22×10^{-4}	−4810
55	8 (9)	0.46	0.223	0.238	7.67×10^{-4}	−4291
56	9 (11)	0.17	0.077	0.095	2.86×10^{-4}	−4879
57	8 (9)	0.28	0.136	0.147	4.71×10^{-4}	−4584
58	9 (10)	0.28	0.173	0.103	4.59×10^{-4}	−4597
59	10 (11)	0.17	0.081	0.093	2.89×10^{-4}	−4873
60	8 (10)	0.19	0.086	0.101	3.11×10^{-4}	−4831
61	8 (11)	0.22	0.107	0.117	3.72×10^{-4}	−4721
62	8 (11)	0.23	0.107	0.121	3.80×10^{-4}	−4709
63	6 (9)	0.29	0.182	0.104	4.75×10^{-4}	−4578
64	7 (9)	0.19	0.090	0.104	3.22×10^{-4}	−4813

C.4   Global Sensitivity Analysis

For the uncertain model parameters, standard deviations are determined from the confidence intervals of the parameter estimation, Tables 4.2 and 5.5. The standard deviation of the distribution coefficient C_0 is given in Equation 4.19:

$$\begin{aligned}
C_0 &\sim \mathcal{N}(1.02, 0.013), \\
\widetilde{k_1 a} &\sim \mathcal{N}(1.094, 0.026), \\
\tilde{k}_{PO_1} &\sim \mathcal{N}(7.13, 0.32), \\
\tilde{k}_{PO_y} &\sim \mathcal{N}(0.644, 0.05), \\
k_{PO_x} &\sim \mathcal{N}(0.0105, 4.34 \times 10^{-4}), \\
l_{opt} &\sim \mathcal{N}(0.178, 4.85 \times 10^{-3}), \\
m_{IM_2} &\sim \mathcal{N}(2.646, 8.93 \times 10^{-3}), \\
k_{PO_1 \cdot BP_3} &\sim \mathcal{N}(424.2, 26.56), \\
k_{PO_1 \cdot IM_2} &\sim \mathcal{N}(880.3, 25.10), \\
k_{IM_{2c} \cdot BP_5} &\sim \mathcal{N}(0.682, 0.036), \\
k_{IM_{2b} \cdot BP_4} &\sim \mathcal{N}(0.887, 0.066), \\
k_{IM_{2c} \cdot ART} &\sim \mathcal{N}(30.07, 1.32).
\end{aligned} \tag{C.22}$$

C.5   Process Optimization

The optimized parameters of the process optimization are given in Tables C.9 and C.10.

Table C.9: Optimized parameters of process optimization for nominal settings. A * indicates that the value has been fixed during optimization.

#	l_{photo} cm	l_{syn} cm	$\dot{V}_{1,0}$ ml/min	$[DHAA]_0$ mol/l	$x_{O_2,0}$ 1	$[DCA]$ mmol/l	P_{LED} %	$[TFA]$ mol/l
1	400^*	700^*	0.140	0.000	1.0	0.500	64	0.099
2	400^*	700^*	0.154	0.200	1.0	0.554	73	0.089
3	85	1000	0.071	0.000	1.0	0.850	100	0.071
4	110	1000	0.087	0.050	1.0	0.850	100	0.070
5	173	1000	0.116	0.200	1.0	0.850	100	0.068
6	280	1000	0.162	0.400	1.0	0.850	100	0.065
7	400^*	700^*	0.091	0.000	1.0	0.428	50	0.067
8	400^*	700^*	0.094	0.050	1.0	0.440	52	0.066
9	88	1000	0.064	0.000	1.0	0.850	100	0.065
10	116	1000	0.080	0.050	1.0	0.850	100	0.064
11	183	1000	0.108	0.200	1.0	0.850	100	0.061
12	400^*	700^*	0.400	0.500	1.0	0.850	100	0.137
13	488	119	0.400	0.500	1.0	0.850	100	0.400
14	400^*	700^*	0.400	0.500	1.0	0.850	100	0.119
15	745	0	0.400	0.500	1.0	0.850	100	0.400

Table C.10: Optimized parameters of process optimization for robust settings. A * indicates that the value has been fixed during optimization.

Normed $\mathbb{V}[STY]$	l_{photo}	l_{syn}	$\dot{V}_{l,0}$	$[DHAA]_0$	$x_{O_2,0}$	$[DCA]$	P_{LED}	$[TFA]$
1	cm	cm	ml/min	mol/l	1	mmol/l	%	mol/l
0.08	628	343	0.293	0.467	1.0	0.638	85	0.218
0.28	627	209	0.375	0.496	1.0	0.799	98	0.353
0.34	617	183	0.384	0.498	1.0	0.820	99	0.381
0.43	600	162	0.392	0.499	1.0	0.836	99	0.393
0.48	588	152	0.395	0.499	1.0	0.841	100	0.396
0.50	583	148	0.396	0.499	1.0	0.842	100	0.397
0.55	570	142	0.397	0.500	1.0	0.845	100	0.398
0.77	525	128	0.399	0.500	1.0	0.849	100	0.400
0.87	509	124	0.400	0.500	1.0	0.849	100	0.400
0.91	502	122	0.400	0.500	1.0	0.850	100	0.400
0.97	492	120	0.400	0.500	1.0	0.850	100	0.400
0.98	490	120	0.400	0.500	1.0	0.850	100	0.400
0.99	489	120	0.400	0.500	1.0	0.850	100	0.400
1.00	488	119	0.400	0.500	1.0	0.850	100	0.400
1.00	488	119	0.400	0.500	1.0	0.850	100	0.400